PhD Thesis

# Generation and characterization of spatially structured few-photon states of light

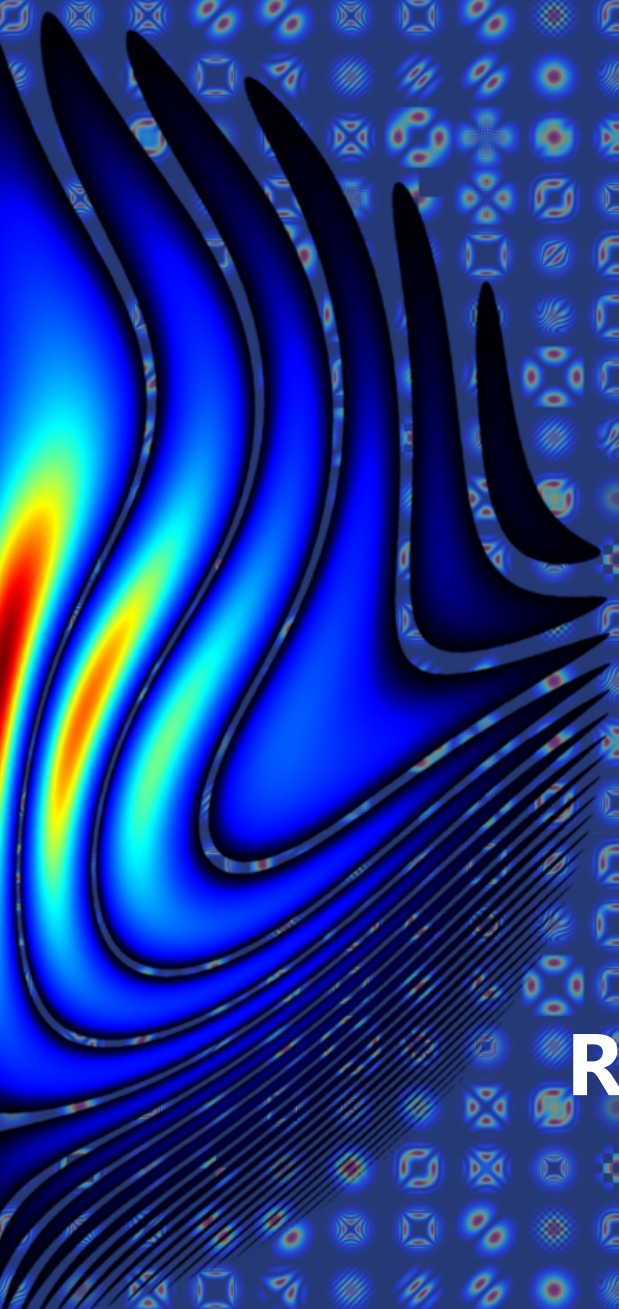

Radosław Chrapkiewicz

# Generation and characterization of spatially structured few-photon states of light

By

RADOSŁAW CHRAPKIEWICZ


Faculty of Physics
UNIVERSITY OF WARSAW

PhD Thesis
2015

Supervisor: dr hab. Wojciech Wasilewski

# ABSTRACT

The present doctoral dissertation discusses the results of research on the characterization of spatial structure and statistical properties of few-photon states of light generated i.a. with the use of a new source based on multimode atomic memory. The dissertation comprises nine chapters grouped into the following parts: a literature and theoretical introduction, and three main parts providing the experimental results.

Part I discusses the characteristics of a scientific complementary metal-oxide semiconductor camera equipped with an image intensifier (I-sCMOS) constructed by our group. We provide theoretical models of saturation of photon-number-resolving detectors which relate qualitatively to our camera. We perform experimental tomography of the I-sCMOS camera and use its results for high-fidelity reconstruction of the original statistics of the impinging light.

In Part II we present an atomic memory setup in warm rubidium vapors where the write-in and readout occur due to collective Raman scattering. The memory is able to store information about the spatial structure of light. We describe the experimental setup thoroughly, with particular attention to the filtering system. We characterize multimode Raman scattering and investigate the storage performance of the memory which is limited by diffusional decoherence. We demonstrate spatial correlations between delayed Stokes and anti-Stokes photons. Using the I-sCMOS camera together with an advanced filtering system we observe spatial correlations down to single atomic excitations per memory mode.

In Part III we discuss the use of the I-sCMOS camera to observe the Hong-Ou-Mandel two-photon interference with spatial resolution. We study the influence of finite spatial distinguishability of photons on the interference results, which leads us to measurements of the local spatial structure of a single photon.

We observe and examine closely the following relatively unexplored phenomena. In Part I we investigate seemingly nonclassical effects in measurements of photon counts statistics on the camera. In Part II we are the first ones to show multimode Raman scattering in atomic memories. Finally, in Part III we describe the first observation of the Hong-Ou-Mandel effect with spatial resolution which is studied further in terms of finite spatial distinguishability of the interfering photons.

In this thesis, we present the following novel experimental methodology. We use a new-type of I-sCMOS camera. We implement and perform the reconstruction of photon statistics based on tomographic characterization of the detector. We also build an efficient filtering system for photons generated in atomic memory. Moreover, we create an accurate method of measuring diffusion coefficients in atomic memory. We present our own methods of spatial characterization of the properties of light. Eventually, we introduce an entirely novel method: holographic measurement of the phase structure of a single photon using i.a. a specially developed phase reconstruction algorithm.

The presented results fall within the scope of contemporary research in quantum optics and have a number of possible applications, as discussed in the final remarks section.

## STRESZCZENIE

Niniejsza praca doktorska prezentuje wyniki badań poświęconych charakteryzacji struktury przestrzennej i właściwości statystyk kilkufotonowych stanów światła generowanych m.in. z użyciem nowego źródła opartego na wielomodowej pamięci atomowej. Praca składająca się z 9 rozdziałów podzielona jest na wstęp literaturowy i teoretyczny oraz trzy części zawierające merytoryczne wyniki badań.

Kolejno w części I prezentujemy i charakteryzujemy skonstruowany układ kamery sCMOS ze wzmacniaczem obrazu (I-sCMOS). Przedstawiamy teoretyczne modele nasycania detektorów rozróżniających liczbę fotonów, które jakościowo odnoszą się do kamery. Przeprowadzamy eksperymentalną tomografię kamery I-sCMOS a jej wyniki wykorzystujemy do wiernej rekonstrukcji pierwotnych statystyk światła padającego na kamerę.

W części II prezentujemy układ pamięci atomowej w ciepłych parach rubidu, do której zapis i odczyt odbywa się w wyniku kolektywnego rozpraszania Ramana. Pamięć jest w stanie przechować informacje na temat przestrzennej struktury światła. Dokładnie opisujemy układ doświadczalny, w szczególności pod kątem układu filtrowania. Charakteryzujemy wielomodowe rozpraszanie Ramana oraz badamy zdolność przechowywania pamięci ograniczoną dekoherencją dyfuzyjną. Demonstrujemy korelacje przestrzenne pomiędzy opóźnionymi w czasie fotonami Stokesa i anty-Stokesa. Używając kamery I-sCMOS i zaawansowanego systemu filtrowania obserwujemy korelacje przestrzenne aż do reżimu pojedynczych wzbudzeń atomowych na mod pamięci.

W części III wykorzystujemy kamerę I-sCMOS do badania zjawiska interferencji dwufotonowej Hong-Ou-Mandela obserwowanego z rozdzielczością przestrzenną. Studiujemy wpływ skończonej widzialności przestrzennej na wynik interferencji, która służy nam do pomiaru lokalnej struktury przestrzennej pojedynczego fotonu.

Zaobserwowaliśmy i zbadaliśmy następujące słabo zbadane zjawiska. W części I badamy pozorne efekty nieklasyczne w statystykach zliczeń fotonów zmierzonych za pomocą kamery. W części II po raz pierwszy pokazujemy wielomodowe rozpraszanie Ramana w pamięciach atomowych. Natomiast w części III prezentujemy pierwszą obserwację efektu Hong-Ou-Mandela z rozdzielczością przestrzenną, którą następnie badamy pod kątem wpływu skończonej rozróżnialności przestrzennej interferujących fotonów.

Na potrzeby tej pracy zostały stworzone i opracowane następujące, nowe metodologie badawcze. Stosujemy nowego typu kamerę I-sCMOS, opracowujemy rekonstrukcje statystyk fotonów na podstawie tomograficznej charakteryzacji detektora. Konstruujemy skuteczny układ filtrowania fotonów w pamięci atomowej. Tworzymy nową dokładną metodę pomiaru współczynników dyfuzji w pamięci atomowej. Prezentujemy także własne metody charakteryzacji przestrzennej statystycznych właściwości światła. W końcu, pokazujemy zupełnie nowatorską metodę holograficznego pomiaru struktury fazy pojedynczego fotonu, wykorzystującą m.in. specjalnie stworzony algorytm rekonstrukcji fazy.

Zaprezentowane wyniki wpisują się w kontekst współczesnych badań w optyce kwantowej, a także posiadają szereg potencjalnych zastosowań, przedyskutowanych w podsumowaniu pracy.

# ACKNOWLEDGMENTS

This doctoral dissertation presents the results of my four years' work in the Laboratory of Quantum Memories, established by Dr. Wojciech Wasilewski, where I had the privilege of working since its very beginning. I first met Wojtek during pre-academic optical workshops in 2005, and since 2007 our cooperation has proved very fruitful. I am grateful to him for creating exceptional conditions for research and development, from which I have greatly benefited. I also thank Wojtek for the immense amount of knowledge he has relayed to me as well as for camaraderie, great atmosphere of working and for countless hours he spent on teaching and guiding me, which required considerable patience. I feel very fortunate to have been Wojtek's first PhD student.

Special thanks are also due to Prof. Czesław Radzewicz, who not only supervised me during most of my PhD studies but also was my tutor during my individual interfaculty undergraduate studies. It should be stressed that it was him who during my pre-academic scientific workshops in 2005 enthused me with his interest in optics and introduced me to his Ultrafast Phenomena Lab at the beginning of my undergraduate education. In the last ten years he has always offered me advice and his mentorship was of prime importance to me during the initial stages of my academic training.

I would also like to acknowledge my younger colleagues Michał Dąbrowski and Michał Jachura, who have been the only people I have worked with directly at the optical table during my PhD studies and they have always proved reliable and contributed to amiable atmosphere in the lab. Our fruitful and pleasant cooperation has resulted in the co-authorship of scientific papers. I especially appreciate Michał Jachura for a quick introduction to the experiments with spontaneous parametric down-conversion and two-photon interference and for showing me how to turn ordinary descriptions of experiments into small masterpieces. I am also grateful to Prof. Konrad Banaszek and to Dr. Rafał Demkowicz-Dobrzański for their collaboration, which has brought very interesting results and taught me an entirely different approach to solving the investigated problems. I thank Rafał for initiating me to convex programming and to Konrad for his valuable support and for letting me in on the secret of top-level scientific writing.

My work in the Laboratory of Quantum Memories was a very enjoyable experience thanks to perfect work culture and easily accessible assistance. I am also grateful to my colleagues from the Ultrafast Phenomena Lab for their help and friendly cooperation. I acknowledge Michał Parniak for always being helpful and for numerous inspiring discussions we have had. Many thanks, particularly for help with the electronics, go to Jarosław Iwaszkiewicz, Dr. Marcin Piasecki, Janusz Rogoziński, and Marek Trzaskowski. Paweł Spryszak quickly provided me with reliable equipment and apparatus. C. Samojłowicz helped with patent procedures. I would also like to thank M. Dąbrowski, K. Gołos, M. Jachura, F. Kiałka and M. Parniak for reading this dissertation and providing valuable comments and corrections, and Szymon Żuchowski for the language editing of the manuscript.

Last but not least I would like to express my gratitude to my family for their continuous support. I am particularly grateful to my dear wife Gosia for her inexhaustible patience with my time-consuming optical hobby as well as for constant motivation for work.

**Financial support**

My experimental work involved considerable expenditure and would not have been possible, had it not been for the financial support of several institutions. The experiments were part of research grants of the National Science Center. The research described in Part II of the present dissertation was financed by the Sonata grant no. DEC-2011/03/D/ST2/01941 with Dr. Wojciech Wasilewski as the its principal investigator. The research described in Parts I and III was financed by the Preludium grant no. DEC-2013/09/N/ST2/02229 with myself as its principal investigator. During my PhD studies I was supported by the Foundation for Polish Science, first as a holder of the scholarship of the TEAM Programme supervised by Prof. Konrad Banaszek, and then as an awardee of the START Programme. I appreciate the remarkable support from the Modern University scholarship at the University of Warsaw as well as the SPIE Optics and Photonics Education Scholarship.

Apart from the aforementioned sources my research together with the necessary equipment were financed by such projects as the National Laboratory for Quantum Technologies, PhoQuS@UW (Grant Agreement no. 316244), Polish NCBiR under the ERA-NET CHIST-ERA project QUASAR, and Iuventus Plus (Ministry of Science and Higher Education of Poland).

## Submitted papers

1. **R. Chrapkiewicz**, M. Jachura, K. Banaszek, W. Wasilewski, "Hologram of a single photon", pre-print: arXiv:1509.02890 (2015).
2. M. Jachura, **R. Chrapkiewicz**, R. Demkowicz-Dobrzański, W. Wasilewski, K. Banaszek, "Mode engineering for realistic quantum-enhanced interferometry", pre-print: arXiv:1504.05435 (2015).

## Journal papers

1. M. Dąbrowski, **R. Chrapkiewicz**, W. Wasilewski, "Magnetically tuned, robust and efficient filtering system for spatially multimode quantum memory in warm atomic vapors", Journal of Modern Optics, Special Issue: Qauntum Memories (published online) (2015).
2. M. Jachura, **R. Chrapkiewicz**, "Shot-by-shot imaging of Hong–Ou–Mandel interference with an intensified sCMOS camera", Optics Letters 40, 1540-1543 (2015). (2015).
3. M. Dąbrowski, **R. Chrapkiewicz**, and W. Wasilewski, "Hamiltonian design in readout from room-temperature Raman atomic memory", Optics Express 22, 26076-26091 (2014).
4. **R. Chrapkiewicz** , W. Wasilewski, and K. Banaszek, "High-fidelity spatially resolved multiphoton counting for quantum imaging applications", Optics Letters 39, 5090-5093 (2014).
5. **R. Chrapkiewicz**, "Photon counts statistics of squeezed and multimode thermal states of light on multiplexed on-off detectors", Journal of the Optical Society of America B 31, B8-B13 (2014).
6. **R. Chrapkiewicz**, W. Wasilewski, and C. Radzewicz, "How to measure diffusional decoherence in multimode Rubidium vapor memories?", Optics Communications 317, 1-6 (2014).
7. **R. Chrapkiewicz** and W. Wasilewski, "Generation and delayed retrieval of spatially multimode Raman scattering in warm rubidium vapors", Optics Express 20, 29540-29552 (2012).
8. **R. Chrapkiewicz**, W. Wasilewski, "Multimode Spontaneous Parametric Down-Conversion in a Lossy Medium", Journal of Modern Optics 57, 345-355 (2010).

## Conference papers

1. **R. Chrapkiewicz**, M. Dąbrowski and W. Wasilewski, "High-Capacity, Single-Photon-Level Warm Atomic Memory Storing up to 120 Spatial Modes", CLEO: 2015 Postdeadline Paper Digest, paper JTh5B.8 (2015).

2. M. Dąbrowski, M. Parniak, D. Pęcak, **R. Chrapkiewicz** and W. Wasilewski „Spontaneous and parametric processes in warm rubidium vapours", Latvian Journal of Physics and Technical Sciences 51 (5), 21–34 (2014).

3. **R. Chrapkiewicz** and W. Wasilewski, „Multi-Spatial-Mode Optical Memory with Collective Raman Scattering Interface", OSA Technical Digest Quantum Information and Measurement (QIM), paper: W6.18 (2013).

4. **R. Chrapkiewicz** and W. Wasilewski, „Spatially multimode Raman scattering: optical memory and new, direct method for measuring diffusion", International Quantum Electronics Conference (IQEC), paper: IA_P_19 (2013).

5. **R. Chrapkiewicz** and W. Wasilewski, „From the Parametric Down-Conversion to the Raman Scattering: Nonlinear and Quantum Phenomena in Lossy Media", OSA Technical Digest Frontiers in Optics (FiO), paper: FWY3 (2011).

## Patents pending

1. **R. Chrapkiewicz**, W. Wasilewski, "Przestrajalny, wąskopasmowy filtr optyczny do filtrowania wiązek laserowych i sposób filtrowania wiązek laserowych", P.408059, Polish Patent Office, Warsaw (29.04.2014).

2. **R. Chrapkiewicz**, W. Wasilewski, "Układ pomiarowy do wyznaczania położenia płaszczyzny ogniskowej i długości ogniskowej układu optycznego oraz sposób wyznaczania położenia pła szczyzny ogniskowej i długości ogniskowej układu optycznego", P.412267, Polish Patent Office, Warsaw (8.05.2015).

## Miscellaneous

1. M. Jachura, **R. Chrapkiewicz**, "Coalescing Photon Pairs Caught on Camera", Optics & Photonics News 12 (Optics in 2015), 42 (2015).

# Contents

CHAPTER 1

# OVERVIEW AND THEORETICAL INTRODUCTION

Light has always been useful and informative in studying nature, principally in experiments involving imaging techniques. At the same time, the light's nature itself motivated research in physics which led to the concept of photons – single light corpuscles (Planck, 1901; Einstein, 1905). Since then scientists have developed a very precise and experimentally confirmed description of photons and their interaction with matter – the quantum electrodynamics theory. Likewise, advances in theoretical and experimental studies on optical photons ushered the field of quantum optics.

In this thesis we present methods conceived for generation and characterization of weak light with a spatial structure, quantify the nonclassical properties of light in imaging experiments and report on the construction of a novel source of spatially multimode photons based on a high-capacity atomic memory. In all of the presented experiments the key role was played by cameras sensitive to single photons.

Below we briefly review the most important aspects of quantum optics relevant to this thesis, give the motivation for this work and introduce the key topics. Further in this chapter we provide important theoretical background to aid the understanding of the results presented in the subsequent parts of the thesis.

## 1.1 Important applications of nonclassical light

Quantum optics has played a leading role in both validation of principles of quantum mechanics and in applying nonclassical effects which could outperform classical devices and protocols. Experiments in quantum optics are feasible for a couple of reasons. Firstly, the optical domain benefits from relatively small decoherence effects as photons weekly interact with the environment and additionally they are not polluted by thermal noise within the optical frequency range. Secondly, nonclassical optical effects could be obtained in a laboratory with the use of rapidly evolving optical technologies after the invention of a laser (Maiman, 1960). Moreover, experiments can utilize standard optical laboratory equipment – for instance the transformations on qubits implemented in a polarization state of photons can be performed using merely linear optics elements such as polarizers and wave plates.

### 1.1.1 Validation of quantum mechanics with photons

There have been numerous tests of the foundations of quantum mechanics with the use of photons. The first challenge was to prove the existence of photon as a particle. Initially, that issue was not entirely clear as the photoelectric effect explained by Einstein (1905), who coined the term of "Lichtquant", can be described in a semiclassical theory with a classical light and nonclassical atoms (Mandel and Wolf, 1995). The existence of photons was ultimately confirmed by Kimble *et al.* (1977), who observed the anti-bunching effect showing that light quanta are indivisible particles.

Entanglement is perhaps the most intriguing and counter-intuitive quantum mechanical phenomenon. Einstein, Podolsky and Rosen (EPR) in their seminal paper (Einstein *et al.*, 1935) raised the issue of a contradiction between physical reality and the completeness of the quantum mechanical description of an entangled system, now called the EPR paradox. In their original formulation they considered a state of two distanced particles entangled in continuous variables of positions and momenta. Despite the authors' claims that the quantum mechanical description may have been incomplete, the EPR paradox has been experimentally demonstrated using photons (Howell *et al.*, 2004) and in particular photons imaged by single-photon-sensitive cameras (Moreau *et al.*, 2014).

The EPR paradox was also reformulated by Bell (1964) to match systems with the entanglement between discrete degrees of freedom, such as spin. He derived inequalities whose violation proves nonclassical behavior of a system that cannot be explained by any unknown and inaccessible parameters, called hidden variables. The violation of Bell's inequalities became the subject of many experiments with photons, e.g. (Tittel *et al.*, 1998; Dada *et al.*, 2011; Giustina *et al.*, 2013), and now it is considered as a standard test for entanglement between the polarization states of photons.

Nonetheless some experimental imperfections in these realizations undermined their validity and have been perceived as loopholes. For instance a finite efficiency of the detectors applied, that used to be low for photons, may be considered as a source of an erroneous interpretation of the result as undetected particles might change the statistics. However, with the state-of-the-art superconducting detectors (Hadfield, 2009) this loophole can be closed. Nowadays there should no longer be any skepticism concerning experimental proofs of Bell's inequalities violations as the most important loopholes have already been closed (Salart *et al.*, 2008; Giustina *et al.*, 2013). In particular this year Hensen *et al.* (2015) has witnessed the first entirely loophole-free experiment using electron spins and soon after that loophole-free experiments have been reported for photons (Shalm *et al.*, 2015; Giustina *et al.*, 2015).

### 1.1.2 Quantum communication

Another motivation for research with single light quanta are their possible applications. One can see a significant gain of using single photons instead of classical beams in data transmission. Namely, the security in communication links can be guaranteed by the laws of quantum mechanics (Gisin *et al.*, 2002) as any attempt of single photon interception inevitably leads to its loss. Therefore single photons (Bennett and Brassard, 1984) or alternatively their entangled states (Ekert, 1991) are a vital resource to a reliable distribution of a cryptographic key.

In the former method, proposed by Bennett and Brassard (1984) and known as the BB84 protocol, information sent to a receiver is encoded in the polarization state of photons. The sender randomly switches a basis of a qubit coding, e.g. between linear and circular polarization. The receiver measuring photons' polarization state also randomly switches bases. The sending and receiving polarization basis are announced publicly and then bits sent in about a half of the cases where the

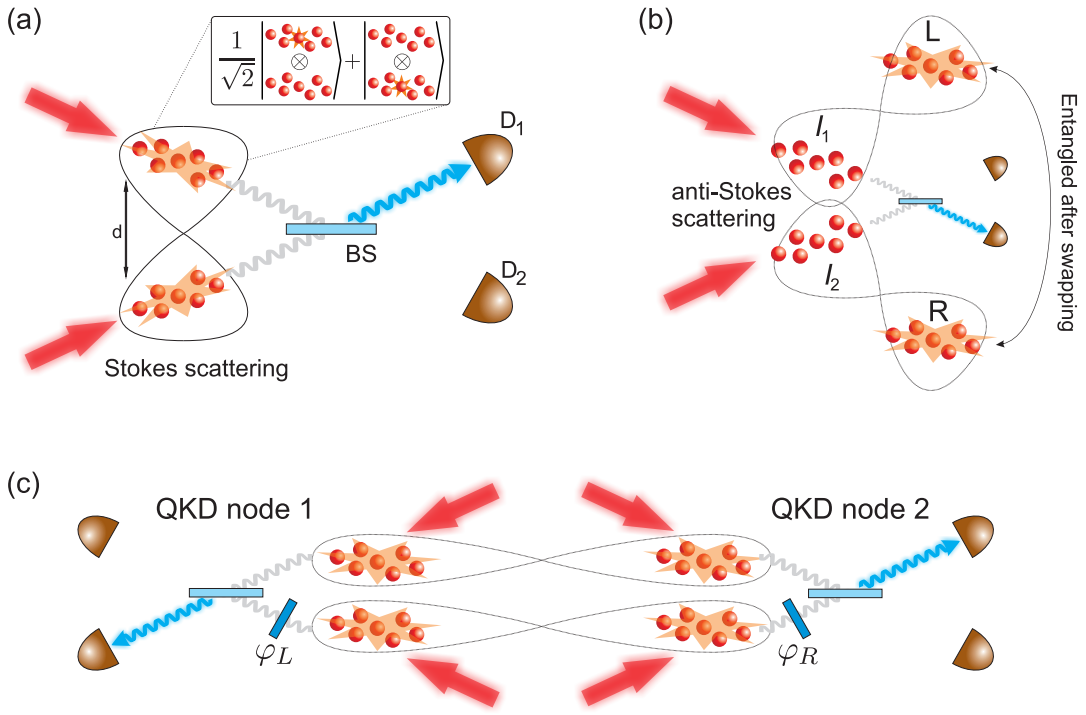


Figure 1.1: Principles of the DLCZ protocol for long distance quantum communication (Duan *et al.*, 2001). (a) Two ensembles of atoms spaced by $d$ can be entangled in the Raman scattering process creating superposition of excitations (inset). The entanglement generation is conditioned on a Stokes photon detection on one of the detectors $D_1, D_2$ after a beam splitter (BS). (b) The entanglement can be swapped onto more distanced ensembles $L$ and $R$ by reading out excitations from $I_1, I_2$ in the anti-Stokes scattering. (c) Two sets of entangled ensembles can be used for the quantum key distribution (QKD) in the modified Ekert protocol where phase shifts $\varphi_{L,R}$ changes the basis of measurement.

bases coincidentally agreed are treated as a secret key. Any eavesdropping attempt causes unavoidable errors and can be revealed.

The latter method, the Ekert protocol named after its inventor (Ekert, 1991), utilizes entangled states distributed between two communicating nodes and applies a similar measurement method. While the sender is performing a measurement in its node, it projects the state in the remote, receiver node. The protocol assumes a prior creation of the entanglement between the nodes. At the moment it remains a challenging task over long distances due to the attenuation of optical fibers and inevitable photon losses.

### 1.1.3 Quantum key distribution over long distances with atomic ensembles

In classical communication networks the losses are typically compensated by laser amplifiers distributed ca. every 100 km of the network. The quantum states, however, cannot be amplified or cloned in the classical sense (Wootters and Żurek, 1982), thus another approach has to be applied to make quantum communication networks feasible. In 2001 a protocol of long distance quantum communication has been proposed (Duan *et al.*, 2001). The DLCZ protocol, named after its founders, requires atomic ensembles used as memories which can store information in the form of atomic excitation.

The concept of the DLCZ protocol is sketched in Fig. 1.1. At first, the two ensembles are en-

tangled by scattering a single photon in the Raman process that transfers the atoms into an excited state[1]. Entangled state is created once the photon is detected after a beam splitter as depicted in Fig. 1.1(a). One detection event implies that only one, either a first or second ensemble, was excited assuming the scattering probability was kept very low. Application of the beam splitter changes the measurement basis into a superposition of two ensemble modes[2]. In consequence we obtain an entangled state in which either first ensembles was excited and the second remained in the ground state or *vice versa*. Such an operation can be performed on ensembles distanced up to a range of transmission of the Raman scattered photon.

Thereafter, to increase the communication distance, the entanglement can be swapped between two pairs of ensembles. For the sake of clarity of the description let us call the ensembles consecutively $L, I_1, I_2, R$, where both $L, I_1$ and $I_2, R$ are entangled pairwise in the procedure described above. As illustrated in Fig. 1.1(b) the goal is to entangle ensembles $L$ and $R$ at a distance doubling the initial communication range. To achieve this one can transfer atoms in ensembles $I_1$ or $I_2$ back into the ground state by scattering a single photon in the anti-Stokes Raman process. Applying similar procedure with a beam splitter, as shown in Fig. 1.1(b), detection of a single photon means that excitation in $I_1$ or $I_2$ group has been transferred into a ground state. The resulting state can be represented as a coherent superposition of two scenarios. In the first one, if detected photon was emitted by $I_1$, it means that $L$ remained in the ground state while $R$ in the excited state. In the second one, if the photon was generated by $I_2$ ensemble, the opposite occurs. Eventually the ensembles $I_1, I_2$ are left in the ground state and the atoms in $L, R$ are now entangled.

The Ekert protocol in its direct form can be applied to the polarization or spin entangled state. It can be also adopted here if one uses two pairs of entangled ensembles. As depicted in Fig. 1.1(c), coincidental detection of photons in the anti-Stokes scattering process in both pairs of ensembles combined by beam splitter transformation corresponds to the measurements on entangled qubit states. Additional inclusion of the phase $\varphi_L$ and $\varphi_R$, marked in the scheme in Fig. 1.1(c), is equivalent to the measurement on a different basis, required in the Ekert protocol.

The processes of entanglement, its swapping and communication are probabilistic, yet they can be repeated until success. Essentially, repetitions do not require starting the whole process from the beginning as an excitation, once created, is stored until readout. Thus, DLCZ protocol provides a realistic method for creating a distanced entanglement bypassing the limits of attenuation range of communication channels. In this thesis the Raman, light-matter interface and the atomic storage proposed by Duan *et al.* (2001), are studied in the context of increasing ensemble storage capacity by extending its operation onto many spatial modes (Chrapkiewicz and Wasilewski, 2012; Chrapkiewicz *et al.*, 2015a).

Till now the quantum cryptography has gone through its first commercially sold implementations (Moore, 2007). Perhaps robust experimental implementations of protocols such as DLCZ may lead to further dissemination of this technology and may facilitate creation of quantum communication networks (Kimble, 2008).

### 1.1.4 Quantum computing

The important task of contemporary quantum engineering is to build a universal quantum computer (Steane, 1998). Such computer would have the ability to perform unitary gate operation on

[1] We shall formally describe the excited state of an ensemble in Sec. 1.5.4.

[2] For convenience of readers unfamiliar with this topic we discuss the beam splitter transformations in the context of photon interference in Sec. 1.6.1.

qubits, particularly in superposition states, such as $(|0\rangle + |1\rangle)/\sqrt{2}$. Operations on coherent combinations of $|0\rangle$ and $|1\rangle$ on multiple inputs of the quantum processor tend to be perceived as simultaneous processing of all combinations of 0, 1 seeding each input. In a generic case that would result in superpositions of different results on registers outputs that would be hard to interpret. However, a few algorithms returning intelligible results have been proposed. For instance, the most famous Shor's algorithm promises essential speed-up in a prime factorization of large numbers (Shor, 1997) which is the cornerstone of contemporary asymmetric encryption systems using publicly announced and private keys (Rivest *et al.*, 1978). The crux of the Shor's algorithm is to translate prime factorization into a problem of searching for periodicity of some functions and which, in turn, can be tackled by the quantum Fourier transform.

Implementations of general quantum logic gates require interaction between at least two qubits. This requirement may also imply that such qubits are more prone to decoherence while interacting with the environment. The most common implementations up to date include quantum gates on trapped ions (Haffner *et al.*, 2008). They achieved control of a dozen or more ions probably saturating the prospects of scalability of this technology. Another approach is to use superconducting gates and qubits (Blais *et al.*, 2004; Kelly *et al.*, 2015). Arguably the first "quantum computer" called *D-wave* has been sold. It is based on superconducting qubits (Merali, 2011), yet it operates rather in a manner of a quantum simulator solving multiparameter optimization problems with the use of quantum annealing (Johnson *et al.*, 2011). A recent employment of J. Martinez's group by the Google company to work on their own universal quantum computer on superconducting qubits (Simonite, 2014) shows that this technology is, nevertheless, considered very promising.

In this pursuit to build a quantum computer photons play an increasingly important role. Interaction between single photons can be achieved in highly non-linear media, such as Rydberg atoms (Peyronel *et al.*, 2012) or surface plasmons (Chang *et al.*, 2007). However, an interesting avenue to achieve universal quantum computing merely requires linear optical devices (Knill *et al.*, 2001). Quantum gates can be realized in a probabilistic way, and the nonlinear interaction is replaced by multiphoton interference, measurements, post-selection and memories (O'Brien, 2007). In practice linear optics quantum computing requires indistinguishable photons that can interfere, interferometers with adjustable phase and efficient photon detectors. Recently there has been large progress in increasing quantum efficiency of photodetectors using superconductors (Hadfield, 2009). Moreover, integrated optical circuits of scalable complexity can be already manufactured using femtosecond laser writing in glasses (Davis *et al.*, 1996).

Multiphoton interference in linear optics circuits can be utilized to simpler and more realistic applications, such as simulations. Currently much effort is devoted to the class of experiments called boson sampling (Crespi *et al.*, 2013; Spagnolo *et al.*, 2014; Spring *et al.*, 2013). The name refers to the sampling of a multi-photon bosonic wave function subjected to a random-walk propagation in an integrated system of waveguides and interferometers mentioned above. The result of such propagation is hard to calculate, yet it may be used to emulate other physical systems (Peruzzo *et al.*, 2010a; Aspuru-Guzik and Walther, 2012).

The missing brick to realize both quantum computation and simulation with linear optics is the high-repetition source of multiple, indistinguishable photons. Multiplexed sources based on nonlinear crystals require accidental concurrent emission of photons from many stochastic sources whose probability decreases exponentially with a desired number of photons. Nunn *et al.* (2013) proposed a method utilizing multiple atomic memories to synchronize multiple single photon sources. As we show in this thesis a source of multiple synchronized photons can be obtained using just a single, spatially multimode atomic memory (Chrapkiewicz *et al.*, 2015a).

### 1.1.5 Quantum metrology

The last major application of photons we discuss in this introductory chapter are sensitive measurements whose precision can benefit from preparation of light in nonclassical states (Giovannetti *et al.*, 2006). The most commonly considered class of experiments where quantum states are advantageous over classical states can be expressed as a phase estimation problem. As light acquires phase along its propagation in a medium, one may estimate the properties of a medium, such as density or length. The problem can be tackled using interferometry. For instance, an investigated object placed in one arm of the interferometer influences the ratio of intensities or numbers of photons at one output to the other. Those measurements give information about the introduced phase change.

Fluctuations in the number of photons in the coherent light scale as a square root of the mean number of photons used. This stands for an ultimate classically available precision of the intensity measurements which translates into the uncertainty of phase. In applications where one cannot afford applying high light intensities, maximum information per photon has to be extracted. This restriction applies to the probing of delicate materials (Wolfgramm *et al.*, 2012), measurements on living organisms (Taylor *et al.*, 2013) and raising sensitivity of interferometers chasing for gravitational waves (LIGO Collaboration, 2013). Light prepared in nonclassical squeezed or entangled states can bring enhancement in sensitivity beyond classical limitations (Giovannetti *et al.*, 2006; Demkowicz-Dobrzański *et al.*, 2012, 2014).

The highest sensitivity per photon in the quantum interferometry can be achieved with so called N00N states. This name originates from the mathematical representation of these states $(|N,0\rangle + |0,N\rangle)/\sqrt{2}$ which denotes a superposition of $N$ photons in one interferometer arm and none in the other or *vice versa*. Such state acquires phase difference between the arms $N$-times faster than a single photon used in a similar situation. This results in $\sqrt{N}$ times higher precision *per* used photon as compared to any multiple-single-photon or best classical experiment (Demkowicz-Dobrzański *et al.*, 2014). Recently high-photon-number, i.e. $N \leq 5$, states have been generated for the first time by mixing the coherent states with squeezed vacuum (Afek *et al.*, 2010). The N00N states with $N = 2$ are relatively straightforward to produce and they will be discussed further in this thesis. Such states yielding an increase of a precision by factor of $\sqrt{2}$ found numerous proof-of-principle demonstrations, e.g. (Rarity *et al.*, 1990; Crespi *et al.*, 2012; Wolfgramm *et al.*, 2012; Jachura *et al.*, 2015).

### 1.1.6 Imaging with nonclassical light

Another large class of measurements whose sensitivity can be raised due to nonclassical effects is imaging. As we indicated in the beginning, imaging has been the primary application of optics and its interconnection with quantum optics is the natural course of things. In particular the above-mentioned techniques of quantum metrology and N00N states can be used in phase-contrast microscopy to reduce noise of a created image (Ono *et al.*, 2013). Another way to suppress the noise of images formed by weak light is to use two-mode squeezed states to obtain a spatially resolved reference on the fluctuations of the number of photons across the image (Brida *et al.*, 2010). Such treatment can reduce noise below the shot noise level, decreasing effectively the number of photons needed to form a sharp image.

However the crucial issue nowadays, especially for biologists, is to raise the resolution of microscopy beyond the diffraction limit. This limitation can be already circumvented by the methods which brought the Nobel Prize in chemistry to their discoverers in 2014. Nevertheless, these meth-

ods of fluorescence microscopy are subject to numerous restrictions. In particular they may require special preparation of a sample or extremely high light intensities (Hell and Wichmann, 1994; Huang *et al.*, 2009). Nonclassical phenomena can also aid to solve this problem, e.g. by utilizing the photon-anti bunching effect (Paul, 1982) to localize single-photon emitters beyond the diffraction limit (Schwartz and Oron, 2012; Schwartz *et al.*, 2013; Cui *et al.*, 2013; Gatto Monticone *et al.*, 2014). Possible applications of N00N states may raise resolution of imaging techniques. Tsang (2009) proposed a measurement method that raises the density of interference fringes to sub-wavelength regime that already went through an experimental proof-of-principle demonstration (Rozema *et al.*, 2014).

Another large class of experiments called ghost imaging utilizes entanglement to create an image with light which has never gone through an imaged object (Pittman *et al.*, 1995). The object is probed by entangled photon detected by a single-pixel bucket detector. The signal on the detector triggers an intensified camera collecting counterpart photons that form the actual image (Morris *et al.*, 2015). Such method can find its application in scenarios where one of the entangled photons is in a frequency range where high-resolution cameras do not exist as for instance in the terahertz regime (Stantchev *et al.*, 2015) important for security scanning. Finally, let us mention a recent quantum imaging technique that does not detect photons that have gone through an object (Lemos *et al.*, 2014) which opens an entirely new class of imaging experiments.

### 1.1.7 Spatial structure and localization of photons

Apart from imaging techniques the spatial structure of single photons is an extensively explored resource itself, studied in a context of both fundamental physics and applications. Experiments with photons in Laguerre-Gaussian modes carrying orbital angular momentum are of particular interest. Recently, Fickler *et al.* (2012) set a record for the entanglement between photons of angular momentum up to $300\hbar$ which raises an important question of the upper, macroscopic limits of observable nonclassical phenomena. On the other hand Giovannini *et al.* (2015) demonstrated that spatial structure of photons effectively slows down their propagation speed.

In terms of applications, structured photons are important for free-space quantum key distribution channels (Walborn *et al.*, 2006; Vallone *et al.*, 2014) that enable establishing communication links even in turbulent air (Krenn *et al.*, 2015) and may be relevant for some quantum computation schemes (Abouraddy *et al.*, 2012). There are several characterization methods of spatially structured photons based on tomographic techniques such as self-referencing using an inverting Sagnac interferometer (Smith *et al.*, 2005) or weak values measurements (Lundeen *et al.*, 2011). In this thesis we introduce and discuss a method (Chrapkiewicz *et al.*, 2015b) that directly resorts to photon-localization techniques, such as scanning fiber coupled detectors (Peeters *et al.*, 2009) or high-resolution, single-photon-sensitive cameras (Chrapkiewicz *et al.*, 2014a; Jachura and Chrapkiewicz, 2015b).

Attention of theoreticians reading this work may be drawn to the fact that localization of photons is a highly complicated issue that has stirred many controversies. Moreover, the definition of the photon wave function has not been clear for a long time. Problems with theoretical description of photons include the definition of its position operator, differences between photon number and energy densities, and unfeasibility of preparing photons in a state where both electric and magnetic field are sharply localized. After a several-decades-long debate on these topics, reviewed in (Keller, 2005; Saari, 2012), a proper description of a photon wave function has been formulated by Białynicki-Birula (1996). Moreover, he correctly ended the discussion on the localization, i.a. pointing out the inaccuracy of the explanations in textbooks (Mandel and Wolf, 1995), concluding that

photons can be localized at best with an exponentially falling tail (Białynicki-Birula, 1998). The finale of the discussion on the wave function and localization of a photon might be the first derivation of uncertainty relations for a photon which remarkably differs from that known for massive particles (Białynicki-Birula and Białynicka-Birula, 2012).

From the experimental point of view, localization of photons is made possible, for instance, by spatially resolving the photoelectric effect, as we show later in this thesis. Here, however, we always localize photons with a resolution lower than the wavelength and we do not approach length scales where the aforementioned problems occur.

## 1.2 Quantum description of a single photon

Photons and their spatial structure are the focal issues of this thesis. In Part III we demonstrate a method to retrieve the single-photon transverse wave function. Below we present a compact quantum mechanical description of a single photon accompanied by the references for more curious readers searching for a deeper insight into a literature. We keep a notation partially consistent with the textbook by Garrison and Chiao (2008) and we refer to some derivations in (Scully and Zubairy, 1997; Gerry and Knight, 2005; Mandel and Wolf, 1995).

### 1.2.1 Quantized field

A quantized electromagnetic (EM) field is described in free space by electric and magnetic field operators[3]. Both operators fulfill the analogous equations as the classical Maxwell and wave equations (Białynicki-Birula, 1996). Here we concentrate only on the effects related to the electric field of the photon. A free-space quantized field operator can be decomposed on plane-waves and polarization components indexed discretely by $s$ is expressed as follows:

$$\hat{\mathbf{E}}(\mathbf{r}) = i\sum_s \int \frac{d^3k}{(2\pi)^3}\sqrt{\frac{\hbar\omega_k}{2\varepsilon_0}}\mathbf{e}_{\mathbf{k},s}e^{i\mathbf{k}\cdot\mathbf{r}}\hat{a}_s(\mathbf{k}) + \text{H.c.}, \tag{1.1}$$

where $\omega_k = c|\mathbf{k}|$ is a frequency associated with the $\mathbf{k}$-vector and $\mathbf{e}_{\mathbf{k},s}$ denotes the unit-length vector of a polarization. $\hat{a}_s(\mathbf{k})$ is the annihilation field operator and together with its Hermitian conjugate $\hat{a}_s^\dagger(\mathbf{k})$, the creation field operator, they obey bosonic commutation relations:

$$[\hat{a}_s(\mathbf{k}), \hat{a}_{s'}^\dagger(\mathbf{k}')] = (2\pi)^3\delta_{ss'}\delta(\mathbf{k}-\mathbf{k}'), \quad [\hat{a}_s(\mathbf{k}), \hat{a}_{s'}(\mathbf{k}')] = 0. \tag{1.2}$$

The Hamiltonian $\hat{H}$ of the quantized EM field is expressed similarly as in classical theory by the square of electric and magnetic field operators and it equals:

$$\hat{H} = \sum_s \int \frac{d^3k}{(2\pi)^3}\hbar\omega_k\hat{a}_s^\dagger(\mathbf{k})\hat{a}_s(\mathbf{k}). \tag{1.3}$$

In Eq. (1.3), $\hbar\omega_k$ stands for the well-known energy of a single photon in plane wave mode, which was initially postulated by Planck. It can be viewed as a weighting factor in the expression for the energy operator which, upon omitting of $\hbar\omega_k$, becomes the operator of the total number of photons:

$$\hat{n} = \sum_s \int \frac{d^3k}{(2\pi)^3}\hat{a}_s^\dagger(\mathbf{k})\hat{a}_s(\mathbf{k}). \tag{1.4}$$

[3] An elegant way to treat electric and magnetic fields simultaneously is to use Riemann-Silberstein vector formalism (Białynicki-Birula and Białynicka-Birula, 2013). The field quantization relating only to electric and magnetic field can be found in (Białynicki-Birula and Białynicka-Birula, 2004).

The Hamiltonian defined in Eq. (1.3) enables determination of the time evolution of the field operators following the Heisenberg equations:

$$\frac{\mathrm{d}\hat{a}_s(\mathbf{k})}{\mathrm{d}t} = \frac{i}{\hbar}[\hat{H}, \hat{a}_s(\mathbf{k})] = -i\omega_k \hat{a}_s(\mathbf{k}). \tag{1.5}$$

where we directly applied Eq. (1.2). Time evolution can be also directly included in the electric field operator in Eq. (1.1) yielding decomposition on propagating plane waves.

### 1.2.2 Single photon wave packet

A photon is a single excitation of EM field represented formally by the state $|1\rangle$. A single photon state can be treated as an eigenstate of the photon number operator $\hat{n}$ defined in Eq. (1.4), of the eigenvalue equals the unity:

$$\hat{n}|1\rangle = |1\rangle. \tag{1.6}$$

We can also define the action of the creation operator on the vacuum – the ground state of the EM field $|0\rangle$. In particular, $\hat{a}_s^\dagger(\mathbf{k})$ creates a single photon in a plane-wave mode:

$$|1\rangle_{\mathbf{k},s} = \hat{a}_s^\dagger(\mathbf{k})|0\rangle, \tag{1.7}$$

whereas the action of the annihilation operator on the vacuum simply returns zero: $\hat{a}_s(\mathbf{k})|0\rangle = 0$. Such a single-photon state, similarly to classical plane waves, is in fact unphysical as it has an infinite energy, which can be readily verified by evaluation of $\langle 1|_{\mathbf{k},s}\hat{H}|1\rangle_{\mathbf{k},s}$ resorting to Eqs. (1.2,1.3). Therefore, instead of plane-wave modes, we shall further consider photons that are created in wave packets:

$$|1\rangle_f = \sum_s \int \frac{d^3k}{(2\pi)^3} f_s^*(\mathbf{k})\hat{a}_s^\dagger(\mathbf{k})|0\rangle, \tag{1.8}$$

where $f_s(\mathbf{k})$ stands for a single photon mode or wave packet whose normalization ensures a finite energy of a photon:

$$\sum_s \int \frac{d^3k}{(2\pi)^3}|f_s(\mathbf{k})|^2 = 1. \tag{1.9}$$

We can readily verify that the photon in a wave packet defined by Eq. (1.8) is indeed an eigenstate of the photon number operator from Eq. (1.4):

$$\hat{n}|1\rangle_f = \sum_{s,s'}\iint \frac{d^3k\, d^3k'}{(2\pi)^6} f_s^*(\mathbf{k})\hat{a}_{s'}^\dagger(\mathbf{k}')\hat{a}_{s'}(\mathbf{k}')\hat{a}_s^\dagger(\mathbf{k})|0\rangle = \sum_{s,s'}\iint \frac{d^3k\, d^3k'}{(2\pi)^6} f_s^*(\mathbf{k})\hat{a}_s^\dagger(\mathbf{k})\delta_{ss'}\delta(\mathbf{k}-\mathbf{k}')|0\rangle = |1\rangle_f, \tag{1.10}$$

where we apply the commutation relation to rewrite:

$$\hat{a}_{s'}^\dagger(\mathbf{k}')\hat{a}_{s'}(\mathbf{k}')\hat{a}_s^\dagger(\mathbf{k}) = \hat{a}_{s'}^\dagger(\mathbf{k}')(\hat{a}_s^\dagger(\mathbf{k})\hat{a}_{s'}(\mathbf{k}') + \delta_{ss'}\delta(\mathbf{k}-\mathbf{k}') \tag{1.11}$$

and the first term vanishes on the vacuum state.

We can also check if the wave packet defined by Eq. (1.8) travels in a free space similarly to classical light pulses. So as to verify this, one has to evaluate the mean value of the local energy of the electric field $\varepsilon_0\hat{\mathbf{E}}^{(-)}(\mathbf{r},t)\hat{\mathbf{E}}^{(+)}(\mathbf{r},t)/2$ on the state $|1\rangle_f$, where superscripts $(\pm)$ denote the positive or negative frequency terms of the electric field operators and the time dependence follows from Eq. (1.5).

### 1.2.3 Paraxial photons in spatial domain

As we further demonstrate experimentally in this thesis, photons can be localized within a certain resolution. Theoretical description of photons in a spatial domain is possible; yet, it requires some additional assumptions. Here we restrict ourselves only to paraxial photons, which is justified in experiments where photons are typically spatially tailored by optical systems, such as lenses or fibers. Moreover, the considered photons shall be quasi-monochromatic and any time dependence is omitted. Those photons have constituent wave vectors $\mathbf{k}$ close to the propagation axis directed along the $\mathbf{k}_0$ wave vector and belonging to a small subspace around it:

$$Q = \left\{\mathbf{k} \text{ satisfying: } \mathbf{k} = \mathbf{k}_0 + \mathbf{k}', \ |\mathbf{k}'| \ll |\mathbf{k}_0|\right\}. \tag{1.12}$$

Under such assumption we can introduce the annihilation field operator in a spatial domain and then taking the Fourier transform in the space limited to paraxial wave vectors:

$$\hat{\tilde{a}}(\mathbf{r}) = \int_Q \frac{d^3k}{(2\pi)^3} \hat{a}(\mathbf{k}) e^{i\mathbf{k}\cdot\mathbf{r}}. \tag{1.13}$$

For the sake of simplicity, from now on we shall consider by default only one polarization mode unless otherwise stated. As the $Q$ space encompasses only finite wave vectors that are close to $\mathbf{k}_0$, photons created by the operator $\hat{\tilde{a}}^\dagger(\mathbf{r})$ occupy larger volume than defined by the wavelength scale $(2\pi/\mathbf{k}_0)^3$ and thus they cannot be considered as sharply localized. Further, to simplify the notation, we shall use $\hat{a}(\mathbf{r})$ instead of $\hat{\tilde{a}}(\mathbf{r})$, which still should be easily distinguishable from the counterpart operator in a k-vector space by its argument.

We can also introduce a paraxial wave packet of a single photon as an analogy to Eq. (1.8):

$$|1\rangle_\psi = \int d^3r \ \psi^*(\mathbf{r}) \hat{a}^\dagger(\mathbf{r})|0\rangle, \tag{1.14}$$

where $\psi(\mathbf{r})$ is a wave packet mode which is normalized in a standard way, i.e.:

$$\int d^3r \ |\psi(\mathbf{r})|^2 = 1. \tag{1.15}$$

$\psi(\mathbf{r})$ can also be treated as a coarse-grained wave-function of a single photon (Lundeen *et al.*, 2011) whose modulus square is expressed a probability distribution of detection of a photon in a small, reciprocal to $Q$, volume around the point $\mathbf{r}$.

$$p(\mathbf{r}) = |\langle 0|\hat{a}(\mathbf{r})|1\rangle_\psi|^2 = |\psi(\mathbf{r})|^2. \tag{1.16}$$

## 1.3 Few-photon states of light

The few-photon states of light mentioned in the title of the thesis refer to a broad notion of a weak light treated quantum-mechanically in its description or, from the experimental point of view, by photon counting methods. To be consistent with the introduced single photon states, we extend the description onto higher number of photons and modes in pure states as well as in mixed ones.

### 1.3.1 Fock states – single mode description

So far we introduced a theoretical description of single photons in a momentum domain and, for paraxial photons, in spatial domain. Now we proceed to describing states of light with higher number of photons occupying the same mode $\psi(\mathbf{r})$. It is convenient to introduce field operators that create and annihilate photons in a single, specific mode exclusively. The annihilation operator in this mode takes the form:

$$\hat{a}_\psi = \int d^3r\, \psi(\mathbf{r})\hat{a}(\mathbf{r}). \tag{1.17}$$

Hereinafter for simplicity of notation we shall skip the subscript denoting the mode wave packet and we use the $\hat{a} \equiv \hat{a}_\psi$ symbol should only one mode be discussed.

The annihilation and the creation operators act as ladder operators in a space of exact number of photon states, called Fock states:

$$\hat{a}^\dagger|n\rangle = \sqrt{n+1}|n+1\rangle, \quad \hat{a}|n\rangle = \sqrt{n}|n-1\rangle. \tag{1.18}$$

$|n\rangle$, a general Fock state, denotes a state where exactly $n$ photons occupy a given mode and it is an eigenstate of the photon number operator $\hat{n}$ defined as follows:

$$\hat{n}|n\rangle = \hat{a}^\dagger\hat{a}|n\rangle = n|n\rangle.$$

### 1.3.2 Coherent state

A classical example of a state available at hand in experiment is a coherent state. It is customarily associated with a single mode of coherent radiation generated by a laser. Formally a coherent state $|\alpha\rangle$ is an eigenstate of the annihilation operator:

$$\hat{a}|\alpha\rangle = \alpha|\alpha\rangle, \tag{1.19}$$

and resorting to this property one can find its decomposition in the Fock basis:

$$|\alpha\rangle = e^{-\frac{1}{2}|\alpha|^2}\sum_{n=0}^{\infty}\frac{\alpha^n}{\sqrt{n!}}|n\rangle. \tag{1.20}$$

From that decomposition we can determine the probability of finding $n$ photons in the state:

$$p(n) = |\langle n|\alpha\rangle|^2 = e^{-\langle n\rangle}\frac{\langle n\rangle^n}{n!}, \tag{1.21}$$

which is a well-known Poisson statistics appearing in semi-classical photodetection theory (Goodman, 2015), exemplified later in Fig. 1.4. $\langle n\rangle = |\alpha|^2$ stands for the mean number of photons in the state:

$$\langle n\rangle = \sum_{n=0}^{\infty} np(n), \tag{1.22}$$

whereas the variance of the number of photons defined as:

$$\langle(\Delta n)^2\rangle = \langle(n-\langle n\rangle)^2\rangle = \langle n^2\rangle - \langle n\rangle^2, \tag{1.23}$$

equals the mean for coherent states:

$$\langle(\Delta n)^2\rangle_{\text{coh}} = \langle n\rangle. \tag{1.24}$$

This is the lowest classically attainable photon number variance for a fixed mean and in some sense it marks a boundary between classical and nonclassical states.

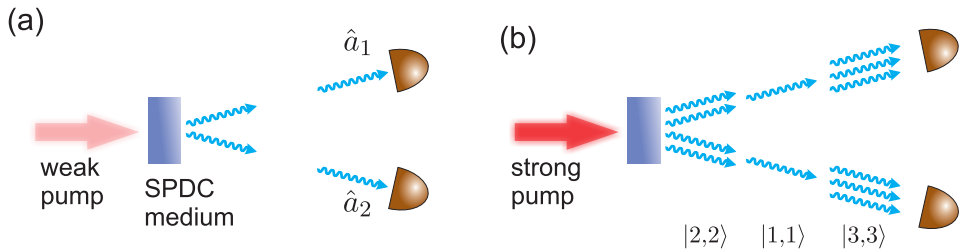


Figure 1.2: Squeezed vacuum can be created in the spontaneous parametric down-conversion process (SPDC) where pump photons split into photons in conjugate modes $\hat{a}_1$ and $\hat{a}_2$. (a) In the low gain regime i.e. using a weak pump, photons are produced in pairs. Detection of one of the photons heralds the other photon in the latter mode. (b) In the high-gain regime with the strong pump one can create higher number of photons that ideally are equally distributed between the modes, c.f. Eq. 1.33. Nearly equal numbers of photons detected in two modes can be treated as a signature of the nonclassical behavior, c.f. Sec. 1.4.3.

### 1.3.3 Fock states - multimode description

We can nos consider multimode states of light. They occupy higher number of modes which are described by set of normalized functions $\psi_i(\mathbf{r})$ to be pairwise orthogonal:

$$\int d^3r\, \psi_i^*(\mathbf{r})\psi_j(\mathbf{r}) = \delta_{ij}.$$

Each mode has associated field operators $\hat{a}_i, \hat{a}_i^\dagger$ defined in Eq. (1.17) acting for $i$-th mode only and fulfilling discrete commutation relations:

$$[\hat{a}_i, \hat{a}_j^\dagger] = \delta_{ij},\ [\hat{a}_i, \hat{a}_j] = 0. \tag{1.25}$$

In further discussion we shall consider states decomposed in the multimode Fock basis. The general vector in this space, of exactly $n_i$ photons in $i$-th mode is created from the vacuum by multiple action of respective mode creation operators:

$$|n_1, n_2, \ldots\rangle \equiv |n_1\rangle_{\psi_1} \otimes |n_2\rangle_{\psi_2} \otimes \ldots = (n_1! n_2! \cdots)^{-1/2} (\hat{a}_1^\dagger)^{n_1} (\hat{a}_2^\dagger)^{n_2} \ldots |0\rangle. \tag{1.26}$$

### 1.3.4 Squeezed vacuum

Squeezed vacuum is doubtlessly the most widespread nonclassical light exploited in experiments these days. Routinely it is generated in non-linear crystals in the spontaneous parametric down-conversion process (SPDC) but it can also be produced in other non-linear media, such as near-resonant atoms (Boyer *et al.*, 2008b). It has versatile applications: in a low-gain regime it can be a source of heralded photons, in a high-gain regime it can serve as a source of high-number-of-photons states and in continuous variable measurements as a resource in interferometry enabling sub-shot noise measurements. Below we focus on selected properties of squeezed vacuum in the photon-number domain. Comprehensive reviews on squeezed light can be found in textbooks: (Drummond and Ficek, 2004; Lvovsky, 2015).

To gain insights on the properties of squeezed light we shall consider simplified model of a non-degenerate SPDC where a pump photon can spontaneously split into two photons in modes 1,2 of respective field operators $\hat{a}_1$ and $\hat{a}_2$ as depicted in Fig. 1.2(a). Neglecting any quantum features of a pump beam we can write the squeezing Hamiltonian of the interaction governing such process:

$$\hat{H}_{\mathrm{sqz}} = \frac{i\hbar}{2\tau}(\zeta \hat{a}_1 \hat{a}_2 - \zeta^* \hat{a}_1^\dagger \hat{a}_2^\dagger), \tag{1.27}$$

where, $\tau$ is the time scale, $\zeta$ is the coupling coefficient dependent on the pump beam intensity, nonlinearity coefficient etc. If modes 1 and 2 are initially unoccupied, their joint state evolves in the Schroedinger picture as $e^{-i\hat{H}t/\hbar}|0\rangle$. When the time of interaction equals $\tau$ the resulting state can be represented as

$$|\Psi_\zeta\rangle = \hat{S}_{1,2}(\zeta)|0\rangle, \tag{1.28}$$

where $\hat{S}_{1,2}(\zeta)$ is the two-mode squeezing operator defined as:

$$\hat{S}_{1,2}(\zeta) = e^{(\zeta \hat{a}_1 \hat{a}_2 + \zeta^* \hat{a}_1^\dagger \hat{a}_2^\dagger)/2}. \tag{1.29}$$

For our purposes it will be convenient to express the squeezed state in the Fock basis. At first we consider a low-gain regime i.e. a small coupling coefficient $|\zeta| \ll 1$. We can then restrict to the first to term of the Taylor expansion of the squeezing operator from Eq. (1.29):

$$|\Psi_{\zeta:|\zeta|\ll 1}\rangle = \hat{S}_{12}(\zeta)|0\rangle \simeq \left(1 + \frac{1}{2}(\zeta \hat{a}_1 \hat{a}_2 + \zeta^* \hat{a}_1^\dagger \hat{a}_2^\dagger)\right)|0\rangle = |0\rangle + \frac{\zeta^*}{2}|1,1\rangle. \tag{1.30}$$

Formally, the state from Eq. (1.30), visualized in Fig. 1.2(a), consists primarily of vacuum which means that in measurements virtually no photons will be detected:

$$p(0,0) = |\langle 0|\Psi_{\zeta:|\zeta|\ll 1}\rangle|^2 \simeq 1. \tag{1.31}$$

Nonetheless, such a state can be extremely useful if we apply a post-selection procedure and repeat measurements until we detect a photon in one of the modes. Such a scenario describes a source of heralded single photons. Ideally, without any losses, the conditional probability of finding one photon in mode 1 conditioned on detection a photon in mode 2 approaches the unity:

$$p(n_1 = 1|n_2 = 1) = 1. \tag{1.32}$$

It is also instructive to consider a high-gain regime, i.e. large coupling coefficients $\zeta$. In the evolution governed by the Hamiltonian in Eq. (1.27) only pairs of photons can be created (or annihilated), thus we expect the state to consists of equal-number-of-photons terms: $|\Psi_\zeta\rangle = \sum_{n=0}^{\infty} c_n|n,n\rangle$. Derivation of the exact form of the coefficients $c_n$ can be found in: (Schumaker and Caves, 1985; Wasilewski, 2007; Lvovsky, 2015), and here we present the final decomposition in the Fock states basis, sketched also in Fig. 1.2(b):

$$|\Psi_\zeta\rangle = \sqrt{1-|\xi|^2}(|0,0\rangle + \xi|1,1\rangle + \xi^2|2,2\rangle + \ldots), \tag{1.33}$$

where $\xi = \tanh(|\zeta|)e^{i\phi}$, $\zeta = |\zeta|e^{i\phi}$ (Drummond and Ficek, 2004). Theoretically we could apply the similar post-selection procedure to create heralded higher-photon-number Fock states. Such procedure might be realized in the future with emerging transition-edge-sensor superconducting detectors of the quantum efficiency approaching 98% (Fukuda *et al.*, 2011) and the photon-number-resolving capability (Hadfield, 2009).

In an experiment we commonly deal with a rich modal structure of the generated light. Squeezing process can occur in pairs of conjugated modes where each pair remains uncorrelated with another and is characterized by different coupling coefficients $\zeta_i$ (Wasilewski *et al.*, 2006). The resulting multimode squeezed state consisting of $\mathscr{M}$ pairs of conjugate modes can be represented as a product state of two-mode squeezed states, each defined by Eq. (1.33):

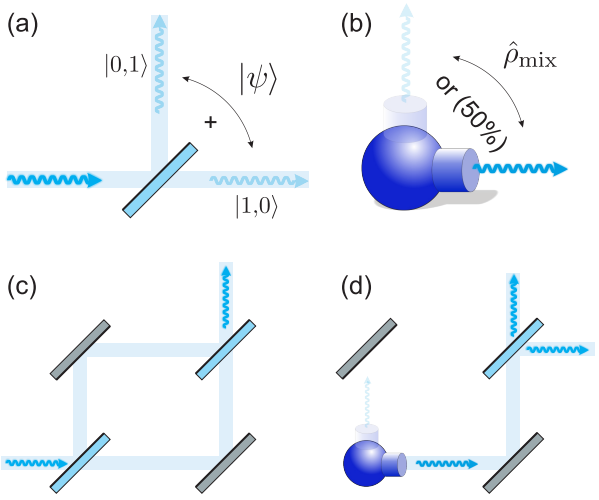


Figure 1.3: Difference between a pure superposition and a mixed state can be seen considering two seemingly similar situations. (a) A photon that impinged on a beam splitter transforms into a superposition of two events: photon's transmittance $|1,0\rangle$ or reflection $|0,1\rangle$. (b) Alternatively photons can be placed in the same modes by e.g. switched single photon source that interchangeably rotates the direction of emission. The latter situation is described by the mixed state $\hat{\rho}_{\mathrm{mix}}$. (c) The difference between pure and mixed states can be revealed by a unitary operation, here performed by a Mach-Zender interferometer. For a pure state we observe constructive interference at one of the outputs whereas (d) for a mixed state, photons equiprobably leave two distinct outputs of the interferometer.

$$|\Psi^{(\mathcal{M})}\rangle = \bigotimes_{i=1}^{\mathcal{M}} |\Psi_{\zeta_i}\rangle = \hat{S}_{1,2}(\zeta_1)\cdot\ldots\cdot\hat{S}_{(2\mathcal{M}-1),2\mathcal{M}}(\zeta_{\mathcal{M}})|0\rangle. \tag{1.34}$$

### 1.3.5 Mixed states

So far we have considered only pure states in a coherent superposition of Fock states. Now we shall introduce the formalism to describe a wider class of states to occur in experiment: light from incoherent sources, statistical mixtures of pure states or partially traced multimode inseparable states.

Firstly, let us show a simple and intuitive picture demonstrating the difference between two similar states: a pure state in a coherent superposition and a mixed state in the statistical mixture of pure states. As an example of a pure, coherent superposition we shall take the state of the photon after a beam splitter presented in Fig. 1.3(a). A photon can either go through a beam splitter $|1,0\rangle$ or can be reflected what can be denoted as $|0,1\rangle$. The resulting superposition state is $(|1,0\rangle + |0,1\rangle)/\sqrt{2}$ and the probability of finding photon on either side of the beam splitter equals $1/2$.

A seemingly similar situation is depicted in Fig. 1.3(b) where the photons are randomly placed either in transmitted $|1,0\rangle$ or reflected $|0,1\rangle$ modes. Repeated measurements in both scenarios would yield the same statistics for appearance of photons. Differences between those two distinct situations can be revealed by considering these states inserted to a Mach-Zender interferometer as shown in Fig. 1.3(c-d). The first case in Fig. 1.3(c) relates to a pure state that undergoes a unitary evolution and that has the ability to interfere. As a consequence the photon always appears in one output port of the interferometer. The second case depicted in Fig. 1.3(d) representing a statistical mixture of $|1,0\rangle$ or $|0,1\rangle$ results in photons leaving randomly one of the two output ports of the interferometer.

The latter case can be described by a formalism of mixed states and expressed by a density matrix operator. It takes a form $\hat{\rho}_{\text{mix}} = (|1,0\rangle\langle 1,0| + |0,1\rangle\langle 0,1| + |1,0\rangle\langle 0,1| + |0,1\rangle\langle 1,0|)/2$, denoting a statistical mixture of photons in either $|1,0\rangle$ or $|0,1\rangle$ states where $1/2$ stands for the probability of occurrence of each situation. For comparison, the density matrix for the previously described pure state is following $\hat{\rho}_{\text{pure}} = (|1,0\rangle + |0,1\rangle)(\langle 1,0| + \langle 0,1|)/2$. Both can be expressed in a matrix representation in a basis $|1,0\rangle, |0,1\rangle$:

$$\hat{\rho}_{\text{mix}} = \frac{1}{2}\begin{pmatrix} 1 & 0 \\ 0 & 1 \end{pmatrix}, \quad \hat{\rho}_{\text{pure}} = \frac{1}{2}\begin{pmatrix} 1 & 1 \\ 1 & 1 \end{pmatrix}. \tag{1.35}$$

Noticeably the density matrix $\hat{\rho}_{\text{mix}}$ does not have any off-diagonal elements, present in $\hat{\rho}_{\text{pure}}$, traditionally called *coherence* elements.

Formally a density matrix can represent a set of random events that a system will be found in a pure states $|\psi_i\rangle$ with a probability $p_i$:

$$\hat{\rho} = \sum_i p_i |\psi_i\rangle\langle\psi_i|. \tag{1.36}$$

There are three conditions imposed on a density matrix $\hat{\rho}$: hermiticity $\hat{\rho}^\dagger = \hat{\rho}$, normalization of probability distribution $\text{Tr}\{\hat{\rho}\} = 1$ and its positive definiteness $\hat{\rho} \geq 0$ which are equivalent for the standard conditions on the complete set of probabilities i.e. $\sum_i p_i = 1$, $p_i \geq 0$. Noticeably, a density matrix can also represent a pure state $|\psi\rangle$; then, the sum in Eq. (1.36) consists of just a single term $\hat{\rho} = |\psi\rangle\langle\psi|$.

To calculate the expectation value of an observable $\hat{O}$ in this formalism one has to sum up weighted expectation values for each state which can be cast in a compact form of the matrix trace:

$$\langle\hat{O}\rangle_{\hat{\rho}} = \sum_i p_i \langle\psi_i|\hat{O}|\psi_i\rangle = \text{Tr}\{\hat{\rho}\hat{O}\}. \tag{1.37}$$

In experiments we very often deal with multimode states with a limited access to some modes. Then we can consider states only in those reachable modes by performing a partial trace over inaccessible modes. For instance, in case of a two-mode state described jointly by a density matrix $\hat{\rho}_{1,2}$, the access to mode 1 exclusively results in a following state:

$$\hat{\rho}_1 = \text{Tr}_2\{\hat{\rho}_{1,2}\}, \tag{1.38}$$

where $\text{Tr}_2$ denotes a partial trace in a subspace of a second mode.

### 1.3.6 Thermal states

Now we consider a mixed state which is observed in a single mode out of a two-mode squeezed state. Following Eqs. (1.33,1.38) we trace over the second mode obtaining the density matrix:

$$\hat{\rho}_{\text{th}} = \text{Tr}_2\{|\Psi_\zeta\rangle\langle\Psi_\zeta|\} = (1-|\xi|^2)\sum_{n=0}^{\infty} |\xi|^{2n}|n\rangle\langle n|. \tag{1.39}$$

The resulting mixed state, called a single mode thermal state, corresponds to a state in the thermal equilibrium with a reservoir of a temperature $T$. Then, the substitution of $|\xi|^2 = e^{-\hbar\omega/k_B T}$ transforms Eq. (1.39) into the Maxwell-Boltzmann statistics.

We can evaluate the mean number of photons in the thermal state:

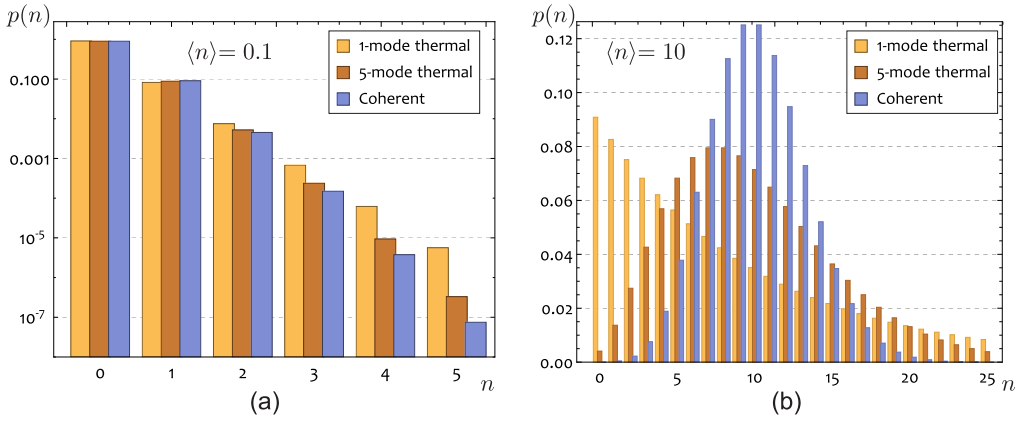


Figure 1.4: Comparison of coherent and thermal single- and multimode statistics. (a) For a low mean number of photons $\langle n\rangle = 0.1$ the coherent state has the noticeably fastest fall-off in the probability distribution. (b) For a larger mean number of photons $\langle n\rangle = 10$ one can see that the five-mode thermal statistics has a distribution of a width in between that of the coherent and single thermal mode statistics with a long exponentially falling tail.

$$\langle n\rangle = \mathrm{Tr}\{\hat{\rho}_{\mathrm{th}}\hat{n}\} = (1-|\xi|^2)\sum_{n=0}^{\infty} n|\xi|^{2n} = (1-|\xi|^2)|\xi|^2\frac{\partial}{\partial(|\xi|^2)}\sum_{n=0}^{\infty}|\xi|^{2n} = \frac{|\xi|^2}{1-|\xi|^2}. \tag{1.40}$$

It is convenient to rewrite Eq. (1.39) by parametrizing it only by the mean number of photons:

$$\hat{\rho}_{\mathrm{th}} = \frac{1}{1+\langle n\rangle}\sum_{n=0}^{\infty}\left(\frac{\langle n\rangle}{1+\langle n\rangle}\right)^n |n\rangle\langle n|. \tag{1.41}$$

The corresponding photon number statistics is plotted for two values of mean photon number in Fig. 1.4. We can also find a variance of a number or photons defined in Eq. (1.23) by evaluating $\mathrm{Tr}\{\hat{\rho}_{th}\hat{n}^2\}$ with the aid of the following mathematical fact: $\sum_{n=0}^{\infty} n^2|\xi|^{2n} = |\xi|^4\partial/\partial(|\xi|^2)\sum_{n=0}^{\infty}|\xi|^{2n}/2$. Eventually we obtain the variance that scales quadratically with the mean number of photons, significantly faster than for coherent states:

$$\langle(\Delta n)^2\rangle_{\mathrm{th}} = \langle n\rangle + \langle n\rangle^2. \tag{1.42}$$

We can carry out a similar mathematical procedure to characterize jointly one set of modes in the multimode squeezed states defined by Eq. (1.34). For the sake of simplicity we shall assume the same squeezing for each pair of modes entailing the same mean number of photons: $\langle n_i\rangle = (1-|\xi_i|^2)^{-1} = n_0$. We consider $\mathscr{M}$ modes to be detected together. The photon number distribution will be a multimode thermal statistics and its properties can be found by considering the sum of $\mathscr{M}$ independent variables of a single-mode thermal statistics. In particular the mean photon number is the sum of the means in each mode:

$$\langle n\rangle = \mathscr{M}\, n_0, \tag{1.43}$$

and the variance is the sum of variances in each of constituent modes, which, according to Eq. (1.42), is:

$$\langle(\Delta n)^2\rangle_{\mathscr{M}\mathrm{th}} = \mathscr{M}(n_0+n_0^2) = \langle n\rangle + \frac{\langle n\rangle^2}{\mathscr{M}}. \tag{1.44}$$

Noticeably, for $\mathscr{M} \gg \langle n \rangle$, the variance approaches the mean, similarly as for the Poisson statistics, Eq. (1.24). Such property can be intuitively understood by reminding the fact that a Poisson statistics characterizes stochastic processes where events occur equiprobably in many uncorrelated bins translating here into many weakly populated modes.

Finally we give the photon number distribution whose full derivation can be found in (Goodman, 2015):

$$p_{\mathscr{M}\mathrm{th}}(n) = v \frac{(n+\mathscr{M}-1)!}{n!} w^{n+\mathscr{M}-1}, \tag{1.45}$$

where $v = \left(\mathscr{M}/(\langle n \rangle + \mathscr{M})\right)^{\mathscr{M}} / (\mathscr{M}-1)!$, $w = \langle n \rangle / (\mathscr{M} + \langle n \rangle)$. It can be readily checked that for $\mathscr{M} = 1$, Eq. (1.45) is simplified to a formula for a single mode thermal state Eq. (1.41). I can be also rigorously shown, see (Goodman, 2015), that within the limit of the large number of modes the multimode statistics approaches the Poisson statistics:

$$p_{\mathscr{M}\mathrm{th}}(n) \xrightarrow[\langle n \rangle / \mathscr{M} \to 0]{} e^{-\langle n \rangle} \frac{\langle n \rangle^n}{n!}, \tag{1.46}$$

which confirms our previous observation on the variance approaching the mean number of photons. In Fig. 1.4 we compare the photon number statistics for the single, multimode-thermal and coherent states.

The presented theory of thermal states of light can be readily generalized to the regimes of high photon numbers. Then the discrete photon number distributions in Eq. (1.41) and Eq. (1.45) transform into continuous distributions of light intensities: the exponential distribution for single-mode thermal states and the gamma distribution for the multimode thermal states. We refer to this fact in Part II while discussing the high-photon-number regime measurements of the Raman scattering.

## 1.4 Common measures of nonclassicality in photon counting experiments

As we indicated at the beginning of this thesis, nonclassical states of light can be very useful in various protocols. However, in real experiments the available states of light may have poorer properties than the ideal states, which limits their usability. Here we introduce several measures of nonclassicality that let us classify the states in question either into the classical or nonclassical category. By definition a classical state can be represented as a statistical mixture of coherent states. It follows that classical states fulfill inequalities derived in the semi-classical radiation theory (Goodman, 2015).

### 1.4.1 Mandel parameter – variance reduction

For a classical light the variance of the number of photons cannot be smaller than for a coherent state, hence we have $\langle (\Delta n)^2 \rangle \geq \langle n \rangle$. The commonly used parameter of nonclassicality is the $Q$-Mandel parameter:

$$Q_M = \frac{\langle (\Delta n)^2 \rangle}{\langle n \rangle} - 1, \tag{1.47}$$

which measures the ratio of the variance to the mean photon number. The classicality criterion takes the form of:

$$Q_M \geq 0, \tag{1.48}$$

| state | variance (given mean $\langle n\rangle$) | $Q_M$ | $g^{(2)}$ |
|---|---|---|---|
| coherent | $\langle n\rangle$ | 0 | 1 |
| thermal | $\langle n\rangle + \langle n\rangle^2$ | $\langle n\rangle$ | 2 |
| $\mathscr{M}$-mode thermal | $\langle n\rangle + \langle n\rangle^2/\mathscr{M}$ | $\langle n\rangle/\mathscr{M}$ | $1+1/\mathscr{M}$ |
| $n$-th Fock | 0 | -1 | $1-1/n$ |

Table 1.1: Comparison of variances, Q-Mandel parameters and $g^{(2)}$ autocorrelation functions evaluated for the discussed one-mode states of light. The values for the coherent state can be treated as the lowest classically attainable values of the consecutive parameters. Noticeably the mutlimode thermal states present properties intermediate between that of the coherent and thermal state, and in the regime of a large number of modes their properties approach the coherent states.

and the minimal value is $Q_M = -1$ for the Fock states. The exemplary values taken by this parameter are summarized in the Table 1.1.

### 1.4.2 Autocorrelation function $g^{(2)}$ and photon anti-bunching

Another measure of nonclassicality is the second order autocorrelation function $g^{(2)}$. This measure of nonclassicality directly refers to the photon anti-bunching property (Paul, 1982). Ideal single photon, a Fock state, is indivisible thus once it impinges a beam splitter it can be detected only at one output, never on two outputs simultaneously, as depicted in Fig. 1.5(a). In general an investigated state may contain a fraction of pairs, threes of photons which may generate coincidences on two detectors as in Fig. 1.5(b).

The autocorrelation function is defined for classical light of intensity $I$: $g^{(2)} = \langle I^2\rangle/\langle I\rangle^2$. For a quantized field the definition changes into:

$$g^{(2)} = \frac{\langle \hat{a}^{\dagger 2}\hat{a}^2\rangle}{\langle \hat{a}^\dagger\hat{a}\rangle^2} = \frac{\langle \hat{n}(\hat{n}-1)\rangle}{\langle \hat{n}\rangle^2} = 1 + \frac{\langle (\Delta n)^2\rangle - \langle n\rangle}{\langle n\rangle^2}. \tag{1.49}$$

As for classical states the photon number variance always has to be larger than the mean number of photons we have:

$$g^{(2)} \geq 1 \quad \text{(classical)}. \tag{1.50}$$

On the other hand, as the minimal possible variance is zero, the lower limit for the autocorrelation function for nonclassical states is:

$$g^{(2)} \geq 1 - \frac{1}{\langle n\rangle} \quad \text{(general)},$$

and this inequality is saturated by the Fock states. The values evaluated for exemplary states are presented in the Table 1.1. The highest value of $g^{(2)} = 2$ is displayed by a single mode thermal states, however there is no upper bound on this value and $g^{(2)} > 2$ has been observed for instance for a superthermal light (Hong *et al.*, 2012).

The connection between the $g^{(2)}$ autocorrelation function and the anti-bunching effect of photons can be illustrated by the following approximate treatment. For very weak light, i.e. $\langle n\rangle \ll 1$ , Eq. (1.49) simply yields $g^{(2)} \simeq 2p(2)/p(1)^2$, where $p(1) \ll 1$ is the probability of having one and $p(2) \ll 1$ for a pair of photons respectively. Both probabilities $p(1)$ and $p(2)$ are measurable in the experimental configuration presented in Fig. 1.5, assuming $p(n > 2) \simeq 0$. For instance, the approximated formula clearly equals zero for single photons and unity for weak coherent states, where $p(1) \simeq \langle n\rangle$ and $p(2) \simeq \langle n\rangle^2/2$, assuming $\langle n\rangle \ll 1$.

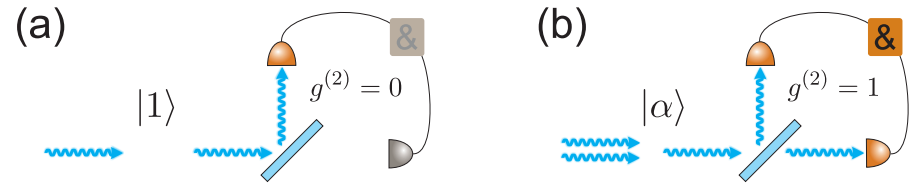


Figure 1.5: Antibunching properties of weak light can be verified by splitting it and measuring on two detectors. (a) True single photons always appear on one side of the beam splitter and coincidental detection at two detectors never occurs. (b) The weak coherent state always has a certain contribution of pairs of photons yielding occasional detection of coincidences. This simple measurements scheme enables evaluation of the approximate value of the autocorrelation function $g^{(2)} \simeq 2p(2)/p(1)^2$.

Now let us compute $2p(2)/p(1)^2$ for heralded photons from SPDC that are the most common source of single photons. A photon detected in one mode of a squeezed state indicates that the other photon is present in a conjugate mode as we previously sketched in Fig. 1.2(a). Typical detectors such as avalanche photo diodes do not have a photon number resolution and they can only distinguish "zero" or and "at least one photon" events. Thus a state conditioned on a detection event in the second mode may contain higher number of photons, as we illustrated in Fig. 1.2(b).

The heralded state is the state in mode 1 conditioned on a detection of at least one photon in the mode 2. We can calculate the approximate $g^{(2)}$ function by evaluating the probabilities of single and pairs of photons in that state. Assuming that $n_i$, $i = 1,2$, denotes the number of photons in each mode, these probabilities shall be $p(1|n_2 \geq 1)$ and $p(2|n_2 \geq 1)$ respectively. To find them, we use Eq. (1.33) to calculate first:

$$p(n_2 \geq 1) = 1 - p(n_2 = 0) = |\xi|^2, \quad p(n_1 = 1) = (1-|\xi|^2)|\xi|^2, \quad p(n_1 = 2) = (1-|\xi|^2)|\xi|^4, \tag{1.51}$$

which combined, assuming $|\xi|^2 \ll 1$, yield the following expression on heralded, i.e. conditioned, probabilities:

$$p(1|n_2 \geq 1) = \frac{p(n_1 = 1)}{p(n_2 \geq 1)} \simeq 1, \quad p(2|n_2 \geq 1) = \frac{p(n_1 = 2)}{p(n_2 \geq 1)} \simeq |\xi|^2. \tag{1.52}$$

We now see that for a heralded single photon the autocorrelation function equals approximately $g^{(2)} \simeq 2|\xi|^2$ and can be arbitrarily low and approach zero value as for a Fock state.

### 1.4.3 Fano noise reduction factor

Now we proceed to discussing measures of nonclassicality for two-modes states, such as a two-mode squeezed state. The characteristic feature for this state, defined in Eq. (1.33) is the equal number of photons between the modes as we previously sketched in Fig. 1.2(b). Deviation from a perfect balance is measured by the Fano factor or noise reduction factor defined as follows:

$$R = \frac{\langle(\Delta(n_1 - n_2))^2\rangle}{\langle n_1\rangle + \langle n_2\rangle} = \frac{\langle(\Delta n_1)^2\rangle + \langle(\Delta n_2)^2\rangle - 2\mathrm{cov}(n_1, n_2)}{\langle n_1\rangle + \langle n_2\rangle}, \tag{1.53}$$

which takes the value $R = 0$ for the two-mode squeezed light. On the other hand, by considering classical two-mode coherent state $|\alpha\rangle \otimes |\alpha'\rangle$ we obtain $R = 1$, where covariance between number of photons in two-mode coherent state is zero. For any other classical states we have the inequality:

$$R \geq 1. \tag{1.54}$$

In case of large discrepancy between mean numbers of photons in the two modes one can weight the photon number of photons to obtain the operator:

$$\hat{W} = \Big(\frac{\hat{n}_1}{\langle n_1\rangle} - \frac{\hat{n}_2}{\langle n_2\rangle}\Big) \Big/ \sqrt{\frac{1}{\langle n_1\rangle} + \frac{1}{\langle n_2\rangle}}, \tag{1.55}$$

whose variance can serve as a more sensitive experimental measure of nonclassicality[4]:

$$\langle (\Delta \hat{W})^2 \rangle \geq 1. \tag{1.56}$$

### 1.4.4 Cross-correlation function, photon-bunching

The last measure of nonclassicality to be discussed is a two-mode, cross correlation function introduced for modes 1 and 2. A classical definition of two light fields of intensities $I_1, I_2$ is $g^{(2)}_{12} = \langle I_1 I_2\rangle / \langle I_1\rangle\langle I_2\rangle$. It is reformulated for quantized fields as follows:

$$g^{(2)}_{12} = \frac{\langle \hat{a}_1^\dagger \hat{a}_2^\dagger \hat{a}_1 \hat{a}_2\rangle}{\langle \hat{a}_1^\dagger \hat{a}_1\rangle\langle \hat{a}_2^\dagger \hat{a}_2\rangle} = \frac{\langle n_1 n_2\rangle}{\langle n_1\rangle\langle n_2\rangle} = 1 + \frac{\mathrm{cov}\,(n_1, n_2)}{\langle n_1\rangle\langle n_2\rangle}. \tag{1.57}$$

The cross-correlation function measures bunching properties of two-mode light. It becomes large if the numbers of photons are correlated whereas it equals unity for entirely uncorrelated number of photons in modes 1 and 2.

The following inequality always holds true:

$$\frac{\langle n_1 n_2\rangle}{\langle n_1\rangle\langle n_2\rangle} \leq \sqrt{\frac{\langle n_1^2\rangle\langle n_2^2\rangle}{\langle n_1\rangle^2\langle n_2\rangle^2}}. \tag{1.58}$$

It originates from the Cauchy-Schwartz inequality for two vectors[5]. For classical light where a number of photons are replaced by classical light intensities and the inequality can be expressed using classical field correlations functions (Reid and Walls, 1986):

$$g^{(2)}_{12} \leq \sqrt{g^{(2)}_{11}\, g^{(2)}_{22}} \quad \text{(classical)}, \tag{1.59}$$

where $g^{(2)}_{ii}$ denotes the autocorrelation function in $i$-th mode. However quantum mechanical calculations combining Eq. (1.58) with definition in Eq. (1.49) yield the ultimate limit for nonclassical states:

$$g^{(2)}_{12} \leq \sqrt{\Big(g^{(2)}_{11} + \frac{1}{\langle n_1\rangle}\Big)\Big(g^{(2)}_{22} + \frac{1}{\langle n_2\rangle}\Big)} \quad \text{(general)}. \tag{1.60}$$

For a small mean number of photons the cross-correlation can be arbitrarily large. As a specific example we evaluate the cross-correlation function for the two mode squeezed vacuum, Eq. (1.33). By computing $\langle n_1 n_2\rangle$ and taking $\langle n_i\rangle$ from Eq. (1.40) we obtain the cross-correlation for two-mode squeezed states:

[4] This measure is a generalization of the Fano noise reduction factor and it was proposed by Wasilewski (2007).

[5] It can be readily derived starting from vectors $\hat{n}_1|0\rangle$, $\hat{n}_2|0\rangle$ to obtain $|\langle n_1 n_2\rangle|^2 \leq \langle n_1^2\rangle\langle n_2^2\rangle$.

$$g_{12}^{(2)} = 1 + \frac{1}{|\xi|^2} \geq 2. \tag{1.61}$$

Customarily in experiments it is assumed that $g_{12}^{(2)} > 2$ indicates that a state is nonclassical although formally the nonclassical criterion, i.e. violating inequality Eq. (1.59), requires separate measurements of each corresponding autocorrelations functions $g_{ii}^{(2)}$. Moreover, this measure of nonclasicality becomes particularly useful as it does not depend on the efficiency of the detectors.

## 1.5 Collective Raman scattering

In Part II of this thesis we study a source of photons based on the Raman scattering in atomic ensembles similar to that in the previously described DLCZ protocol (Duan *et al.*, 2001). Here we briefly introduce the most important properties and the principle of operation of the source. Different aspects of the theory of Raman scattering such as various regimes of operation can be found in the literature: (Raymer and Mostowski, 1981; Mostowski and Sobolewska, 1984; Raymer, 2004; Gorshkov *et al.*, 2007; Kołodyński *et al.*, 2012).

More specifically we describe two subsequent collective Raman processes: the spontaneous Stokes scattering and the anti-Stokes scattering determined by the outcome of the first process. We generalize the system presented in DLCZ protocol to many spatial modes. Here, in the introductory chapter, we present the plane-wave model that explains the correlation between wave vectors of Stokes and anti-Stokes photons. In the successive sections we discuss the interaction of two light fields with a single atom and then with an ensemble of atoms. Taking interchangeably one of the fields to be classical, we present a compact model of both Stokes and anti-Stokes scattering processes. Moreover we discuss the formalism of collective excitations that describes the state of the atoms after scattering on an ensemble.

### 1.5.1 Interaction of light with a single atom in Λ-system

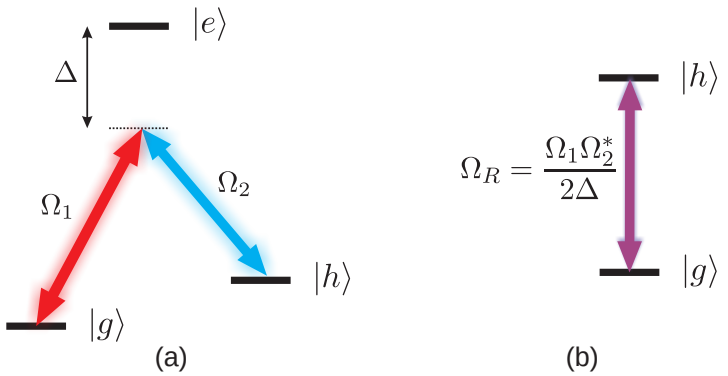


Figure 1.6: (a) Raman scattering in a three-level atom in Λ−configuration. Two long-lived levels $|g\rangle$ and $|h\rangle$ are coupled in two-photon resonance by fields of the Rabi frequency $\Omega_1$ and $\Omega_2$, detuned from the upper level $|e\rangle$ by $\Delta$. For large detunings $\Delta$ the level $|e\rangle$ is virtually unpopulated. (b) Thereafter a description of the system can be simplified in the adiabatic elimination process to two levels $|g\rangle, |h\rangle$ and the effective field of the two-photon Rabi frequency $\Omega_R = \Omega_1\Omega_2^*/2\Delta$.

We consider a three level atom in the so-called Λ configuration, as depicted in Fig. 1.6(a). The atom can be optically excited from one of two long-lived levels $|g\rangle, |h\rangle$ to the upper level $|e\rangle$. We

introduce single atom transition operators defined as follows:

$$\hat{\sigma}_{ij} = |i\rangle\langle j|. \tag{1.62}$$

For instance $\hat{\sigma}_{hg} = |h\rangle\langle g|$ excites an atom from the level $|g\rangle$ to $|h\rangle$. The transition operators fulfill the following commutation relations, as can be readily derived from the definition:

$$[\hat{\sigma}_{ij}, \hat{\sigma}_{i'j'}] = \delta_{ji'}\hat{\sigma}_{ij'} - \delta_{ij'}\hat{\sigma}_{i'j}. \tag{1.63}$$

Our goal is to derive coupling between levels $|g\rangle$ and $|h\rangle$. We shall create collective excitations in the two-photon optical transitions through the third level $|e\rangle$. As depicted in Fig. 1.6 the atom interacts with two light fields of respective electric field operators $\hat{\mathbf{E}}_1$ and $\hat{\mathbf{E}}_2$ oscillating with the frequencies $\omega_1$ and $\omega_2$ closing two-photon transition between $|g\rangle$ and $|h\rangle$:

$$\omega_1 - \omega_2 = \omega_{gh}. \tag{1.64}$$

The two fields will be used to describe the processes of Raman scattering. In the Stokes scattering the first field will be treated as a strong driving beam whereas the second field will describe the scattered photons. Next, to describe the anti-Stokes scattering, the role of the fields will be switched. We start with a general description when we treat both fields quantum mechanically.

The first field is detuned from $|g\rangle \leftrightarrow |e\rangle$ by $\Delta = \omega_{ge} - \omega_1$. The convenient way to describe the interacting system of light and an atom is the interaction picture and the subsequent application of the rotating wave approximation[6]. The Hamiltonian of interaction that governs the evolution takes the form of:

$$\hat{H} = \frac{\hbar}{2}(\Delta\hat{\sigma}_{ee} - \hat{\Omega}_1\hat{\sigma}_{eg} - \hat{\Omega}_2\hat{\sigma}_{eh}) + H.c., \tag{1.65}$$

where $\hat{\Omega}_i$ stands for the Rabi frequency operator expressed by the dipole moments of one-photon transitions $d_{ge} = \mathbf{d}_{ge}\cdot\mathbf{e_1}$, $d_{he} = \mathbf{d}_{he}\cdot\mathbf{e_2}$, where $\mathbf{e}_i$, $i = 1,2$ stands for the unit vector along the vector of respective electric field. The $\hat{\Omega}_i$ operators localized at the atom position $\mathbf{r}$ are defined as:

$$\hat{\Omega}_1 = i\frac{d_{ge}}{\hbar}\int \frac{d^3k}{(2\pi)^3}\sqrt{\frac{\hbar\omega_k}{2\varepsilon_0}}\hat{a}_1(\mathbf{k})e^{i\mathbf{k}\cdot\mathbf{r}}e^{-i\omega_k t}e^{i\omega_1 t}, \tag{1.66}$$

$$\hat{\Omega}_2 = i\frac{d_{he}}{\hbar}\int \frac{d^3k}{(2\pi)^3}\sqrt{\frac{\hbar\omega_k}{2\varepsilon_0}}\hat{a}_2(\mathbf{k})e^{i\mathbf{k}\cdot\mathbf{r}}e^{-i\omega_k t}e^{i\omega_2 t}. \tag{1.67}$$

The time dependence in the above operators originates from the interaction picture. The central frequencies of light fields are matched to the two photon transition as in Eq. (1.64).

The second term in Eq. (1.65) corresponds to the one-photon transition between the levels $|g\rangle, |e\rangle$: the annihilation of a photon by the $\hat{\Omega}_1$ operator excites the atom by $\hat{\sigma}_{eg}$ from $|g\rangle$ to $|e\rangle$. A similar action corresponding to the transition between $|h\rangle, |e\rangle$ can be associated with the third term of Eq. (1.65).

[6] Derivations starting from the dipole approximation and the interaction of the general form $-e\hat{\mathbf{r}}\cdot\hat{\mathbf{E}}$ can be found in many textbooks cf. (Scully and Zubairy, 1997).

### 1.5.2 Adiabatic elimination

Large detunings $\Delta$ diminish the role of the level $|e\rangle$ as it mediate two-photon transitions between $|g\rangle, |h\rangle$ exclusively. We can drop it from the description by applying the procedure of adiabatic elimination (Brion *et al.*, 2007). The procedure considered in the interaction picture assumes that operators involving $|e\rangle$ follow adiabatically other transition operators, such as $\hat{\sigma}_{gg}, \hat{\sigma}_{gh}$ etc. Additionally the population of the excited state can be neglected. To be more specific, we shall take

$$\frac{\mathrm{d}\hat{\sigma}_{eg}}{\mathrm{d}t} = \frac{\mathrm{d}\hat{\sigma}_{eh}}{\mathrm{d}t} = 0. \tag{1.68}$$

The time derivatives can be found from the respective Heisenberg equation:

$$\frac{\mathrm{d}\hat{\sigma}_{ei}}{\mathrm{d}t} = \frac{i}{\hbar}[\hat{H}, \hat{\sigma}_{ei}]. \tag{1.69}$$

The Hamiltonian commutator with $\hat{\sigma}_{eg}$ can be evaluated applying commutation relations in Eq. (1.63), which yields:

$$[\hat{H}, \hat{\sigma}_{eg}] = \hbar\Delta\hat{\sigma}_{eg} - \frac{\hbar}{2}\hat{\Omega}_1^\dagger\hat{\sigma}_{gg} + \frac{\hbar}{2}\hat{\Omega}_1^\dagger\hat{\sigma}_{ee} - \frac{\hbar}{2}\hat{\Omega}_2^\dagger\hat{\sigma}_{hg}. \tag{1.70}$$

Now we can use our second assumption that population of $|e\rangle$ can be neglected, i.e. $\hat{\sigma}_{ee} \simeq 0$, and compare the above commutator to zero in order to obtain:

$$\hat{\sigma}_{eg} = \frac{1}{2\Delta}(\hat{\Omega}_1^\dagger\hat{\sigma}_{gg} + \hat{\Omega}_2^\dagger\hat{\sigma}_{hg}). \tag{1.71}$$

Repeating the above procedure enables elimination of the transition operators between the levels $|h\rangle$ and $|e\rangle$, which equals:

$$\hat{\sigma}_{eh} = \frac{1}{2\Delta}(\hat{\Omega}_1^\dagger\hat{\sigma}_{gh} + \hat{\Omega}_2^\dagger\hat{\sigma}_{hh}). \tag{1.72}$$

Now we can substitute $\hat{\sigma}_{eg}, \hat{\sigma}_{eh}$ and their Hermitian conjugates to our initial Hamiltonian in Eq. (1.65) to find the effective Hamiltonian $\hat{H}_{\mathrm{eff}}$ involving directly only the levels $|g\rangle$ and $|h\rangle$:

$$\hat{H}_{\mathrm{eff}} = -\frac{\hbar}{2\Delta}(\hat{\Omega}_1^\dagger\hat{\Omega}_1\hat{\sigma}_{gg} + \hat{\Omega}_2^\dagger\hat{\Omega}_2\hat{\sigma}_{hh} + \hat{\Omega}_1\hat{\Omega}_2^\dagger\hat{\sigma}_{hg} + \hat{\Omega}_1^\dagger\hat{\Omega}_2\hat{\sigma}_{gh}). \tag{1.73}$$

The first two terms of Eq. (1.73) describe the Stark shift of the levels $|g\rangle$ and $|h\rangle$. The third term proportional to $\hat{\Omega}_1\hat{\Omega}_2^\dagger\hat{\sigma}_{hg}$ describes the atomic transition from $|g\rangle$ to $|h\rangle$ levels, the annihilation of one photon in mode 1 and the creation of a photon in mode 2. The last term of Eq. (1.73) is responsible for the opposite action. As a result of the adiabatic elimination we were able to simplify the system in question to a two-level system, as in Fig. 1.6(b). This is an exact analogy to the two-level atom coupled to the field of the Rabi frequency $\Omega_R = \Omega_1\Omega_2^*/2\Delta$, customarily called the two-photon Rabi frequency.

### 1.5.3 Collective scattering in an ensemble of atoms

Now we shall consider a large ensemble of $N$ identical atoms uniformly distributed in a certain volume. The atoms are illuminated with classical light detuned by $\Delta$ from the $|g\rangle \leftrightarrow |e\rangle$ resonance. In such a situation Raman scattering can occur and generate a photon of a frequency different from the beam driving the process. We assume that all of the atoms are initially in a ground state $|g\rangle$.

A formal description of this process called the Stokes scattering requires a generalization of the previously derived Hamiltonian in Eq. (1.73) onto the whole ensemble and a summation over all of

the atoms. Moreover, as we indicated before, the first field $\Omega_1(\mathbf{r}_i)$ should be treated as a classical c-number. Finally, for the sake of simplicity, we take only the terms changing the atomic states[7]. Then the sum over all atoms whose positions are denoted as $\mathbf{r}_i$ for $i-$th atom is expressed as follows:

$$\hat{H}_S = -\frac{\hbar}{2\Delta}\sum_i \Omega_W e^{i\mathbf{k}_W\cdot\mathbf{r}}\hat{\Omega}_S^\dagger(\mathbf{r}_i)\hat{\sigma}_{hg}^{(i)} + H.c., \tag{1.74}$$

where $\hat{\Omega}_S^\dagger(\mathbf{r}_i)$ refers to the second field of the Stokes photon treated quantum mechanically and $\hat{\sigma}_{hg}^{(i)}$ transfers $i-$th atom from $|g\rangle$ to $|h\rangle$. We treated the first field as a strong classical beam in a plane-wave mode of the wave vector $\mathbf{k}_W$, where $\Omega_W$ denotes the classical Rabi frequency of the field. Then we rewrite the Hamiltonian expressing the Rabi field operator of the Stokes photon in the full form defined by Eq. (1.67):

$$\hat{H}_S = -i\frac{d_{he}}{2\Delta}\sqrt{\frac{\hbar\omega_S}{2\varepsilon_0}}\int\frac{d^3k_S}{(2\pi)^3}\sum_i \Omega_W \hat{a}_S^\dagger(\mathbf{k}_S)\hat{\sigma}_{hg}^{(i)} e^{i(\mathbf{k_W}-\mathbf{k}_S)\cdot\mathbf{r}_i} e^{-i(\omega_{k_S}-\omega_S)t} + H.c. \tag{1.75}$$

The terms associated with atoms enter in the above formula only through the sum. We can collect them together by taking $\mathbf{K} = \mathbf{k}_W - \mathbf{k}_S$ to define an operator:

$$\hat{b}^\dagger(\mathbf{K}) = \frac{1}{\sqrt{N}}\sum_i e^{i\mathbf{K}\cdot\mathbf{r}_i}\hat{\sigma}_{hg}^{(i)}, \tag{1.76}$$

which excites any atom and imprints on the spatially varying phase. As we show later, the operator $\hat{b}^\dagger(\mathbf{K})$ has properties similar to the creation operator. With this notation, the Hamiltonian of the Stokes scattering takes the form:

$$\hat{H}_S = \frac{\hbar\kappa}{2}\int\frac{d^3k_S}{(2\pi)^3}\hat{a}_S^\dagger(\mathbf{k}_S)\hat{b}^\dagger(\mathbf{k}_W-\mathbf{k}_S)e^{-i(\omega_{k_S}-\omega_S)t} + H.c., \tag{1.77}$$

where $\kappa$ denotes a coupling coefficient expressed as:

$$\kappa = -i\frac{d_{he}\Omega_W}{\Delta}\sqrt{\frac{N\omega_S}{2\hbar\varepsilon_0}}. \tag{1.78}$$

The Hamiltonian of the Stokes scattering derived in Eq. (1.77) has a form closely resembling the squeezing Hamiltonian defined in Eq. (1.27), yet extending the description to many spatial modes in the plane-wave basis. Thus we expect the Stokes scattering to produce a state close to the squeezed state of atoms and light. This is because here we deal with two classes of operators: $\hat{a}_S^\dagger$ creates Stokes photons whereas $\hat{b}^\dagger$ excites atoms.

### 1.5.4 Stokes scattering of a single photon and generation of a single excitation

To gain insight into the state of the atoms and light, we consider a simple situation where a single photon has been scattered, summarized in Fig. 1.7. Initially the atoms are in the ground state expressed as a product state and denoted by:

$$|0\rangle_b = |g\rangle_1 \otimes \ldots \otimes |g\rangle_N. \tag{1.79}$$

[7] Formally it requires changing the basis to states rotating with respective frequencies as in the standard procedure of the interaction picture.

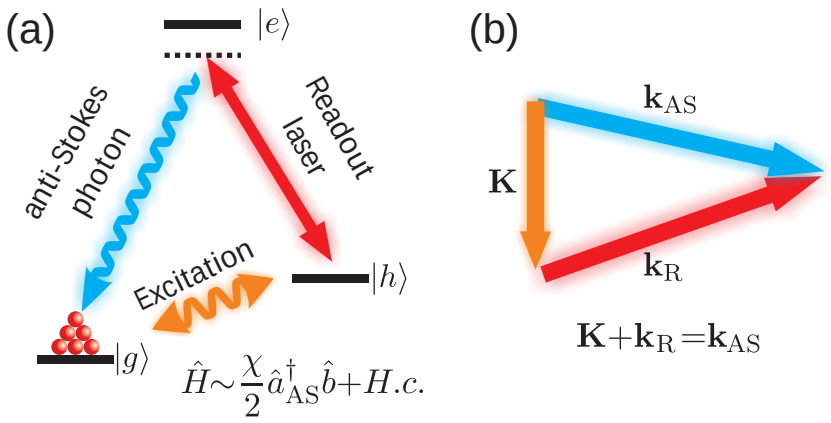


Figure 1.7: (a) Level diagram for the Stokes scattering. Strong beam of the write laser scatters a single Stokes photon and creates one of the atoms in the excited state $|h\rangle$. Effectively, since all atoms have participated in the process, a collective excitation is created. (b) Phase matching condition relating the wave vectors of the write laser $\mathbf{k}_{\mathrm{W}}$, the Stokes photon $\mathbf{k}_S$ scattered in a random direction, and the wave vector of collective excitation $\mathbf{K}$.

With a certain probability one photon from a driving beam can be annihilated to create a single photon closing a two-photon transition between levels $|g\rangle$ and $|h\rangle$. A single photon scattering is accompanied by a single atom excitation to the $|h\rangle$ level. In a scenario where one cannot physically distinguish which atom has scattered a photon a collective excitation occurs meaning that each atom has participated in this process. The approximate result of the Stokes scattering in the $\mathbf{k}_S$ direction can be found in the first order of perturbation theory, which simply corresponds to the action of the Hamiltonian on a joint initial state of atoms and light. Then we consider only a single term of $\hat{H}_S$ describing single plane-wave modes of atoms and plane-wave modes of light:

$$\hat{a}^{\dagger}_S(\mathbf{k}_S)\hat{b}^{\dagger}(\mathbf{K})|0\rangle_{\mathbf{k}_S}|0\rangle_b = |1\rangle_{\mathbf{k}_S}|1\rangle_{b,\mathbf{K}}, \tag{1.80}$$

where the wave vector appearing in the atomic operator depends on the driving beam direction $\mathbf{K} = \mathbf{k}_W - \mathbf{k}_S$ as summarized in the phase matching condition in Fig. 1.7(b). While the single photon state $|1\rangle_{\mathbf{k}_S}$ has already been discussed, the resulting state of the atoms $|1\rangle_{b,\mathbf{K}}$ requires further explanations. Following the definition of $\hat{b}^{\dagger}(\mathbf{K})$ in Eq. (1.76) and the ground state of the ensemble in Eq. (1.79) we obtain:

$$|1\rangle_{b,\mathbf{K}} = \hat{b}^{\dagger}(\mathbf{K})|0\rangle_b = \frac{1}{\sqrt{N}}\sum_{i=1}^{N} e^{i\mathbf{K}\cdot\mathbf{r}_i}|g\rangle_1\otimes\ldots\otimes|h\rangle_i\otimes\ldots\otimes|g\rangle_N. \tag{1.81}$$

The interpretation of a collective excitation of the atoms is sketched in Fig. 1.8. The sum in Eq. (1.81) denotes a superposition of single atom excitations[8]. More precisely either the first atom was excited to $|h\rangle$ level while the rest of them remained in $|g\rangle$, or the second atom was excited and so forth.

Moreover, upon scattering atoms experience slightly different conditions, namely depending on their position they interact with waves of different phases. For instance an $i$-th atom placed in a position $\mathbf{r}_i$ interacts with a driving beam of a phase $e^{i\mathbf{k}_W\cdot\mathbf{r}_i}$ and a photon of a phase $e^{-i\mathbf{k}_S\cdot\mathbf{r}_i}$, hence, the atom acquires a spatially dependent phase $e^{i\mathbf{K}\cdot\mathbf{r}_i}$. In the Schroedinger picture the$i$-th

[8]Such a state is highly nonclassical maximally entangled and called a W or first Dicke state. Recently it has been created for 41 atoms (Haas *et al.*, 2014).

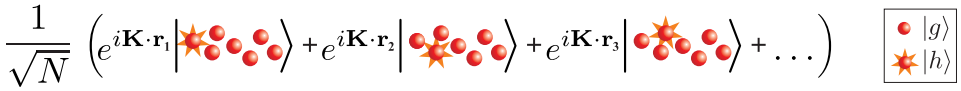


Figure 1.8: Pictorial representation of a collective excitation of an atomic ensemble $|1\rangle_{b,\mathbf{K}}$ that is created upon scattering of a single photon in the Stokes process. In each term of the state exactly one atom is in the excited $|h\rangle$ state whereas the rest remains in the ground state $|g\rangle$. The phase multiplicative factors $e^{i\mathbf{K}\cdot\mathbf{r}_i}$ depend on the position of the $i$-th excited atom and they are determined by the wave vectors of the driving beam and the Stokes photon. Since the terms evolve like plane waves, the collective state is often called a spin wave.

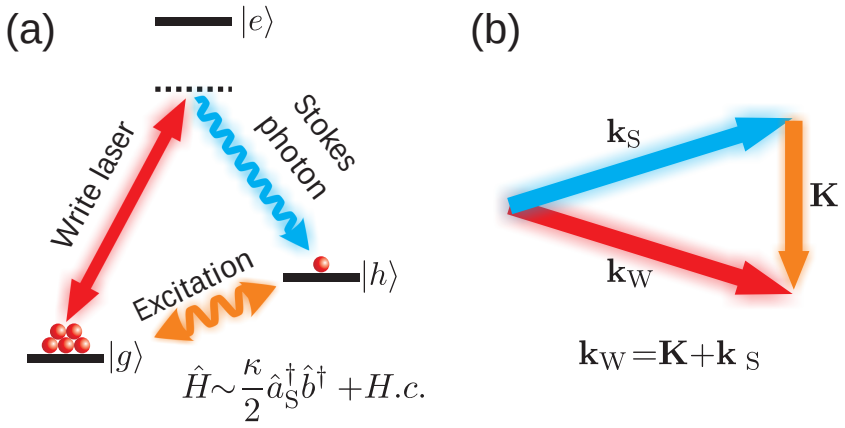


Figure 1.9: (a) Level diagram for the anti-Stokes scattering. Readout laser coupling to the state $|h\rangle$ transfers the single collective excitation back to the ground level $|g\rangle$ producing an anti-Stokes photon. (b) The direction of the anti-Stokes photon described by its wave vector $\mathbf{k}_{\mathrm{AS}}$ is now determined by the wave vectors of the collective excitation $\mathbf{K}$ and the driving readout beam $\mathbf{k}_{\mathrm{R}}$, as illustrated by the exemplary phase matching condition.

atom phase evolves as $e^{i(\mathbf{K}\cdot\mathbf{r}_i-\omega_{gh}t)}$, thus such collective excitations are often called spin waves when $|g\rangle$ and $|h\rangle$ levels correspond to different spins of the atom.

Despite similarities to the generation of photon pairs in SPDC process, here one of the modes corresponds to atomic excitations that remain motionless. In a sense one can perceive atoms as if they were able to remember the direction of the scattered photon. Since the excitations can be long-lived, the atoms can be treated as memory.

### 1.5.5 Readout from atoms

Atomic excitations can be converted back to light in the complementary anti-Stokes process, called alternatively the readout, illustrated in Fig. 1.9. The process is driven by another classical light field called *read* beam of the Rabi frequency $\Omega_R$ and wave vector $\mathbf{k}_R$ which couples[9] off-resonantly levels $|h\rangle$ and $|e\rangle$. The driving light can destroy the atomic excitation and scatter a photon of a frequency closing the corresponding two-photon transition.

Repeating derivation of the Hamiltonian in Eq. (1.77) with switched roles of the fields we obtain the operator for the anti-Stokes process:

[9] One may notice that the driving beam in the readout process can couple also to the ground state $|g\rangle$. The coupling can be minimized by choosing a proper frequency of the beam yet it has a certain, noticeable consequences which are studied in Part II and in (Dąbrowski *et al.*, 2014).

$$\hat{H}_{AS} = \frac{\hbar\chi}{2}\int \frac{d^3k_{AS}}{(2\pi)^3}\hat{a}^{\dagger}_{AS}(\mathbf{k}_{AS})\hat{b}(\mathbf{k}_{AS}-\mathbf{k}_R)e^{-i(\omega_{k_{AS}}-\omega_{AS})t} + H.c., \tag{1.82}$$

where $\omega_{AS}$ is the central frequency of the anti-Stokes photons and $\mathbf{k}_{AS}$ is their wave vector whereas the coupling coefficient is expressed as follows:

$$\chi = -i\frac{d_{ge}\Omega_R}{\Delta}\sqrt{\frac{\omega_{AS}}{2\hbar\varepsilon_0}}. \tag{1.83}$$

Let us consider the state of atoms and light that underwent previously discussed Stokes process. Then, in the first order of perturbation theory, the only non-vanishing term creates an anti-Stokes photon is:

$$\hat{a}^{\dagger}_{AS}(\mathbf{k}_{AS})\hat{b}(\mathbf{K})|0\rangle_{\mathbf{k}_{AS}}|1\rangle_{\mathbf{k}_S}|1\rangle_{b,\mathbf{K}} = |1\rangle_{\mathbf{k}_{AS}}|1\rangle_{\mathbf{k}_S}|0\rangle_b. \tag{1.84}$$

The three modes appearing in the above formula denote subsequently the anti-Stokes photons of the wave vector $\mathbf{k}_{AS}$, Stokes photons of the wave vector $\mathbf{k}_S$ and the atomic collective excitation of the wave vector $\mathbf{K}$. The direction of the Stokes photon has been accidental yet it determined $\mathbf{K}$. Then in the readout process the only term that coupled to the spin wave excitation was proportional to $\hat{b}(\mathbf{k}_{AS}-\mathbf{k}_R)$. As a consequence, the direction of the anti-Stokes photons is fully determined by the Stokes scattering process and its wave vector equals:

$$\mathbf{k}_{AS} = \mathbf{k}_W + \mathbf{k}_R - \mathbf{k}_S. \tag{1.85}$$

As we see the anti-Stokes process is deterministic. It reads the previously stored atomic excitation to produce a photon in a predictable direction, as in Eq. (1.85). Remarkably this process can be postponed and within a certain range of time it can be started at a chosen, arbitrary moment. As we show in Part II combination of Stokes and anti-Stokes scattering can be useful in generating single photons with some advantages over sources based on SPDC.

### 1.5.6 Formalism of collective excitations

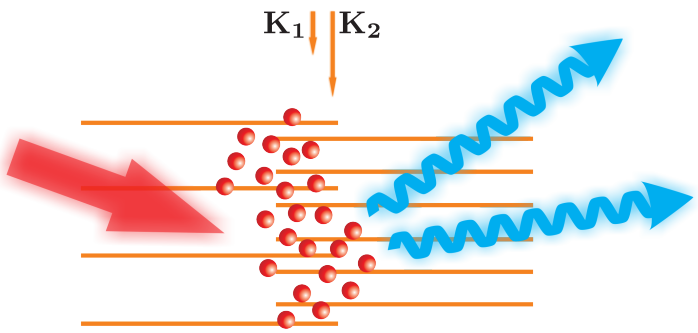


Figure 1.10: Different modes of the collective excitations of distinct wave vectors can be excited independently in the write-in process producing scattered photons in distinguishable directions. The two spin waves of wave vectors $\mathbf{K_1}$ and $\mathbf{K_2}$ are symbolically marked as orange vertical lines whereas we consistently denote a driving beam by a red arrows, and scattered photons are marked blue. The scattering can be perceived as an analogy to diffraction on Bragg grating of certain periodicity components. Note that the picture could as well illustrate the readout process for the reversed wave vectors of the spin waves.

The operator $\hat{b}^\dagger(\mathbf{K})$ introduced in Eq. (1.76) can be treated as a bosonic creation operator under the following circumstances. A direct evaluation of the commutator with the Hermitian conjugate yields:

$$[\hat{b}(\mathbf{K}), \hat{b}^\dagger(\mathbf{K}')] = \delta(\mathbf{K}-\mathbf{K}')\frac{1}{N}\sum_{i=1}^{N}(\hat{\sigma}_{gg}^{(i)} - \hat{\sigma}_{hh}^{(i)}), \tag{1.86}$$

where the delta function is an approximation for very large ensembles.

The expectation value of such an operator taken on the class of ensemble states $|\Psi\rangle$ where most of the atoms occupy $|g\rangle$ is the following:

$$\langle\Psi|[\hat{b}(\mathbf{K}), \hat{b}^\dagger(\mathbf{K}')]|\Psi\rangle \simeq \delta(\mathbf{K}-\mathbf{K}') \;\Leftrightarrow\; [\hat{b}, \hat{b}^\dagger] \simeq \delta(\mathbf{K}-\mathbf{K}'). \tag{1.87}$$

That justifies our treating the $\hat{b}$ and $\hat{b}^\dagger$ as bosonic annihilation and creation operators provided that an ensemble state remains close to its ground state[10] $|0\rangle_b$. Thus, the first excited state representing a symmetric coherent superposition been presented in Eq. (1.81) can be treated as a first Fock state. One can extend the description onto higher Fock states similarly as for a photon. Moreover, we can introduce a similar operator for a number of excitations:

$$\hat{n}_{b,\mathbf{K}} = \hat{b}^\dagger(\mathbf{K})\hat{b}(\mathbf{K}), \tag{1.88}$$

which, similarly as for photons, returns the number of spin waves in the specific mode $\mathbf{K}$.

In close analogy to photon states we can also consider wave packets, multiple excitations in different modes etc. In particular in Fig. 1.10 we present a simple example of simultaneous write-in of two collective excitations.

### 1.5.7 Coherent state of atoms

Here we give a single, specific example of the classical state of atoms – the equivalent of the coherent state. It can be obtained if both light fields in the Stokes Hamiltonian in Eq. (1.77) are treated classically. Then the Hamiltonian $\hat{H}_S$ changes into a displacement operator producing coherent states from a vacuum (Lvovsky, 2015).

We begin with a description emphasizing that each atom should be excited independently and together they form a product state:

$$|\beta\rangle = (1+|\beta|^2)^{-N/2}\bigotimes_{i=1}^{N}(|g\rangle_i + \beta|h\rangle_i), \tag{1.89}$$

where $\beta \ll 1$ is the coherence between the levels $|g\rangle$ and $|h\rangle$. For a further study of decoherence effects we can represent each atomic state by a density matrix:

$$\hat{\rho} = \frac{1}{1+|\beta|^2}\begin{pmatrix} 1 & \beta \\ \beta^* & |\beta|^2 \end{pmatrix}. \tag{1.90}$$

We can compare the product state $|\beta\rangle$ with the collective excitation $|1\rangle$ defined in Eq. (1.81) by expanding it into the Fock collective basis:

$$|\beta\rangle \simeq |0\rangle_b + \beta\sqrt{N}|1\rangle_b + o(\beta^2), \tag{1.91}$$

[10] This approximation is known as the Holstein-Primakoff approximation (Holstein and Primakoff, 1940).

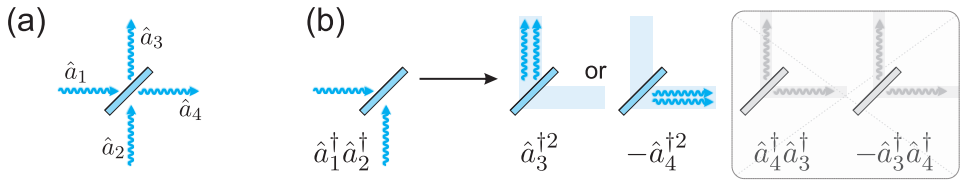


Figure 1.11: (a) The operation of the beam splitter (BS) can be represented as the transformation of two input modes $\hat{a}_1, \hat{a}_2$ and two output modes $\hat{a}_3, \hat{a}_4$ as in Eq. 1.93. (b) Two identical photons feeding two inputs of the BS $\hat{a}_1^\dagger \hat{a}_2^\dagger |0\rangle$ overlap and interferes at the outputs. In consequence, photons leave the BS only in pairs in a state $(\hat{a}_3^{\dagger 2} - \hat{a}_4^{\dagger 2})|0\rangle/2$. This phenomenon, called the Hong-Ou-Mandel effect, is a result of a destructive interference of two probability amplitudes depicted in the grayed out box.

where $o(\beta^2)$ denotes the terms representing the second or higher power of $\beta$, which consists of higher-excited states. For small values of $\beta\sqrt{N} \ll 1$, the state $|\beta\rangle$ can be found in the first excited states with a small probability. These differences between $|\beta\rangle$ and $|1\rangle_b$ can be viewed as an exact analogy to a weak coherent state that is different from a single photon.

If the Stokes scattering occurs at a certain angle, then the resulting state corresponds to a spin wave of the wave vector **K**:

$$\hat{\rho}(\mathbf{r}) = \frac{1}{1+|\beta(\mathbf{r})|^2} \begin{pmatrix} 1 & \beta(\mathbf{r}) e^{i\mathbf{K}\cdot\mathbf{r}} \\ \beta^*(\mathbf{r}) e^{-i\mathbf{K}\cdot\mathbf{r}} & |\beta(\mathbf{r})|^2 \end{pmatrix}. \tag{1.92}$$

More intuitively spin waves in coherent states can be treated as spatially varying atomic coherence with no correlation between the atoms.

## 1.6 Nonclassical interference of single photons

So far we have been discussing states of light where photons occupied specific modes. Now we proceed to describing nonclassical interference phenomena where modes can overlap or the measurements are performed in mode superposition basis. Since the present thesis focuses on spatial structure of light and imaging techniques, we shall consider interference in the context of spatially resolving detection. Here we restrict ourselves to systems involving two-photon states of light. Below we provide a brief introduction and several simple physical examples that are useful in understanding of Part III.

### 1.6.1 Beam splitter mode transformation

The simplest mode transformation can be exemplified by the beam splitter (BS) transformation. A full description of the beam splitter requires at least four distinct modes pairwise for input $\hat{a}_1, \hat{a}_2$, and output $\hat{a}_3, \hat{a}_4$ modes respectively, as depicted in Fig. 1.11(a). In case of a balanced BS, i.e. one that equally transmits in and reflects beams, the relation between the output and input modes can be gathered in a matrix form including the $\pi$ phase shift upon reflection from a one side of the BS:

$$\begin{pmatrix} \hat{a}_3 \\ \hat{a}_4 \end{pmatrix} = \frac{1}{\sqrt{2}} \begin{pmatrix} 1 & 1 \\ -1 & 1 \end{pmatrix} \begin{pmatrix} \hat{a}_1 \\ \hat{a}_2 \end{pmatrix}. \tag{1.93}$$

As the simplest illustration let us consider a single photon impinging on one side of the BS. In other words, here a photon occupies a single input mode while in the other mode there is vacuum state: $|1\rangle_1|0\rangle_2 = \hat{a}_1^\dagger|0\rangle$, where the subscripts relate to the modes described by the ket. To find the state on

the output we can invert the relation in Eq. (1.93) and rewrite the state in the output mode basis, which yields an easily predictable result:

$$|1\rangle_1|0\rangle_2 = \frac{1}{\sqrt{2}}(\hat{a}_3^\dagger - \hat{a}_4^\dagger)|0\rangle = \frac{1}{\sqrt{2}}\Big(|1\rangle_3|0\rangle_4 - |0\rangle_3|1\rangle_4\Big). \tag{1.94}$$

### 1.6.2 Coherent states on a beam splitter

Another simple example illustrating the BS mode transformation is the classical interference of coherent states. Let us consider two states of identical amplitudes feeding two inputs:

$$|\alpha\rangle_1|\alpha\rangle_2 = e^{-|\alpha|^2}e^{\alpha(\hat{a}_1^\dagger+\hat{a}_2^\dagger)}|0\rangle = e^{-|\alpha|^2}e^{\sqrt{2}\alpha\hat{a}_3^\dagger}|0\rangle = |\sqrt{2}\alpha\rangle_3|0\rangle_4. \tag{1.95}$$

The result obviously denotes classical constructive interference in mode 3 and destructive interference in mode 4 and it would change if there were a phase difference between feeding state. As an alternative example we can consider a coherent state feeding only one input of the BS subjected on the output:

$$|0\rangle_1|\alpha\rangle_2 = e^{-\frac{|\alpha|^2}{2}}e^{\alpha(\hat{a}_3^\dagger+\hat{a}_4^\dagger)/\sqrt{2}}|0\rangle = |\alpha/\sqrt{2}\rangle_3|\alpha/\sqrt{2}\rangle_4. \tag{1.96}$$

As we see, we obtain as a result a product state of two entirely uncorrelated coherent states of a half of the initial intensity. From the point of view of quantum mechanical description the outcome may be considered as surprising since the generic output state is path entangled even in case of a single photon in Eq. (1.94).

Since now we shall consider the detection of only two photons, called coincidence events. We shall later refer to the split coherent state in Eq. (1.96) in the context of postselection on two-photon events. The postselected split coherent state is expressed as follows:

$$|0\rangle_1|\alpha\rangle_2 \longrightarrow \frac{1}{4}(\hat{a}_3^{\dagger 2} + \hat{a}_4^{\dagger 2} + 2\hat{a}_3^\dagger\hat{a}_4^\dagger)|0\rangle = \frac{1}{2}(|2\rangle_3|0\rangle_4 + 2|1\rangle_3|1\rangle_4 + |0\rangle_3|2\rangle_4), \tag{1.97}$$

where we only included two-photon terms.

### 1.6.3 Hong-Ou-Mandel interference

A more intriguing situation occurs where two input ports of the beam splitter are simultaneously fed by two single photons, i.e.: $|1\rangle_1|1\rangle_2 = \hat{a}_1^\dagger\hat{a}_2^\dagger|0\rangle$, as depicted in Fig. 1.11(b). Following exactly the same procedure as before, we obtain:

$$|1\rangle_1|1\rangle_2 = \frac{1}{2}(\hat{a}_3^\dagger - \hat{a}_4^\dagger)(\hat{a}_3^\dagger + \hat{a}_4^\dagger)|0\rangle = \frac{1}{2}(\hat{a}_3^{\dagger 2} - \hat{a}_4^{\dagger 2})|0\rangle = \frac{1}{\sqrt{2}}(|2\rangle_3|0\rangle_4 - |0\rangle_3|2\rangle_4). \tag{1.98}$$

The result now is definitively less intuitive as we do not have any terms responsible for the situation where two photons leave the opposite output ports. Such terms as $\hat{a}_3^\dagger\hat{a}_4^\dagger$ and $-\hat{a}_4^\dagger\hat{a}_3^\dagger$ have canceled out in a specific, destructive interference. This effect, called the Hong-Ou-Mandel (HOM) interference, was named after the researchers who first demonstrated it experimentally: (Hong *et al.*, 1987). It is one of the simplest, yet no less profound quantum phenomena with no classical counterparts and has been exploited experimentally for the last three decades. The resulting state is a simplest non-trivial N00N state discussed before[11].

[11] As we see, using a beam splitter the N00N states for $N = 1$ and $N = 2$ can be created, regrettably this procedure cannot be continued and the evaluation of the next inductive step fails and one has to rather resort to procedures described in (Afek *et al.*, 2010).

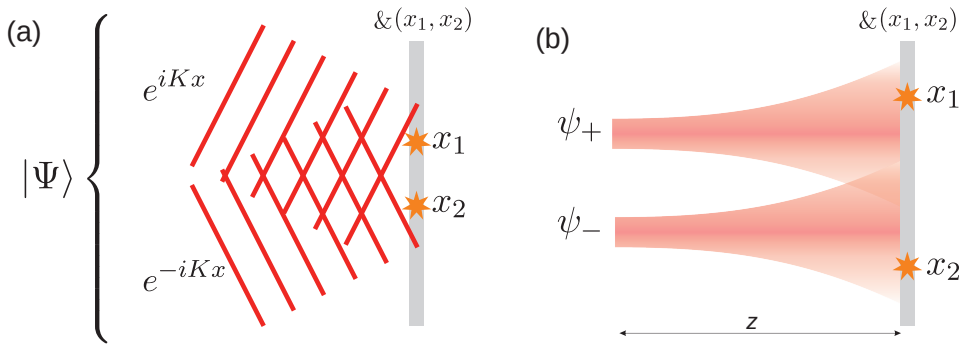


Figure 1.12: (a) The two-photon state $|\Psi\rangle$ in spatially overlapping plane wave modes can be characterized by measuring spatially resolved coincidence events. Repeated detection of photons around $x_1$ and $x_2$ coordinates can be used to reconstruct the empirical probability distribution $p(x_1, x_2)$, c.f. Fig. 1.13. (b) Two-photon state in two Gaussian modes $\psi_\pm$, initially separated, are subjected to diffraction and begin to overlap. The subsequent spatially resolved detection can reveal the interference patterns in the distribution of coincidences, see Fig. 1.14.

Here, let us highlight the fact that the result of HOM interference is entirely insensitive on the relative phase between the input ports 1 and 2, as seen in Eq. (1.98). This fact, contrasting with the outcome of classical interference as in Eq. (1.95), results from the entirely indeterminate phase of Fock states.

### 1.6.4 Spatially resolved detection of two interfering photons

Above we presented a simple discrete mode description of interference. In our experiments we applied a spatially resolved coincidence detection. For the sake of simplicity let us consider a one-dimensional case only. A camera sensor illuminated by a two-photon state $|\Psi\rangle$ can localize the two photons around the $x_1$ and $x_2$ coordinates. Repeating the detection many times we can measure the empirical probability distribution:

$$p(x_1, x_2) = |\langle x_1, x_2|\Psi\rangle|^2, \tag{1.99}$$

where $|x_1, x_2\rangle = \hat{a}^\dagger(x_1)\hat{a}^\dagger(x_2)|0\rangle$. It should be borne in mind that localized states that appear now refer in fact to our previous, coarse-grained definition for paraxial photons in Eq. (1.13). A simple generalization of the spatial wave packet of a single photon in Eq. (1.14) on a general two-photon state is the following:

$$|\Psi\rangle = \frac{1}{2}\iint dx_1 dx_2 u(x_1, x_2)\hat{a}^\dagger(x_1)\hat{a}^\dagger(x_2)|0\rangle, \tag{1.100}$$

where $u(x_1, x_2)$ stands for a normalized two-photon mode function[12]. For instance, if we consider a product state of two photons in modes $\psi_1, \psi_2$, i.e. $|\Psi\rangle = |1\rangle_{\psi_1}|1\rangle_{\psi_2}$, the two-photon mode function shall be: $u(x_1, x_2) = \psi_1(x_1)\psi_2(x_2)$. Alternatively for two photons in the same mode $\psi_i$, i.e. $|\Psi\rangle = |2\rangle_{\psi_i}$ the proper mode function is $u(x_1, x_2) = \psi_i(x_1)\psi_i(x_2)$.

In general we can readily connect the mode function with the probability of spatially resolved detection $p(x_1, x_2)$. To evaluate Eq. (1.99) for our general state defined in Eq. (1.100) it is useful to follow the relation:

[12]The two-photon mode function should not be confused with the two-photon quantum wave function $\Psi(x_1, x_2)$ which has to be symmetrized as for each indistinguishable bosons: $\Psi(x_1, x_2) = (u(x_1, x_2) + u(x_2, x_1))/\sqrt{2}$.

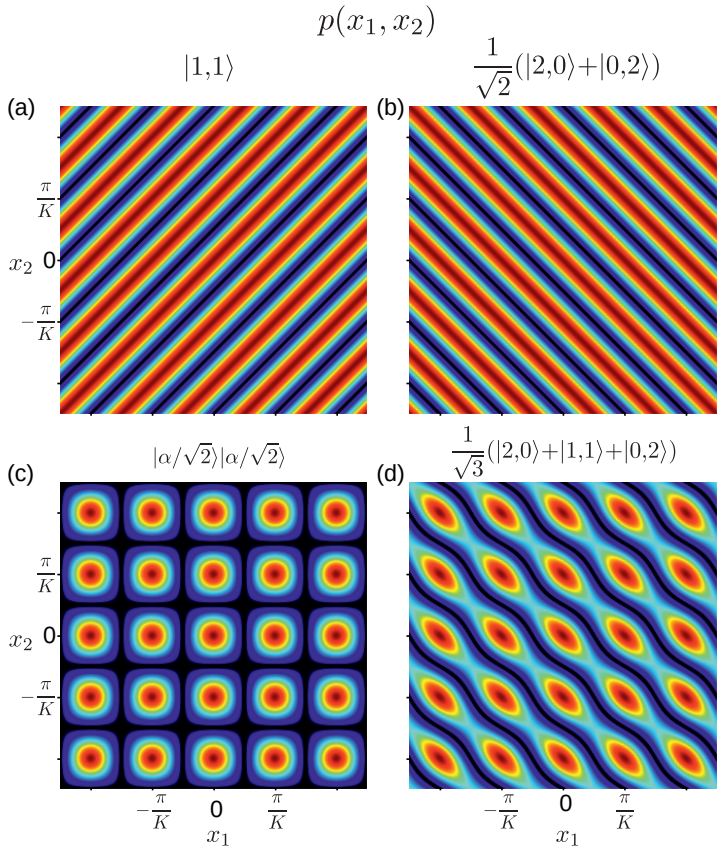


Figure 1.13: Probability distributions of spatially resolved coincidences $p(x_1, x_2)$ of two-photon states in two plane-wave modes $e^{iKx}$ and $e^{-iKx}$, as depicted in Fig. 1.12(a). Since photons are indistinguishable bosons, each point accounts for a two-photon interference where first photon went to $x_1$ and the second $x_2$ or *vice versa*. (a) Two single Fock states yield a fringe pattern despite their lack of a global phase, which can be understood as a result of their local phase difference. (b) Interference pattern for the N00N state is sensitive of the phase difference between the superposition terms. (c) The coherent state split onto two parts and subjected to postselection, described by Eq. (1.97), on two-photon coincidence events yields a separable pattern similar to the classical second-order field correlation. (d) Example of the interference pattern of the generic two-photon state.

$$\langle 0|(\hat{a}(x_1)\hat{a}(x_2)\hat{a}^\dagger(x')\hat{a}^\dagger(x''))|0\rangle = \delta(x_1 - x')\delta(x_2 - x'') + \delta(x_1 - x'')\delta(x_2 - x'), \tag{1.101}$$

which results from the commutation relations understood in the coarse grain sense. And as a consequence we obtain a symmetric probability distribution :

$$p(x_1, x_2) = |\langle x_1, x_2|\Psi\rangle|^2 = \frac{1}{2}|u(x_1, x_2) + u(x_2, x_1)|^2. \tag{1.102}$$

### 1.6.5 Interference of two photons in plane-wave modes

As the first specific example, let us consider two photons in two unnormalized plane-wave modes corresponding to the situation depicted in Fig. 1.12(a):

$$\psi_1(x) = e^{iKx},\ \psi_2(x) = e^{-iKx}. \tag{1.103}$$

Upon classical illumination of the two coherent fields one could observe the standard intensity interference pattern. Here, let us study how the two-dimensional distribution of coincidences depends on the state of the incoming photons. First let us consider two photons in a product of Fock states:

$$|1\rangle_{\psi_1}|1\rangle_{\psi_2} \longrightarrow p(x_1,x_2) = 2\cos^2(K(x_1-x_2)), \tag{1.104}$$

whose distribution of coincidences is presented in Fig. 1.13(a). At a first glance the fringe pattern contradicts the disability of interference of two independent photons. Here, however, the pattern remains insensitive to the relative difference of the global phases of photons in two modes, as can be readily checked. The observed fringe pattern results from nonclassical interference of probability amplitudes of the two events visualized in Fig. 1.13. Either the photon from mode 1 went to $x_1$ coordinate and the photon from mode 2 went to $x_2$ or *vice versa.* The resulting fringe pattern originates from the local phase difference and we shall dwell upon this type in interference in Chapter 9.

As a second example we consider the two photons in a N00N state:

$$\frac{1}{\sqrt{2}}(|2\rangle_{\psi_1}|0\rangle_{\psi_2} - |0\rangle_{\psi_1}|2\rangle_{\psi_2}) \longrightarrow p(x_1,x_2) = 2\cos^2(K(x_1+x_2)). \tag{1.105}$$

The probability distribution of coincidences presented in Fig. 1.13(b) is clearly sensitive on the relative phase between the modes.

Finally in Fig. 1.13(c) we present a coincidence pattern under illumination of classical light. The pattern is separable – one could obtain the same result classically if the second order correlation function of light intensities was considered. In other words, the pattern can be obtained as a product of classical intensity fringes. Fig. 1.13(d) is presented to visualize a generic two-photon state in between all of the previously discussed states.

### 1.6.6 Interference of two photons in Gaussian beam modes

In connection with the results presented in Part III let us consider photons interfering in two Gaussian beam modes. The physical situation is depicted in Fig. 1.12(b). Two normalized Gaussian beam modes, separated by $a$ and of a width $\sigma$ are defined for a plane in $z$ position:

$$\psi_\pm(x) = \frac{1}{\sqrt{\sqrt{\pi}(\sigma^2 + iz/k)}} e^{-\frac{(x\pm a/2)^2}{2(\sigma^2+iz/k)}}. \tag{1.106}$$

In Fig. 1.14 we demonstrate coincidence patterns for three different two photon states: (a) product of Fock states, (b) N00N state and (c) the classical state described by Eq. (1.97). The last one again yields separable patterns analogous to the classical second order correlations functions. The first row, corresponding to $z = 0$, clearly indicates the difference between the states, in particular Fig. 1.14(b) shows that photons always emerge together either within $\psi_+$ or $\psi_-$ mode. The last row approaches the far fields, which becomes similar to the previous results with photons in the plane-wave modes, as in Fig. 1.13.

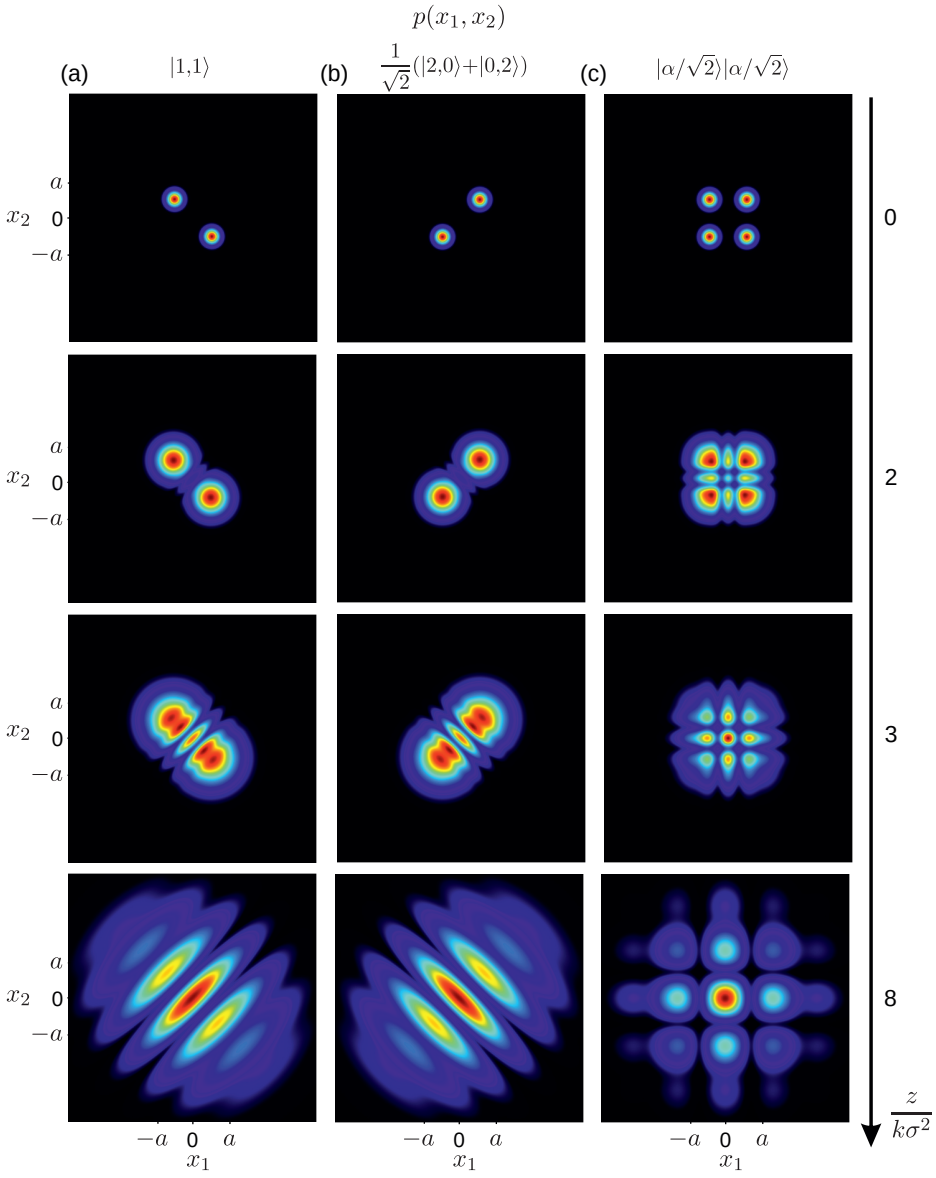


Figure 1.14: Expected results of the spatially resolved detection of two-photon states in the diffracting Gaussian modes as depicted in Fig. 1.12(b). Separation between modes has been set to $a = 6\sigma$, where $\sigma$ represents the beam width. Patterns have been presented in four propagation distances described by a dimensionless parameter $z/k\sigma^2$. We depict three states: (a) the product of a single photon, Fock states, (b) the N00N state and (c) the classical states, split coherent state postselected on coincidence events, described by Eq. (1.97).

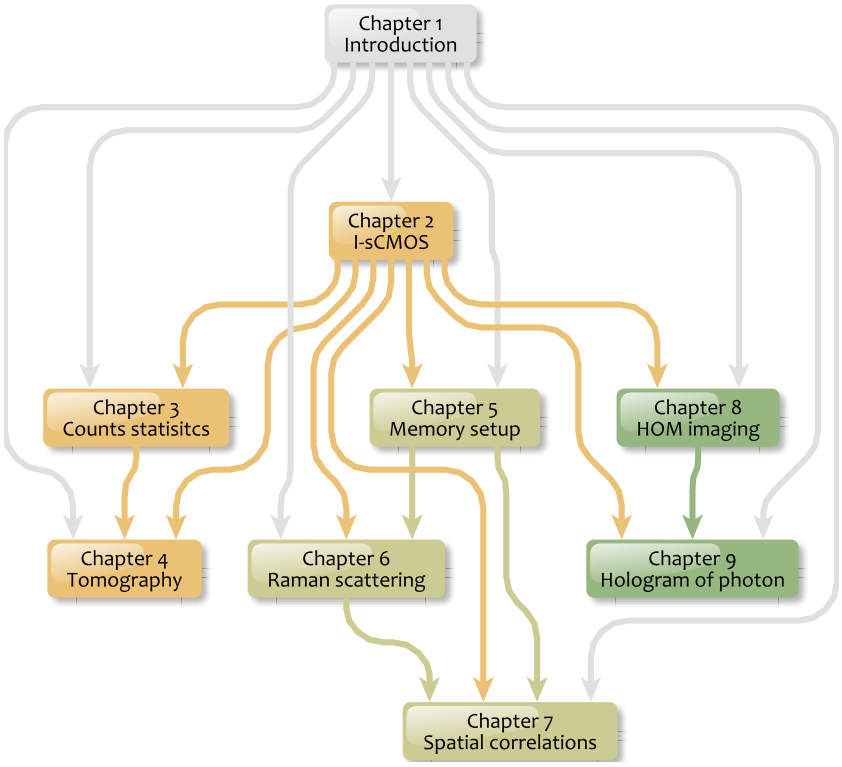


Figure 1.15: Relations between following chapters in the thesis and the flow of information marked with arrows.

## 1.7 Scope and structure of the thesis

The present thesis is divided into nine chapters grouped in three parts followed by five appendices. Mutual relations between the chapters are presented in a diagram in Fig. 1.15, where we mark the flow of information with arrows.

In Part I we present single-photon-sensitive detection with a new sCMOS camera equipped with an image intensifier. That part discusses the principle of operation and detection characteristic of the camera system. We focus on statistical properties of the detected light. Part II includes a description of a new source of photons based on atomic memory with a Raman scattering interface. We characterize the spatial properties of the generated light. Part III describes experiments with spatially resolved two-photon interference.

To facilitate the reading of this thesis we introduce a regular structure that is repeated throughout the thesis. Each part begins with a short introduction presenting an overview of its content and with a concise literature review to place the topic in a broader context. Each chapter also begins with one-page summary describing briefly the content of the following sections. On the first page of each chapter there is a figure that introduces the main topic graphically. Finally, each chapter has its own conclusions section summarizing the crucial results in order of their appearance in the text.

Finally we gather all of the important findings that appeared in all parts and chapters “Final remarks and outlook”. It is also where we discuss possible applications of our results.

# Part I

# Photon counting using a single-photon-sensitive camera

The first part of the chapter treats of a new tool for quantum optics — an intensified sCMOS (I-sCMOS) camera and its photon counting properties. In Chapter 2 we present the hardware description and we describe the photon counting process. Chapter 3 presents theoretical models of photon counting in the context of artificially nonclassical effects seen in count statistics. Chapter 4 summarizes the experimental results of the camera tomography and its application for high-fidelity photon statistics reconstruction.

The constructed and characterized I-sCMOS camera can be compared with other single-photon-sensitive cameras, such as the intensified and electron multiplying CCD (ICCD and EM CCD, respectively). Those two types have been used in many experiments in quantum optics, such as qualifying correlations in nonclassical light (Oemrawsingh *et al.*, 2002; Haderka *et al.*, 2005; Blanchet *et al.*, 2008; Tasca *et al.*, 2013; Machulka *et al.*, 2014), the EPR-paradox measurements (Edgar *et al.*, 2012; Moreau *et al.*, 2012, 2014) or quantum imaging experiments (Lugiato *et al.*, 2002; Kolobov, 2007; Gatti *et al.*, 2008; Fickler *et al.*, 2013; Lemos *et al.*, 2014).

Moreover, the presented results, especially from Chapter 3, are relevant to a broader class of photon number resolving (PNR) detectors. Such detectors have many implementations, including superconducting transition-edge sensors (Brida *et al.*, 2012), as fiber loop detectors (Banaszek and Walmsley, 2003; Rehacek *et al.*, 2003), multipixel photon counters (MPPC) (Afek *et al.*, 2009) and also the discussed single photon sensitive cameras (Haderka *et al.*, 2005; Blanchet *et al.*, 2008).

The methods derived in Chapter 3 and 4 are conform with contemporary efforts to develop adequate criteria of nonclassicality based on empirical counts statistics (Sperling *et al.*, 2012a; Kiesel and Vogel, 2012; Sperling *et al.*, 2013).

In Chapter 4 we use the concept of quantum detector tomography process (Lundeen *et al.*, 2008; Feito *et al.*, 2009). Our results employed for reconstructing statistics can practically increase the illumination levels for experiments with cameras, like in (Haderka *et al.*, 2005; Blanchet *et al.*, 2008; Machulka *et al.*, 2014).

**Contribution**[1]

All of the results presented in this part were obtained with the major contribution of R.C. In particular in Chapter 2 R.C. performed final assembly of the camera and its basic characterization, in Chapter 3 R.C. derived all formulas and conceived the schemes for photons statistics reconstruction, in Chapter 4, R.C. performed all measurements, wrote the software and analyzed the data, implemented numerical algorithms and obtained all of the presented results.

The electronics and hardware design of the camera were prepared by J.I. and W.W. The drivers were written by W.W. Significant improvements of the tomography scheme were conceived by K.B. R.D.-D. introduced the principles of convex optimization to R.C.. Chapter 2 was supervised by W.W. and Chapter 4 was supervised by K.B. and W.W.

[1] All of the people who contributed to the results are listed in the Acknowledgments and here their names appear abbreviated as initials.

CHAPTER 2

# SETUP AND BASIC PROPERTIES OF AN INTENSIFIED SCIENTIFIC CMOS (I-SCMOS) CAMERA

In this Chapter we describe the basic properties of an intensified scientific complementary metal-oxide semiconductor (sCMOS) camera. The camera system has been constructed by our group and is used in the majority of the experiments described in the entire thesis.

In Sec. 2.1 we start from discussing the principle of operation of the hardware. In particular in Sec. 2.2 we describe the operation of the image intensifier and in Sec. 2.3 we present the assembly of the whole camera system.

Then in Sec. 2.4 we discuss typical recorded signals from individual single photons. In Secs. 2.5-2.6 we present typical initial processing of data collected by the camera. Finally in Sec. 2.7 we address the issue of saturation effects which can essentially influence a photon count statistics.

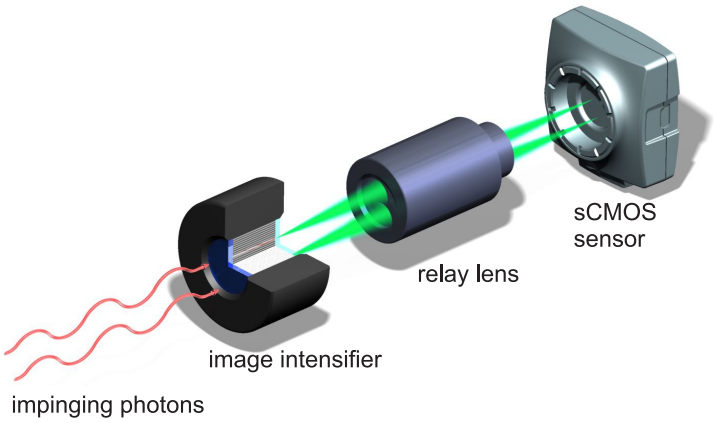


Figure 2.1: General scheme of the assembly of an intensified sCMOS camera. Photons impinging on the image intensifier induce electrons that are multiplied inside and reconverted into light on a phosphor screen. The phosphor is imaged on the sCMOS camera sensor via a bright relay lens. The camera system has the ability to detect individual single photon events.

## 2.1 Camera with an image intensifier

An image intensifier is a device that indirectly amplifies light, preserving its spatial structure. In the first step light is converted into charge that is multiplied and hits a phosphor screen forming a brighter image. The phosphor screen can be optically coupled to digital cameras. There are two ways of optical coupling: the image on the phosphor screen can be directly transferred onto the camera sensor using an image preserving fiber optic plate or it can be relayed via a lens.

Cameras with image intensifiers are utilized under weak illumination. They can operate in two modes. Most commonly they are used under illumination of at least thousands of photons when an amplified signal can form an image at each frame. In the other mode, with high gain of the image intensifier, the camera has the ability to detect single photons. Then single photons produce signal that is visible on the camera sensor. Here we investigate the latter mode.

Customarily image intensifiers are combined with charge couple device (CCD) cameras and the combination is known as intensified CCD (ICCD) cameras. Recently a new type of camera sensor has appeared on the market: a scientific complementary metal-oxide semiconductor (sCMOS). It outperforms its CCD counterparts in two important properties: the noise level and the framerate. sCMOS sensors have very low readout noise at a high frame readout rate of 100 frames per second, $5.5{\cdot}10^6$ pixels each. In 2012 we decided to combine a newly available sCMOS camera with an image intensifier, creating an intensified sCMOS (I-sCMOS) camera that at that time was commercially unavailable. A simplified scheme of the key parts of the setup is depicted in Fig. 2.1.

The low noise of the sCMOS camera enables us to register relatively weak single photon signals i.e. phosphor flashes and to distinguish them from the background. A high frame rate is also essential for quantum optics application where we typically operate with low photon numbers per frame and we have to collect large statistics. In practice the frame rate can be significantly increased by reducing the number of camera rows to be readout. We can achieve frame rates up to several thousands of frames per second (fps).

## 2.2 Construction of an image intensifier and microchannel plate (MCP)

The image intensifier is the key part of the system that converts single photons into detectable signal. Its schematic construction is depicted in Fig. 2.2. We have used third generation image intensifiers manufactured by Hamamatsu, models: V7090D-71-G262 and V7090D-71-G232, and we use their full specification (Hamamatsu, 2009).

The image intensifier comprises three main parts: a photocathode, a microchannel plate (MCP) and a phosphor screen. Photons coming through the input window are converted into electrons on the photocathode. One photon induces one photoelectron with a probability described by the quantum efficiency (QE) coefficient. Our photocathode with a diameter of 18 mm is made of gallium arsenide (GaAs) which has the highest efficiency, QE=20% for photons of the wavelength of 800 nm where we operated.

An important parameter characterizing a photocathode is the dark count rate, i.e. the rate of accidental, thermally induced electrons. Customarily it is expressed by manufacturers in equivalent background illumination. We measured that number at room temperature to be ca. 9 dark counts per 100 ns for the entire image intensifier.

Single photo electrons are attracted to the MCP by a gate voltage $V_{in} = -200$ V applied in short pulses. Normally the voltage between the photocathode and MCP equals +50 V and turns off the image intensifier. Electrons reach the proximate MCP that consists of ca. 9 millions of channels

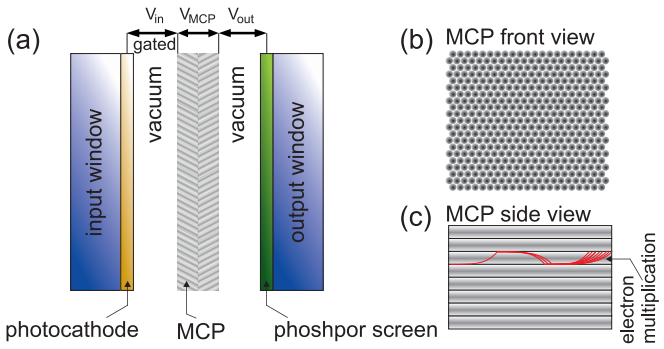


Figure 2.2: (a) Schematic of an image intensifier. Photons entering through the input window impinge on the photocathode where the photoelectric effect occurs. Induced electrons are accelerated by the gated voltage $V_{\text{in}}$ to the microchannel plate (MCP) where they are multiplied under the voltage $V_{\text{MCP}}$. Multiplied electrons are accelerated by the output voltage $V_{\text{out}}$ and they eventually hit the phosphor screen that emits flashes outgoing through the output window. (b) MCP seen frontally consists of ca. 9 millions of tubes, each acting as an electron multiplier. (c) An electron entering a single tube hits its walls many times producing large avalanche of charge.

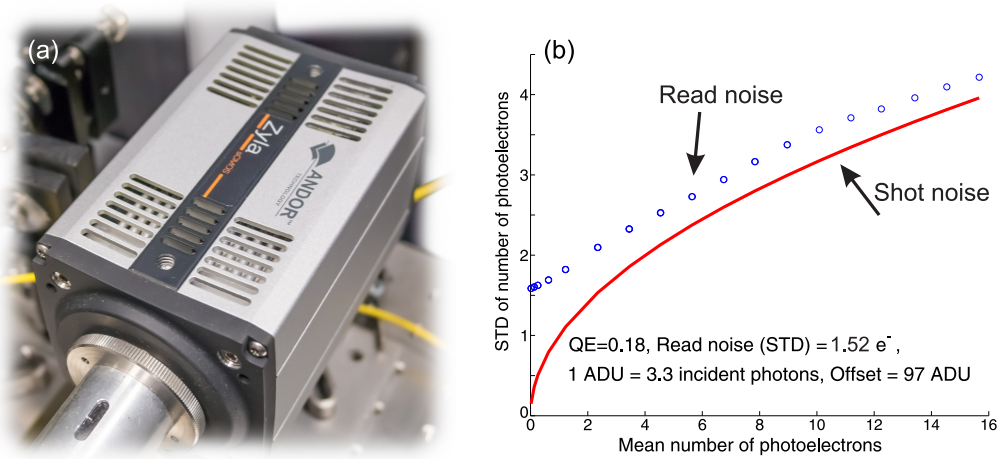


Figure 2.3: (a) Photograph of the Andor Zyla sCMOS camera used as a sensor in the image intensification scheme. (b) Measured noise properties of the sCMOS sensor indicate very small read noise that enables us to distinguish single photon event flashes generated in two-stage MCP plate. The standard deviation of the number of photoelectrons is plotted against the mean number of photoelectrons and slightly exceeds the light shot noise. Data have been collected through illuminating the camera by laser pulses of a known energy corresponding to the mean number of photons. Additionally, the calibration of the camera yielded a quantum efficiency, a conversion factor and its offset in analog-to-digital units (ADU) for a single pixel.

each acting as independent multiplier. MCP is under high voltage $V_{\text{MCP}}$ that accelerate electrons in small, separated channels each of ca. 6 $\mu$m in diameter. The channels are tilted by several degrees from the axis, thus the electrons hit the channel walls and produce a growing charge avalanche. As marked in Fig. 2.2(a), the channels are additionally twisted in the middle to prevent electrons from passing directly through them. Avalanches of charge starting typically from one photoelectron per channel vary in magnitude. Typically for a two-stage MCP such as described, the gain, i.e. the mean multiplication factor, is about $10^5$. We can vary the effective gain by changing the MCP voltage $V_{\text{MCP}}$ within the range of 250 V – 1750 V.

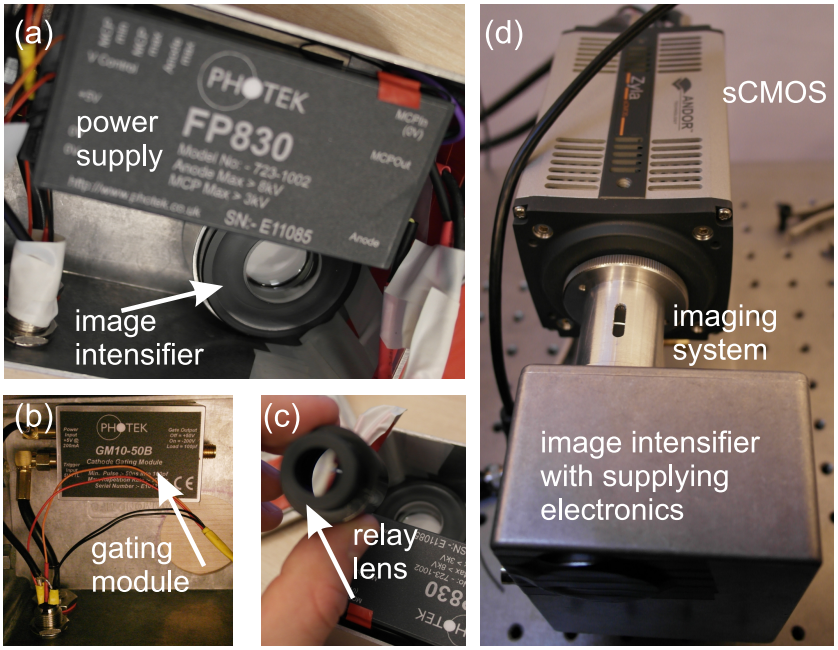


Figure 2.4: Photographs of subsequent construction steps of the intensified sCMOS camera. (a) Image intensifier requires high voltage power supply and (b) additional gate module that switches the input voltage between the phtocatchode and the MCP. (c) Image intensifier is optically coupled by a relay lens of an aperture $f/1.1$ . (d) The whole assembly allows fine focus adjustment and convenient electronic connections to a computer via camera link cables (in the back) and digital trigger signal (not shown).

Electrons leaving MCP are accelerated by a high voltage $V_{\text{out}} = 6000$ V and hit the phosphor screen producing bright flashes. A typical phosphor flash has a diameter of 66 $\mu$m and highly random brightness determined by the stochastic avalanche process. We used two types of phosphor differing mostly in their decay time. The intensity of the type P43 decays to 10% of the peak value within 1 ms, whereas for the type P46 the decay is much faster, down to 200 ns.

The image intensifier is powered by an external gating module manufactured by Photek, GM10-50B for phosphor P43 and GM300-3 for phosphor P46, enabling gating down to 50 ns and 5 ns, respectively. High voltage is delivered by a separate module produced by Photek, model FP830. The MCP voltage was adjusted by a low voltage controller, set between 0 and 5 V, and we shall refer to these settings later.

## 2.3 Assembly of I-sCMOS camera

Phosphor flashes emitting green light in the wide angle are imaged by a relay lens manufactured by Stanford Computer Optics of an f-number $f/\# = 1.1$. The imaging length of the lens was 105 mm and the magnification equaled $-0.44$, resulting in an image size of the phosphor screen of 8 mm in diameter.

The last element of the system is an sCMOS camera manufactured by Andor, model Zyla 5.5 Megapixel, portrayed in Fig. 2.3(a) and with a detailed specification (Andor, 2012). The size of a single pixel is 6.5 $\mu$m $\times$ 6.5 $\mu$m and thus the image of the phosphor corresponds to a circle of 1230 pixels in diameter, hence we effectively used about $1.2 \cdot 10^6$ pixels altogether.

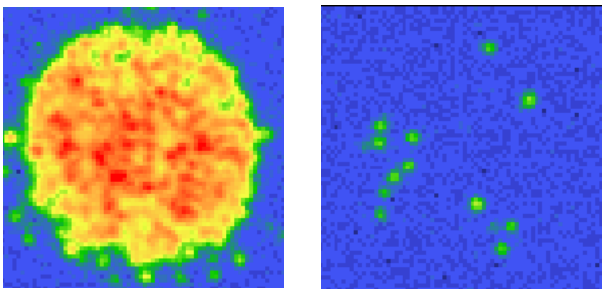


Figure 2.5: Single shots for (a) high and (b) low illumination levels. (a) High-noise image of a circular aperture tailoring the illuminating light formed by merged phosphor spots. (b) Attenuated light brings detection of single spots related to single photoelectron emission events that can be easily identified, distinguished and counted.

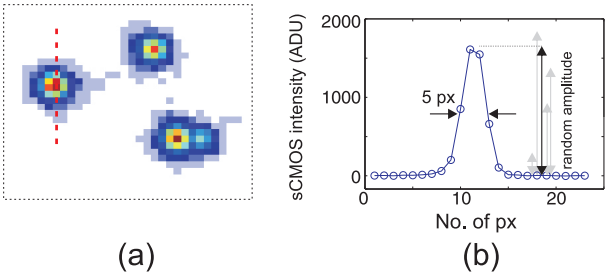


Figure 2.6: (a) Exemplary cropped image from a single frame of the camera. The registered spots correspond to the detection of single photon events. Red dashed line marks (b) a cross section of a single photon spot that typically has a diameter of 4-5 px and it is easily distinguishable from a vaguely fluctuating background.

We operated the camera in the fastest rolling shutter mode enabling the readout of the full frame at a speed of 100 frames per second. The readout time is roughly proportional to the number of rows read. For instance, while reading out 22 rows we achieve a frame rate of 7000 fps. Details of the camera time synchronization and its different mode operation can be found in the camera manual (Andor, 2012). We examined the noise characteristics of the sCMOS sensor and confirmed its excellent low-noise properties as we summarize in Fig. 2.3(b). The signal on a single pixel was digitized to 2048 analog-to-digital units (ADU). The average pixel offset was at the level of 100 ADU and slightly varied across the sensor, though by no more than 5 ADU. Moreover, the standard deviation of the signal under no illumination was at the level of 2.5 ADU that corresponded to 1.5 electrons.

The assembly of the full system is presented in Fig. 2.4 where we illustrate the described parts being mounted together. Fig. 2.4(d) presents the mounted setup with the image intensifier and its drivers case, a tube guiding the relay lens that is coupled to the sCMOS camera.

## 2.4 Photodetection properties of the I-sCMOS studied on raw images

In Fig. 2.5 we present typical images recorded with the I-sCMOS camera lit by an attenuated laser beam passing through a circular aperture whose surface was imaged on the photocathode. Fig. 2.5(a) shows the image at a high illumination level of a few thousands of photons. When only a few dozens of photons reach the camera in the weakened laser pulse, we register an image consisting of single

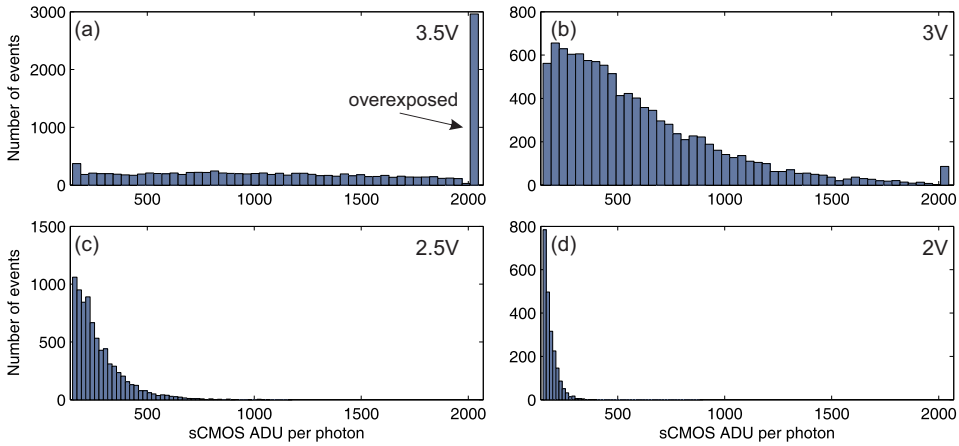


Figure 2.7: Amplitudes of phosphor flashes vary from shot to shot as the MCP multiplication process is highly stochastic. Histograms of the corresponding amplitudes of single photon spots are plotted against the ADU pixel counts register. The electron multiplication factor in MCP is changed by the $V_{\mathrm{MCP}}$ high voltage set and modified by an analog controller. (a-d) Subsequent histograms from high to low gain for four selected controller voltages (upper-right corner). (a) High gain saturates and overexposes the sCMOS sensor whereas (d) low gains give signals close to the offset and the background noise.

spots, as presented in Fig. 2.5(b). Each spot corresponds to an individual act of photoelectron emission at the photocathode. Individual spots can be counted providing a sound basis for estimating the number of incident photons.

In Fig. 2.6(a) we study a typical zoomed image showing clearly the spatial structure of individual single photon flashes. They are registered on the sCMOS sensor as Gaussian-like spots of a 5-pixel full width at half maximum – their exemplary cross-section is depicted in Fig. 2.6(b). The amplitude of single photon spots is highly random due to the avalanche process in MCP. The average intensity of the brightest pixel is significantly higher than the camera noise level thus they are easily recognizable. Virtually each photon that induced a photoelectron is always registered.

The distribution of single photon flash amplitudes depends on the gain of the MCP. We measured the distributions for several settings of the analog MCP gain controller. Fig. 2.7 presents the results for four settings. For controlling voltages exceeding 3V a significant fraction of single photon events have amplitudes overexposing the sCMOS sensor. For controlling voltages below 2.5 V one can see that the distribution of amplitudes is close to exponential. It means that flashes with a small amplitude are the most probable. To balance the effective number of single photon events above the noise level and below overexposure amplitudes we set the controlling voltage to 2.75 V in most of experiments.

As we see from Fig. 2.7 the distributions of flash amplitudes are very widespread. They change very subtly for avalanches triggered by a several photons (Basden *et al.*, 2003; Harpsoe *et al.*, 2012). Therefore, the individual flash amplitude virtually does not provide any useful information and has to be kept simply within the detectable range of the sCMOS sensor.

## 2.5 Real-time localization of photons

Although single photon flashes have a finite width, their central position can be found quite accurately. Fig. 2.8 depicts a situation where single photon spots are clearly separated from each other. Spots are identified and localized in real time by a software routine written in C language, com-

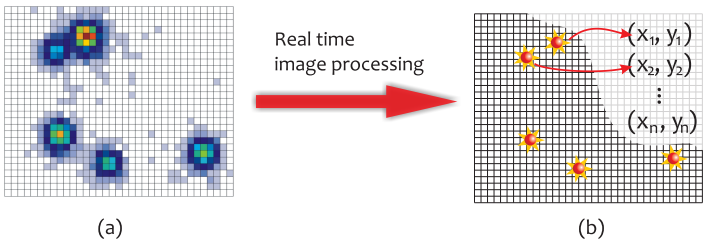


Figure 2.8: Cropped image of five photon events on the pixel mesh of sCMOS sensor. We associate a photon event after exceeding a certain adjustable threshold and then we fit to the local maxima Gaussian functions. Their centers are found with a subpixel resolution in the real-time software algorithm analyzing grabbed frames. Eventually we store and process only the photons coordinates that are used in the postprocessing, for example to count photons in a selected region.

piled to the DLL library. The routine returns the central position of the spots from a raw image with subpixel accuracy.

The software finds the local maxima that exceed a set threshold. In most of our experiments we set the threshold for single photon events to be 130 ADU. The local maximum has to have the highest intensity within two or three pixels' radius depending on the setting. The precise location of the spot is found by fitting a twodimensional paraboloid to the logarithm of the pixel intensity within the same two or three pixels' radius. A fast and efficient fitting is performed by evaluating a numerical integral on the neighboring pixel intensities. The routine also returns Gaussians amplitudes that can be useful, for instance, to study intensity distributions, such as presented in Fig. 2.7.

Running the real-time software algorithm has several advantages and significantly simplifies the experiment. First of all, it reduces the amount of stored data enormously. Instead of storing large raster frames we store only double precision numbers describing the positions of the photons and flash amplitudes. Naturally, it also simplifies and expedites data analysis. We prepared a set of Matlab packages and classes capable of efficient processing of preprocessed data taken by camera. Below we give the simplest examples of photo counting applications. In Chapter 4 we demonstrate advanced calibration of the camera treated as a photon-number resolving detector.

## 2.6 Basic photocounting properties of the I-sCMOS

Experimental characterization of the light described further in the thesis refers both to its spatial and statistical properties. The full information extracted from the frames – the photon event locations – usually has to be reformulated into useful quantities, such as photon numbers or photon number distribution. Below we give simplest examples of such characterization.

Fig. 2.9 presents an exemplary single frame grabbed by the camera and its possible postprocessing. Such a frame is preprocessed and yields the positions of the spots which are easily handled in the analysis. For instance, one can divide a sensor into finite size squares – macropixels – and count the photons inside them. The division is performed at the data analysis stage and can be readily modified in order to better adjust the processed data. The photon counting inside individual macropixels is performed by the software simply by assigning subsequent photons to the corresponding regions. As a result we obtain the spatial distribution of the photon number. By collecting many frames we are able to evaluate the desired statistical properties of light afterwards.

A direct counting of photons is a simple way to determine the quantum efficiency (QE) of a camera system. If individual single photon spots are well spaced, as in Fig. 2.9, then the number of

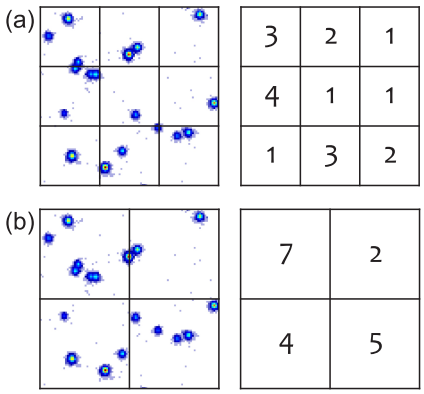


Figure 2.9: The camera sensor can be divided in the post processing stage into macropixels of different sizes. Within each macropixel photoevents can be counted.

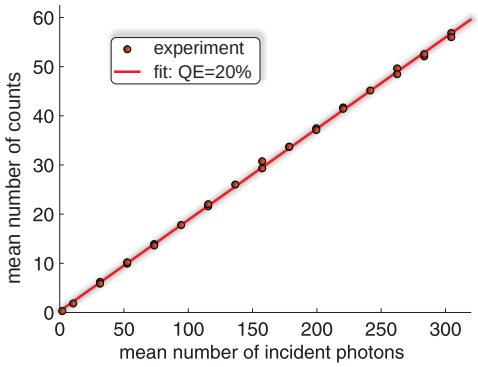


Figure 2.10: Mean number of single photon spots – counts plotted versus mean number of incident photons for a calibrated coherent state illumination. The linear coefficient equals the quantum efficiency of the whole camera system, i.e. 20%.

spots virtually equals the number of the photoelectrons induced. Through illuminating the camera by laser pulses of a known energy corresponding to a known mean number of photon per pulse we can find the QE directly. Fig. 2.10 summarizes such a measurement where we illuminated a large area of the image intensifier with a calibrated light. From a linear fit we found QE=20%, as specified for the GaAs photocathode for a wavelength of photons of 800 nm.

This measurement was carried out as follows. We set the gate duration and the power of the incident laser which went through a series of calibrated filters. The signal was shaped in short rectangular pulses. From the filter calibration and pulse duration we drew the mean number of incident photons. We altered the duration of the light pulse to obtain different mean number of incident photons. Frame by frame we collected counts and we calculated their statistics.

Moreover, we have tested the noise statistics of the registered number of counts. They are practically Poissonian at the shot noise level, as in Fig. 2.11. This gives rise to hope that we should also be able to see the correlations of counts below shot noise level with the use of a nonclassical source of light.

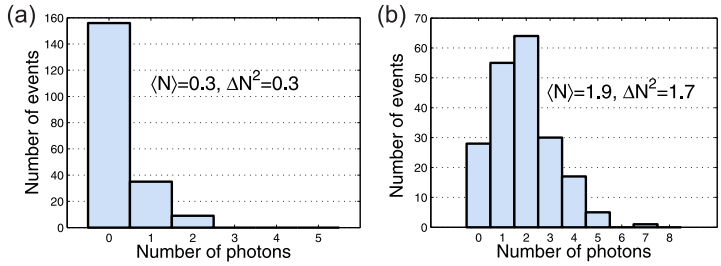


Figure 2.11: Histograms of the number of counts for two exemplary number of mean incident photon number are close to the Poissonian distribution. The variance of counts is close to the mean number of counts.

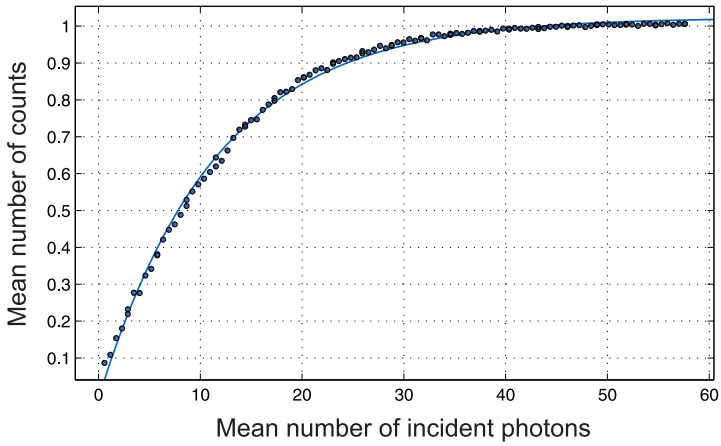


Figure 2.12: Mean number of observed photons vs. average number of incident photons $|\alpha|^2$ detected on a single bin area agrees well with the single APD photon counting model.

## 2.7 Simple saturation effects

So far we have considered photon counting under the assumption that individual single spots should originate from single photons and be far enough to be distinguished. This, however, is merely a simplified picture. In order to study statistical nonclassical properties of light one cannot neglect the probability the two photons were registered as a single photon event. Thorough analysis and interpretation of counts statistics is nontrivial and thence, in the next two Chapters we study this problem theoretically and experimentally.

In this Chapter we shall illustrate the problem on a simple example where we focused a laser beam tightly on the surface of the camera. The size of the focal spot encompassed several neighboring MCP channels and in consequence a coherent laser pulse was predominantly registered as a single spot. We counted the mean number of spots around the focal spot and present their mean against the mean number of incident photons in Fig. 2.12. We clearly see that the mean number of counts approaches unity. The presented example is identical with that for a single Geiger-type on-off detector.

## 2.8 Conclusions

The presented I-sCMOS camera setup offers high-resolution, high-speed ability to count photons. An important feature of the image intensifier is its low dark-count rate. Thus, for short gate times

and cropped frames we can virtually neglect the influence of the dark counts. The presented technology is a direct extension of intensified CCD (ICCD) cameras, yet it outperforms them in speed and low sensor noise. The latter feature easily enables the operation in the photon counting mode with a two-stage MCP.

At low illumination levels, the camera system can easily distinguish single phosphor flashes from the background. We extract their positions from each frame in real-time software routine and subsequently associate them with single photoelectron emissions. Here we have demonstrated that if photon events are well distanced, then the number of counts is close to that of photoelectrons. None of the less, saturation effects arise quickly along with the illumination intensity.

In the next two Chapters we shall study advanced photon counting properties of the system.

CHAPTER 3

# THEORETICAL PHOTON COUNTING PROPERTIES OF A CAMERA

In this Chapter we discuss the theory of photon counting properties of a camera. We focus on saturation effects that distort the registered statistics of counts. At first in Sec. 3.1 we introduce the notation and describe the general photon counting process divided into constituent effects.

Starting from Sec. 3.3 we introduce a simplified model of a camera treated as a matrix of on-off detectors. We evaluate measures of nonclassicality directly on counts statistics to highlight detrimental effects of saturation. In Secs. 3.5-3.6 we present analytical results for coherent and multimode thermal states. In Sec. 3.7 we show the numerical results for the two-mode squeezed state.

Thereafter, in Secs. 3.8-3.9, we present an alternative empirical way to characterize detection properties of a camera. We describe the theoretical background of a camera calibration in a general framework of quantum detector tomography (QDT). In Sec. 3.10 we show algorithms for reconstruction of statistics of the registered light using the results of QDT calibration.

The results described in this Chapter are supported by Appendices A-B. The experimental demonstration for QDT of the I-sCMOS camera is studied separately in Chapter 4.

## 3.1 Subsequent effects in photon-counting

Below, we briefly discuss the general photon counting properties and take the opportunity to introduce a notation used in the current Chapter and in the subsequent one. In Fig. 3.1 we summarize

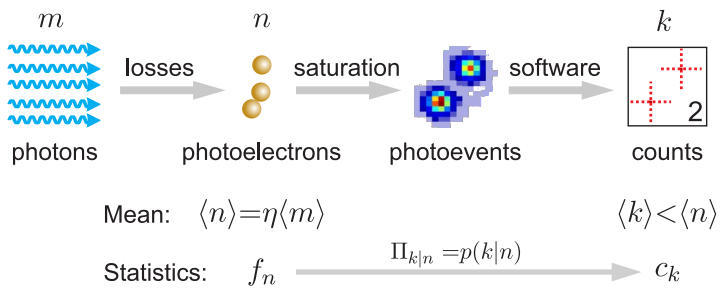


Figure 3.1: Subsequent steps and effects in the photon-counting process along with the nomenclature used.

the whole photon counting process and the idea of achieving both photon counting and spatial resolution.

As illustrated in Fig. 3.1, several processes occur starting from camera illumination to actual interpretation of the detection results. If $m$ photons illuminate a camera, only part of them induce $n$ photoelectrons. The mean number of photoelectrons $\langle n \rangle$ is proportional to the mean number of photons $\langle n \rangle = \eta \langle m \rangle$, and the ratio between those two quantities is described by a quantum efficiency $\eta$. Photoelectron emission eventually leads to bright spots on the camera sensor, called photoevents. An individual photoevent may be triggered by more then one photoelectron. Finally a software routine localizes and counts the photoevents. In the end we obtain $k$ counts out of $n$ photoelectrons and $m$ photons.

The first process of losses converting photons into photoelectrons is well known, thus we shall briefly remind its properties in Sec. 3.4. Yet, we shall focus on the process of saturation. It may additionally decrease the number of counts $k$ , as compared to the number of photoelectrons $n \geq k$. The saturation of an intensified camera originates from two effects. Firstly, more then one photoelectron may go into a single channel of a microchannel plate. Secondly, photoelectrons that went into proximate channels may create a merged spot. With no ability to resolve these two or more spots they will all be associated with one photoevent and treated as a single count.

The direct effects of saturation are manifold. In a single shot chances that $n$ photoelectrons will yield $k$ counts are described by the conditional probability $p(k|n)$. On average the mean number of counts is always inferior to the mean number of photons $\langle k \rangle < \langle n \rangle$. In the end the statistics of counts $c_k$ and photoelectrons $f_n$ are generally different.

## 3.2 Photon counts statistics measured on camera tiles

In Fig. 3.2 we introduce an exemplary division of a camera detection area into tiles or macropixels. Such a division combines spatial resolution with the photon number resolution. From now on we shall discuss the photon counting properties of individual tiles. These properties are described by conditional probability distribution for all possible combinations of counts and photon numbers. We gather the probabilities in a matrix form for the $i$-th tile $\Pi^{(i)}$. The matrix elements simply denote specific conditional probabilities:

$$\Pi^{(i)}_{k|n} \equiv p(k|n), \tag{3.1}$$

where we use a suggestive notation for matrix indices $k|n$ underlying their meaning. The photoevent statistics on a single, $i$-th tile $c^{(i)}_k$ depends on the photon number distribution $f^{(i)}_n$ through the conditional probability distribution $\Pi^{(i)}_{k|n}$:

$$c^{(i)}_k = \sum_n \Pi^{(i)}_{k|n} f^{(i)}_n. \tag{3.2}$$

Pairs of tiles can be used to measure joint statistics of counts that can be useful, e.g. for measuring the correlation between photon numbers. The formula Eq. (3.2) can be generalized to pairs of tiles labeled $(i_1, i_2)$, as depicted in Fig. 3.2, and it takes the form:

$$c^{(i_1,i_2)}_{k_1,k_2} = \sum_{n_1,n_2} \Pi^{(i_1)}_{k_1|n_1} \Pi^{(i_2)}_{k_2|n_2} f^{(i_1,i_2)}_{n_1,n_2}. \tag{3.3}$$

where $c^{(i_1,i_2)}_{k_1,k_2}$ and $f^{(i_1,i_2)}_{n_1,n_2}$ denote, respectively, the joint photo-event statistics and the joint photon number distribution.

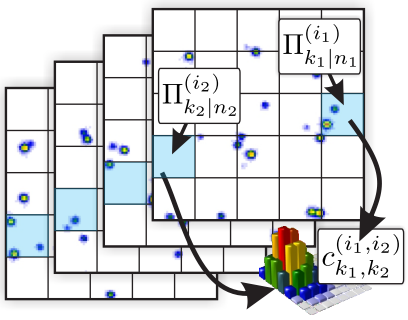


Figure 3.2: Idea of the measurements with both spatial and photon number resolution. Camera detection area is divided into an array of tiles enabling measurements of one- or two-dimensional joint counts statistics. The essence of the photon-counting properties of consecutive tiles is mathematically described by distributions of conditional probabilities $\Pi_{k|n}$.

As we have seen, the crux of the operation of a tile is encoded in the distributions of conditional probability $\Pi$. They characterize fully the tiles operation and determine the counts statistics. As we show later in this Chapter, they can be used to invert formulas Eqs. (3.2-3.3) to find original photon statistics. Nonetheless, the conditional probabilities have first to be determined and this is the subject of our further consideration.

## 3.3 Camera modeled as a matrix of on-off detectors

To gain insight into the influence of saturation effects on counts statistics we need to find the conditional probabilities $\Pi$ for a camera tile. Starting from this section until Sec. 3.7 we shall consider a simplified model of the camera operation.

An intensified camera may be represented as a regular array of pixels, as presented in Fig. 3.3. They should be counterparts of single photon detection areas sharing common features, such as a finite size or limited ability to resolve just between zero and at-least-one photons. Due to the latter feature they are called “on-off detectors” as each simply returns 0 or 1. Apparently, beside the aforementioned similarities, the real response of an intensified camera yields photoevents that are nearly continuously distributed .

An array of detectors naturally has a certain spatial resolution. Single detectors may be treated as pixels and can be naturally grouped into macropixels, cf. Fig. 2.9 with Fig. 3.3. An intensified camera detects single photons as bright spots of a certain size on the sensor. A frame can effectively capture a finite number of photoevents proportionally to its size.

Single tiles are similar to popular multiplexed on-off detectors based on the photon chopping concept (Paul *et al.*, 1996). The operation of a uniformly illuminated tile consisting of a finite number of $N$ on-off detectors (Fig. 3.4(b)) is equivalent to a system of beam splitters that split and redirect light onto $N$ on-off detectors, as presented in Fig. 3.4(b). The multiplexed on-off detectors have been implemented in various forms, including fiber loop detectors (Banaszek and Walmsley, 2003; Rehacek *et al.*, 2003; Achilles *et al.*, 2004) and multi-pixel photon counters (Afek *et al.*, 2009).

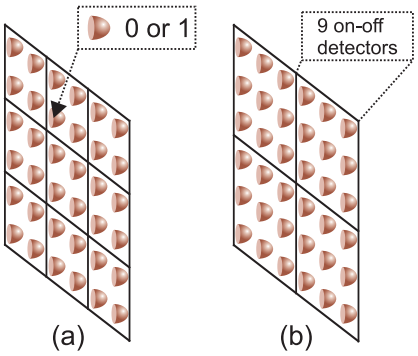


Figure 3.3: An intensified camera can be simply modeled as an array of on-off detectors. The presented setting can have certain spatial and photon number resolution upon division on marcopixels, similarly to Fig. 2.9.

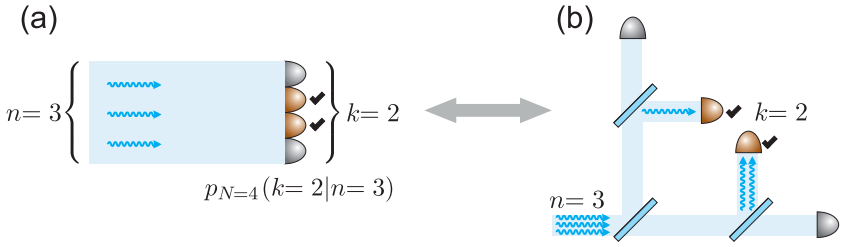


Figure 3.4: (a) $N$ juxtaposed uniformly illuminated on-off detectors are equivalent to (b) $N$ detectors after the set of beam splitters. The scheme has a photon number resolution although saturation effects quickly arise with the impinging photon number. As a consequence the number of counts $k < n$ approximates only the number of photons.

## 3.4 Photon number resolution through "photon chopping"

The simple model of a multiplexed detector of a perfect quantum efficiency can be described analytically. In particular we can give the conditional probability of obtaining $k$ counts, provided that the detector was illuminated by $n$ photons, as derived by Paul *et al.* (1996):

$$p_N(k|n) = \frac{1}{N^n}\binom{N}{k} k! S(n,k), \tag{3.4}$$

where $S(n,k) = 1/k!\sum_{i=0}^{k}(-1)^i\binom{k}{i}(k-i)^n$ is the Stirling number of the second kind (Weisstein, 2015). We can verify that Eq. (3.4) agrees with some of the simplest examples. For instance, we have $p_N(0|n) = 0$ for all $n \geq 1$, which means all of the photons cannot be lost due to saturation. Another example describes chances for exactly one registered count: $p(1|n) = 1/N^{n-1}$.

For few-photon states of light it is enough to study the conditional probabilities $p_N(k|n)$ for a finite number of the impinging photons $n$. We presented the values of probabilities for $N = 2$ in Fig. 3.5 (a) and $N = 4$ in Fig. 3.5 (b). As we see, the detector is saturated for large $n \gg N$ and virtually always returns $N$ counts.

Now we can return to discussing the effects of a finite quantum efficiency $\eta$ of the detector in the model Eq. (3.4). The photon losses are described by the standard binomial distribution

$$p_\eta(m|n) = \binom{n}{m}\eta^m(1-\eta)^{n-m} \tag{3.5}$$

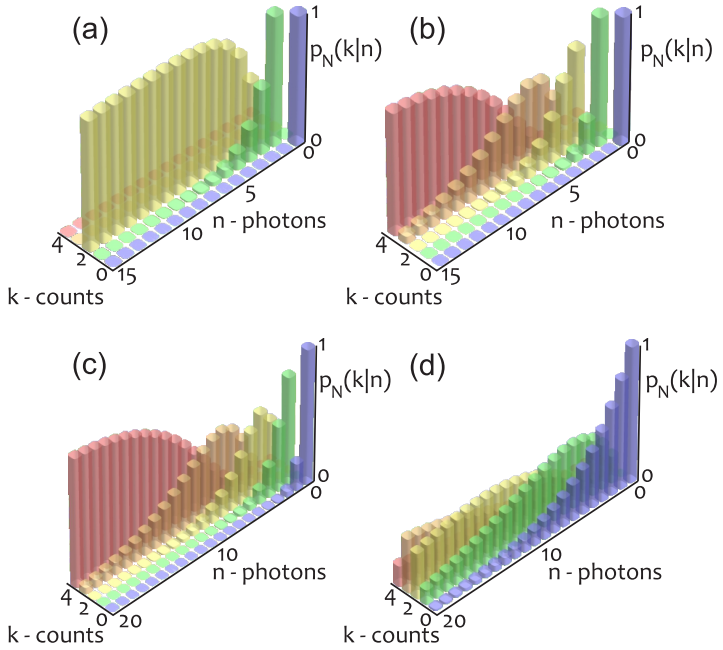


Figure 3.5: Distributions of conditional probabilities $p_N(k|n)$ for $k$ counts (count layer) under illumination of exactly $n$ photons (Fock layer). A detector consists of $N$ multiplexed on-off detectors, each with a quantum efficiency $\eta$. Probability values are presented for: (a) $N = 2$, $\eta = 1$ (b) (a) $N = 4$, $\eta = 1$ (c) $N = 4$, $\eta = 0.8$ (d) $N = 4$, $\eta = 0.2$ where the last one corresponds to the QE of the camera setup.

for $n$ impinging photons and $m$ induced photoelectrons. We can combine Eq. (3.4) and Eq. (3.5) to find the effective conditional probabilities including both losses and saturation:

$$p(k|n) = \sum_{m=0}^{\infty} p_N(k|m)\, p_\eta(m|n). \tag{3.6}$$

It can be performed analytically for specific $n$ and $k$, for instance $p_N(0|n) = (1-\eta)^n$ or

$$p_N(1|n) = N(1-\eta)^n \left( \left( \frac{\eta - \eta N + N}{N - \eta N} \right)^n - 1 \right). \tag{3.7}$$

We have presented the corresponding set of conditional probabilities for $N = 4$ in Fig. 3.5 (c-d).

Here we consider a model for an idealized detector that is subject to certain assumptions. The constituting on-off detectors are identical and they share the same quantum efficiency $\eta$. Moreover, the dark counts and the crosstalk between the component on-off detectors are excluded from our model, as it may also be done for intensified cameras.

## 3.5 Coherent state on a multiplexed detector

With the model of multiplexed on-off detectors we can study the measurable quantities for a specific class of states encountered in an experiment. Let us start with the coherent states of the Poissonian photon statistics $f_n^{\mathrm{coh}} = \langle n \rangle^n e^{-\langle n \rangle} / n!$. For the sake of simplicity any losses will be included in the photon statistics, as for the coherent state they simply scale down the mean number of photons. The PNR detector measures the history of the collected counts yielding the counts statistics $c_k$, which can be expressed as $c_k = \sum_{n=k}^{\infty} p_N(k|n) f_n^{\mathrm{coh}}$.

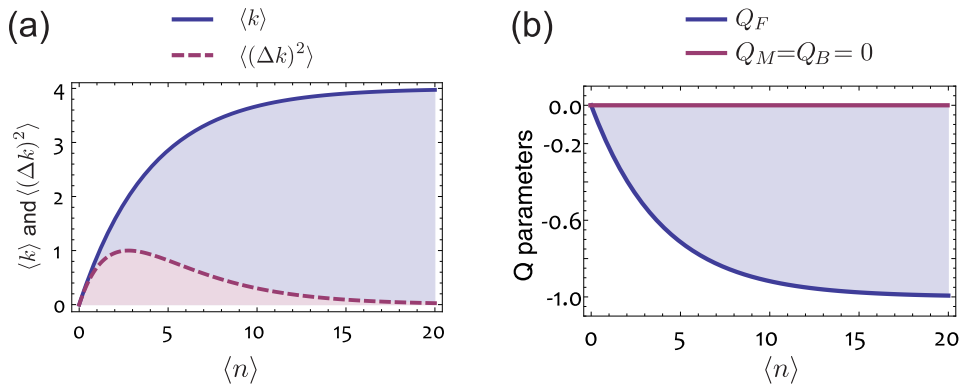


Figure 3.6: (a) Mean and variance of counts for a coherent state on a detector with $N = 4$. (b) Measured $Q_F$ parameter is artificially nonclassical contrary to $Q_B = Q_M = 0$.

Although the formula for the counts statistics cannot be simplified, as it is represented through a sum, we can evaluate the statistics moments using some mathematical properties of the Striling number of the second kind appearing in Eq. (3.4). The derivation of the moments using Eq. (3.4) is presented in Appendix A.

We can study the saturation effects by evaluating the mean $\langle k\rangle$ and the variance $\langle(\Delta k)^2\rangle$ of counts, which equal:

$$\langle k\rangle = N(1-e^{-\langle n\rangle/N}), \tag{3.8}$$

$$\langle(\Delta k)^2\rangle = N(1-e^{-\langle n\rangle/N})e^{-\langle n\rangle/N}. \tag{3.9}$$

The values of both quantities are presented against the mean number of incoming photons in Fig. 3.6 (a). We see that the mean value saturates at $\langle k\rangle = N$ and the variance simply drops down to zero.

This reduction of variance leads to the seemingly nonclassical properties of the measured light. In the introductory Chapter 1 we introduced one of the nonclassicality criteria as the negativity of the Mandel parameter $Q_M = \langle(\Delta n)^2\rangle/\langle n\rangle - 1$. The parameter can also be evaluated directly on counts statistics

$$Q_F = \langle(\Delta k)^2\rangle/\langle k\rangle - 1. \tag{3.10}$$

The combination of Eqs. (3.8-3.9) yields negative values of the parameter:

$$Q_F = e^{-\langle n\rangle/N} - 1 < 0, \tag{3.11}$$

as we additionally illustrate in Fig. 3.6 (b). In particular $Q_F$ is negative even for small values of the mean photon number $\langle n\rangle$ illuminating the detector. This simple example highlights the fact that the counts cannot be treated equivalently to the photon numbers and the evaluation of the nonclassical criteria may lead to a false interpretation.

Recently Sperling *et al.* (2012a) have proposed a modified criterion of nonclassicality is based on the subbinomial parameter defined as follows:

$$Q_B = N\frac{\langle(\Delta k)^2\rangle}{\langle k\rangle(N-\langle k\rangle)} - 1. \tag{3.12}$$

$Q_B$ is negative only for nonclassical states and for coherent states reconstructing the true value of $Q_M$ Mandel parameter, as depicted in Fig. 3.6 (b).

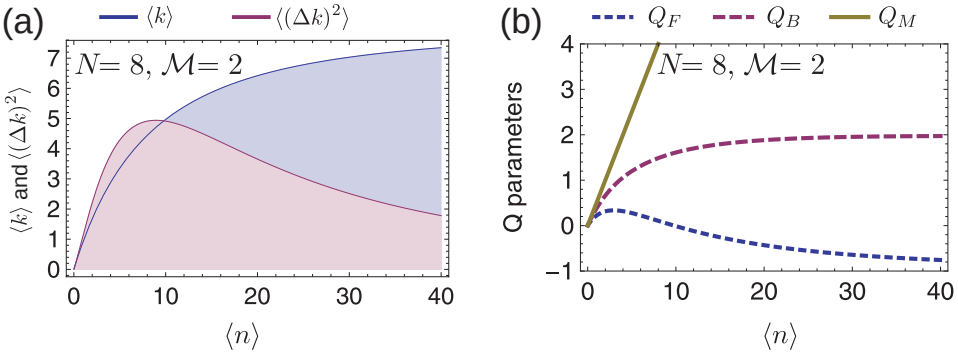


Figure 3.7: (a) Mean and variance of counts, (b) input $Q_M$, measured $Q_F$ and binomial $Q_B$ parameters versus mean number of photons in the two-mode ($\mathcal{M}=2$) thermal state on a detector with $N=8$.

## 3.6 Multimode thermal states of light on multiplexed detectors

Now we shall proceed to calculations for single and multimode thermal states of light. This example can illustrate the measurement of a single subsystem of multimode squeezed states of light. The light statistics for single- and multimode thermal states have been given before in Eq. (1.41) and Eq. (1.45) in Chapter 1. Similarly to the discussion of coherent states, our description here is limited to the results an their physical consequences whereas mathematical derivations are presented in Appendix A.

We provide an exemplary mean and variance for a single-mode thermal state:

$$\langle k\rangle_{\mathrm{Th},\mathcal{M}=1}=\frac{\langle n\rangle N}{\langle n\rangle+N}, \tag{3.13}$$

$$\langle(\Delta k)^2\rangle_{\mathrm{Th},\mathcal{M}=1}=\frac{\langle n\rangle N^2(\langle n\rangle N+\langle n\rangle+N)}{(\langle n\rangle+N)^2(2\langle n\rangle+N)}. \tag{3.14}$$

Analytical formulas for $\langle k\rangle_{\mathrm{Th},\mathcal{M}}$ and the variance $\langle(\Delta k)^2\rangle_{\mathrm{Th},\mathcal{M}}$ can be found for all $\mathcal{M}$-mode states and for each $N$ although they do not have any compact general representation. For further exemplification we shall simply give analytical expressions for $\langle k\rangle_{\mathrm{Th},\mathcal{M}}$ for two-mode $\mathcal{M}=2$ thermal state:

$$\langle k\rangle_{\mathrm{Th},\mathcal{M}=2}=\frac{\langle n\rangle N(\langle n\rangle+4N)}{(\langle n\rangle+2N)^2}. \tag{3.15}$$

Analytical formulas for variances and higher number of modes can be readily found using any symbolic computation software following the scheme presented in Appendix A. Means and variances for the two-mode state are presented in Fig. 3.7(a).

Just as for a coherent state let us evaluate the Mandel parameters for counts statistics and compare them in Fig. 3.7(b) with a theoretical value $Q_M=\langle n\rangle/\mathcal{M}$ and with the subbinomial parameter $Q_B$ defined in Eq. (3.12). We clearly see that the detector quickly becomes saturated with the illumination level and for mean photon numbers $\langle n\rangle>10$ the empirical $Q_F$ parameter becomes negative. Therefore, similarly to r coherent states, thermal states can be also falsely identified as nonclassical should the counts statistics be taken blindly. This problem is resolved by evaluating the subbinomial parameter $Q_B$ although its value is far from the actual Mandel parameter $Q_M$.

Finally let us study how saturation rises along with the number of on-off detectors $N$. In Fig. 3.8 we show the empirical $Q_F$ parameter for a single-mode and four-mode thermal state plotter to increase $N$. Depending on the mean number of input photons $\langle n\rangle$ and the number of detectors $N$,

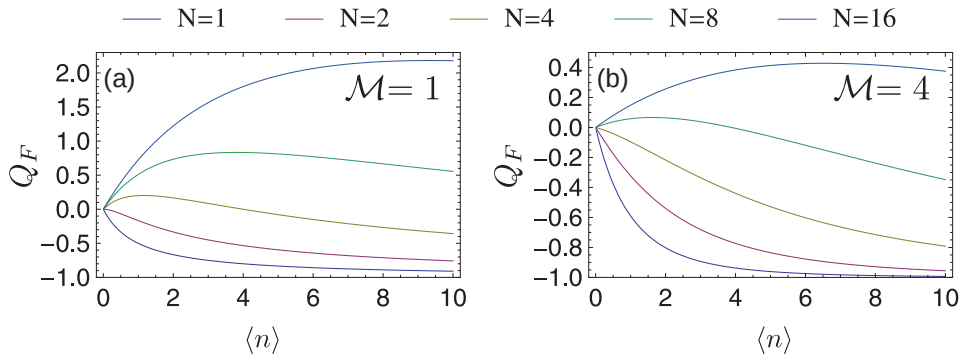


Figure 3.8: Theoretical values for empirical $Q_F$ parameters for (a) single-mode thermal state, (b) multimode thermal state $\mathcal{M} = 4$ plotted versus mean number of photons $\langle n \rangle$ for different $N$. Depending on the parameters of the state and the detector counts statistics may seem classical or artificially nonclassical.

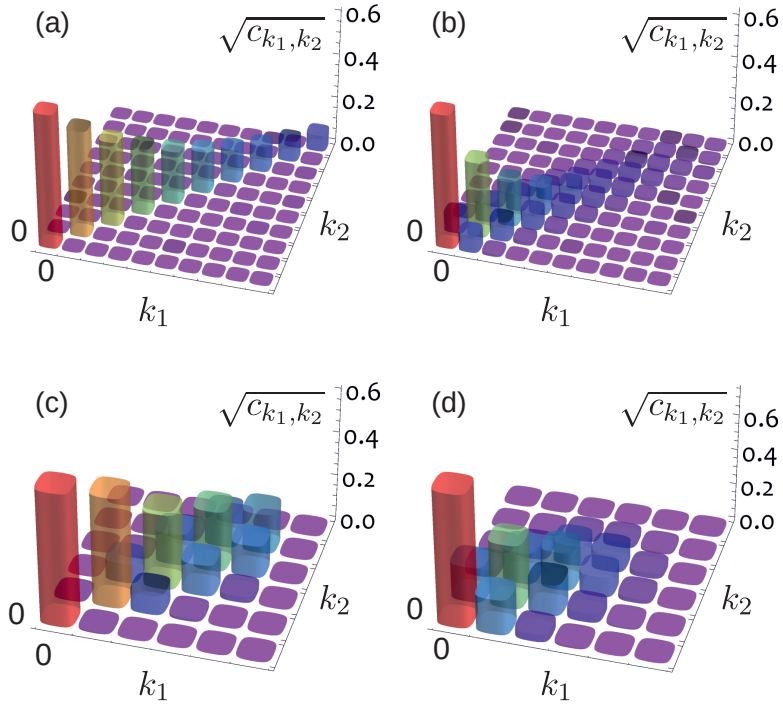


Figure 3.9: Joint statistics for a two-mode squeezed state with $\xi = 0.8$ measured by two multiplexed detectors. We plot the values of $\sqrt{c_{k_1,k_2}}$ for better visualization purposes. Statistics are presented for the following parameters values: (a) $N = \infty$, $\eta = 1$. (b) $N = \infty$, $\eta = 0.8$. (a) $N = 4$, $\eta = 1$. (a) $N = 4$, $\eta = 0.5$.

the measured $Q_F$ parameters can be artificially nonclassical. We also see that even for the relatively large number of detectors $N = 16$ the saturation effects become quickly noticeable even for $\langle n \rangle \simeq 1$.

## 3.7 Properties of counts statistics for squeezed states

Above we have considered measurements on a single multiplexed detector that can represent a single macropixel of a camera. Now we turn to studying possible correlation measurements with

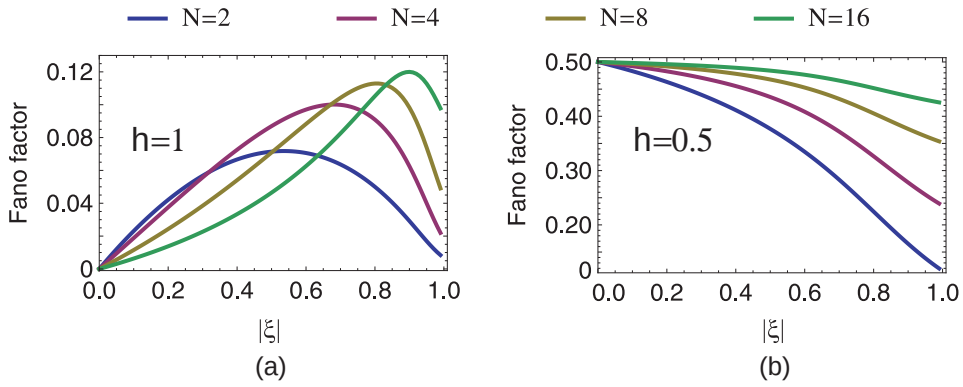


Figure 3.10: Fano factors versus squeezing parameter $\xi$ for different numbers of $N$ detectors with (a) $\eta = 1$ (b) $\eta = 0.5$. A lower number of detectors $N$ can artificially increase the correlation and consequently decrease the Fano factor.

two tiles ,such as in Fig. 3.1. We focus on the properties of joint counts statistics of the two-mode squeezed state of light $|\Psi_\zeta\rangle$ discussed in Chapter 1. In particular the joint photon statistics have been given in Eq. (1.33) for a parameter $\xi$, such as $|\xi| = \tanh(|\zeta|)$. We have also discussed nonclassical measures, such as the Fano factor, which for such a state equals $R = 0$, and the second-order cross-correlation function $g^{(2)} = 1 + 1/|\xi|^2 \geq 2$. In Fig. 3.9(a) we demonstrate exemplary photon statistics for $\xi = 0.8$.

Here we cannot skip the influence of losses on the squeezed state, as they critically affect the measures on nonclassicality. They can be incorporated into the photon statistics through Eq. (3.5). The statistics of an exemplary squeezed state after losses are presented in Fig. 3.9(b). We see that losses decrease the correlation between the number of photons.

Now we return to the discussion of the simple model with two multiplexed detectors. The joint counts statistics $c_{k_1,k_2}$ are related with photoelectron statistics $f_{n_1,n_2}$ through a standard formula:

$$c_{k_1,k_2} = \sum_{n_1=k_1}^{\infty} \sum_{n_2=k_2}^{\infty} p_N(k_1|n_1)\, p_N(k_2|n_2)\, f_{n_1,n_2}. \tag{3.16}$$

The effect of the inclusion of both losses and saturation on the counts statistics are presented in Fig. 3.9(c-d).

Let us quantify the properties of the counts statistics by evaluating the related measures directly on the counts statistics. The empirical Fano noise reduction factor has the form:

$$R = \frac{\langle (\Delta(k_1 - k_2))^2 \rangle}{\langle k_1 \rangle + \langle k_2 \rangle}. \tag{3.17}$$

It has been evaluated numerically for a finite number of detectors $N$ and the losses scaled by $\eta$ parameter. We present the Fano factors in Fig. 3.10 against the parameter $|\xi|$. Ideally, without losses, as in Fig. 3.10(a), we see that the saturation deteriorates the sub-Poissonian correlation, and yet $R > 0$ remains nonclassical. However the saturation effects improve the sub-Poissonian properties artificially for finite quantum inefficiencies, as in Fig. 3.10 (b).

In a similar manner, we can consider the second-order correlation function, which – if evaluated on counts statistics – can be expressed as:

$$g^{(2)} = \frac{\langle k_1 k_2 \rangle}{\langle k_1 \rangle \langle k_2 \rangle}. \tag{3.18}$$

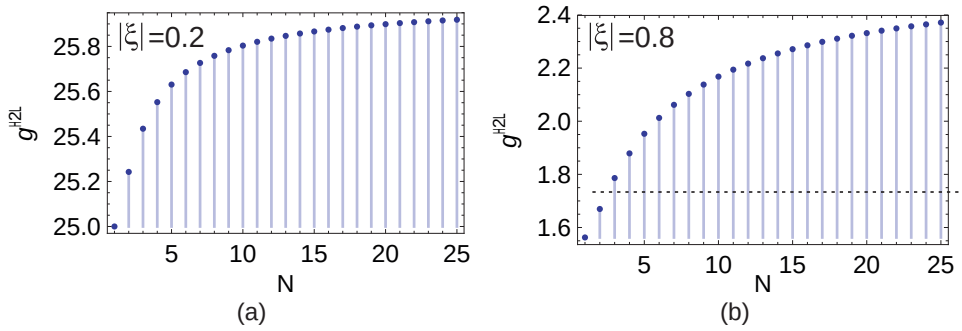


Figure 3.11: Second-order correlation function $g^{(2)}$ versus different numbers $N$ of detectors for $\eta = 1$ for $|\xi| = 0.2$ (a) and for $|\xi| = 0.8$ (b) for two-mode squeezed states. A finite number $N$ of component on-off detectors decreases $g^{(2)}$ which for two-mode squeezed state always is higher than two, $g^{(2)} > 2$. $g^{(2)}$ is decreased by no more than one. For $|\xi|^2 > 1/2$ and sufficiently low $N$, the observed counts statistics do not preserve their initial superbunching properties as in (b).

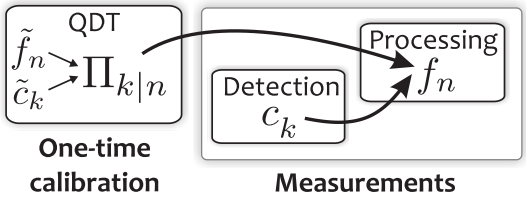


Figure 3.12: A camera tile can be calibrated in the one-time quantum detector tomography (QDT) process. Known photon statistics $\tilde{f}_n$ and counts statistics $\tilde{c}_k$ are used to determine distribution of conditional probabilities that characterize the operation of the tile. Then the measurement values of $\Pi_{k|n}$ can be used to reconstruct the photon statistics out of the measured count statistics.

It can be seen in Fig. 3.11 that the finite number of constituent on-off detectors $N$ decreases $g^{(2)}$ maximally by one. This effect is only significant for extremely high squeezing parameters, as exemplified in Fig. 3.11(b).

We see that nonclassical states are likely to preserve their nonclassical properties also seen in counts statistics. However the classical states, such as the coherent or thermal one, routinely yield counts statistics that are artificially nonclassical. Therefore the analysis of counts statistics can confirm the classicality of a state, whereas the opposite reasoning is likely to be erroneous.

## 3.8 Idea of quantum detector tomography

The introduced model of multiplexed on-off detectors is sufficient to qualitatively predict the results measured on a real intensified camera. However, as we observed, even subtle changes in the counts statistics can readily make them artificially nonclassical. For the most reliable characterization of the states of light more accurate operation of the camera has to be described. In Fig. 3.12 we present the general idea of a tomographic calibration of the camera and then the reconstruction of photon statistics, given the tomography results and count statistics.

Counts statistics are determined by distributions of conditional probabilities and statistics on the input light through Eq. (3.2). Initially in a measurement we do not know any values from the right-hand side of the formula, neither the photon statistics $f_n$ nor the conditional probabilities $\Pi_{k|n}$. In order to find the photon statistics $f_n$ we have to know at least the values of the probabilities

$\Pi_{k|n}$. They could be found in the model discussed before but for quantitative analysis an experimental characterization will be more reliable.

The conditional probabilities $\Pi_{k|n}$ can be characterized with a known set of states of statistics $\tilde{f}_n$ yielding measurable counts statistics $\tilde{c}_k$. They are mutually related through the analogous formula

$$\tilde{c}_k = \sum_{n=k}^{\infty} \Pi_{k|n} \tilde{f}_n, \tag{3.19}$$

where the summation starts from $n = k$, as we reasonably assume that the number of counts cannot exceed the number of photons. Ideally $\Pi_{k|n}$ might be found straightforward provided that arbitrary Fock states on the input were at our disposal. Then for each state $|n'\rangle$ on the input we could directly measure $\tilde{c}_{k'} = \Pi_{k'|n'}$. Yet, since Fock states are difficult to create, to revert Eq. (3.19) we can use an available class of states, such as coherent states whose statistics can be precisely determined. In the next section we discuss step by step how to perform this procedure in practice.

If we are able to find $\Pi_{k|n}$ from Eq. (3.19), then we can readily determine the unknown arbitrary photon statistics, supposing the counts and conditional probabilities are known. The procedure can also be applied to two-dimensional joint statistics.

## 3.9 Reconstruction of the conditional probabilities $\Pi_{k|n}$

Our task is to determine the distributions of the conditional probability $\Pi$. The procedure is to be eventually accomplished numerically, thus the matrix $\Pi$ has to have finite dimensions. At first we can stick to finite values of counts, as in the experiment their number is upper bounded by a certain $k_{\max}$.

Moreover, we have to truncate the latter Fock dimension denoting the number of the impinging photons. We shall truncate the base of Fock states down to $M$ and thus our task will be to find the elements of the finite matrix $\Pi$ of conditional probabilities of the size $(M+1) \times (k_{\max}+1)$, where $\Pi_{n|k} = p(k|n)$. The truncation can be justified assuming that a detector is saturated and responds in the same way to the number of incoming photons superior to $M$. Formally it means that for each $n \geq M$ and each $k \leq M$ we have $\Pi_{k|M} = \Pi_{k|n}$. If it be so, the Eq. (3.19) can be rewritten as:

$$\begin{aligned} \tilde{c}_k &= \sum_{n=0}^{\infty} p(k|n)\tilde{f}_n = \sum_{n=0}^{M-1} p(k|n)\tilde{f}_n + p(k|M) \sum_{n=M}^{\infty} \tilde{f}_n = \\ &= \sum_{n=0}^{M-1} p(k|n)\tilde{f}_n + p(k|M)\Big(1 - \sum_{n=0}^{M-1} \tilde{f}_n\Big) = \sum_{n=0}^{M-1} p(k|n)\tilde{f}_n + p(k|M)\bar{f}_M, \end{aligned} \tag{3.20}$$

where $\bar{f}_M = 1 - \sum_{n=0}^{M-1} \tilde{f}_n$. Such a procedure additionally ensures that $(\tilde{f}_0\ \tilde{f}_1\ \cdots\ \bar{f}_M)$ is the normalized finite probability distribution.

Furthermore, Eq. (3.20) determines the eventual form of a truncated matrix $\Pi$ to be:

$$\Pi = \begin{pmatrix} 1 & 0 & \cdots & 0 \\ p(0|1) & p(1|1) & \cdots & 0 \\ p(0|2) & p(1|2) & \cdots & 0 \\ \vdots & \cdots & \ddots & \vdots \\ p(0|M) & p(1|M) & \cdots & p(k_{max}|M) \end{pmatrix}. \tag{3.21}$$

The matrix is lower triangular, as we assume that the number of counts cannot exceed the number of the impinging photons $p(k > n|n) = 0$. The last row should be treated as the saturation limit . Note that we do not assume that the saturated detector returns only a specific number of counts, as for simple multiplexed on-off detectors. The matrix $\Pi$ fulfills only two of the conditions imposed by the mathematical properties of the discreet probability distributions:

$$\underset{k,n}{\forall}\ 0 \leq \Pi_{k|n} \leq 1, \quad \underset{n}{\forall} \sum_{k=0}^{k_{\max}} \Pi_{k|n} = 1. \tag{3.22}$$

As we have already mentioned, a set of states of known statistics is to be used to characterize $\Pi$. The easiest and most sufficient choice is to take coherent states of a Poissonian statistics. We can repeat the procedure for different mean photon numbers. In the $i$-th measurement the probability distribution for photons will be:

$$\tilde{f}_n^{(\mathrm{i})} = \frac{\bar{n}_i^n}{n!} e^{-\bar{n}_i}, \text{ for } 0 \leq n \leq M-1, \qquad \bar{f}_M^{(i)} = 1 - \sum_{n=0}^{M-1} \tilde{f}_n^{(i)}, \tag{3.23}$$

where the values of means $\bar{n}_i$ are sampled many times from the interval $0 \lesssim \bar{n}_i \lesssim M$. The input photon statistics yield the corresponding counts statistics $\tilde{c}_k^{(i)}$.

Both photon and counts statistics for all measurements performed can be gathered in matrices. Eventually we can rewrite Eq. (3.20) to a matrix equation:

$$\begin{pmatrix} \tilde{c}_0^{(1)} & \tilde{c}_1^{(1)} & \cdots & \tilde{c}_{k_{\max}}^{(1)} \\ \vdots & \vdots & \ddots & \vdots \\ \tilde{c}_0^{(L)} & \tilde{c}_1^{(L)} & \cdots & \tilde{c}_{k_{\max}}^{(L)} \end{pmatrix} = \begin{pmatrix} \tilde{f}_0^{(1)} & \tilde{f}_1^{(1)} & \cdots & \bar{f}_M^{(1)} \\ \vdots & \vdots & \ddots & \vdots \\ \tilde{f}_0^{(L)} & \tilde{f}_1^{(L)} & \cdots & \bar{f}_M^{(L)} \end{pmatrix} \begin{pmatrix} 1 & 0 & \cdots & 0 \\ p(0|1) & p(1|1) & \cdots & 0 \\ p(0|2) & p(1|2) & \cdots & 0 \\ \vdots & \cdots & \ddots & \vdots \\ p(0|M) & p(1|M) & \cdots & p(k_{max}|M) \end{pmatrix}, \tag{3.24}$$

where $L$ denotes the total number of measurements. Eq. (3.24) can be presented simply as

$$\mathbf{C} = \mathbf{F}\Pi, \tag{3.25}$$

where $\mathbf{C}$ is the $L \times (k_{\max}+1)$ matrix of counts statistics such as $(\mathbf{C})_{ik} = \tilde{c}_k^{(i)}$, and similarly $\mathbf{F}$ denotes the $L \times (M+1)$ matrix of photon statistics where $(\mathbf{F})_{in} = \tilde{f}_n^{(i)}$.

In order to find $\Pi$, one has to invert Eq. (3.25). This is an ill-posed problem when we have more equations than variables to find. It would be tempting to simply evaluate the pseudo-inversion of the matrix $\mathbf{F}$. Unfortunately, the pseudo-inversion that can be evaluated on rectangular matrices inevitably leads to unphysical $\Pi$ values, such as negative of higher than one. Moreover, the pseudo-inversion procedure amplifies noise to a large extent.

Instead, to reconstruct $\Pi$ from the measured and known statistics we will resort to convex optimization methods (Boyd and Vandenberghe, 2004). In particular we reformulate the problem of solving matrix equation Eq. (3.25) to minimize of the norm of matrix $||\mathbf{C} - \mathbf{F}\Pi||$ under the conditions imposed on $\Pi$ from Eq. (3.22). The matrix norm $||\cdot||$ could be selected to expedite the numerical computation and we typically used the Frobenius norm[1].

[1] The Frobenius norm of a matrix $\mathbf{A}$ is defined as $||\mathbf{A}|| = \sqrt{\sum_{i,j} (\mathbf{A})_{i,j}^2}$. We tested other norms such as the largest singular value and the results were nearly the same; yet, the Frobenius norm is relatively fast to compute and intuitive to interpret.

Nevertheless, the straightforward matrix norm minimization is sensitive to noise so we have to heuristically add another condition that helps us to approach the correct and physical solution. We follow the same approach as proposed by Lundeen *et al.* (2008) and add a next term to the minimization . Specifically we ought to ensure a certain smoothness of the resulting distributions $\Pi$ by adding an extra penalty function. The final task is to solve the optimization problem under the conditions of Eq. (3.22):

$$\min_{\Pi}\left\{||\mathbf{C}-\mathbf{F}\Pi||+\gamma\sum_{n,k}(\Pi_{k|n}-\Pi_{k+1|n})^2\right\}, \tag{3.26}$$

where the parameter $\gamma$ serves to adjust the desired smoothness. Its meaning and proper choice is studied on real data in the next Chapter. Eq. (3.26) represents a convex optimization problem similar to minimization of a quadratic norm. We can solve it using the CVX optimization package that returns global solutions for convex optimization problems (Grant *et al.*, 2015). In Appendix B we present the code used for the matrix $\Pi$ reconstruction.

## 3.10 Reconstruction of photon statistics

The reconstructed matrix of conditional probabilities $\Pi$ can be used to find unknown photon statistics in an arbitrary measurement. Then we have to invert Eq. (3.2) with a known $\Pi_{k|n}$ and $c_k$. We apply the similar procedure to solve the convex optimization problem. It can be formulated as:

$$\min_{\mathbf{f}}\left\{||\mathbf{c}-\mathbf{f}\Pi||+\gamma\sum_{n=0}^{M-1}(f_n-f_{n+1})^2\right\}\quad\text{satisfying:}\quad\forall_n\,0\le f_n\le 1\text{ and }\sum_n f_n=1. \tag{3.27}$$

where $\mathbf{c}=(c_0\ c_1\ \cdots\ c_{k_{\max}})$ is a vectorized distribution of the measured counts statistics and $\mathbf{f}=(f_0\ f_1\ \cdots\ \bar{f}_M)$ denotes the vectorized photon statistics to be reconstructed. Just as before we shall heuristically introduce a penalty function whose contribution is scaled by $\gamma$. Again, the CVX code is presented in Appendix B.

We can also reconstruct the joint photon statistics $f_{n_1,n_2}$ supposing we know the joint count statistics $c_{k_1,k_2}$ measured on two tiles, labeled 1 and 2. Then the statistics are related through Eq. (3.3). The procedure requires prior characterization of both tiles operation to determine the conditional probabilities $\Pi^{(1)}$ and $\Pi^{(2)}$ , respectively. Eq. (3.3) can be rewritten into a matrix form:

$$\mathbf{C}'=(\Pi^{(1)})^T\mathbf{F}'\Pi^{(2)}, \tag{3.28}$$

where $\mathbf{C}'$ is the $(k_{\max}+1)\times(k_{\max}+1)$ matrix of counts statistics where $(\mathbf{C}')_{k_1,k_2}=c_{k_1,k_2}$ and similarly $\mathbf{F}'$ denotes the $(M+1)\times(M+1)$ matrix of elements $(\mathbf{F}')_{n_1,n_2}=f_{n_1,n_2}$ to be found. The reconstruction again can be formulated as a convex optimization problem:

$$\min_{\mathbf{F}'}\left\{||\mathbf{C}'-\Pi^{(1)\mathrm{T}}\mathbf{F}'\Pi^{(2)}||_2+\gamma\sum_{n_1,n_2=0}^{M-1}((f'_{n_1,n_2}-f'_{n_1,n_2+1})^2+(f'_{n_1,n_2}-f'_{n_1+1,n_2})^2+(f'_{n_1,n_2}-f'_{n_1+1,n_2+1})^2)\right\}, \tag{3.29}$$

with standard conditions imposed on the probability distribution:

$$\forall_{n_1,n_2}\ 0\le f_{n_1,n_2}\le 1\text{ and }\sum_{n_1,n_2=0}^{M}f_{n_1,n_2}=1. \tag{3.30}$$

The regularization term ensures the smoothness of the statistics in three directions.

Successful realization of both one- and two-dimensional statistics reconstruction is feasible only for light intensities far from the saturation limits. For an entirely saturated detector there is no sound basis to infer the statistics. We demonstrate the calibration of the camera and the reconstruction of the statistics in the next Chapter describing experimental results.

## 3.11 Conclusions

In this Chapter we discussed two possible ways of characterization the photon number resolving capabilities of an intensified camera.

At first, in Sec. 3.3, we constructed a simplified model related to multiplexed on-off detectors and the photon chopping concept. Using the presented model we studied the saturation effects that influence the measured counts statistics, as compared to the statistics of the impinging photons that induced photoelectrons. We showed that nonclassical measures evaluated straightforward on the counts statistics can show artificial nonclassical features even for classical illumination. In Secs. 3.5-3.6 we discussed simple examples of coherent states and multimode thermal states finding the analytical results for the measures of nonclassicality. Moreover, in Sec. 3.7 we checked the influence of the saturation effect on squeezed states and we made sure that the counts statistics virtually always remain nonclassical.

Not only do the results emphasize the vagueness of direct measurements of nonclassicality properties of light with such a detection scheme, but they also provide a quantitative model that can be easily incorporated into state-of-the-art photon number resolving detectors, such as fiber loop detectors (Banaszek and Walmsley, 2003; Rehacek *et al.*, 2003; Achilles *et al.*, 2004) or multipixel photon counters (Afek *et al.*, 2009). A summary of the results was published in (Chrapkiewicz, 2014).

Thereafter we extended the qualitative analysis in Sec. 3.8 to build a particular model of the camera operation through calibration. In Sec. 3.9 we presented a theoretical approach to single-tile tomography. The calibration process relies on measurements with known states and on numerical solution of the convex optimization problem. Later, in Sec. 3.10, we showed the methods for one- and two-dimensional statistics reconstruction. The presented methods underlie the results of the paper (Chrapkiewicz *et al.*, 2014a).

In the next Chapter 4 we apply the introduced methods of characterization of photon counting properties to experimentally reconstruct photon statistics. Furthermore, some of the results are comparable with the provided simple model of multiplexed on-off detectors.

CHAPTER 4

# EXPERIMENTAL CHARACTERIZATION OF PHOTON COUNTING PROPERTIES OF THE INTENSIFIED SCMOS CAMERA

In this Chapter we present the experimental study of photon counting properties of the intensified sCMOS camera within the framework discussed in the previous Chapter. Not only did we determine the camera tiles operation but we also successfully employed the found conditional probabilities $\Pi_{k|n}$ to reconstruct one- and two-dimensional photon statistics. The demonstrated procedure removed artificial nonclassical features from the raw statistics of camera photo-events.

Let us start by presenting the setup used for camera calibration in Sec. 4.1. Next in Sec. 4.2 we shall compare the properties of counts statistics with the results for multiplexed on-off detectors derived in Sec. 3.5. Then, in Sec. 4.3, we perform and carefully study the results of the numerical procedure to determine the conditional probabilities $\Pi_{k|n}$ using a software code presented in Appendix B.

We verify the correctness of the retrieved probabilities $\Pi_{k|n}$ by performing a high-fidelity reconstruction of one- and twodimensional statistics of few-photon states. Demonstrations discussed in Secs. 4.4-4.4 are performed for coherent states and their statistical mixtures.

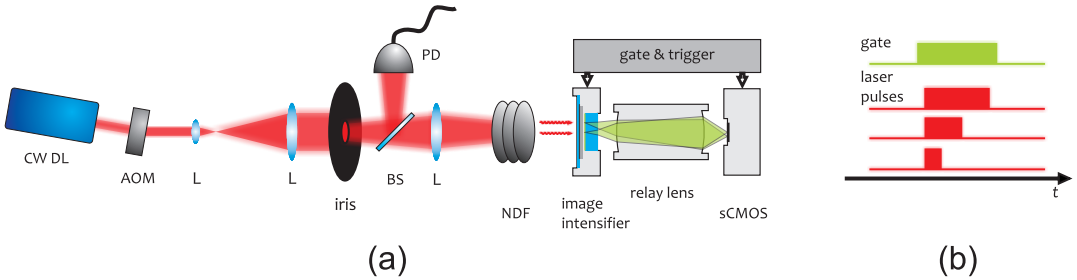


Figure 4.1: Setup for quantum detector tomography of an I-sCMOS camera. (a) Acousto-optical modulator (AOM) forms rectangular light pulses (b) from a continuous wave diode laser (CW LD). A nearly flat-top beam is formed with the use of an expanded beam and an iris whose surface is imaged on the I-sCMOS camera. Few-photon pulses are obtained through strong attenuation by neutral density filters (NDF) and their energy is monitored by a photodiode (PD) after a beam splitter (BS).

## 4.1 Experimental setup for characterizing camera macropixels

The crux of the quantum detector tomography (QDT) is to measure the response of a detector probed by a set of known states. The response of the detector involves losses due to a finite QE of a photocathode, and to non-linear saturation. Since the losses modify light statistics in a perfectly known way described by Eq. (3.5), we focus on pure saturation effects exclusively. Yet, they introduce undesirable artificial features into the measured statistics, therefore we aim to operationally remove them from measured count statistics through a statistics reconstruction process.

In this Chapter we incorporate losses into the photon statistics, so thatwe can effectively discuss photoelectron statistics exclusively. We measure the counts statistics $\tilde{c}_k^{(i)}$ inside finite-size macropixels illuminated by pulses of coherent states. Photons that induced photoelectrons have the Poissonian statistics $\tilde{f}_n^{(i)}$ of the mean $\bar{n}_i = \eta\bar{m}_i$, where $\eta = 20\%$ is the photocathode QE and $\bar{m}_i$ is the mean number of impinging photons before losses.

The experimental setup is presented in Fig. 4.1. For illumination we used a continuous wave laser beam operating at a wavelength of 795 nm. To create few-photon coherent states, we tailored 100 ns–5.5 $\mu$s pulses with an acousto-optical modulator. They fit in the gate time of 6 $\mu$s of the image intensifier, as depicted in Fig. 4.1(b). Moreover, the beam was attenuated by a set of neutral density (ND) filters. ND filters were calibrated separately and their total attenuation was found to be $2.5 \cdot 10^{-8}$. The energy of the laser pulses was continuously measured by a photo diode, thus in each measurement we were able to accurately know the mean photon number impinging on a camera.

We illuminated the circular region of the camera with a relatively flat intensity distribution achieved by imaging the small iris aperture as presented in Fig. 4.1 (a). We checked the capability of multiphoton counting for circular shape tiles of two different sizes illustrated in Fig. 4.2. The choice of two different sizes aimed at studying the compromise between a resolution and saturation

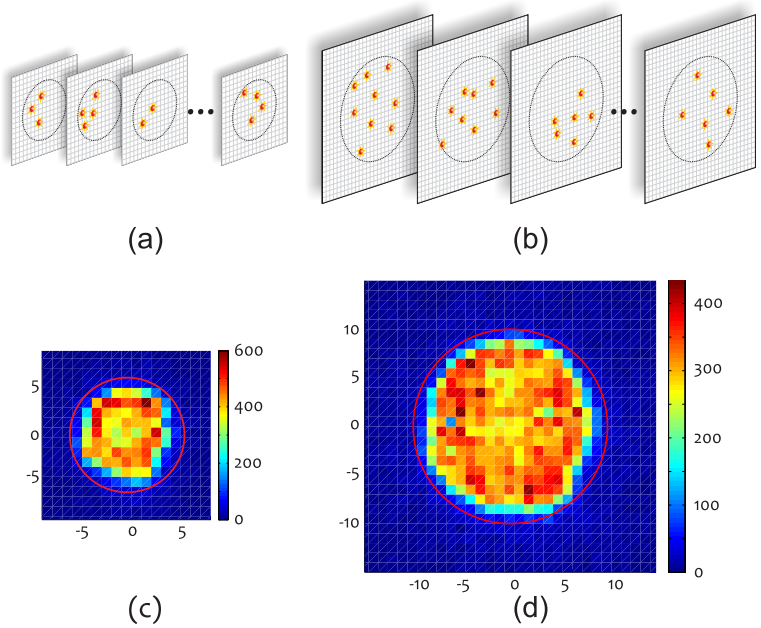


Figure 4.2: For experimental demonstration we selected macropixels as two circular regions of 11 px (left panel) and 20 px (right panel) in diameter. (a-b) Visualized experimental positions of the photo-events are accumulated as (c-d) two-dimensional histograms of counts computed for 1 px×1 px binning.

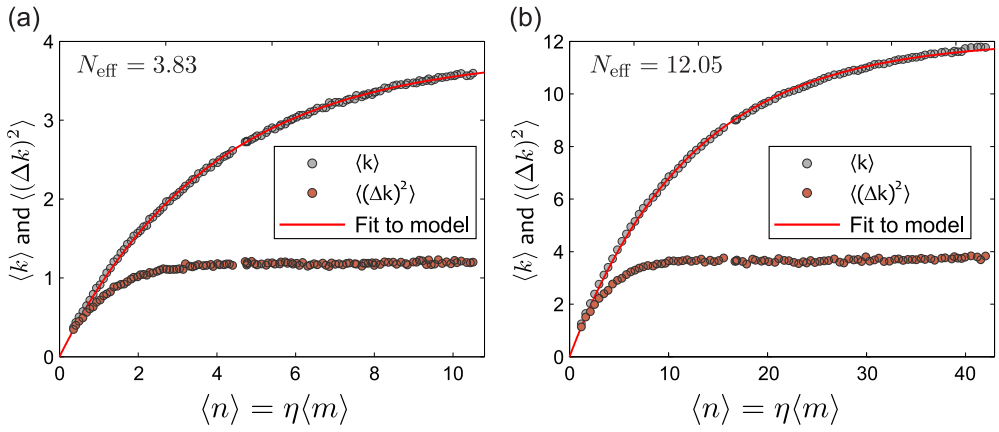


Figure 4.3: In the experiment we use few-photon coherent states. We vary their mean number of photons that induce photoelectrons $\langle n\rangle = \eta\langle m\rangle$. The measured mean $\langle k\rangle$ and variance $\langle(\Delta k)^2\rangle$ of counts inside two macropixels clearly saturate with increasing $\langle n\rangle$. The mean of counts $\langle k\rangle$ was fitted to the model Eq. (4.1) to obtain the effective number of single photon regions $N_{\mathrm{eff}}$ for a tile of (a) 11 px and (b) 20 px in diameter.

effects. The peak powers of laser beams before attenuation were respectively 125 $\mu$W and 446 $\mu$W. For a gate aperture duration of 6 $\mu$s the expected number of dark counts were $2.9\cdot10^{-4}$ and $9.4\cdot10^{-4}$ , which can be entirely neglected as compared with the used illumination.

In Fig. 4.2(a-b) we present exemplary experimental data of photo-event positions in several frames for average count rates 3.8 and 7.9 respectively. The frames can be stacked together to obtain distribution of counts across the camera pixels. In Fig. 4.2(c-d) we present histograms of photons positions from $10^5$ frames in our experimental configurations showing the circular regions of relatively sharp edges.

## 4.2 Counts and photon statistics

At first for each individual tile we measured the mean number of counts $\langle k\rangle$ and variance $\langle(\Delta k)^2\rangle$ for different mean numbers of incoming photons $\langle n\rangle = \eta\langle m\rangle$ that induced photoelectrons. The results are presented in Fig. 4.3 where each data point was obtained from the acquisition of $10^4$ frames. The mean number of the counts $\langle k\rangle$ fits is saturated similarly to the simple model of $N$ multiplexed on-off detectors illuminated by coherent states, discussed in Chapter 3. We fit the model to the experimental results applying the formula:

$$\langle k\rangle = N_{\mathrm{eff}}(1 - e^{-\langle n\rangle / N_{\mathrm{eff}}}). \tag{4.1}$$

The fit of the parameter $N_{\mathrm{eff}}$ plays a similar role to the number of on-off detectors. Although we deal with virtually continuous positions of single photo-event spots they occupy a finite space. Thus $N_{\mathrm{eff}}$ denotes the ratio of a tile size to the effective singe photo-event size, which is approximately 25 sCMOS pixels each. We shall call it the effective number of single photon regions, which it equals $N_{\mathrm{eff}} = 3.83 \pm 0.01$ for a smaller tile and $N_{\mathrm{eff}} = 12.05 \pm 0.04$ for a bigger one.

Apparently the variance of the number of counts $\Delta k^2$ plotted in Fig. 4.3 does not agree with the predictions of the simple model in Eq. 3.6, cf. Fig. , and instead of dropping to zero it approaches the constant value. This points to a more elaborated nature of photon counting process for our camera as compared to an array of on-off pixels.

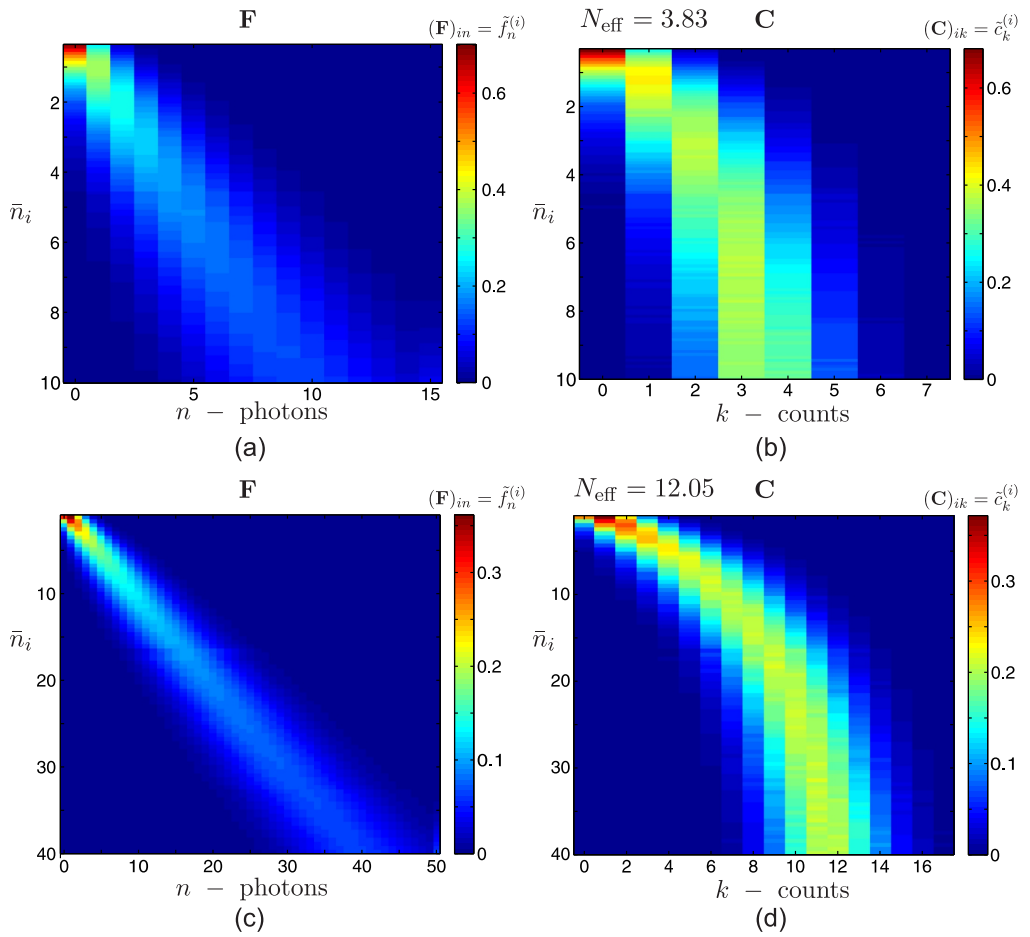


Figure 4.4: Input photoelectrons and the measured counts statistics **F** and **C**. Matrices (a-b) refer to a macropixel of $N_{\text{eff}} = 3.83$ and (c-d) for $N_{\text{eff}} = 12.05$. (a,c) Input probe states statistics **F** (in rows) versus the mean number of photoelectrons $\bar{n}_i$. The photon space was truncated to (a) $M = 15$ and (c) $M = 50$, respectively. (c,d) Empirical counts statistics **C** (in rows) versus $\bar{n}_i$.

In Fig. 4.4 we present the input photoelectron statistics gathered in matrices **F** (left panel) and the empirical measured counts statistics presented in matrix **C** (right panel). Both matrices **F** and **C** are inputs for the QDT procedure. Consecutive rows of matrices correspond to subsequent measurements. The statistics are presented for around 100 coherent probe states of an almost uniformly distributed mean number of photons. Each row of matrices **F** contains the distribution of probability, as in Eq. (3.23).The truncation of the photon space was set to $M = 15$ and $M = 50$ and in the bottom right corners of matrices **F** in Fig. 4.4 we see increasing values of $\bar{f}_M$ fulfilling the rows normalization conditions.

Let us note that the empirical probability for null counts, i.e. $\tilde{c}_0^{(i)}$, should agree with the expected probability of no photoelectrons $\tilde{f}_0^{(i)} = e^{-\bar{n}_i}$. We checked that the first columns of matrices **C** containing sets of $\tilde{c}_0^{(i)}$ perfectly matched the predictions and additionally confirmed the ratio of the number of the impinging photons to the photoelectrons.

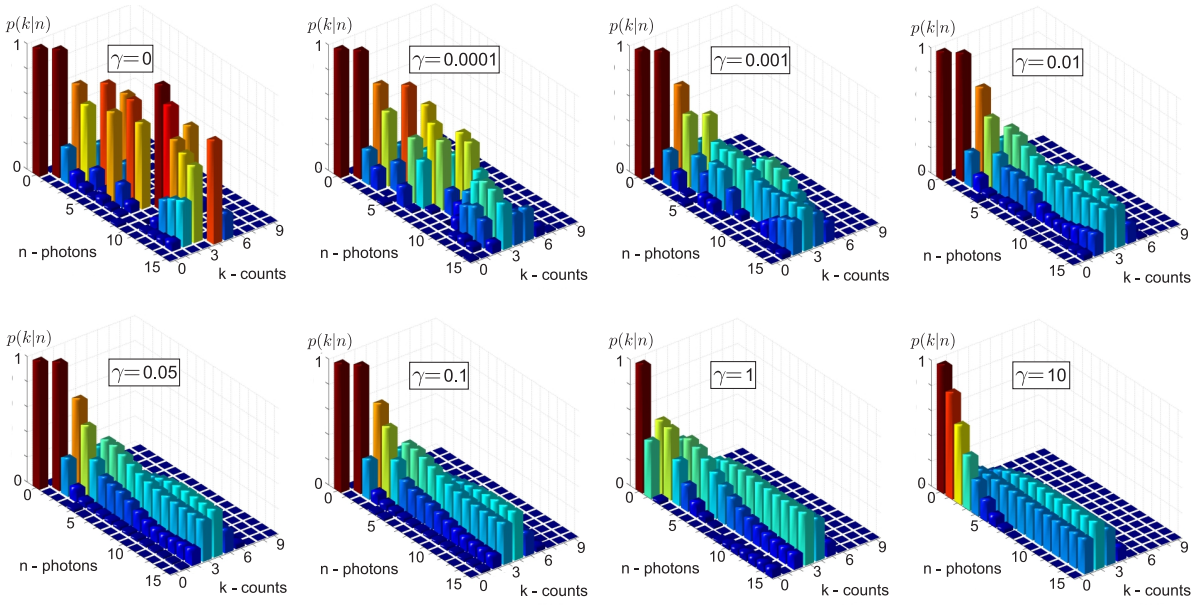


Figure 4.5: Reconstructed matrices of conditional probabilities Π for a macropixel of $N_{\mathrm{eff}} = 3.83$ for different regularization coefficients $\gamma$. For small values of $\gamma$ the reconstruction yields high-noise results, whereas for the large $\gamma$ regularization results in artificially smooth and unphysical distributions.

## 4.3 Study of regularization in the reconstruction of Π

Equipped with matrices of photoelectron and counts statistics **F** and **C**, we can proceed to reconstructing the distribution of conditional probabilities Π characterizing the operation of both tiles PNR . We solved the numerical optimization problem defined in Eq. (3.26) conditioned on Eq. (3.22) using the CVX package and the script described in Appendix B.

The optimization problem has one arbitrary parameter: the regularization coefficient $\gamma$. At first let us study the results of Π reconstruction for different values of $\gamma$ to understand the role of penalty function in Eq. (3.26).

In Fig. 4.5 we present results of the reconstruction process of Π for different regularization coefficients $\gamma$ for a smaller macropixel and in Fig. 4.6 for a larger one. The results vary from high-noise only and random for $\gamma = 0$ to nonphysically smooth for $\gamma = 10$. Nonetheless, within that range of parameters the good choice of $\gamma$ seems to remain arbitrary.

We can quantify the reliability of the reconstruction by checking whether the three following conditions have been fulfilled. (1) Firstly, a photoelectron virtually cannot be lost, thus we shall require $p(k = 0|n = 1) = 0$, whereas $p(k = 1|n = 1) = 1$. (2) Secondly, zero number of counts can occur only in case of no induced photoelectrons, thus $p(0|n > 0)) = 0$. (3) Last but not least, we expect to observe tile saturation and specifically predict a saturated response that does not change with increasing values of $n' > n$:

$$p(k|n \gg N_{\mathrm{eff}}) \simeq p(k|n' > n \gg N_{\mathrm{eff}}). \tag{4.2}$$

As can be seen from Fig. 4.5 and 4.6 artificially smooth solutions for large $\gamma$ do not fulfill the criteria (1) and (2). On the other hand for a small $\gamma$ there is no apparent saturation required by condition (3). All of the three conditions seem to be fulfilled in the middle region of parameters $\gamma$ , yet the proper selection method is still unclear.

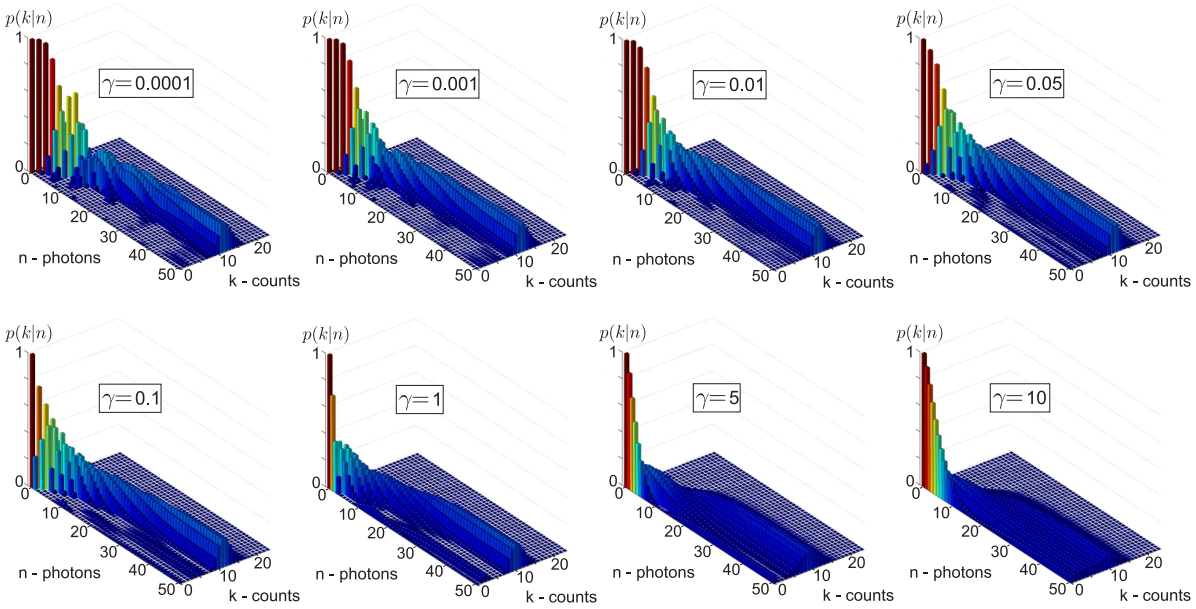


Figure 4.6: Reconstructed matrices of conditional probabilities Π for a macropixel of $N_{\text{eff}} = 12.05$ for different regularization coefficients $\gamma$. As in Fig. 4.5, we observe a transition from high-noise to unconscionably smooth solutions.

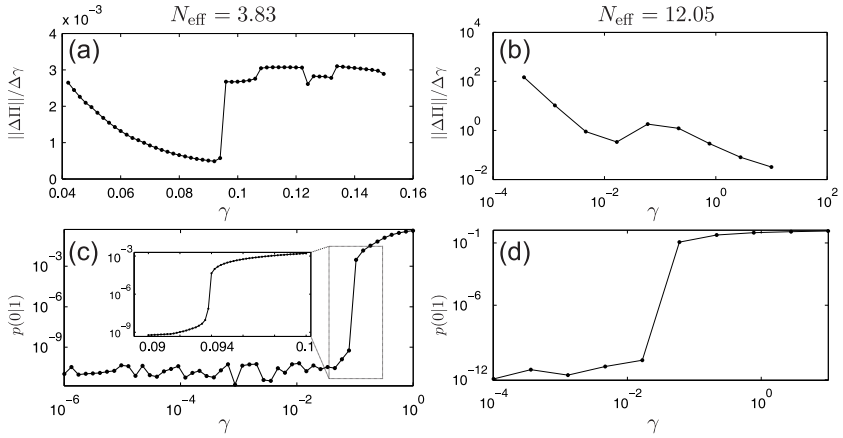


Figure 4.7: (a-b) Normalized change of Π with the increments in the regularization constant $\gamma$ reveal a sudden transition. (c-d) The transition can be associated with an abrupt leap in $p(0|1)$, whilst the regularization term starts to dominate in the optimization problem. The optimal parameter $\gamma$ for reconstruction should be set just below the transition.

For the ultimate selection of a proper regularization coefficient we quantitatively studied how Π changes with small changes of $\gamma$. Firstly we quantified the differences between the reconstructed matrices Π for incremental changes in $\gamma$. Specifically we evaluated the norm of differences between the two results of reconstruction and divided them according to the change in the regularization coefficient: $||\Delta\Pi||/\Delta\gamma$. The results for both tiles are depicted in Fig. 4.7(a-b). The total number of reconstructions is smaller for the larger tile due to significantly longer computation time of the reconstruction. As we see, in the middle of $\gamma$ range there is a noticeable change in the value $||\Delta\Pi||/\Delta\gamma$.

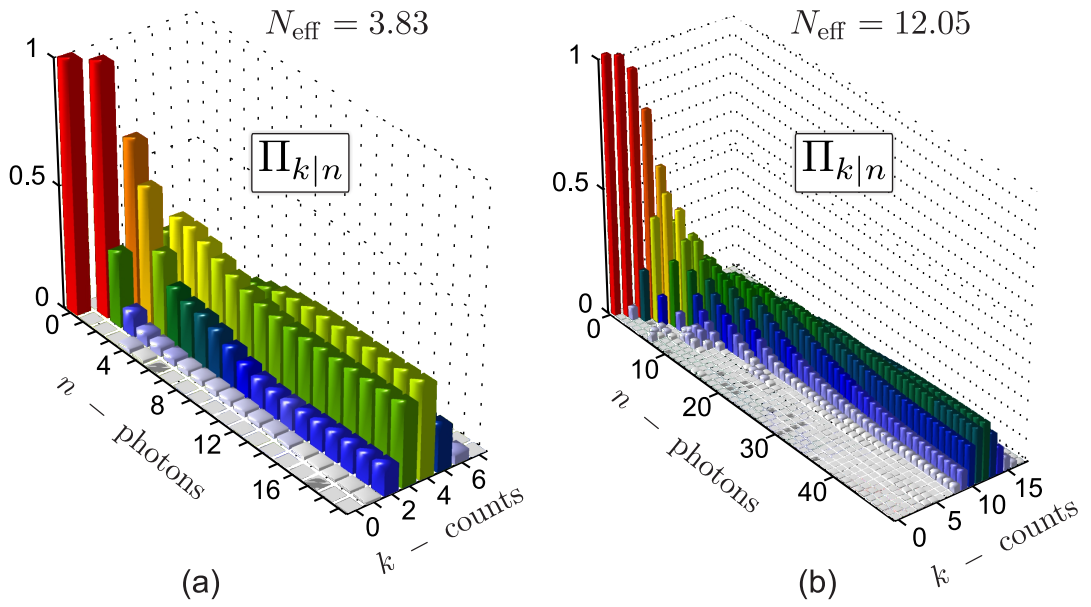


Figure 4.8: The most faithful values of conditional probabilities $\Pi_{k|n}$ reconstructed with regularization parameters (a) $\gamma = 0.09$ for a smaller tile and (b) $\gamma = 0.01$ for a larger tile. PNR operation of two tiles. The saturation of $\Pi$ for a high number of photons $n$ that induced photoelectrons reveals a stochastic response of the detector in the saturation regime.

This may suggest that for higher values of $\gamma$ the regularization term dominates.

To verify our suspicions, we plotted the values of reconstructed conditional probabilities $p(0|1)$. In the condition (1) we stipulate that a negligible value of $p(0|1)$ confirms the expected physical operation of a tile. Indeed, we see a threshold value of $\gamma$ that , when exceeded, yields an abrupt increase in $p(0|1)$ by six and eleven orders of magnitude for small and large tiles, respectively. Therefore, we decided to pick $\gamma$ as a reasonable regularization coefficient just below that giant leap . For a smaller tile we picked $\gamma = 0.09$ and for the larger one $\gamma = 0.01$.

The final result of QDT meeting all of the three conditions (1-3) for a faithful reconstruction are presented in Fig. 4.8. From the reconstructed values of conditional probabilities $\Pi_{k|n}$ we see that a tile of the intensified camera saturates in a different manner than a typical multiplexed detector. For instance, for large $n' > n_{\mathrm{sat}}$ the tile returns a random number of counts $k$ of statistics given by $c_k = \Pi_{k|n'} = \Pi_{k|n_{\mathrm{sat}}}$. That agrees with our previous observation that the variance of the number of photo-event counts $\langle(\Delta k)^2\rangle$ converges to a nonzero value.

## 4.4 Reconstruction of one-dimensional statistics

The ultimate verification of the correctness and effectiveness of the found conditional probabilities $\Pi_{k|n}$ is a reconstruction of the known statistics. As a test state we shall take again the coherent states used for the tomography procedure.

As a qualitative measure of the effectiveness of reconstructed probabilities $\Pi_{k|n}$ used for statistics reconstruction the Mandel parameter $Q_M$ will be evaluated and compared with the expected zero value for coherent states, as well as with the empirical value $Q_{\mathrm{F}}$ evaluated on the counts defined in Eq. (3.10). Moreover, we shall show the fidelity of reconstruction

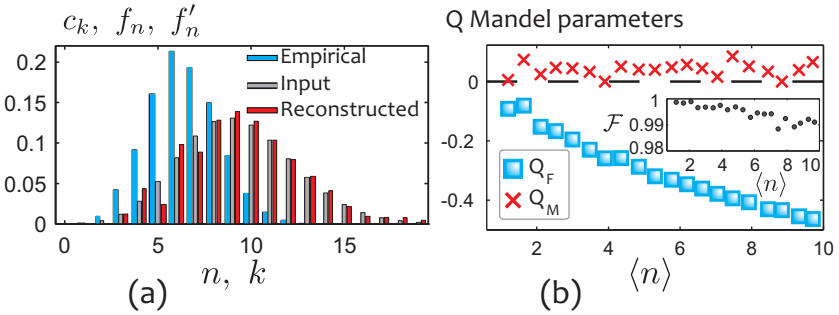


Figure 4.9: (a) Exemplary reconstruction of photoelectron statistics $f'_n$ based on the measured counts statistics $c_k$ at a tile of the size $N_{eff} = 12.05$. The mean number of photoelectrons was $\langle n \rangle = 9.3$, whereas the mean number of counts $\langle k \rangle = 6.5$. (b) Mandel parameters for counts $Q_F$, for reconstructed statistics $Q_M$ for coherent states with variable mean photoelectron number $\langle n \rangle$. Inset: fidelity of reconstruction exceed 99% for most data points.

$$\mathscr{F} = \sum_{n=0}^{M} \sqrt{f_n f'_n}, \tag{4.3}$$

where $f_n$ in the known input statistics and $f'_n$ is the reconstructed statistics.

We performed a state reconstruction for the tile of the size $N_{\text{eff}} = 12.05$. In Fig. 4.9 (a) we compare the measured empirical counts distribution $c_k$ with input statistics known *a priori* and reconstructed statistics $f'_n$. Here the Mandel parameter evaluated directly for the counts statistics is always considerably below zero even for an illumination level of 0.05 photoelectrons per single photon detection area, minimally down to $Q_F = -0.45$. After the reconstruction we retrieve the classical value of Mandel parameter $Q_M = 0.04$, which is close to the expected zero value. In Fig. 4.9 (b) we present Mandel $Q$ parameters. The fidelity of reconstruction is high i.e. $\mathscr{F} \gtrsim 0.99$ for different mean values $\langle n \rangle$.

## 4.5 Reconstruction of joint statistics

Further verification of our method can be performed in the reconstruction of joint statistics. Bare counts statistics can exhibit artificial sub-shot-noise correlation even for the illumination of classical states . Here as test states we used a statistical mixture of coherent states illuminating two tiles labeled $i = 1, 2$.

We prepared classically correlated states as a statistical mixture of two attenuated laser beams which have nontrivial joint statistics. The mean number of photons $\langle n_i \rangle$ at the $i-$th tile were equiprobably switched between $\bar{n}_i$ and $\bar{n}'_i$. The state that undergoes only photon counting measurements may be formally represented as a density matrix:

$$\hat{\rho} = \frac{1}{2}|\alpha_1\rangle\langle\alpha_1| \otimes |\alpha_2\rangle\langle\alpha_2| + \frac{1}{2}|\alpha'_1\rangle\langle\alpha'_1| \otimes |\alpha'_2\rangle\langle\alpha'_2|, \tag{4.4}$$

where $|\alpha_i|^2 = \bar{n}_i$, $|\alpha'_i|^2 = \bar{n}'_i$. The mean number of photons in subsystems equals $\langle n \rangle_i = (\bar{n}_i + \bar{n}'_i)/2$. The state exhibits classical correlations of photon numbers between subsystems and the Fano noise reduction factor defined in Eq. (1.53) equals $R = 1$. The covariance between the photon numbers in a subsystem becomes particularly simple: $\text{cov}(n_1, n_2) = (\bar{n} - \bar{n}')^2/4$ for $\bar{n} = \bar{n}_i$ and $\bar{n}' = \bar{n}'_i$. Thus,

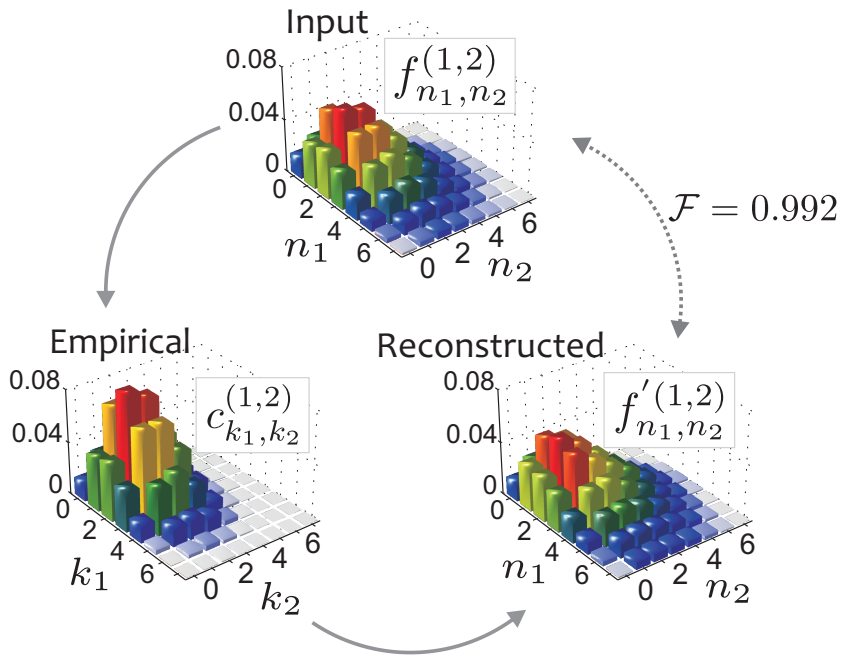


Figure 4.10: Histograms of joint statistics on a pair of tiles of sizes $N^{(1)}_{\text{eff}} = 4.9$ and $N^{(2)}_{\text{eff}} = 6.3$. The raw measured counts statistics $c^{(1,2)}_{k_1,k_2}$ are reconstructed to $f'^{(1,2)}_{n_1,n_2}$, which overlaps with the input state statistics $f^{(1,2)}_{n_1,n_2}$ with high fidelity $\mathcal{F}$. Two tiles characterized in QDT process were illuminated by an equiprobably alternated statistical mixture of coherent states, with $\bar{n}_1 = 2$, $\bar{n}'_1 = 3.7$.

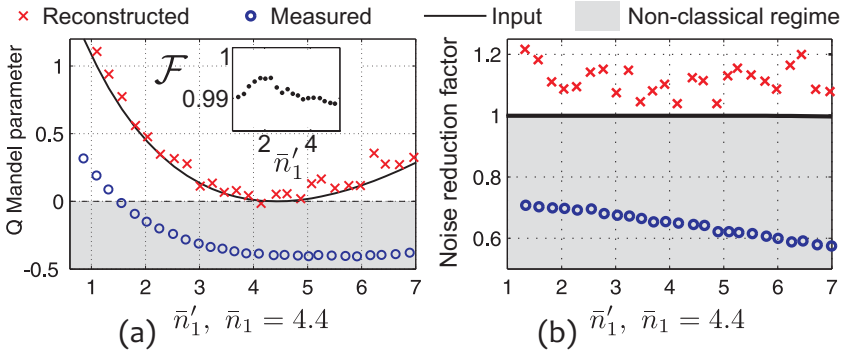


Figure 4.11: Results of joints statistics reconstruction of statistical mixtures of coherent states. (a) Mandel parameters for counts $Q_F$ are super-Poissonian for $\bar{n}'_1 < 1.5$ , yet they are unequivocally fixed to the expected classical values for all data points. (b) Fano noise reduction factor evaluated for the counts is always artificially nonclassical, whereas the reconstructed values consistently remain classical and are close to the expected values.

the larger discrepancy between the switched means of photons, the higher classical correlation we expect. Moreover, the Mandel parameters of marginal statistics are $Q_M > 0$ for $\bar{n}_i \neq \bar{n}'_i$.

The state $\hat{\rho}$ is obtained by simply selecting two different mean number of photons illuminating the camera. There is one beam that simultaneously illuminates two tiles created in postprocessing from the two halves of a larger macropixel illustrated in Fig. 4.2. The tiles are characterized independently in the QDT procedure described before. The postselected tiles differ slightly in size and their effective sizes quantified in effective numbers of single photon regions are found to be $N^{(1)}_{\text{eff}} = 4.9$

and $N_{\mathrm{eff}}^{(2)} = 6.3$, respectively. Owing to the QDT we determine the conditional probabilities $\Pi_{k_1|n_1}^{(1)}$ and $\Pi_{k_2|n_2}^{(2)}$.

Thereafter, we perform a numerical reconstruction of photoelectrons joint statistics $f_{n_1,n_2}^{\prime(1,2)}$ from counts statistics $c_{k_1,k_2}^{\prime(1,2)}$ following the procedure summarized in Eq. (3.29) and Eq. (3.30) using a numerical implementation described in Appendix B. In Fig. 4.10 we present typical results of reconstruction of exemplary joint statistics with high fidelity $\mathscr{F} = 0.992$. Which is noteworthy, we succeeded in fixing the artificial sub-Poissonian correlation appearing in bare counts statistics. The Fano factor before reconstruction $R = 0.71$ seemed to be nonclassical. It was raised up to a classical value $R = 1.01$ after reconstruction.

In Fig. 4.11 we study the reconstruction properties for a fixed number of photoelectrons $\bar{n}_1 = 4.4$ as a function of $\bar{n}_1'$. It is instructive to examine the properties of marginal of statistics. In Fig. 4.11(a) we plot the empirical and the reconstructed Mandel parameters $Q_F$ and $Q_M$, respectively. The parameter evaluated on the marginal agrees excellently with the predictions. In Fig. 4.11(b) we also present the noise reduction factor for a variety of test states. For each data point the Fano noise reduction factor, which was artificially nonclassical before reconstruction, was fixed and raised to classical values.

For test states with $\bar{n}_1' < 1.5$ we observe an interesting situation where directly measured marginal statistics are super-Poissonian ($Q_F > 0$) and the joint statistics remained sub-Poissonian ($R < 1$). This situation mimics the two-mode squeezed state where the marginal statistics are super-Poissonian and thermal. Without the reconstruction procedure the correlated classical state could be easily mistaken with its quantum counterpart.

Similarly to the reconstruction of one-dimensional statistics here we succeeded to reliably reconstruct joint statistics up to the light intensity level corresponding to one photoelectron per single photon detection area $\langle n_i \rangle = (\bar{n}_i + \bar{n}'_i)/2 \simeq N^{(i)}$. We removed artificial nonclassical effects from the reconstructed statistics and the fidelity of reconstruction consistently exceeded $\mathscr{F} > 0.99$.

## 4.6 Conclusions

In this Chapter we demonstrated the first and successful tomography of the photon counting properties of an intensified camera. In Sec. 4.3 we faithfully reconstructed the distributions of conditional probabilities $\Pi_{k|n}$ accurately characterizing the saturation effects on the detector. The procedure required the understanding of the role of regularization in the numerical solution of the convex optimization problem. We determined the optimal regularization yielding physical description of a camera operation.

The results of the tomography indicated significantly different camera photon counting properties than those previously introduced in Sec. 3.3, derived from the analytical model of multiplexed on-off detectors. Although the macropixels of an intensified camera can be perceived as groups of finite number of detectors, they are saturated in a different manner.

The main achievement of this Chapter was the reconstruction of photon statistics presented in Secs. 4.4-4.5. We verified the correctness of the calibration performing one- and two-dimensional statistics reconstruction. We used classical states of artificially nonclassical counts statistics. They consistently yield classical values of Mandel and Fano noise reduction parameters after reconstruction.

To our knowledge, that has been the first application of the results of the QDT technique. The extensively used theoretical procedure is introduced in Chapter 3 and software codes can be found in Appendix B. The summary of main results was published in (Chrapkiewicz *et al.*, 2014a).

The significance of the results is twofold. Firstly, we showed that data processing in our method is universal owing to the application of QDT techniques, avoiding altogether the need to develop analytical description of the hardware (Haderka *et al.*, 2005) which is apparatus-specific and may often become overly complex. Secondly, we pushed the limit of useful operation of our method up to one photoelectron per single photo-event detection area on average and significantly extended the operation regime used in the previous works (Haderka *et al.*, 2005; Blanchet *et al.*, 2008; Machulka *et al.*, 2014).

The demonstrated results emphasized how challenging the measurements of nonclassical properties of light at high illumination levels could be. Although we demonstrated that the reconstruction of photon statistics is feasible and brings expected results, it is still a relatively laborious process. Nonetheless, it must be performed to claim nonclassicality of a measured state in any case if more than one photon is detected on single macropixels of a camera.

# Part II

# Spatial properties of photons generated in multimode atomic memory

The results presented in Part II relate to a source of spatially multimode photons based on atomic memory using warm rubidium vapors. In Chapter 5 we present the consecutive parts of our setup, paying special attention to the properties of the constructed filtering system. In Chapter 6 we demonstrate the generation, storage and retrieval of speckle-like patterns of spatially multimode Stokes and time-delayed anti-Stokes scattering. We also quantify the storage properties by accurately characterizing the diffusional decoherence phenomenon. Finally, in Chapter 7, we study the spatial correlations between the Stokes and anti-Stokes photons and reach the single photon level.

The presented study can be placed in a broader context of current developments in quantum memories reviewed comprehensively in the following papers (Lvovsky *et al.*, 2009; Simon *et al.*, 2010; Bussieres *et al.*, 2013; Heshami *et al.*, 2015). In general, quantum memories hold promise for realizing many important quantum protocols, such as long-distance quantum communication (Duan *et al.*, 2001; Kimble, 2008), quantum computations (Bustard *et al.*, 2013; Humphreys *et al.*, 2014), as well as for the generation of multiphoton states (Nunn *et al.*, 2013).

The current research on quantum memories tests their possible implementations in different media, such as cold gases of alkali metals (Radnaev *et al.*, 2010), NV-centers in diamonds (Maurer *et al.*, 2012), optical phonons in diamonds (Lee *et al.*, 2011), doped solid states crystals (Clausen *et al.*, 2011), and warm atomic vapors (Bashkansky *et al.*, 2012), which we study in this part.

So far there have been different implementations of interfacing memories in warm atomic vapors with light. The most important types of interfaces include electromagnetically-induced transparency (Veissier *et al.*, 2013), gradient echo memory (Hosseini *et al.*, 2009) and finally Raman scattering (Reim *et al.*, 2010), which is studied in this thesis.

**Contribution**

All of the results presented in this Part were obtained with a major contribution of R.C. Experiments were initially carried out by R.C. and W.W., where R.C. performed measurements, built the optical setups and analyzed the data, while W.W. built the electronics, prepared the software and supervised the whole research. During the research on four-wave-mixing process M.D. joined the group and the roles slightly changed. M.D. was predominantly involved in running measurements and rebuilding the setup, R.C. wrote the software to control the experiment and to analyze the data and performed part of measurements, whereas W.W. supervised the whole experiment keeping on constructing the electronics together with J.I.

CHAPTER 5

# EXPERIMENTAL SETUP FOR RAMAN SCATTERING IN WARM ATOMIC VAPORS

This chapter is devoted to the experimental setup for generation, storage and retrieval of spatially multimode photons. Photons are generated in the collective Raman scattering introduced theoretically in Sec. 1.5. In this chapter we explain all of the components and introduce experiment-specific nomenclature used further in Chapters 6 and 7.

At first in Sec. 5.1 we present the general idea of a setup necessary to generate collective Raman scattering in rubidium vapors. Then we discuss in detail the consecutive elements of the setup, starting from the driving lasers and ending with the detection system. In particular Sec. 5.2 describes our specific implementation in rubidium-87 ($^{87}$Rb) vapors. Then we overview the important parts of the full setup. In Sec. 5.2 we focus on the laser system, the pulse sequence, frequencies and beam shaping. Sec. 5.3 describes the main cell filled with $^{87}$Rb vapors mixed with the buffer gas. Sec. 5.4 presents the most important properties of the system that filters photons generated in the Raman scattering from the driving lasers and the fluorescence. Finally Sec. 5.5 describes the detection system.

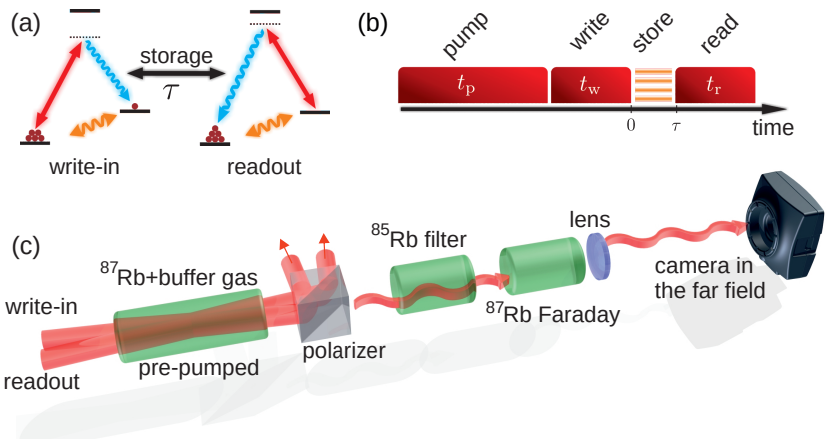


Figure 5.1: General idea of the experiment. (a) Raman scattering: write-in process generating Stokes photons and readout producing anti-Stokes photons. (b) Experimental sequence. (c) Essential parts of the setup.

## 5.1 Experimental overview

We generate, store and retrieve photons in the collective Raman scattering in warm rubidium vapors. Since our setup stores collective excitation carrying information about photons direction and number, it can be referred to as a setup of atomic memory.

Fig. 5.1 summarizes the essence of the experiment. Photons are interfaced with atomic collective excitations via off-resonant Raman transitions illustrated in Fig. 5.1(a) and described in detail in Chapter 1, Sec. 1.5. In practice each measurement run consists of four main steps depicted in Fig. 5.1(b). Firstly, the atoms are pumped, then we write in atomic excitations in the Stokes scattering process. Atomic excitations can be stored for an adjustable time $\tau$ and finally they are read out in the anti-Stokes scattering process. The simplified sketch of most important elements of the setup is displayed in Fig. 5.1(c). These are the driving laser beams, the main glass cell that contains warm alkali atom vapors ($^{87}$Rb), the filtration system and the detection system.

Our setup enables us to operate the atomic memory in a spatially multimode regime which means that we can couple to many spin wave modes simultaneously. In consequence the scattered light is also spatially multimode. Such multimode operation is natural and readily achievable in other parametric processes, such as the SPDC in non-linear crystals and four-wave mixing in atomic vapors (Boyer *et al.*, 2008b,a). Nonetheless, it is rather uncommon for atomic memories and requires special filtering and a detection system.

Filtration is necessary to extract spatially structured few-photon light out of the strong driving beams detuned in wavelengths by only ca. 0.014 nm. Since we want to preserve spatial structure of photons keeping their transmittance high, the filtration is the most challenging part of the setup. At the end we apply a spatially resolved detection system that is sensitive to single photons. In all of the presented experiments the camera is placed in the far field and resolves angular direction of the incoming photons.

In Fig. 5.2 we present a detailed picture of the full experimental setup. Important parts of the setup are photographed and presented in Figs. 5.4-5.6, 5.9. In the next sections we study in detail consecutive parts of the setup and explain their properties.

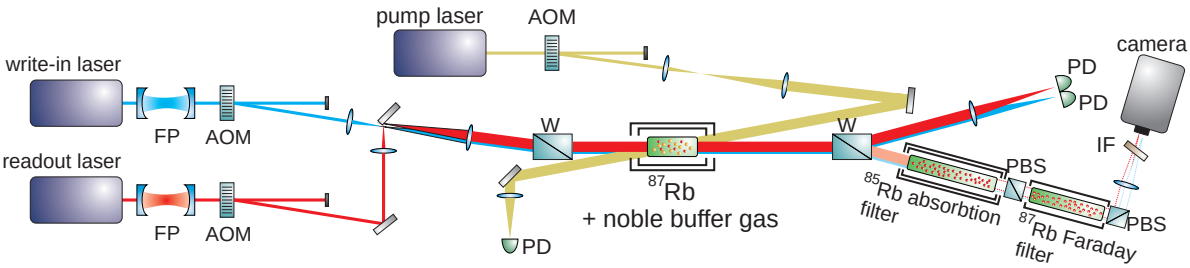


Figure 5.2: Experimental setup. Write and read lasers were spectrally and spatially cleaned with Fabry–Perrot filters (FP). The pulses were shaped by acousto-optic modulators (AOM). A shielded cell with $^{87}$Rb vapors was illuminated by the write, read and pump beam. The far field of the Raman scattering was observed on a camera and the background of the scattering beams was suppressed by polarization and spectral filtering: Wollaston polarizer (W), $^{85}$Rb cell and $^{87}$Rb Faraday filter. An interference filter (IF) separated the spontaneous emission background during the pumping. The pulse sequence was monitored using photodiodes (PD).

## 5.2 Laser system and pulse sequence

In this section we describe driving lasers appearing in the operational sequence in Fig. 5.1(b). Their exemplary frequencies are plotted against $^{87}$Rb levels in Fig. 5.3 although in some experiments frequencies of write and read lasers varied.

**Pump laser** We begin with optical pumping of an ensemble of $^{87}$Rb atoms to the $F = 1$ level. This is accomplished by a pump laser manufactured by Toptica, DL 100. Initially we used a type of distributed feedback (DFB) diode laser; yet, in later experiments we switched to external cavity diode lasers (ECDL).

The wavelength of the laser was set to ca. 780 nm so as to couple the $5^2S_{1/2}$, $F = 2$ state with the Doppler broadened manifold of $5^2P_{3/2}$ excited states, as illustrated in Fig. 5.3(a). The power of the laser entering the cell was up to 70 mW.

We parameterize beam widths by the full width at $1/e^2$. That refers to the double of the commonly used $w$-parameter characterizing the width of the Gaussian beam. The $2w$ diameter of pump beam inside the memory cell varied in experiments from 4 mm up to 18 mm. The typical duration of a pump pulse in the sequence sketched in Fig. 5.3(b) was set to $t_p = 780$ $\mu$s.

The combination of laser power, beam widths and pulse duration ensured bleaching of the medium in the volume where the Raman scattering took place. The pumping efficiency was approximately 98%.

**Write and read lasers** As the lasers driving the Raman scattering processes we use the ECDL DL 100 lasers by Toptica, polarized linearly. We drive spontaneous Stokes transition with the write laser

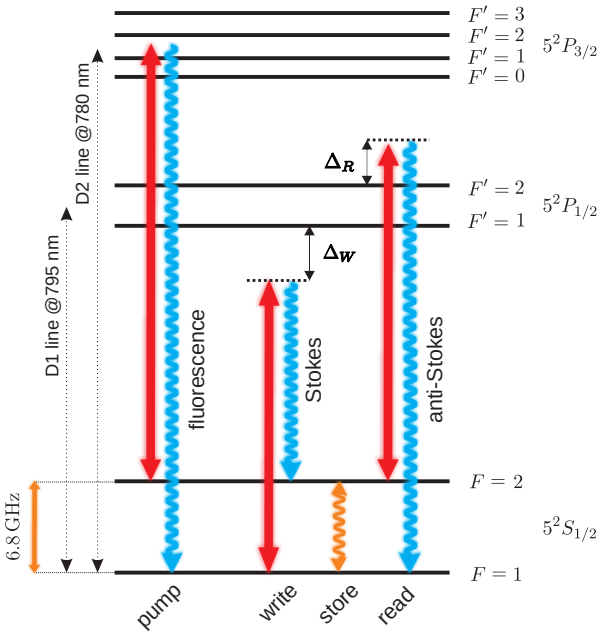


Figure 5.3: (a) Driving lasers and photons frequencies against the $^{87}$Rb energy level structure. At first rubidium atoms are pumped on the D2 line to the $F = 1$ ground level. Then spontaneous Stokes scattering generates collective excitations, stored in the dark for a time $\tau$. Finally the anti-Stokes scattering converts atomic excitations to photons.

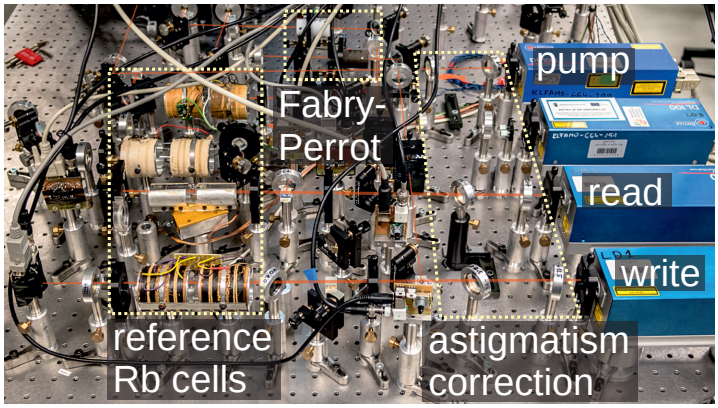


Figure 5.4: Part of the setup for preparing laser beams involves pre-shaping by beams astigmatism correction, setting up frequencies with the aid of reference rubidium cells. Write and read beams were additionally cleaned up with Fabry-Perrot cavities.

detuned from the resonance $F = 1 \rightarrow F' = 1$ typically by $\Delta_W \approx 1$ GHz. Stokes photons close the two-photon transition $F = 1 \rightarrow F = 1$ through a virtual level. The Stokes scattering creates collective excitations that are stored in the dark for a certain adjustable time $\tau$. At the end collective excitations are converted to anti-Stokes photons by sending a read laser pulse. The frequency of the read laser is detuned to the blue from $F = 2 \rightarrow F' = 2$ transition by typically $\Delta_R \approx 1$ GHz.

The powers for Raman driving beams in the cell were up to 20 mW. The $2w$ beam diameters varied in the range from 1 mm to 8 mm.

Usually the write pulse was preceded by a short $\sim 5$ $\mu$s gap after pumping. Then the write laser pulse lasted typically between $t_w = 100$ ns$-10$ $\mu$s. The storage time $\tau$ varied up to several tens of microseconds. Finally the read pulses had a similar duration to that of write pulses $t_r = 100$ ns$-10$ $\mu$s. We applied longer pulses exclusively to study the four-wave mixing process in Sec. 7.3. The specific pulse duration and frequency of the laser will be given along with the description of particular experiments.

**Setting up lasers frequencies** In Fig. 5.4 we present a photograph of the laser system and, in particular, of the reference cells used for frequency settings. The frequencies of the lasers were set with an accuracy < 50 MHz. Although all lasers were equipped with locking systems, such as DAVLL (McCarron *et al.*, 2007) or beat note lock, their frequency was relatively stable within a few hours up to <150 MHz. The stability of the laser frequency was checked by analyzing the beating radio frequency spectrum. The passive frequency stability was sufficient for off-resonant experiments with Raman scattering.

**Beam shaping** The beams from semiconductor laser diodes are typically astigmatic at the beginning. Firstly the shape of all of the laser beams was improved by pairs of anamorphic prisms inside the laser heads. Next, as photographed in Fig. 5.4, the residual astigmatism of beams was corrected with sets of two tilted lenses.

Beams of the write and read laser were additionally filtered spatially and spectrally using Fabry-Perrot cavities with FSR=13.6 GHz seen as part of the setup in Fig. 5.4, photographed in close-up in Fig. 5.5(a). As a result we obtained nearly perfectly Gaussian beams for driving lasers.

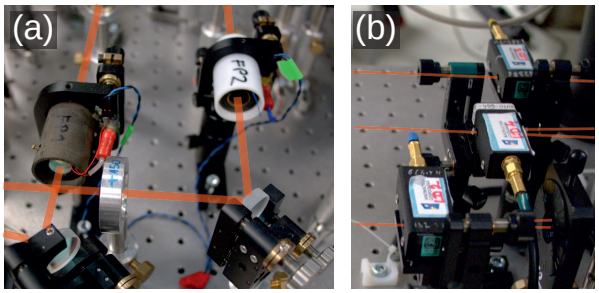


Figure 5.5: (a) Fabry-Perrot cavities used for spatial and spectral filtering of write and read lasers. (b) Nearly rectangular pulses were tailored using acousto-optical modulators.

**Tailoring the light pulses** Subsequently all the three lasers went through acousto-optical modulators (AOM) pictured in Fig. 5.5(b). The first order of diffraction appears only when an acoustic wave with a power of 2 W and a frequency of 80 MHz is passing through an AOM crystal. By that means we tailor nearly rectangular laser pulses of a duration as little as ~100 ns.

**Enlarging and combining beams** The pump beam, enlarged with a telescope sketched in Fig. 5.2, was sent to the main cell. It counter-propagates the other driving beams. Fig. 5.2 depicts the method of overlapping of the write and the read beams. They were combined by approaching their focal spots inside the telescope enlarging the diameter of beams inside the cell. In consequence the read beam was tilted by 13 mrad with respect to the write beam. That resulted in directing the scattered photons onto separate regions of the camera.

## 5.3 Rubidium cell

All the three laser beams enter the main cell with atomic vapors, where the Raman scattering occurs. As the main memory cell we used a cylindrical quartz cell (Precision Glassblowing), 100 mm long and 25 mm in diameter. An exemplary cell abstracted from the system is photographed in Fig. 5.3(a). The cell was filled with almost isotopically pure $^{87}$Rb. The admixture of residual $^{85}$Rb did not exceed 2%. Although in some experiments we used paraffin coating on the cell walls, we did not observe any obvious advantages of such coatings for our setup.

The main cell was additionally filled with noble buffer gas at a pressure of the order of 1 Torr. The specific type of gases with pressures will be given in for particular experiments descriptions. To briefly sum it up, we tested cells filled with neon, krypton and xenon.

The cell was mounted inside a two-layer magnetic shielding suppressing the stray magnetic field below $10^{-3}$ gauss. The shielding is photographed in Fig. 5.3(b). Occasionally we demagnetized the shield to constantly ensure its high performance.

Cells were heated with bifilar wound copper coils in which the current was turned off during laser pulse operation. The atom density in the main $^{87}$Rb cell was tuned by changing the temperature of the cell within the range of $60°C - 100°C$. For instance, the Doppler-broadened optical depth was 135 at $95°C$ . It was estimated by measuring the absorption spectrum for the write laser attenuated to a fraction of saturation intensity right before the cell. The result of such a measurement was fitted with a theoretical model yielding the gas temperature and absorption coefficient in the resonance. We give specific temperatures and optical depths along with the description of specific experiments.

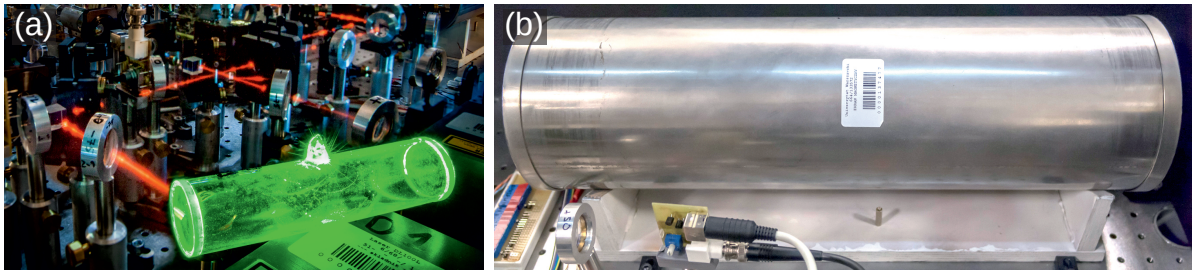


Figure 5.6: (a) Photograph of a $^{87}$Rb cell with buffer gas (artificial illumination) (b) During experiments, the $^{87}$Rb cell is enclosed in double-layer magnetic shielding preventing atoms from decoherence in stray magnetic field.

## 5.4 Filtering system

### 5.4.1 Motivation for filtering

In order to examine the properties of scattered photons, the latter have to be separated from strong driving beams. A typical drive laser pulse of a duration of 5 $\mu$s and a power of 20 mW consists of $4\times10^{11}$ photons, detuned by merely 0.014 nm from the photons to be observed. Therefore we need a filtration system that can damp the driving beams by around $10^{11}$ while keeping high transmittance for the scattered photons that are spatially multimode. The last condition prevents us from using a Fabry-Perrot cavity that is used to this end in single spatial mode setups (Kuzmich *et al.*, 2003; Manz *et al.*, 2007; Bashkansky *et al.*, 2012).

The Raman scattered light has a linear polarization orthogonal to the driving lasers. Thus as the first step of filtration, we apply polarization filtering. Raman scattered photons leave one of the ports of the Wollaston prisms after the main cell, as depicted in Fig. 5.2. The Wollaston prisms have a finite extinction ratio and they let through $10^{-5}$ of the initial laser pulse energies.

As a next step of filtration we utilized a spectral filter using a $^{85}$Rb cell with a high absorption coefficient of the driving lasers and a transmission of Raman-scattered light at the level of 80%. The lines of this filter are broadened magnetically.

In the experiments on single photon level we additionally used a Faraday filter based on the $^{87}$Rb isotope. Not only does the Faraday filter improve the absorption of the driving beams but it also narrows the transmittance spectrum. The latter ability is necessary to damp omnidirectional spontaneous fluorescence directly from the excited state. We have verified that the fluorescence has an intensity proportional both to the concentration of Rubidium and to the buffer gas. That indicates that the fluorescence originates from the collisions of $^{87}$Rb with buffer gas atoms and it is arguably due to the scattering of the laser light by long-lived Rb-buffer gas molecules, as observed in similar systems by Hedges *et al.* (1972). The fluorescence was observed in our setup; likewise it was reported by other groups (Eisaman *et al.*, 2004; Manz *et al.*, 2007; Bashkansky *et al.*, 2012) and described theoretically (Shen, 1974; Rousseau *et al.*, 1975; Raymer and Carlsten, 1977; Childress *et al.*, 2005). Which is noteworthy, the Faraday filter stops the four-wave mixing contribution discussed in detail in Sec. 7.3.

### 5.4.2 Absorption filter

The absorption filter consists of a 30-cm-long rubidium $^{85}$Rb cell. The cell is placed in transverse static magnetic field emitted by ferrite magnets located on both sides of the rubidium cell. By chang-

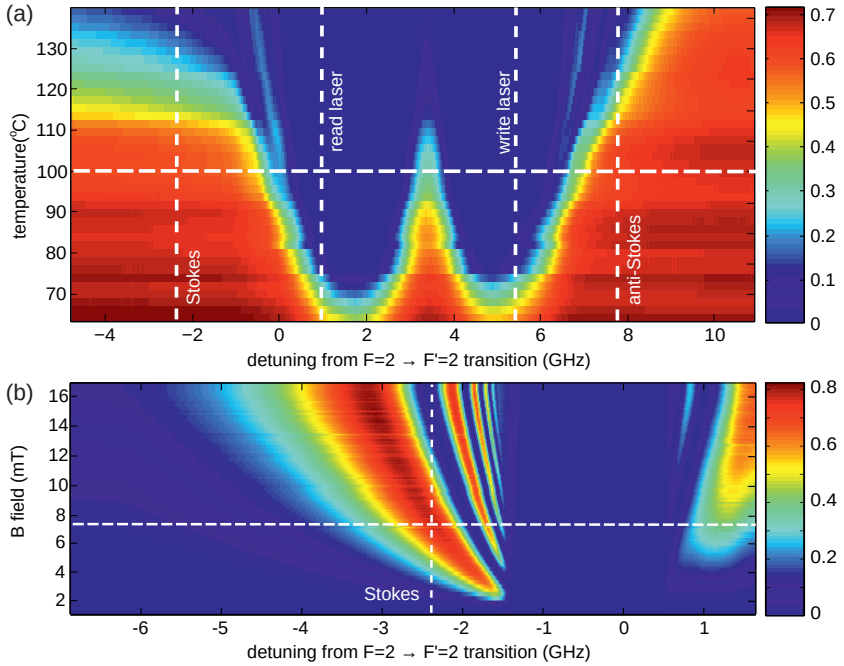


Figure 5.7: Transmission spectra for (a) $^{85}$Rb absorption filter and (b) $^{87}$Rb Faraday filter with exemplary settings marked with white dashed lines. The detuning on the horizontal axis is measured from $F = 2 \rightarrow F' = 2$ transition on the D1-line of $^{87}$Rb. (a) Absorption lines of $^{85}$Rb are significantly broadened due to a transverse magnetic field of approximately $10^{-2}$ T. (b) Exemplary transmission spectra of the Faraday filter zoomed to the vicinity of the $^{87}$Rb $F = 2 \rightarrow F' = 2$ resonance in the cell heated up to $T = 110^{o}$C for different values of the longitudinal magnetic field.

ing the distance between the magnets, we effectively change the magnetic field inside the cell and thence broadening of the line. For our purposes we set the magnetic field to $10^{-2}$ T to move $^{85}$Rb lines close enough to $^{87}$Rb where the driving lasers operate. Moreover, the filter is placed inside the shielding to avoid disturbing the main memory cell operation. Further technical details of the filter construction can be found in Appendix C as well as (Chrapkiewicz and Wasilewski, 2014; Dąbrowski *et al.*, 2015).

The transmission and the width of the filter lines are additionally tuned by changing the temperature of the filter, as presented in Fig. 5.7(a). In practice its operational range is limited to ca. $90^{o}$C – $120^{o}$C to reconcile the absorption of drive lasers with the high transmission of the Raman-scattered light. With this filter we achieved an additional $10^{5}$ factor in damping the driving beams.

### 5.4.3 Faraday filter

We utilize a Faraday filter which consists of two orthogonal polarizers of an extinction of $10^{4}:1$ and a Faraday rotator based on $^{87}$Rb isotope vapors in 30-cm-long cell. We use the standard configuration of the filter reported e.g. in (Zielińska *et al.*, 2012; Kiefer *et al.*, 2014). A unique technical feature of the system is water cooling to compensate the relatively high power emitted by coils generating magnetic field.

The rotation of the polarization occurs in the $^{87}$Rb cell and it is caused by uniform, longitudinal magnetic field tuned up to ca. 20 mT. Magnetic field splits the $^{87}$Rb Zeeman sublevels and thus the orthogonal circular polarizations of light have different refractive indices that change rapidly

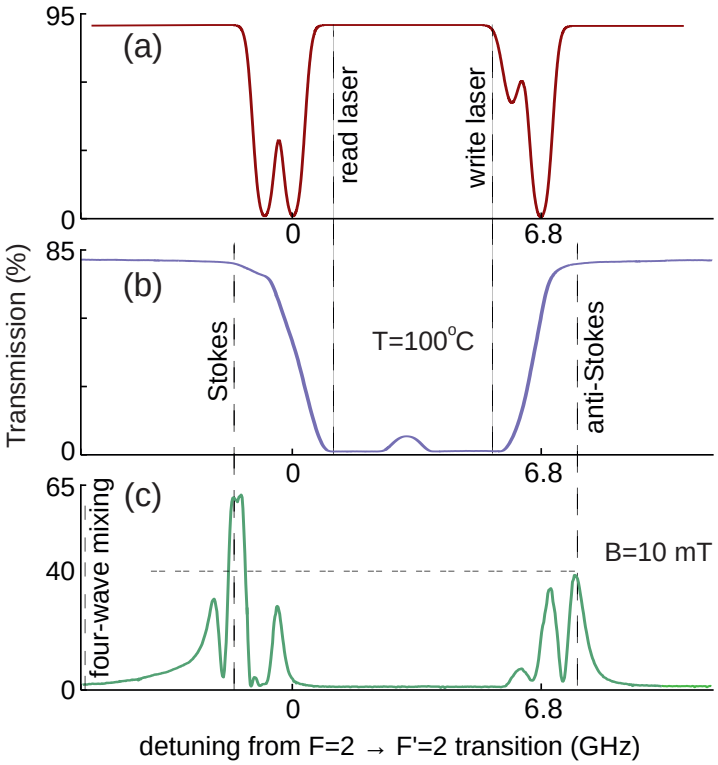


Figure 5.8: Transmission spectra of (a) the main cell with $^{87}$Rb isotope (theory), (b) $^{85}$Rb absorption filter at $T = 100^oC$ in $10^{-2}$ T transverse magnetic field and (c) $^{87}$Rb Faraday filter for the longitudinal magnetic field amplitude 10 mT and temperature $T = 102^oC$. The frequency of the laser beams and scattered Stokes and anti-Stokes light are marked by detunings measured from the $F = 2 \rightarrow F' = 2$ transition on the D1-line in $^{87}$Rb. (c) Additionally we mark the frequency of the contribution from Stokes scattering in readout due to the four-wave mixing process, studied in detail in Sec. 7.3.

near the resonances. In consequence they experience polarization rotation that depends on the frequency. Since the $^{87}$Rb cell is placed in between two orthogonal polarizers, the setup effectively behaves as a tunable spectral filter.

Exemplary transmission spectra are presented in Fig. 5.7(b). We see that an increase in magnetic field shifts a transmission maximum away from the resonance. The peak position of transmission corresponds to 90° of polarization rotation. Next, narrower transmission lines result from the polarization rotation by higher angles: 270°, 450° etc. The transmission lines are also tuned by temperature whose rise effectively detunes them. Further technical details of the filter construction and its properties can be found in (Dąbrowski *et al.*, 2015).

Both the absorption filter and the Faraday filter can be tuned so as to obtain high transmission for Stokes photons and high damping of the driving lasers. Fig. 5.8 presents a sample transmission through all component cells and filters. For instance by properly adjusting the temperature and magnetic field in both filters we are able to attenuate the driving beams by a factor of $10^{11}$ and reach a transmission of 65% for the Stokes and 45% for the anti-Stokes light. As marked in Fig. 5.8(c), the application of the Faraday filter additionally removes the contribution of Stokes scattering in readout discussed in Sec. 7.3.

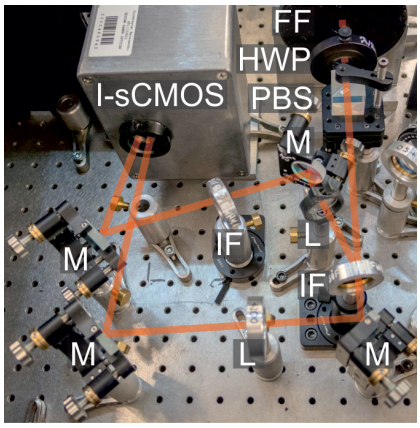


Figure 5.9: Imaging and detection system used in experiments with single photons, where Stokes and anti-Stokes photons emitted near D1 and D2 lines of $^{87}$Rb are separated using interference filters (IF).

## 5.5 Imaging system

**Far field** A camera have been placed in the far field, such as provided by the focal plane of a single cell. In practice to reduce the volume of spreading Raman scattering we used two or three lenses along the optical system. The ABCD matrix (Siegman, 1986) of such system was antidiagonal, additionally ensuring the transformation of the Gaussian beam waists into other beam waists. Accurate calibration of the camera sensor position was performed with a method involving two sparse diffraction gratings presented in detail in (Chrapkiewicz and Wasilewski, 2015).

**I-sCMOS** The ultimate detector used in the setup was an intensified sCMOS camera. Apart from the photon counting mode studied in detail in Part I, the camera was also used for higher illumination levels and lower gains of the image intensifier. In such a mode continuous images were obtained, such as in Fig. 2.5. This figure depicts a granulated, fluctuating image of a circular aperture formed by several thousands of photons. Visible granulation of the image origins from the nonuniform spatial structure of the charge generated in different channels of the microchannel plate. At high illumination levels signals proportional to the mean intensity of incident light can be measured.

In that camera operation mode the signal variance scales as a square of the mean incident intensity and it is significantly higher than the shot noise of the incoming light due to the stochastic nature of the intensification process. Moreover, the images formed at high illumination levels are blurred by phosphor response and the point spread function of the relay lens. This is a typical mode of operation for intensified cameras (such as for night vision) where images of a relatively clear structure are formed at each frame.

**EM CCD** In the early experiments we used an electron multiplying charged couple device (EM CCD) camera manufactured by Hamamatsu, ImageEM. The camera multiplies electrons on each pixel. The statistical properties of the response of the EM CCD camera are similar to those of the I-sCMOS in low-gain mode. The signal variance scales proportionally to the intensity of the illuminating light. That specific model displayed noise that was too high for us to observe single photons. The EM CCD camera provided higher resolution than the I-sCMOS, as there was no blur connected with the finite spread of phosphor flashes. However, its significant disadvantage was the lack of gat-

ing. Light, such as the fluorescence generated upon pumping to illuminate the camera prior to the actual exposure, induced photoelectrons seen as a blur in the eventual picture.

## 5.6 Conclusions

To sum up, we have presented the setup for the experiment where spatially multimode Raman scattering is generated with collective atomic excitations followed by a coherent readout with time-delay in anti-Stokes scattering process. We began with a general overview in Sec. 5.1 and then provided a detailed description of the constituent parts in the successive sections. Subsequently, in Sec. 5.2 we described the lasers settings and in particular their pulse sequence and frequencies against the $^{87}$Rb lines. Next, in Sec. 5.3, the main cell with $^{87}$Rb was described. Then in Sec. 5.4 we studied the details of the filtering system and finally in Sec. 5.5 we focused on the applied imaging and detection system.

The presented setup is conceptually similar to the atomic memory utilized in the DLCZ protocol (Duan *et al.*, 2001), described in Sec. 1.1.3. Systems capable of generating, storing and reading out single spatial modes have already been demonstrated e.g. in Rb atoms (van der Wal *et al.*, 2003; Eisaman, 2006; Bashkansky *et al.*, 2012) or in $H_2$ molecules (Bustard *et al.*, 2013, 2015). However, the presented setup is the first and, to the best of our knowledge, the only atomic memory of DLCZ type with capacity of many spatial modes.

The exclusive multimode capability of our system has been achieved by applying several unique solutions. Firstly, the applied cells filled with $^{87}$Rb with a buffer gas were carefully chosen so as to balance diffusional decoherence with decoherence due to spin-exchanging collisions. A detailed study on this topic is presented in the next Chapter 6. Secondly, the constructed filtering system is characterized by extraordinary performance and provides excellent transmittance for spatially structured photons. We presented a novel solution of the tunable $^{85}$Rb absorption filter (Chrapkiewicz and Wasilewski, 2014; Dąbrowski *et al.*, 2015). The combination with the Faraday filter (Heifetz *et al.*, 2004) provides further control of the transmittance spectrum. The whole filtering system has been described in a recent paper (Dąbrowski *et al.*, 2015). Last but not least, as far as we know, we are the only quantum optics group that uses the I-sCMOS providing both ultra-low-noise single-photon sensitivity, high speed and high spatial resolution. Excellent properties of the camera system described in Part I are confirmed in experimental results further in this part and in Part III.

CHAPTER 6

# SPATIAL PROPERTIES OF RAMAN SCATTERING IN AN ENSEMBLE OF DIFFUSING ATOMS

In this chapter we describe experimental observations of collective Raman scattering. We rely on the previously described theoretical introduction presented in Chapter 1, Sec. 1.5 as well as the setup presented in Chapter 5. Here we restrict ourselves to a high intensity regime where in each run we populate many spin waves by macrospopic excitations.

We start in Sec. 6.1 with explaining the expected results in experimental situation with a finite volume of atomic ensemble as depicted in Fig. 6.1(a). We explain that such a situation leads to spatially multimode scattering. In Sec. 6.2 we present experimental results for spatially mutlimode Raman scattering. Then we study the mean angular dependence and the evolution of Stokes scattering in Sec. 6.3.

Next we focus on the role of thermal motion of atoms at the readout process as visualized in Fig. 6.1(b). Starting from Sec. 6.4 we study decays of atomic excitations caused by diffusional decoherence. In Sec. 6.4 we present a theoretical model whereas in Sec. 6.5 the complimentary experimental observations. Finally in Sec. 6.6 we extract diffusion coefficients of rubidium atoms in different noble buffer gases.

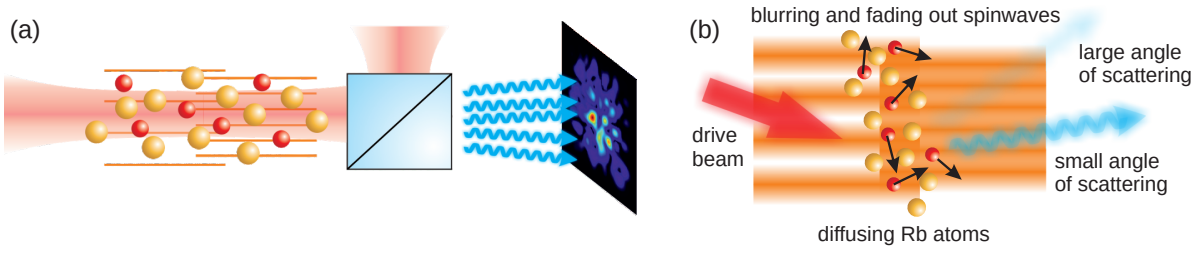


Figure 6.1: (a) Multimode, high-intensity Raman scattering form in single shots speckle patterns observed in the far field. (b) Thermal motion of rubidium atoms in noble buffer gas cause inevitable diffusional decoherence. It blurs the created spin waves and affects the efficiency of scattering at large angles, cf. Fig. 1.10.

## 6.1 Multimode Raman scattering in the high intensity regime

In experiments we deal with beams of a finite diameter. They illuminate a finite volume of atomic ensemble as depicted in Fig. 6.1(a). Thus, we have to extend our description of spatial properties of the Raman scattering started in the introductory Chapter 1, Sec. 1.5. Moreover, here we shall operate in a classical regime with a high number of excitations. The state of the atoms after excitation should be treated as a coherent, classical state introduced in Sec. 1.5.7 .

We assume that the illuminated part of the atomic sample has a pencil shape of a width $w$, set by the write and the read beams, and of a length $L$ directed along the cell axis. Within this volume atomic excitations of the wave vectors $\mathbf{K}$ and $\mathbf{K}'$ differing more than the inverse dimensions of the ensemble volume: $|\mathbf{K}-\mathbf{K}'| > 2\pi[1/w, 1/w, 1/L]$, are distinguishable and independent. Conversely, the excitations of the smaller wave vectors difference are expected to be indistinguishable in a finite volume of an ensemble. This limits the number of independent modes effectively so they may be simultaneously stored in such illuminated ensemble. The indistinguishability of certain spin waves is imprinted on the emitted scattered light. In consequence we expect that the light in the far field should exhibit a finite coherence area. On the other hand the number of independent distinguishable excitations translates to the number of spatial modes of generated light.

One of the possible ways to analyze multimode Raman scattering is to decompose the atomic excitations and light scattered into a pairwise coupled basis (Kołodyński *et al.*, 2012). Then each light mode is coupled with exactly one atomic mode and in each single scattering process we observe populating of certain superpositions of these base spatial modes. In general we can estimate the number of significantly excited modes by the Fresnel number of the write beam $N_{\mathscr{F}} =$

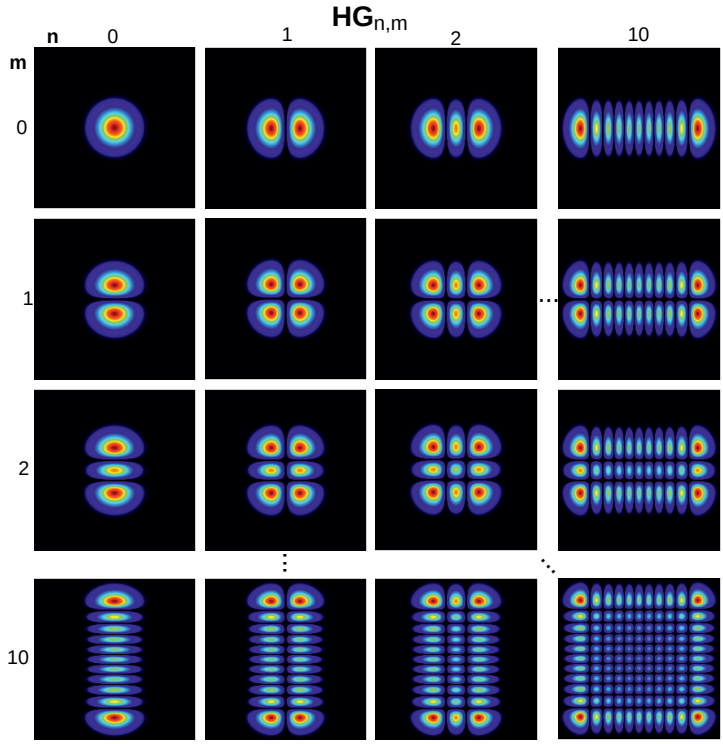


Figure 6.2: Set of Hermite-Gaussian modes that can be used to mimic orthogonal modes specific for high-intensity Raman scattering. See (Pampaloni and Enderlein, 2004) for definitions.

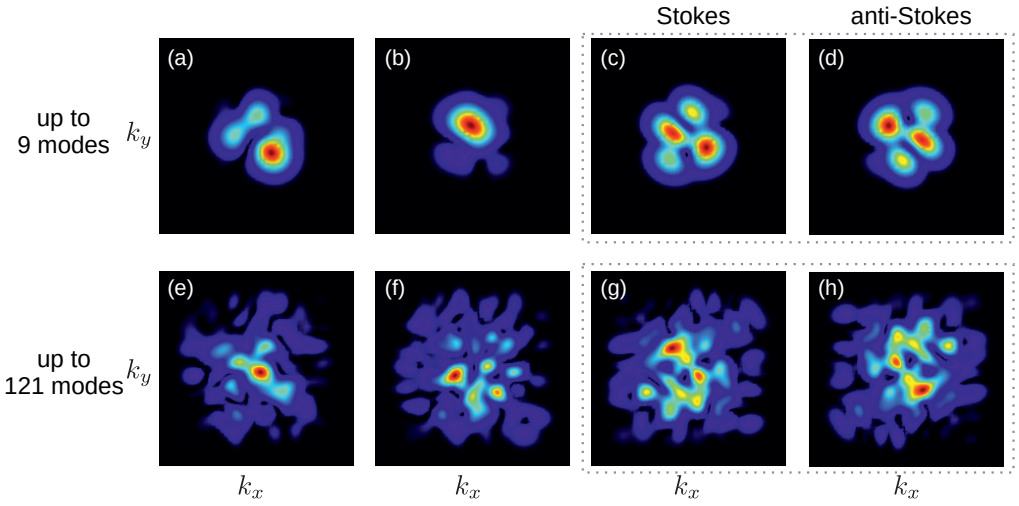


Figure 6.3: Interference of randomly occupied Hermite-Gaussian modes form characteristic speckle patterns that can resemble intensities of Raman scattering in the far field. (a-d) Plots obtained for superposing first 9 HG modes and (e-h) for 121 HG modes, cf. Fig. 6.2. In the last column (d,h) we present expected images for anti-Stokes scattering preceded by (c,g) corresponding Stokes scattering. Scales are the same as in Fig. 6.2.

$|k_w|w^2/(2\pi L)$ if the decoherence is neglected (Raymer and Mostowski, 1981). Exact determination of the set of spin wave modes is a challenging task. It may be performed numerically or analytically only under specific assumptions, such as in a few-photon regime (Kołodyński *et al.*, 2012).

Nonetheless, we can present heuristic analysis that gains insight on the expected high-intensity Raman scattering distributions. In Fig. 6.2 we present an exemplary set of well known Hermite-Gaussian (HG) modes defined in (Kim and Lee, 1999; Pampaloni and Enderlein, 2004), which will be used for illustrating further examples. These light modes are all centered around the write beam while the corresponding spin wave modes are centered around the origin of the **K**-vector space.

During each single realization of the Stokes scattering only certain superpositions are populated. The amplitudes and phases of light in these specific modes are particularly random. As a result we expect to observe a speckle-like diffraction pattern in the far field, as we exemplify in Fig. 6.3, with a set of HG modes[1].

Two rows of plots in Fig. 6.3 illustrate two situations with different numbers of modes taken from the HG basis. From these speckle-like patterns we can infer two qualitative observations. Firstly, the smallest speckle spots have similar size to the central lobes of the highest excited mode. Secondly, the solid angle of the speckle pattern is determined by the highest excited mode of the widest angular spread. Comparing the sizes of the mean angular spread of the scattering pictures with the sizes of speckles on can estimate the number of the excited modes.

Finally in the last column of Fig. 6.3 we visualize the expected anti-Stokes scattering. We anticipate the inverted images of the corresponding Stokes scattering resulting from the phase matching the condition described in Sec. 1.5.5 and depicted in Fig. 1.9(b).

[1] Speckle patterns were computed as modulus square of a sum $I(\mathbf{k}) = |\sum_{n,m} \breve{\alpha}_{n,m} u_{n,m}(\mathbf{k})|^2$, where $u_{n,m}(\mathbf{k})$ denotes othogonal HG modes and $\breve{\alpha}_{n,m}$ are taken as complex variables from the uniform distribution $\arg(\breve{\alpha}_{n,m}) \in (0, 2\pi)$ and $|\breve{\alpha}_{n,m}| \in (0, 1/(n^2+m^2+1))$. The arbitrary choice of modes and probability distributions of their amplitudes yields results corresponding qualitatively to those observed in the experiment.

## 6.2 Generation and delayed retrieval of multimode Raman scattering

### 6.2.1 Experimental conditions

Let us now present an experimental demonstration of the multimode Raman scattering. At first we describe the experimental conditions for these specific measurements. The pump laser was resonant with the $^{87}$Rb D2 line. Its pulse duration 780 $\mu$s and its 4.2 mm full width at $1/e^2$ waist diameter bleached the medium. The write and read peak powers and pulse duration were 17.5 mW, 800 ns and 5 mW, 2 $\mu$s, respectively. Both lasers operated on the D1 line and they were detuned from the $F = 1 \rightarrow F' = 1$ transition by 1 GHz to the red and by 1 GHz from the $F = 2 \rightarrow F' = 2$ transition to the blue for write and read lasers, respectively. Their $1/e^2$ beam diameters were 2.16 mm and 1.76 mm, respectively, and they were tilted inside the main cell by 13 mrad.

The results presented in this section were obtained for a cell filled with 1 Torr of krypton as a buffer gas. The gas temperature was stabilized at 88°C corresponding to a Doppler-broadened optical depth of 130. An interference filter was utilized to cut off the 780 nm spontaneous fluorescence emitted during the initial pumping. The measurements were taken at a speed of 90 Hz by the EM CCD camera whose pixel pitch in the far field corresponded to 76 $\mu$rad angle inside the cell.

To obtain results for this chapter we used only $^{85}$Rb absorption filter. We checked that the laser background was of the order of a few photons in each sequence and it was negligible as compared to the residual fluorescence background signal and the camera noise.

We took the images created by Stokes photons and anti-Stokes photons in the far field measuring distributions of the number of photons $n(\theta_x^{(S)}, \theta_y^{(S)})$ and $n(\theta_x^{(AS)}, \theta_y^{(AS)})$ respectively. In the plane wave model the numbers of photons were directly related with the number of excitations of spin wave modes of a specific k-vector $\mathbf{K}_\perp = |k_s| \times [\theta_x, \theta_y]$.

### 6.2.2 Results

Typical single shots captured by the EM CCD camera are presented in Fig. 6.4. The frames show the speckle pattern of both the Stokes and the anti-Stokes scattering with the highest intensity around the driving beam directions. Single shots of the Raman scattering share some similar features with the model speckles from Fig. 6.3. Moreover, one can see that the anti-Stokes picture is indeed similar to the Stokes one being inverted in relation to the read beam direction. Nonetheless, the retrieved intensities are generally smaller. Moreover, we observe that the speckle features at high angles are apparently cropped.

Further information can be gained from averaging single shots. Fig. 6.5 presents the average of 10,000 frames yielding relatively symmetric Gaussian intensity distributions. The lack of any speckle-like features is due to their entirely random positions in each shot. The angular spread and the mean intensity of the anti-Stokes are significantly smaller than for Stokes scattering. There are consequences of imperfect retrieval efficiency which additionally decreases with the angle of scattering. This problem is studied in detail in Sec. 6.4.

## 6.3 Growth of Stokes scattering

Now we turn to quantifying the evolution of mean Stokes intensities as a function of the write pulse duration $t_w$. Since here we deal with angular symmetry of the obtained mean patterns, we measure the mean number of photons in radial coordinates $n_s(\theta)$, where $\theta = \sqrt{\left(\theta_x^{(S)}\right)^2 + \left(\theta_y^{(S)}\right)^2}$. To obtain

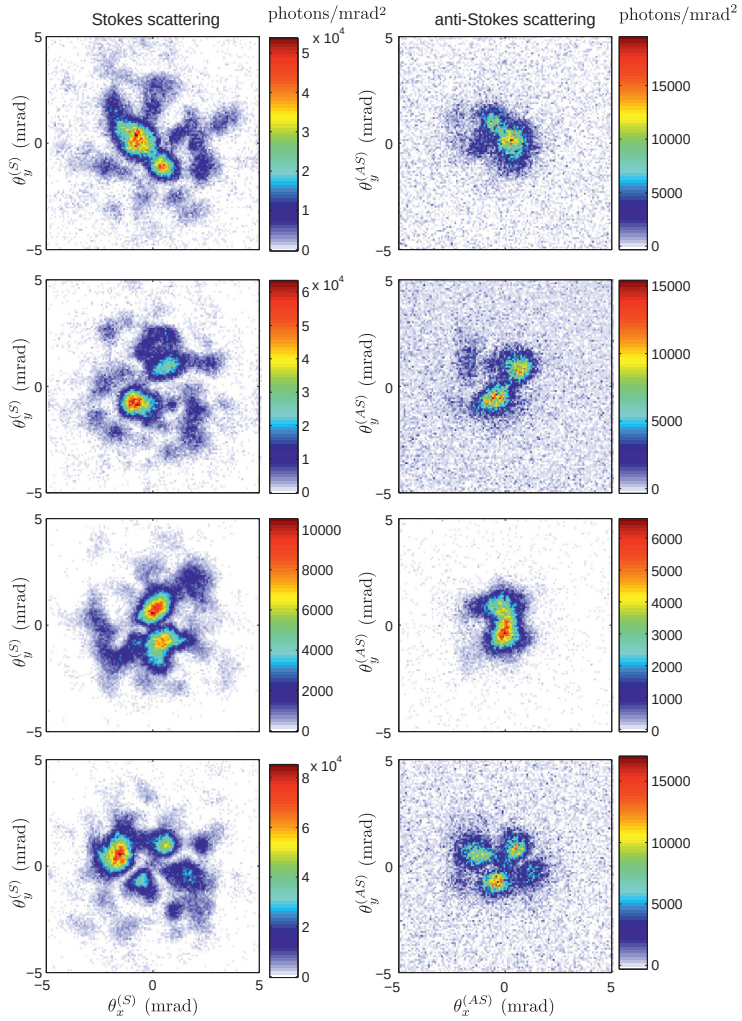


Figure 6.4: In single shots we observe speckle-like pictures of the Raman Stokes (left) and the anti-Stokes (right) scattering intensities. A single speckle comes from an interference between a larger number of spatial modes, similarly to Fig. 6.3. Note that the images for anti-Stokes scattering display similar features but are inverted and cropped. Data collected with cell with 1 Torr of krypton.

$n_s(\theta)$ we perform the averaging over all polar coordinates of two-dimensional distributions of Stokes photons $n(\theta_x^{(S)},\theta_y^{(S)})$, such as that presented in Fig. 6.5(a).

Fig. 6.6(a) shows measurements results of $n_s(\theta)$ for $\theta = 2$ mrad for three different cells, the first two filled with krypton under 1 Torr and 0.5 Torr pressure, and the third filled with neon under 5 Torr pressure. We fitted exponential curves $\exp(\kappa(\theta)t)$+const to the data. We repeated the fitting procedure for all angles $\theta$ and we can present the fitted growth coefficients $\kappa(\theta)$ for the three different cells with the results in 6.6(b).

Apparently the fastest growth is observed for the cell filled with 0.5 Torr of krypton. We note significant difference in the scattering rate between various buffer gases despite comparable density of the atomic sample and write laser power. The differences can be attributed to the decoherence of the excited state due to collisions (Manz *et al.*, 2007). Moreover the growth coefficients decrease with the angle, which can be attributed to the effects of diffusional decoherence studied in next sections.

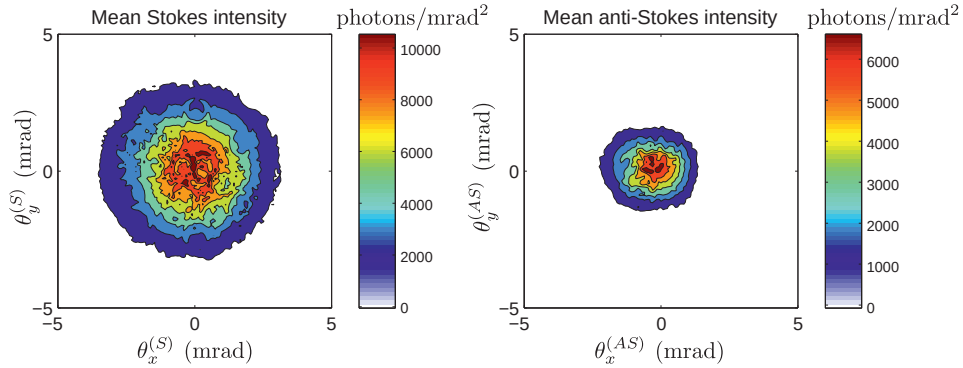


Figure 6.5: The average of the 10,000 of frames as in Fig. 6.4 reveals that the scattering light is emitted symetrically around the direction of the scattering beams placed in the origin of coordinates.

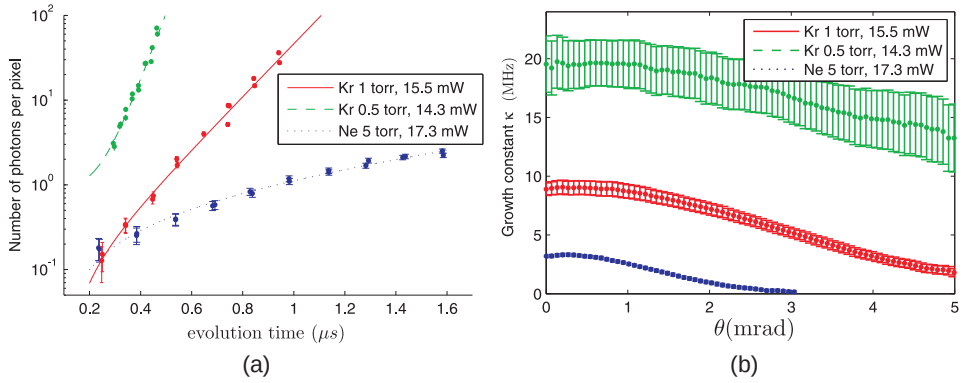


Figure 6.6: (a) Typical growth of the mean intensity of the Stokes scattering $n_s(\theta)$ as a function of the write pulse duration $t_w$ for the scattering angle $\theta = 2$ mrad along with the exponential fit $\exp(\kappa t)$+const. Data taken for three different buffer gasses with similar atomic density. (b) Data points present growth coefficients $\kappa$ as a function of the scattering angle.

## 6.4 Model of diffusional decoherence

### 6.4.1 Blurring of atomic coherence patterns

In this section we introduce a model of diffusional decoherence in the framework of coherent state of atoms introduced in Sec. 1.5.7. Atoms should be treated independently and as uncorrelated, so instead of discussing collective excitations we refer to atomic coherence that is spatially varying. In this formalism the whole process of the Raman scattering can be treated as generation and, after a certain time delay $\tau$, probing patterns of spatially dependent atomic coherence $\rho_{gh}(\mathbf{r})$ between two ground states of rubidium atoms labeled $g$ and $h$ like in the theoretical introduction in Sec. 1.5.

Atomic coherence is initially created in the Stokes scattering process. Since we operate in a spatially multimode regime we create patterns of atomic coherence that comprise many plane-wave components of different periodicities. The atomic coherence decay, due to diffusive motion of the atoms, and the decay rate depend on the periodicity of atomic coherence. In Fig. 6.1(b) we show two exemplary plane-wave components from Fig. 1.10 that suffered blurring due to atomic motion. It can be readily seen from the pictures that patterns of atomic coherence do not change their period but they are blurred with diffusion time.

Atomic coherence can be probed in the anti-Stokes scattering process. Then by measuring the

intensity of the anti-Stokes scattering as a function of the deflection angle we can estimate the amplitudes of certain plane-wave components of spatially varying atomic coherence. Moreover, by adjusting the time between pattern creation and readout, we can calculate the decay rate of different plane-wave components constituting atomic coherence.

We can now formalize the above description. Evolution of atomic coherence in the dark is governed only by the motion of atoms. As an atom moves, its coherence $\rho_{gh}(\mathbf{r}_0)$ at a specific point $\mathbf{r}_0$ reshuffles its values with the neighboring atoms. This effect can be simply described by the diffusion equation with a coefficient $D$ and homogeneous depolarization with a rate $\gamma_0$ (Lowe and Gade, 1967; Glorieux *et al.*, 2012):

$$\frac{\partial}{\partial t}\rho_{gh}(\mathbf{r},t) = D\nabla^2\rho_{gh}(\mathbf{r},t) - \gamma_0\rho_{gh}(\mathbf{r},t). \tag{6.1}$$

This equation can be solved in the Fourier domain:

$$\rho_{gh}(\mathbf{r},t) = e^{-\gamma_0 t}\sum_{\mathbf{K}}\beta(K)e^{-DK^2t}e^{i\mathbf{K}\cdot\mathbf{r}}. \tag{6.2}$$

The solution of the diffusion equation justifies our initial observation from Fig. 6.1(b) that diffusional blurring does not change the periodicity of a specific component, whereas it rather decreases its amplitude. Specifically the evolution of each plane-wave component of initial amplitude $\beta(K)$ and wave vector $K$ decreases exponentially at a rate $\gamma(\mathbf{K}) = \gamma_0 + DK^2$. As long as we deal with position-independent homogeneous depolarization with a rate $\gamma_0$, the measurement of decay rates $\gamma(K)$ is a sound basis for determining diffusional coefficients $D$ as the quadratic term of $\gamma(K)$.

### 6.4.2 Practical retrieval of diffusion coefficients

Although spatially varying atomic coherence $\rho_{gh}(\mathbf{r})$ in each shot is random, the average modulus square of the excitation amplitude $\langle|\beta(K)|^2\rangle$ can be kept constant between in a measurement series under the same experimental conditions. Therefore, we can calculate the average intensity of the light scattered at a certain angle $\theta = K/k_{\mathrm{AS}}$, where $k_{\mathrm{AS}}$ is the wave vector component of anti-Stokes light. By averaging out Eq. (6.2) for a given storage time $\tau$ we obtain:

$$\langle I_{\mathrm{AS}}(\theta = K/k_{\mathrm{AS}},\tau)\rangle = \eta(K)\langle|\beta(K)|^2\rangle e^{-2\gamma(K)\tau}, \tag{6.3}$$

where $\eta(K)$ is the efficiency of readout which can depend on $K$ in general.

The mean intensity of anti-Stokes scattering decays with the diffusion time $\tau$ as $e^{-2\gamma(K)\tau}$. This is the only time-dependent factor in Eq. (6.3) and it can be readily extracted from the measurements data taken for the successive $\tau$. In this way we can obtain decay rates $\gamma(K)$ for a specific angle of observation $\theta = K/k_{\mathrm{AS}}$.

Further analysis for many angles of observation will allow us to single out a diffusional coefficient $D$ in a quadratic dependence of decay rates $\gamma(K) = \gamma_0 + DK^2$. Since the Raman scattering is angularly broad, as e.g. in Fig. 6.4, in each measurement we obtain many points corresponding to a broad span of $K$ vectors. In particular it does not require any alteration in the system and in consequence the vertical axis of dependence $\gamma(K)$ can be determined very accurately.

Summing up the procedure, diffusional coefficients can be obtained by varying only one parameter: the diffusion time $\tau$. Data analysis requires three straightforward steps: averaging, exponential fit and eventually quadratic fit which makes the whole procedure relatively quick and simple to perform.

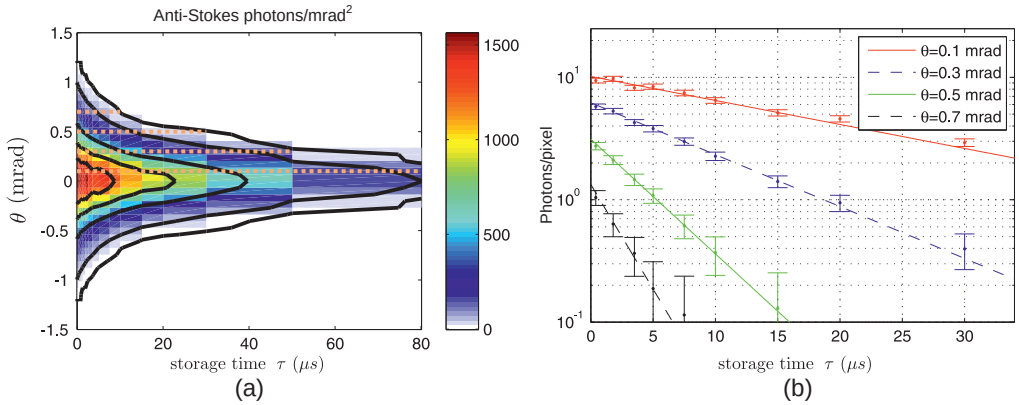


Figure 6.7: (a) Map of the mean number of photons in the anti-Stokes scattering process per EM CCD pixel $\langle I_{\mathrm{AS}}(\theta,\tau)\rangle$ as a function of the storage time $\tau$ and angle of observation $\theta$. Data taken for a cell with xenon at 1 Torr. The black contour lines show levels of 1200, 800, 400, 50, 10 photons per pixel successively. Dashed lines are plotted separately in (b) with exponential decay fits observed for four different angles $\theta$. The decays are visibly faster for higher scattering angles.

### 6.4.3 Influence of the readout with a finite beam width

In the experiment we use the finite size $w$ of the driving laser beam in anti-Stokes scattering that comprises of many plane wave components by itself. This limits effectively the resolution in probing a wave vector space of atomic coherences.

In consequence the angular spread of a read laser beam is transferred onto the angular distribution of the scattered light. In fact for a specific angle of observation $\theta = K/k_{AS}$ we detect scattered light originating from several distinct Fourier components of the atomic coherence pattern. In practice the original decay rate function $\gamma(K)$ is convoluted with a Gaussian function of the width $\sigma$ corresponding to the wave vector $K$ spread to be of the order of the inverse of the driving laser beam size $1/w$. As a result of such convolution we observe an overall increase in the decay rates:

$$\gamma_{\mathrm{obs}}(K) = (\gamma_0 + 2D\sigma^2) + DK^2. \tag{6.4}$$

It is noteworthy that the quadratic dependence on $K$ does not change after the convolution. The sole consequence of a finite beam width is the increase in the constant term in decay rates. To measure the diffusional coefficients we have to ensure that the term $2D\sigma^2$ is small as compared to $DK^2$.

## 6.5 Observation of spin wave decays

### 6.5.1 Experimental conditions

As compared to the results presented in Sec. 6.2 and 6.3 we slightly changed the beam parameters and used different cells. Beam diameters $1/e^2$ and powers of the write and read lasers were 5 mm, 4 mm and 16 mW, 7 mW respectively. The buffer gases used for these measurements were as follows: neon at the pressure of 2 Torr, krypton at 0.5 Torr and 1 Torr and xenon at 1 Torr. The cells temperature were stabilized at 70° C corresponding to an optical depth of 40 and a concentration of rubidium atoms $n = 10^{12}$ cm$^{-3}$.

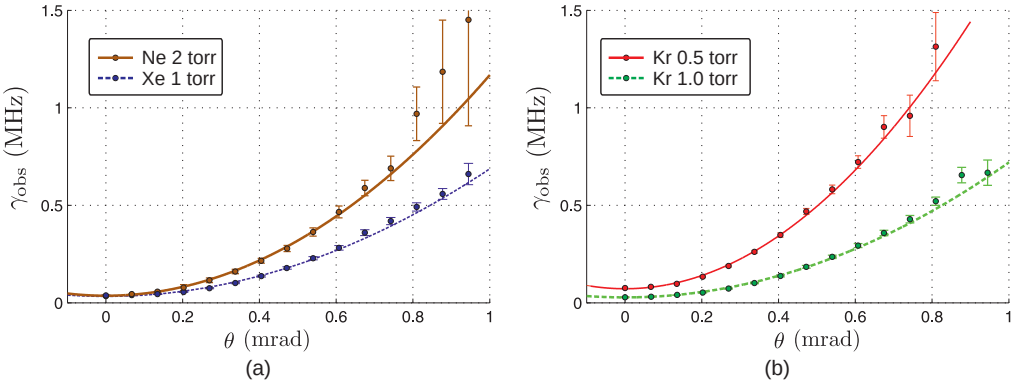


Figure 6.8: Observed decoherence rates $\gamma_{obs}(\theta)$ as a function of the scattering angle corresponding to the atomic coherence wave vectors $K = 2\pi\theta/\lambda$. We fit the data with the quadratic dependence $\gamma_{obs}(\theta) = \gamma_{0,obs} + D\theta^2(2\pi/\lambda)^2$. The quadratic term of the fit yields the diffusion coefficient $D$. Data taken for (a) 1 Torr of xenon and 2 Torr of neon and (b) for krypton at different pressures: 0.5 Torr and 1 Torr.

We repeated the write-store-read sequence multiple times and recorded random patterns of anti-Stokes scattering like in Fig. 6.4. For each cell and each storage time $\tau$, we averaged out 500 images of anti-Stokes scattering, each time obtaining smooth symmetric profiles such as in Fig. 6.5. Moreover, we subtracted the averaged background with e.g. residual spontaneous fluorescence signal taking images for write and read beams turned off but with the pump laser on. Similarly tothe Stokes growth study we additionally averaged data over the polar angle. Eventually we obtained average scattering intensity $\langle I_{AS}(\theta,\tau)\rangle$ as a function of angle $\theta$ and storage time $\tau$.

### 6.5.2 Results

In Fig. 6.7 we study the data obtained for a cell filled with 1 Torr of xenon. Fig. 6.7(a) presents a map of averaged angular profiles of anti-Stokes scattering $\langle I_{AS}(\theta,\tau)\rangle$ a function of the azimuthal angle $\theta = K\lambda/2\pi$ and storage time $\tau$, where $\lambda = 795$ nm. Remarkably we see a noticeable readout signal up to 80 $\mu$s of the storage time.

In Fig. 6.7(b) we plot an average number of photons as a function of the storage time $\tau$ for several chosen values of $\theta$ that are marked with dashed lines in Fig. 6.7(a). As we expected, the decays are significantly faster for higher angles of scattering. The error bars in Fig. 6.7 correspond to one standard deviation uncertainty. Remarkably, the data perfectly follows exponential decays providing a sound basis for studying decay rates for a whole span of wave vectors $K$.

## 6.6 Determination of diffusion coefficients for rubidium in noble buffer gases

### 6.6.1 Diffusional coefficient for specific experimental conditions

We can now proceed to the analysis of the decays rates $\gamma_{obs}(\theta)$ as a function of the deflection angle $\theta$. In Fig. 6.8 we gathered decay rates for the four cells. The data was obtained from the exponential fits as described in Sec. 6.5 and the error bars stand for one standard deviation confidence bound obtained from the exponential fits. Apparently the fits were less accurate for higher-noise signals at high angles of observation.

The decay rates fit the quadratic dependence $\gamma_{\mathrm{obs}}(\theta) = \gamma_{0,\mathrm{obs}} + D\theta^2(2\pi/\lambda)^2$ very well. From the quadratic fits we obtained the diffusion coefficients. In Tab. 6.1 we summarize the fitted values from the exponential decay rates from plots in Fig. 6.8.

| Buffer gas | Pressure (Torr) | $D$ (cm$^2$/s) | $\gamma_{0,\mathrm{obs}}$ (kHz) |
|---|---|---|---|
| Ne | 2 | 91 ± 11 | 38 |
| Kr | 0.5 | 136 ± 9 | 71 |
| Kr | 1 | 57.5 ± 3 | 28 |
| Xe | 1 | 52 ± 3 | 33 |

Table 6.1: Fit parameters yield diffusional coefficients $D$ specifically for the measured cells. Temperature of vapors was set to 70° C .

The diffusion coefficients for krypton cells scaled with the inverse of the nominal pressure values. The uncertainty for the quadratic fits lay in the range of 5-12%, depending on the cell. We verified the found values of $D$ by repeating measurements in different conditions. For instance, we changed the amount of the generated light by altering the writing laser pulse duration and by repeating measurements at different temperatures. The different test yielded consistently the presented values of $D$ and indicated that the errors originated from a slight beam wander, laser power and frequency fluctuations and a small drift of the cell temperature.

To further verify the accuracy of our results and correctness of the model, we carried out reference measurements for krypton at 1 Torr. We aimed at verifying the formula Eq. 6.4 by performing measurements with the use of the write and read beams reduced ca. 3 times. The eventual beam diameters at $1/e^2$ intensity levels were set to 1.6 mm and 1.4 mm respectively. Since the spread of beam wave vectors was significantly higher, the measurements were less accurate. The obtained diffusion coefficient measured lay within the range of 40 cm$^2$/s to 65 cm$^2$/s, which, nevertheless, is consistent with other results .

What is more, the observed decay rate at $K = 0$, $\gamma_{0,\mathrm{obs}}$ listed in the last column of Tab. 6.1 is dominated by excessive contribution due to the finite read beam size, $2D\sigma^2$ in Eq. (6.4). We can state that by quantifying all of the other sources of homogeneous decoherence. We estimate ca. 1.5 kHz of the decay rate due to Rb-Rb collisions and contributions to be smaller than 150 Hz from Rb – buffer gas collisions, based on respective collisional cross-sections (Franz, 1965). Moreover we estimate the decoherence rate by dephasing of atoms in a stray magnetic field due to imperfect shielding to be smaller than 1 kHz.

### 6.6.2 Normalized diffusion coefficients

Having learnt the pressures and the temperatures of the cells, we can normalize the diffusional coefficients to make them comparable and potentially useful for other research. The standard way of normalizing diffusional coefficients is to give them at atmospheric pressure and at 0° C using the standard approximated[2] formula (Hogervorst, 1971; Happer, 1972):

$$D_0 = D\Big(\frac{P}{760\ \mathrm{Torr}}\Big)\sqrt{\frac{T_0}{T}}, \tag{6.5}$$

where $P$ stands for the gas pressure at $T_0 = 0°$C, and $T$ is the temperature upon measurement. Since the temperature is known with good accuracy, the significant contribution to uncertainty of $D_0$ re-

[2]A stricter scaling in a wide range of temperatures and pressures can be found with Chapman-Enskog theory, cf.(Chapman and Cowling, 1991).

sults from the inaccuracy of gas pressure value in cells. It is specified by the manufacturer as 10%. Another source of error is the spread of the measured $D$ values. The normalized diffusion coefficients are presented in Tab. 6.2.

| Buffer gas | $D_0$(cm$^2$/s) – this paper | $D_0$(cm$^2$/s) - previous results |
|---|---|---|
| Ne | 0.20±0.02 | 0.11 (Shuker *et al.*, 2008), 0.18 (Vanier *et al.*, 1974), 0.31 (Franzen, 1959; Arditi and Carver, 1964), 0.48 (Franz, 1965) |
| Kr | 0.068±0.006 | 0.1 (Bouchiat, 1972) 0.04 (Higginbottom *et al.*, 2012) |
| Xe | 0.057±0.007 | No experimental data |

Table 6.2: Measured diffusion coefficients of rubidium atoms in noble buffer gases: Ne, Kr, Xe. The results are normalized to 0°C and 760 Torr . These values were later confirmed independently by another method by Parniak and Wasilewski (2013).

We juxtaposed our coefficients with the data published previously. Our results are consistent with the diffusional coefficients obtained beforehand. Let us note that most of the previously known data were obtained by obsolete methods with laser technology only just emerging. Moreover, those methods were intrinsically more complicated e.g. they had several fit parameters. Noticeably, the previous methods did not even allow measurement of the diffusional coefficients for rubidium in xenon due to their relatively big spin exchange cross-section (Franz, 1965; Bouchiat, 1972; Bhaskar *et al.*, 1982). Thus, we have been the first to present measurements for xenon and to provide the most recent accurate results for other gases. Remarkably the accuracy of the presented data was independently confirmed later in measurements using a different method (Parniak and Wasilewski, 2013).

## 6.7 Conclusions

In conclusion, we demonstrated the generation of spatially multimode Raman scattering. The Stokes scattering was obtained together with collective excitations that were retrieved coherently after an adjustable time delay in the anti-Stokes scattering process. That has been the first experimental demonstration of such a phenomenon. Moreover, we studied the mean evolution of Stokes scattering and decays of anti-Stokes scattering governed by diffusional decoherence. Results have been published in papers (Chrapkiewicz and Wasilewski, 2012; Chrapkiewicz *et al.*, 2014b).

At first, in Sec. 6.1, we explained how a finite volume of atomic ensembles led to the scattering process occurring independently in many spatial modes of light and atomic excitations. Then, we showed how interference of many spatial modes led to speckle patterns that could be observed in the scattering processes. In Sec. 6.2 we presented experimental results and we showed the single shots of high-intensity Raman scattering. The images of anti-Stokes scattering retrieved with a time delay exhibited similar inverted spatial structure to the corresponding Stokes scattering images.

Next, we characterized the evolution of the mean Stokes scattering in Sec. 6.3. We measured the exponential growths of Stokes scattering, which qualitatively agreed with theoretical models (Raymer, 2004). Then we performed studies for different buffer gases and studied the angular dependence of the growth. Our results indicated that the Stokes scattering growth was dominated by the evolution of the fundamental most occupied mode.

The presented results confirm that we are able to store and retrieve spatially varying atomic excitations coherently. They open a way for investigations in a single photon regime, which are studied in the next chapter.

Thereafter, we proceeded to study diffusional decoherence of collective excitations. In Sec. 6.4 we presented a simple theoretical model describing decays of spatially varying atomic coherence in an ensemble of diffusing atoms. Then in Sec. 6.5 we presented corresponding experimental results which agreed with the introduced model. The careful study of diffusional decoherence provided a novel method for measuring diffusion coefficients of atoms tailored to atomic memory applications. Basing on directional characteristics we singled out contribution of the diffusion to the overall decoherence in any given cell without prior knowledge of other decoherence mechanisms. In Sec. 6.6 we extracted diffusion coefficients of rubidium in neon, krypton and xenon. In particular we have been the first to present the data for xenon.

The presented results are of particular relevance to many setups. The diffusion is the main limiting factor for storage times in our memory, as well as in other setups, such as memories using electromagnetically induced transparency (Matsko *et al.*, 2001; Fleischhauer *et al.*, 2005; Eisaman *et al.*, 2005), gradient echo memory (Hosseini *et al.*, 2009, 2011) or broadband Raman memories (Reim *et al.*, 2011; Michelberger *et al.*, 2015). Furthermore, the results turned out to be useful for widefield micowave imaging in rubidium vapors (Horsley *et al.*, 2015) and can be applied in experiments with hyperpolarized xenon (Fink *et al.*, 2005), where no experimental data for diffusion coefficients had been known prior to our research.

CHAPTER 7

# SPATIAL CORRELATIONS BETWEEN STOKES AND TIME-DELAYED ANTI-STOKES PHOTONS

This chapter is devoted to the study of spatial correlations between Stokes and time-delayed anti-Stokes photons. The main experimental results of Part II ultimately prove that our system has the capability of storing spatially varied information about the direction of the scattered photons. We perform experimental demonstrations starting from large number of photons ending up in the single-photon-level regime.

We begin in Sec. 7.1 by demonstrating the intensity correlations for macroscopic light generated in Stokes and anti-Stokes light. In Sec. 7.2 we estimate the number of independent spatial modes in Stokes and anti-Stokes scattering and we study their storage times. In Sec. 7.3 we investigated the four-wave-mixing process that contributes to correlation maps and it is inevitably present at the readout stage. Correlation maps are used to find efficiencies of readout and four-wave mixing in Sec. 7.4. Finally, Sec. 7.5 shows the results of spatial correlations in Raman scattering obtained using spatially resolved photon counting methods. We calculate $g^{(2)}$ cross correlation maps, quantify the number of the stored modes as well as we reach the single photon level where each spin wave mode is typically occupied by around one excitation.

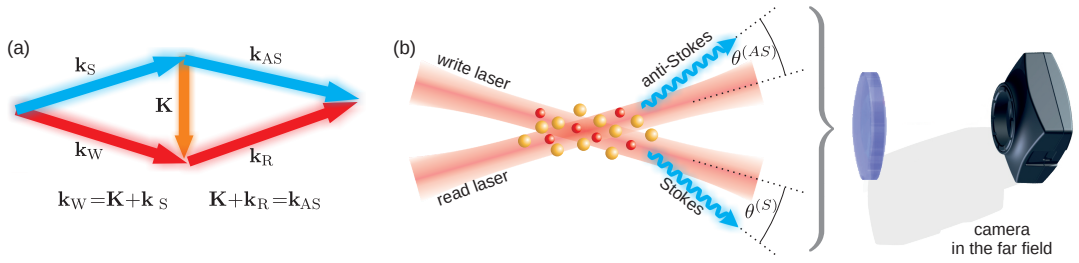


Figure 7.1: (a) Phase matching condition relating wave vectors of driving beams, $\mathbf{k}_W, \mathbf{k}_R$ with Stokes $\mathbf{k}_S$ and time-delayed anti-Stokes scattering $\mathbf{k}_{AS}$ mediated by a spin wave atomic excitation of the wave vector $\mathbf{K}$. (b) In the experiment we observe scattered photons deflected from directions of the write and read lasers by the opposite angles. Directions of filtered photons are angularly resolved in the far field camera detection system.

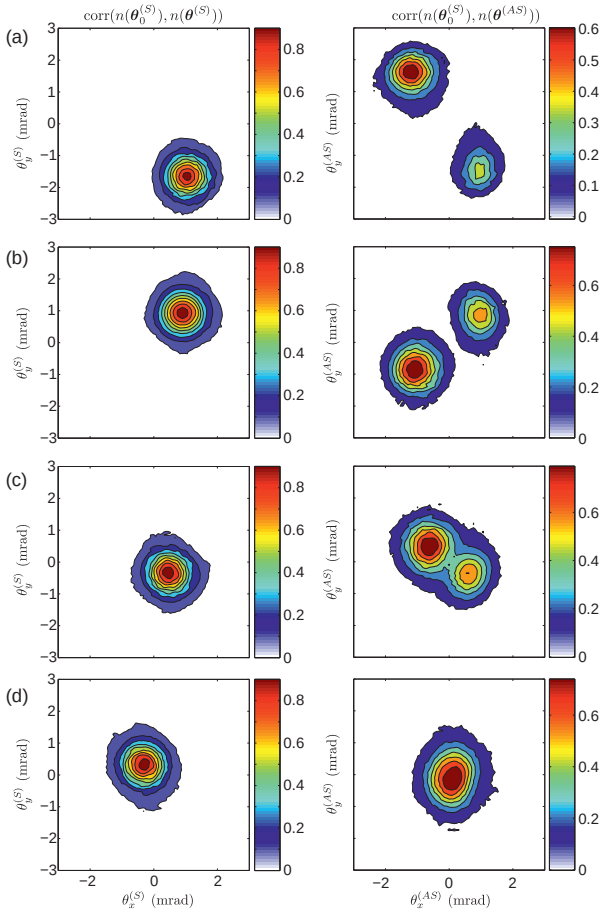


Figure 7.2: Normalized intensity correlation functions $C_{\mathrm{S,S}}(\theta_x,\theta_y;\theta'_x,\theta'_y)$ (left pane) and $C_{\mathrm{A,S}}(\theta_x,\theta_y;\theta'_x,\theta'_y)$ (right pane) between a fixed direction in the Stokes $\theta'_x,\theta'_y$ scattering and any other direction $\theta_x,\theta_y$ in the Stokes and anti-Stokes scattering, respectively. The reference direction $(\theta'_x,\theta'_y)$ mrad corresponds to a point in the center of the spot in the Stokes self-correlation function $C_{\mathrm{S,S}}$ in the left pane. The center of the best correlated spot corresponds to the conjugate direction of the counterpart beam $(\theta_x,\theta_y) = -(\theta'_x,\theta'_y)$. Contours were drawn at the levels 0.1, 0.2 up to 0.9. Results obtained in a cell with Kr buffer gas at 1 Torr.

## 7.1 Intensity correlations between Stokes and anti-Stokes scattering

In the previous Chapter 6 we studied single shots and the means of the Stokes and anti-Stokes scattering. The results indicated clearly that we were able to retrieve light from the ensemble in the anti-Stokes scattering that was conditioned on the previous Stokes scattering process. Nonetheless, as we will show in this chapter, we can extract much more information from that data.

As we indicated in the introduction in Sec. 1.5, we expect that photons scattered in those two time-separated processes, write-in and readout, should exhibit directional correlations dictated by the phase matching condition and as summarized in Fig. 7.1(a). In consequence, as we sketch in Fig. 7.1(b), we expect that a Stokes scattered photon deflected by the angle $\theta^{(\mathrm{S})}$, creates a spin wave, that devolves its wave vector to the anti-Stokes photon. As a result, the anti-Stokes photon will be deflected from the read beam by the inverted angle $\theta^{(\mathrm{AS})} = -\theta^{(\mathrm{S})}$. This inference holds true also for high photon number regime, as well as it can be generalized on a real experimental scenario with a finite number of mode discussed in Sec. 6.1.

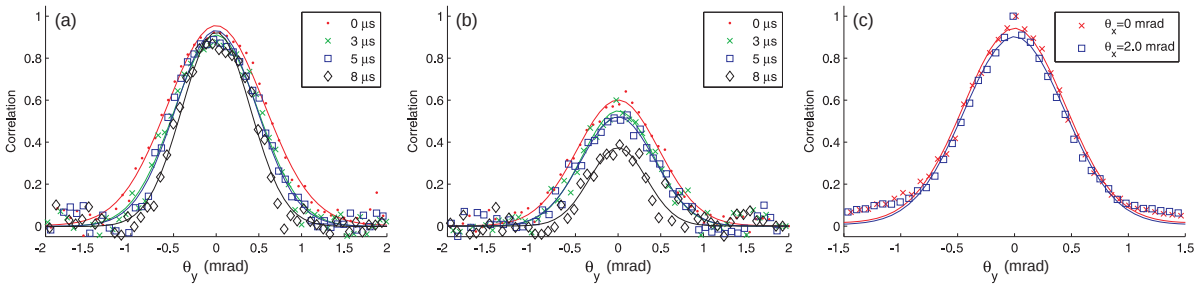


Figure 7.3: Sections of the intensity correlation functions $C_{\mathrm{S},i}(\theta_x,\theta_y;\theta'_x,\theta'_y)$ along $\theta_y$. Cross-correlation $C_{\mathrm{A,S}}$ for (a) $\theta'_x=\theta'_y=\theta_x=0$ and (b) $\theta'_x=-\theta_x=0.7$ mrad, $\theta'_y=0$ calculated for subsequent storage times $t_s$ =0, 3, 5, 8 $\mu$s. (c) Self-correlation $C_{\mathrm{S,S}}$ for $\theta'_x=-\theta_x=0$, 2 mrad, $\theta'_y=0$. The points correspond to experimental data, while the lines correspond to the Gaussian fits.

We begin the presentation of the results with extensive analysis of the experimental results presented in Sec. 6.2. To further analyze the spatial properties of the Raman scattering we calculate the statistical correlation of intensity fluctuations between portions of the scattered light. Here we use an ordinary correlation coefficient known from the statistics, related to celebrated measurements by Hanbury Brown and Twiss (1956). The correlation coefficient is defined for photon number measured in the far field around two angles of coordinates $\boldsymbol{\theta}=(\theta_x,\theta_y)$ and $\boldsymbol{\theta}'=(\theta'_x,\theta'_y)$:

$$C_{\mathrm{S},i}(\boldsymbol{\theta},\boldsymbol{\theta}')=\frac{\langle\Delta n_{\mathrm{S}}(\boldsymbol{\theta})\Delta n_i(\boldsymbol{\theta}')\rangle}{\sqrt{\langle(\Delta n_{\mathrm{S}}(\boldsymbol{\theta}))^2\rangle\langle(\Delta n_i(\boldsymbol{\theta}'))^2\rangle}}, \tag{7.1}$$

where the indices $i=\mathrm{S,A}$ refer either to Stokes or to anti-Stokes photons, whereas $\Delta n_i(\boldsymbol{\theta})=n_i(\boldsymbol{\theta})-\langle n_i(\boldsymbol{\theta})\rangle$ denotes deviation of the photon number from its mean. The signal proportional to photon numbers $n_i(\boldsymbol{\theta})$ is measured on single pixels of EM CCD camera described in Sec. 5.5.

In Fig. 7.2 we show maps of correlation coefficients $C_{\mathrm{S},i}(\boldsymbol{\theta},\boldsymbol{\theta}')$ for four fixed angles $\boldsymbol{\theta}'$ . We depict maps of correlation coefficients as a function of vectorized angle $\boldsymbol{\theta}$ displayed as $C_{\mathrm{S,S}}$ for Stokes, left pane on coordinates $(\theta_x^{(\mathrm{S})},\theta_y^{(\mathrm{S})})$ and as $C_{\mathrm{S,AS}}$ for anti-Stokes in coordinates $(\theta_x^{(\mathrm{AS})},\theta_y^{(\mathrm{AS})})$.

The spots seen on the left panes in Fig. 7.2 represent the correlation between Stokes light emitted in similar directions. The center of the spots correspond to the fixed angle $\boldsymbol{\theta}'$ with respect to which the correlations have been computed. The highest spots in the anti-Stokes right panes correspond to a counter part correlated anti-Stokes light. The position of the centers of $C_{\mathrm{S,AS}}$ highest spots are as expected from the phase matching condition depicted in Fig. 7.1(a), i.e. on the opposite side of the driving beam direction.

In the anti-Stokes–Stokes correlation pane Fig. 7.2 we can see another, weaker correlation spot centered around direction corresponding to the direction of Stokes scattering. It originates from further Stokes scattering induced by the read beam. This process is studied in detail in Sec. 7.3 and in this section we shall focus on pure anti-Stokes scattering exclusively.

Furthermore, we see that sizes of the spots in the correlation maps are similar. The size of the correlation spot is proportional to the size of a speckle in the single shot image Fig. 6.4. Since the correlation value at each point originates from many independent displaced speckles, the correlation spot will be the convolution of the speckle shape with itself. As a result, the width of the correlation spot is enlarged by the factor $\sqrt{2}$ calculated for the Gaussian function cross-sections.

In Fig. 7.3 we analyze the cross-sections through correlation functions along with well-fitting Gaussian functions. In the first two panes Fig. 7.3(a) and Fig. 7.3(b) we compare the anti-Stokes–Stokes correlation functions $C_{\mathrm{S,AS}}(\boldsymbol{\theta},\boldsymbol{\theta}')$ for $\boldsymbol{\theta}'=(0,0)$ mrad and for $\boldsymbol{\theta}'=(0.7,0)$ mrad measured after

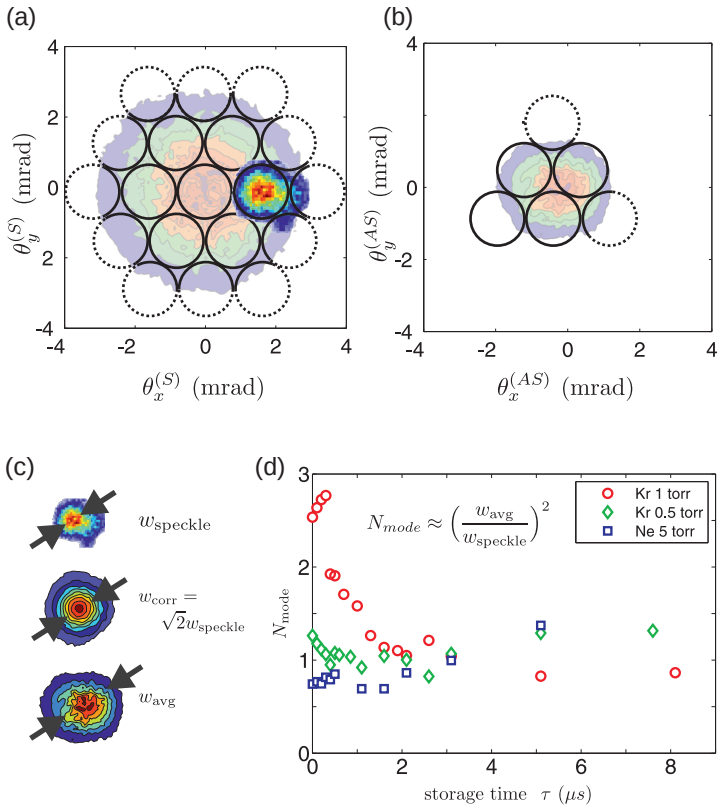


Figure 7.4: Approximate number of modes in the anti-Stokes scattering $N = (w_{\mathrm{avg}}/w_{\mathrm{speckle}})^2$ as a function of storage time.

different storage times up to 8 $\mu$s. We observe subtle angular narrowing for the first case and significant decreasing in the latter case due to a strong influence of diffusional decoherence. What is noteworthy, the width of the correlation of Stokes scattering with itself remains unchanged for different angles of the reference $\boldsymbol{\theta}'$, as depicted in Fig. 7.3(c)

## 7.2 Quantification of the number of the retrieved modes

The evaluated correlation maps are useful for estimating the overall number of modes in the Stokes and anti-Stokes scattering. In Sec. 6.1 we explained that the number of modes $N$ could be approximated as a number of speckle spots that fit into the solid angle occupied by the scattered light, such as that compared in Fig. 7.4(a) for Stokes and Fig. 7.4(b) for the anti-Stokes scattering.

Here we parameterize the sizes of the spots as the $w$ parameters characterizing the Gaussian beams that denote the $1/e^2$ radius of the profile. Consecutively $w_{\mathrm{speckle}}$ is the size of a single speckle, $w_C = \sqrt{2}w_{\mathrm{speckle}}$ denotes the size of the correlation spot and finally $w_{\mathrm{avg}}$ the size of the average scattering profile. A comparison of exemplary profiles is presented in Fig. 7.4(c).

Then we can quantify the number of the generated or retrieved modes by calculating $N = (w_{\mathrm{avg}}/w_{\mathrm{speckle}})^2 = 2(w_{\mathrm{avg}}/w_C)^2$. We begin with calculating the number of modes $N$ for the Stokes field. The angular radius of the average intensity equals $w_{\mathrm{avg}} = 2.8$ mrad, whereas the Stokes-Stokes correlation function size is $w_C = 1$ mrad. In consequence, the total number of modes seen in the Stokes scattering is estimated as $N \simeq 15.7$. This number is well comparable with the estimates

from the model with no decoherence (Raymer and Mostowski, 1981; Kołodyński *et al.*, 2012), where the number of modes is expected to be the Fresnel number of the write beam $N_{\mathscr{F}} = |k_s| w^2/(2\pi L) = 15$.

On the other hand we expect that the number of the retrieved modes will be decreased by the deleterious influence of the decoherence. We evaluate the number of retrieved modes as a function of storage time duration in different buffer gases and present the results in Fig. 7.4. We can see that only for krypton at 1 Torr the number of the retrieved modes exceeds significantly unity within the first two microseconds of the storage times.

## 7.3 Four-wave mixing at the readout process

### 7.3.1 Model

Next we shall perform an in-depth analysis of the physics underlying the second correlation spot seen in Fig. 7.2 related to further Stokes scattering at the readout. Its presence apparently requires a more sophisticated model of the readout process. Here we shall discuss its most important properties and relate them to the observable correlation maps. Further details are presented in our paper (Dąbrowski *et al.*, 2014).

Similarly to the description in the introduction in Sec. 1.5 here we present a simple, plane-wave model of readout covering full four-wave mixing process. Now it has to be extended with the introduction of another Stokes scattering driven by a read beam. Fig. 7.5 summarizes the frequencies and the wave vectors of all of the light fields involved in the model.

The spontaneous Stokes scattering in write-in illustrated in Fig. 7.5(a) is the same as before. Driven by a write beam of a wave vector $\mathbf{k}_{\mathrm{W}}$ it generates a certain number of spin wave excitations $n_b$ with a corresponding wave vector $\mathbf{K}_b$. This number equals the number of the scattered Stokes photons with wave vector $\mathbf{k}_{\mathrm{WS}} = \mathbf{k}_{\mathrm{W}} - \mathbf{K}_b$, labeled WS so it can be distinguished from the Stokes process at the readout.

The readout is depicted on the level diagram in Fig. 7.5(b). This time we include both anti-Stokes and the Stokes light fields using bosonic operators for the corresponding weak field light modes $\hat{a}_{\mathrm{RA}}$

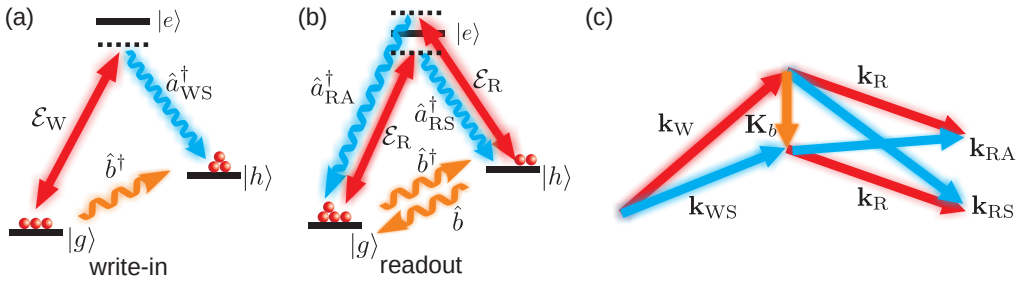


Figure 7.5: Atomic levels and phase matching in the Λ-scheme Raman scattering induced by classical laser field of amplitudes $\mathscr{E}_{\mathrm{W}}$ and $\mathscr{E}_{\mathrm{R}}$ for write and read beams, respectively. (a) In a spontaneous write-in process Stokes photons ($\hat{a}^\dagger_{\mathrm{WS}}$ - mode) and spin wave excitations ($\hat{b}^\dagger$ - mode) are created pairwise. (b) Four-wave mixing in readout involves simultaneous anti-Stokes and Stokes scattering into modes $\hat{a}^\dagger_{\mathrm{RA}}$ and $\hat{a}^\dagger_{\mathrm{RS}}$. (c) Phase matching condition or momentum conservation dictates the wave vectors of single photons coupled to a spin wave excitation with a certain wave vector $\mathbf{K}_b$. The write beam with the $\mathbf{k}_{\mathrm{W}}$ wave vector is scattered as a Stokes photon with the $\mathbf{k}_{\mathrm{WS}}$ wave vector, while the read beam with the $\mathbf{k}_{\mathrm{R}}$ wave vector either scatters Stokes or couples anti-Stokes photons of the respective wave vectors $\mathbf{k}_{\mathrm{RS}}$, $\mathbf{k}_{\mathrm{RA}}$.

and $\hat{a}_{\mathrm{RS}}$. As compared to the simple model derived in Sec. 1.5, here the Hamiltonian describing both the Stokes and the anti-Stokes scattering at the readout stage has the following form:

$$\hat{H}_{\mathrm{R}} = i\hbar\chi\hat{a}^{\dagger}_{\mathrm{RA}}\hat{b} + i\hbar\kappa\hat{a}^{\dagger}_{\mathrm{RS}}\hat{b}^{\dagger} + H.c., \tag{7.2}$$

where $\chi$ and $\kappa$ are the coupling coefficients for anti-Stokes and Stokes Raman transitions, similarly to those derived in Sec. or in (Raymer and Mostowski, 1981). From Eqs. (1.78,1.83) we see that the contribution of each term depends on the detunings from the excited levels. This is an adjustable parameter that allows us to control the interplay between anti-Stokes and Stokes photons.

In Fig. 7.5(c) we analyze the directions of the wave vectors present in the full process. The read laser of a wave vector $\mathbf{k}_R$ couples to the spin wave with a certain wave vector $\mathbf{K}_b$. Then the anti-Stokes and Stokes fields of the wave vectors $\mathbf{k}_{\mathrm{RA}} = \mathbf{k}_{\mathrm{R}} + \mathbf{K}_b$ and $\mathbf{k}_{\mathrm{RS}} = \mathbf{k}_{\mathrm{R}} - \mathbf{K}_b$ are created. Noticeably, the directions of Stokes and the anti-Stokes photons coupled to the same spin wave mode can be entirely distinguished.

### 7.3.2 Experimental conditions

We repeat the experiment in similar conditions as discussed previously in Sec. 6.2.1 Specifically, here we used a $^{87}$Rb cell with krypton at 1 Torr as a buffer gas heated up to $90^{o}$C equivalent to the optical density of 135. The write and read laser detunings were measured from the transition F=1→F=1'. In particular the detuning of the write laser was $\Delta_{\mathrm{W}} = 1.77$ GHz to the red and was kept constant throughout all measurements. The detuning of the read laser $\Delta_{\mathrm{R}}$ measured from F=2→F'=2 varied in consecutive measurements.

The values of the write and read lasers detunings used the beat-note signal acquired on a fast photodiode. The absolute values of detuning were determined precisely with the aid of a Doppler-free saturated absorption spectroscopy inside an auxiliary rubidium cell.

Inside the main cell the powers of the write, read and pump lasers were 6.8 mW, 4.5 mW and 75 mW, respectively. Along the experimental sequence the power of the lasers fluctuated by no more than 5%. Their passively stable frequencies were kept within the range of 50 MHz.

Since the powers of the Raman driving beams were lower than in the previous setting we applied the longer pulses to operate in similar pulse energy regimes. For all of the results presented here we used a 10 $\mu$s long rectangular write pulse and a 40 $\mu$s read pulse.

Here we applied a single $^{85}$Rb absorption filter heated up to 130°C that yielded a measured transmission of 12% for Stokes scattering in write-in and 76% for all of the applied frequencies of anti-Stokes and Stokes photons in readout.

The beam diameters were 6 mm for the pump beam and 4 mm for both write and read beams. The write and read beams were tilted at a lower angle than previously, i.e. $\theta = 2$ mrad.

Finally as a spatially resolved detector we used an intensified sCMOS camera in the low-gain regime, described in Sec. 5.5.

### 7.3.3 Correlation maps

In Fig. 7.6(a) we present the maps of the correlation coefficients $C_{R,i}(\boldsymbol{\theta},\boldsymbol{\theta}')$, equivalent to those in Fig. 7.2. Here we study how the contribution of the anti-Stokes and Stokes processes at the readout changes with the detuning $\Delta_R$ of the read beam. Each correlation map was calculated from $10^5$ single-shot images cropped to the circles marked in the maps corresponding to the solid angle of scattering.

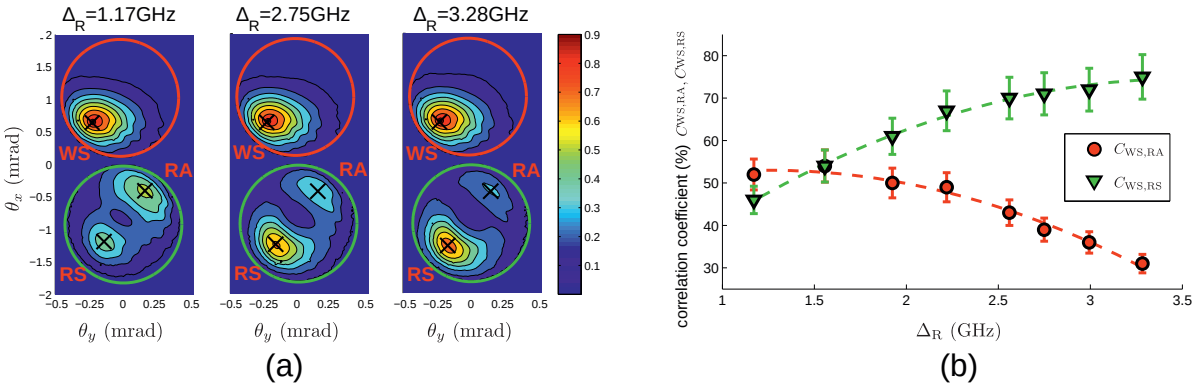


Figure 7.6: (a) Spatial correlation maps for different read laser detunings $\Delta_R$ from $^{87}$Rb F=2 → F'=2 resonance. Red and green circles mark the respective areas where photons scattered at the write and read stages fell. (b) Correlation coefficients at the peaks corresponding to anti-Stokes $C_{WS,RA}$ and Stokes $C_{WS,RS}$ versus detuning $\Delta_R$ with (quadratic) trend.

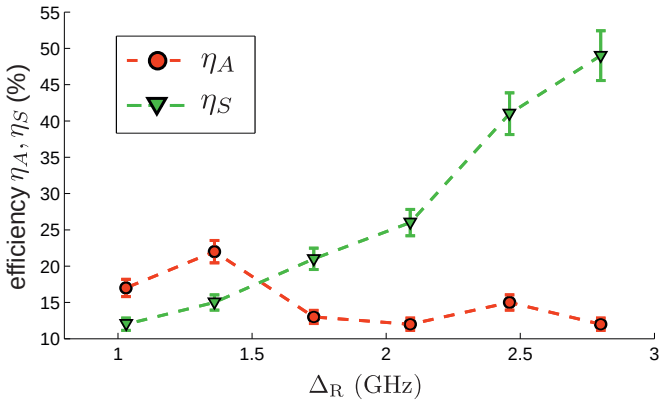


Figure 7.7: Effective gains of the anti-Stokes scattering $\eta_W\eta_R\bar{G}_{RA}$ and the Stokes scattering $\eta_W\eta_R\bar{G}_{RS}$. For the smallest detuning $\Delta_R$ absorption in rubidium cell starts to contribute.

We identify the correlation spots corresponding to finite coherence regions of the Stokes scattering at the write-in, anti-Stokes and Stokes in readout labeled respectively WS, RA and RS. The position of the maxima are in agreement with the phase matching conditions illustrated in Fig. 7.5(c).

By changing the detuning of the read beam within the range of $\Delta_R = 1.17$ GHz to $\Delta_R = 3.28$ GHz we can observe the transition from the anti-Stokes to Stokes scattering domination visually. The transition can also be observed in Fig. 7.6(b) where we extract the maximal coefficients of correlation between the Stokes scattering in the write-in and either anti-Stokes scattering — $C_{WS,RA}$ or the Stokes scattering in readout — $C_{WS,RS}$.

## 7.4 Readout efficiency

### 7.4.1 Model

So far we have not commented on the efficiency of readout. A blind comparison of the mean intensities of light scattered in write-in and readout processes is inadequate as it resolves neither Stokes and anti-Stokes contributions nor non-correlated noises. The measured correlation values together

with the mean intensities and their variances can be used to extract information about the number of the correlated Stokes and anti-Stokes photons. Let us first derive a simple heuristic model enabling subsequent the extraction of qualitative information.

In the experiment we measure a signal $I_{\mathrm{WS}}$ registered at pixel $i = \mathrm{WS}$ calibrated to the number of photons. That signal consists of a part proportional to the number of photons $n_{\mathrm{WS}}$ but it is also contaminated with the camera system read noise $f_{\mathrm{WS}}$:

$$I_{\mathrm{WS}} = t_{\mathrm{WS}} n_{\mathrm{WS}} + f_{\mathrm{WS}}, \tag{7.3}$$

where $t_{\mathrm{WS}}$ is the transmission of the write-in Stokes photons through the filter system found independently. The camera system read noise $f_{\mathrm{WS}}$ is random and its variance scales quadratically with the intensity on the pixel $\langle(\Delta f_i)^2\rangle \sim I_i^2$. We performed the calibration of the I-sCMOS camera in the low gain regime prior to the measurements and we exactly determined the variance of the read noise at each pixel.

The signal at the readout at pixel $i = \mathrm{RA}$ consists of the following contributions:

$$I_{\mathrm{RA}} = t_{\mathrm{RA}} n_{\mathrm{RA}} + t_{\mathrm{RS}} n'_{\mathrm{RS}} + f_{\mathrm{RA}}, \tag{7.4}$$

where $n_{\mathrm{RA}}$ is the number of photons generated in the anti-Stokes at the readout and $n'_{\mathrm{RS}}$ is the number of photons generated in the Stokes at the readout. Since the latter term originates from coupling to the opposite wave vector spin wave it is entirely uncorrelated. $t_{\mathrm{RA}}$ and $t_{\mathrm{RS}}$ are transmissions of the anti-Stokes and the Stokes photons at the readout. Finally $f_{\mathrm{RA}}$ in Eq. (7.4) stands for the camera system read noise at pixel $i = \mathrm{RA}$. Similarly to Eq. (7.4), the signal registered at pixel $i = \mathrm{RS}$ consists of the following terms:

$$I_{\mathrm{RS}} = t_{\mathrm{RS}} n_{\mathrm{RS}} + t_{\mathrm{RA}} n'_{\mathrm{RA}} + f_{\mathrm{RS}}. \tag{7.5}$$

To complete this heuristic model we have to include finite inefficiencies of the processes and to add additional spurious noises from uncorrelated photons emitted at the readout stage. Let $\eta_A$ be the effective efficiency or the anti-Stokes readout relating the number of Stokes photons $n_{WS}$ to the number of the retrieved photons $n_{RA}$:

$$n_{\mathrm{RA}} = \eta_A n_{\mathrm{WS}} + \check{S}_{\mathrm{A}},\ \mathrm{corr}(n_{\mathrm{AS}}, \eta_A n_{\mathrm{WS}}) = 1 \tag{7.6}$$

where $\check{S}_{\mathrm{A}}$ denotes the fraction random number of uncorrelated photons. We treat $n_{RA}$ and $n_{WS}$ as entirely correlated random variables, thus $\check{S}_{\mathrm{A}}$ effectively influences the correlation coefficient. $\eta_A$ physically includes both write-in and anti-Stokes efficiency.

In a similar manner we introduce $\eta_S$ as the effective efficiency of the Stokes scattering at the readout. The number of Stokes photons is expressed as:

$$n_{\mathrm{RS}} = \eta_S n_{\mathrm{WS}} + \check{S}_{\mathrm{S}},\ \mathrm{corr}(n_{\mathrm{WS}}, \eta_S n_{\mathrm{WS}}) = 1 \tag{7.7}$$

where $\check{S}_{\mathrm{S}}$ stands for the amount of uncorrelated Stokes photons. At this time the effective efficiency for Stokes $\eta_S$ scattering can be large, as we expect this process to be amplifying.

Based on Eqs. (7.4)-(7.7) and takingcorr$(n_{\mathrm{WS}}, \check{S}_i) = \mathrm{corr}(n_{\mathrm{WS}}, n'_i) = \mathrm{corr}(n_{\mathrm{WS}}, f_i) = 0$ we find the effective efficiencies of both processes:

$$\eta_{\mathrm{A}} = \frac{t_{\mathrm{WS}}}{t_{\mathrm{RA}}} \frac{C_{\mathrm{WS,RA}} \sqrt{\langle(\Delta I_{\mathrm{WS}})^2\rangle \langle(\Delta I_{\mathrm{RA}})^2\rangle}}{\langle(\Delta I_{\mathrm{WS}})^2\rangle - \langle(\Delta f_{\mathrm{WS}})^2\rangle}, \tag{7.8}$$

$$\eta_{\mathrm{S}} = \frac{t_{\mathrm{WS}}}{t_{\mathrm{RS}}} \frac{C_{\mathrm{WS,RS}} \sqrt{\langle(\Delta I_{\mathrm{WS}})^2\rangle \langle(\Delta I_{\mathrm{RS}})^2\rangle}}{\langle(\Delta I_{\mathrm{WS}})^2\rangle - \langle(\Delta f_{\mathrm{WS}})^2\rangle}. \tag{7.9}$$

| $\Delta_R$ | $\eta_S$ | |
|---|---|---|
| | $t_R = 15\ \mu$s | $t_R = 40\ \mu$s |
| 2.0GHz | 18% | 31% |
| 3.8GHz | 93% | 122% |

Table 7.1: Effective efficiency of the Stokes scattering for different read laser detunings and cropped read laser pulse durations.

### 7.4.2 Results

In the formulas for the effective efficiencies of the anti-Stokes $\eta_A$ and the Stokes processes $\eta_S$ at the readout in Eqs. (7.8-7.9) all of the terms are measured directly. In Fig. 7.7 we present the results of 6 efficiency coefficients for different read laser detunings $\Delta_R$.

The efficiency of the anti-Stokes readout $\eta_R$ weakly depends on the detuning $\Delta_R$ and its highest observed value equals $\eta_R = 22\%$ for $\Delta_R = 1.37$ GHz. Interestingly it exceeds 10% even for very large detunings $\Delta_R > 2$ GHz, where without Stokes process it should not be expected. Clearly this effect benefits from the enhancement due to the full four-wave mixing process.

On the other hand the efficiency of the Stokes scattering $\eta_S$ noticeably increases with $\Delta_R$. Additionally we checked how the efficiencies of the Stokes scatttering scale with the time duration of the read laser. Tab. 7.1 summarizes the experimental results for the two read pulse durations $t_R = 15\ \mu$s and $t_R = 40\ \mu$s. Longer interaction time increases the effective efficiency of the Stokes process indicating its amplifying nature. In particular we can even obtain the efficiencies $\eta_S > 100\%$.

## 7.5 Spatial correlations at the single-photon level

### 7.5.1 Difficulties with entering the single-photon-level regime

The above results were obtained in the high-intensity regime, where each spin wave mode was occupied by up to tens of thousands of excitations. Analogous correlation measurements in the single-photon-level regime required both true single-photon sensitivity of the camera system and a good signal to noise ratio. The first condition was fulfilled by applying the I-sCMOS camera whose construction was initially devoted specifically to this experiment.

Preliminary measurements indicated that the actual Raman scattering signal was severely corrupted by broadband collisional fluorescence[1] that passed through the absorption filter described in Sec. 5.4.2 and Appendix C. In practice the correlation measurements, such as those presented in Sec. 7.3, were possible only in the high-intensity regime where the I-sCMOS camera had to be operated in the low-gain linear mode. That is because the Raman scattering signal grows exponentially with the drive lasers pulse energies in contrast to the linear scaling of the fluorescence signal. Attempts to observe spatial correlations using photon-counting capabilities of the I-sCMOS without more advanced filtration methods failed. It indicated that the few-photon Raman signal was polluted by a large amount of broadband uncorrelated fluorescence and the observed signal virtually consisted of a noise.

[1] Collisional fluorescence should be treated as fluorescence from metastable molecules (Hedges *et al.*, 1972), e.g. RbKr that may be formed for a short time, i.e. of the order of picoseconds. Thus the width of the spectrum is expected to be of the order of hundreds of gigahertz and cannot be filtered exclusively by using a $^{85}$Rb absorption filter of the line width below 10 GHz.

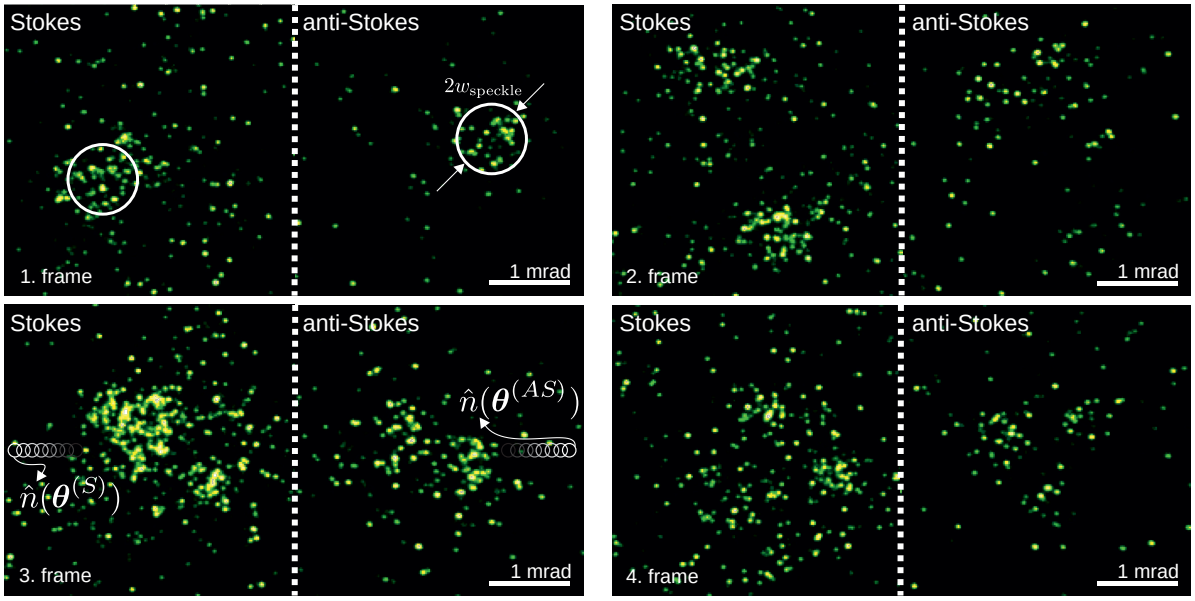


Figure 7.8: Single shots of Raman scattering after the application of the Faraday filter. Images taken by an I-sCMOS camera operating in the high-gain regime reveals distributions of about hundreds of photons grouped in speckle-like patterns. Similar and inverted structures are seen between the Stokes and anti-Stokes camera panes. In the first frame we marked the calculated $2w_{\text{speckle}}$ size of a speckle. In the third frame we marked exemplary 0.022 mrad$^2$ size circles used for photon counting.

### 7.5.2 Single shots upon the introduction of the Faraday filter

The crux of performing measurements at the single photon level, where we could apply the photon counting methods using I-sCMOS camera, was to include the third filtration step – the Faraday filter. The eventual filtering system offered a large transmission of ca. 50% for both Stokes and anti-Stokes photons in relatively narrowband spectral windows while being opaque elsewhere. As we show in Fig. 5.8, Sec. 5.4.3, the widths of transmission lines of the Faraday filter laying outside the absorption line of $^{85}$Rb filter were of the order of one gigahertz. That resulted in expected suppression of the broadband collisional fluorescence by at least two orders of magnitude.

We used the main cell with $^{87}$Rb mixed with krypton at 1 Torr heated up to 75°C degrees. We applied 20 mW and 15 mW of the write and read laser power, respectively. The $1/e^2$ diameters of the driving beams were about $2w = 8$ mm while the pump beam was twice as large. The detunings of the driving lasers were approximately $\Delta_W \approx \Delta_R \approx 700$ MHz from the closest resonances as marked in Fig. 5.3. The images were obtained for pulse durations $t_W = 2$ $\mu$s and $t_R = 1$ $\mu$s with no time-gap in between. The cell in the Faraday filter was heated to 90° C degrees and the longitudinal magnetic field was set to 10 mT.

The first results of the application of the triple filtration system can be seen in single-shot images of the Stokes and the anti-Stokes directly acquired from the I-sCMOS sensor, as presented in Fig. 7.8. Visibly separated single green spots refer to the single Raman scattered photons that induced photoelectrons. Moreover, the registered photons are noticeably grouped in speckle-like patterns, similarly to Fig. 6.4. Interestingly the patterns retrieved in the anti-Stokes process are clearly inverted in relation to the patterns in the Stokes scattering. In the first frame we marked a circle of $2w_{\text{speckle}}$ in diameter whose exact value was found from the correlation measurements described in the next paragraphs. The circle refers to the expected speckle size and as seen in the image is, indeed, com-

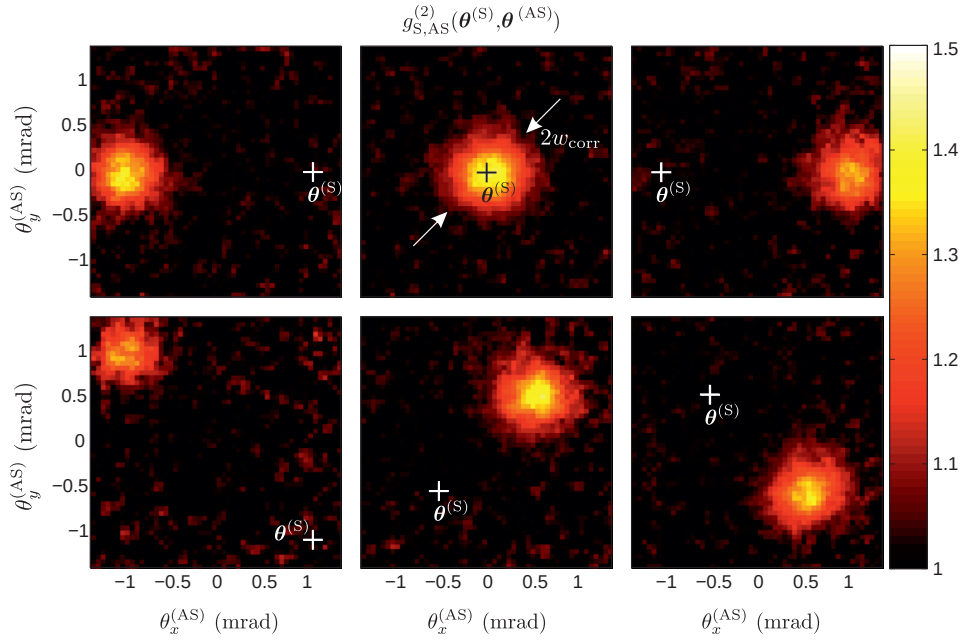


Figure 7.9: Cross-correlation functions between the Stokes and anti-Stokes photons $g^{(2)}_{\mathrm{S,AS}}(\boldsymbol{\theta}^{(\mathrm{S})},\boldsymbol{\theta}^{(\mathrm{AS})})$ centered around driving beam direction. Maps are plotted for a fixed angular position of the Stokes detection region $\boldsymbol{\theta}^{(\mathrm{S})}$ marked with white crosses. The conjugate position of the correlation spots corresponded perfectly with the phase matching condition (Fig. 7.1(a)). Noticeably the Stokes scattering at the readout was cut off by Faraday filter, cf. Fig. 7.6. The mean number of Stokes photoevents per 0.012 mrad$^2$ detection area was maximally 0.28, corresponding to about 130 photons per mode.

parable with the spread of the visible group of the registered photons.

Single shots presented in Fig. 7.8 depict a situation where hundreds of photons are scattered in each shot. This number is small enough for us to distinguish single photon events on I-sCMOS camera and apply photon counting. We can freely decrease the mean number of photons per mode by e.g. shortening the pulse duration of the write laser, as presented in the next paragraphs.

### 7.5.3 $g^{(2)}$ cross-correlations between Stokes and anti-Stokes photons

Similarly to the macroscopic case described in Sec. 7.1, we aim at quantifying the spatial properties of the Raman scattering by calculating correlations between the Stokes and anti-Stokes light. Here we have direct access to the positions of individual photoevents, as described in Part I, rather than to the intensity distributions, as previously discussed across Part II. In each shot we count a number of photons in small circular regions. Angular positions of centers of these circles are denoted by $\boldsymbol{\theta}^{(\mathrm{S})}$ for the Stokes camera pane and $\boldsymbol{\theta}^{(\mathrm{AS})}$ for the anti-Stokes part of the sensor, and the number of photon events in each shot are $\hat{n}(\boldsymbol{\theta}^{(\mathrm{S})})$ and $\hat{n}(\boldsymbol{\theta}^{(\mathrm{AS})})$, respectively. We use circular regions much smaller than the speckle size to achieve high-spatial resolution. Exemplary regions are marked in the third frame of Fig. 7.8.

Depending on the photon flux and the number of the grabbed frames we adjust the size of the circles. Smaller size increases the spatial resolution which entails higher noise due to a lower number of photons per circular region.

Here we evaluate the $g^{(2)}_{\mathrm{S,AS}}$ cross-correlation function between the Stokes and anti-Stokes photons counted in circular regions positioned in $\boldsymbol{\theta}^{(\mathrm{S})}$ and $\boldsymbol{\theta}^{(\mathrm{AS})}$:

$$g^{(2)}_{\mathrm{S,AS}}(\boldsymbol{\theta}^{(\mathrm{S})},\boldsymbol{\theta}^{(\mathrm{AS})}) = \frac{\langle \hat{n}(\boldsymbol{\theta}^{(\mathrm{S})})\,\hat{n}(\boldsymbol{\theta}^{(\mathrm{AS})})\rangle}{\langle \hat{n}(\boldsymbol{\theta}^{(\mathrm{S})})\rangle\langle \hat{n}(\boldsymbol{\theta}^{(\mathrm{AS})})\rangle}. \tag{7.10}$$

As explained in Chapter 1, Sec. 1.4, the values of cross correlation can be directly compared to the nonclassicality criterion.

We repeated measurements in experimental conditions similar to those presented above in Sec. 7.5.2 but we shortened the write pulse duration $t_{\mathrm{W}}$ to decrease the photon flux. We grabbed $10^5$ frames and counted photons in small circular regions of 6 pixels in diameter corresponding to 0.012 mrad$^2$ size. The circles where distributed in both the Stokes and the anti-Stokes scattering camera panes on a $60 \times 60$ rectangular grid with a separation of 0.053 mrad. The highest flux of photons was observed for Stokes photons along the write beam direction. We registered there 0.37 photoevents[2] per circle area on the average.

Fig. 7.9 presents the cross-correlation functions $g^{(2)}_{\mathrm{S,AS}}(\boldsymbol{\theta}^{(\mathrm{S})},\boldsymbol{\theta}^{(\mathrm{AS})})$ evaluated for the fixed position $\boldsymbol{\theta}^{(\mathrm{S})}$ of the circle in the Stokes region, marked with a white cross for reference. Centers of the driving beams are placed in the origin of coordinates. Two dimensional maps plotted in $\theta_x^{(\mathrm{AS})},\theta_y^{(\mathrm{AS})}$ coordinates shows Gaussian-shaped spots centered around the positions $-\boldsymbol{\theta}^{(\mathrm{S})}$ in perfect agreement with the phase matching condition shown in Fig. 7.1(a). In contrast to the previous results discussed in Sec. 7.1-7.4 contribution from the four-wave mixing process at the readout was entirely blocked by the Faraday filter.

As we stated before, the size of the correlation spots was proportional to the size of the single speckles. We fitted the Gaussian function to the cross-section of the spots seen in Fig. 7.9 to obtain a $1/e^2$ diameter of $2w_{\mathrm{corr}} = 1.23$ mrad. The corresponding speckle size $2w_{\mathrm{speckle}} = \sqrt{2}w_{\mathrm{corr}} = 0.87$ mrad is marked in the first frame of Fig. 7.8.

In the view of the discussion on estimation of the number of modes, started in Sec. 7.2 and continued in the next paragraph, the mean number of the photons found in a single speckle area can be treated equally as the mean number of photons per spin wave mode. The maximal density of photons per mode was observed for a straightforward emission and reached up to 60.This estimation includes losses in the filtration and detection system.

### 7.5.4 Estimation of the number of the stored modes

Having determined the correlation and the speckle size, we can estimate the number of modes observed in the Raman scattering, similarly to Sec. 7.2. We have to apply slightly different approach, as compared to Sec. 7.2, where we had at our disposal stimulated Raman signals clearly cutting off from background. Here in the few-photon regime we can only associate photons to the Stokes or anti-Stokes scattering through their mutual correlations. We shall evaluate the approximate number of modes $N$ retrieved in the anti-Stokes scattering and compare the effective speckle size with the solid angle where correlations appears.

Thanks to the rotational symmetry of the means and correlations of Raman scattering around the driving beam directions we can simplify the procedure of quantifying the effective number of the retrieved modes $N$. In Fig. 7.9 we presented two-dimensional cross-sections of four-dimensional functions $g^{(2)}_{\mathrm{S,AS}}(\boldsymbol{\theta}^{(\mathrm{S})},\boldsymbol{\theta}^{(\mathrm{AS})})$, for a fixed $\boldsymbol{\theta}^{(\mathrm{S})}$. We can gain further useful information on plotting other

[2] Photoevents defined in Part I denote indentified individual phosphor flashes that exceeded a set threshold. In the low illumination level where saturation effect studied in Part I are negligible, their number is virtually equal as the number of induced photoelectrons.

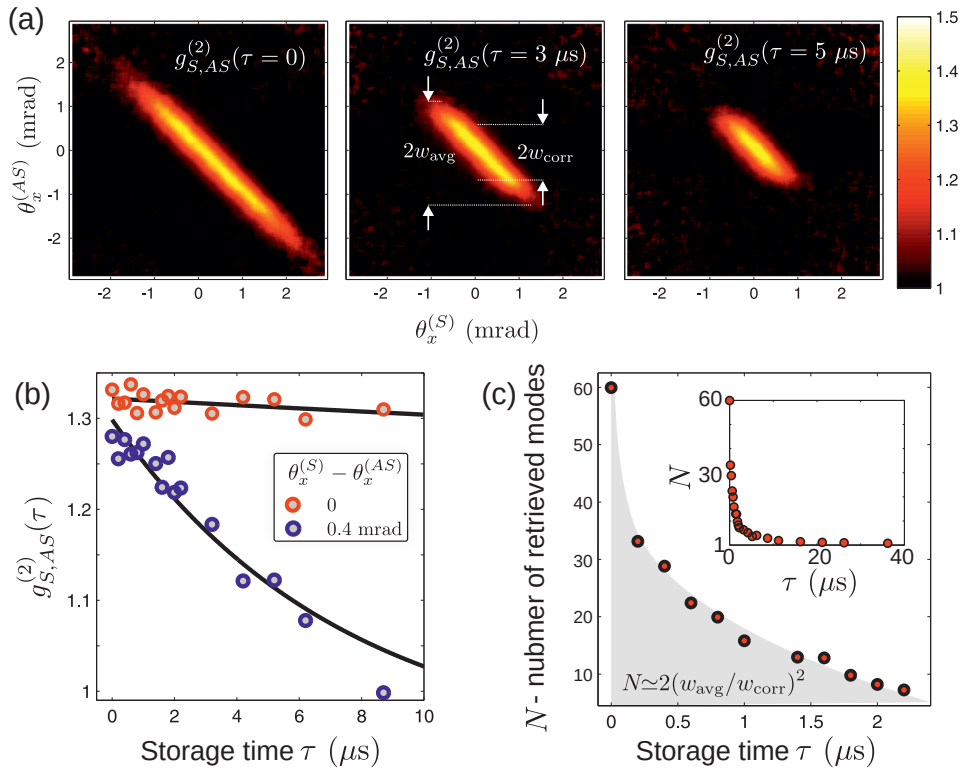


Figure 7.10: (a) Cross-correlation maps $g^{(2)}_{\mathrm{S,AS}}((\theta_x{}^{(\mathrm{S})},0),(\theta_x{}^{(\mathrm{AS})},0))$ between horizontally deflected Stokes and anti-Stokes photons counted in 0.022 mrad$^2$ circular regions. The mean number of Stokes photoevents per region was up to 0.05. (b) $g^{(2)}_{S,AS}$ versus the storage time for two exemplary pairs of directions: lying on the drive beam axis and off-axis. (c) The square of the ratio of the correlation maps widths measured at the edges and in the center can estimate the number of stored modes.

two-dimensional cross-sections, $g^{(2)}_{\mathrm{S,AS}}(\boldsymbol{\theta}^{(\mathrm{S})},\boldsymbol{\theta}^{(\mathrm{AS})})$, specifically for $\theta_y^{(\mathrm{S})} = \theta_y^{(\mathrm{AS})} = 0$. That refers to counting photons only in the circles distributed horizontally in the middle of a camera sensor as illustrated in the third frame of Fig. 7.8.

In Fig. 7.10(a) we plot maps with cross-correlation functions $g^{(2)}_{\mathrm{S,AS}}((\theta_x{}^{(\mathrm{S})},0),(\theta_x{}^{(\mathrm{AS})},0))$ for three different storage times $\tau = 0, 3, 5\ \mu$s. Maps obtained from $3\times10^5$ frames each were obtained under experimental conditions identical as in Sec. 7.5.3. We counted photons in a $1\times250$ stripe made of adjacent circular regions of 0.022 mrad$^2$ each, separated uniformly by 0.023 mrad in each Stokes and anti-Stokes scattering region.

Characteristic longitudinal shapes in Fig. 7.10(a) directed along anti-diagonal reflect the conjugation of opposite direction of Stokes and anti-Stokes scattering resulted from the phase matching condition. Each vertical cross-section of the maps in Fig. 7.10(a) for a fixed $\theta_x{}^{(\mathrm{S})}$ is equivalent to a horizonal cross-section of the maps in the first row of Fig. 7.9. In particular in the middle map of Fig. 7.10(a) we marked $2w_{\mathrm{corr}}$ width, which is the same as found in Fig. 7.9. We also marked the effective width of the correlation function $2w_{\mathrm{avg}}$ , which is an exact analogy to the quantity introduced in Sec. 7.1. In fact, the diameter $2w_{\mathrm{avg}}$ denotes a span of angles $\theta_x{}^{(\mathrm{AS})}$ in which the signal-to-noise ratio of the anti-Stokes is high.

To quantify the storage properties of the memory we repeated measurements taking $10^4$ frames for many storage times and plotting the values of $g^{(2)}_{\mathrm{S,AS}}((0,0),(0,0))$ and $g^{(2)}_{\mathrm{S,AS}}((0.4\,\mathrm{mrad},0),(-0.4\,\mathrm{mrad},0))$

in Fig. 7.10(b). For the latter setting, i.e. the scattering deflected from the driving beam by ±0.4 mrad, the correlation quickly drops to 1 within several microseconds. On the other hand correlations between photons directed along driving beams exhibit a noticeably slower decay rate. These observations are proof of an exact manifestation of the diffusional decoherence affecting spin waves of large wave vectors discussed in Sec. 6.4.

Eventually in Fig. 7.10(c) we evaluate the approximate number of modes reads as $N \simeq 2(w_{\mathrm{avg}}/w_{\mathrm{corr}})^2$. To calculate the $w_{\mathrm{avg}}$ and $w_{\mathrm{corr}}$ we projected maps of cross-correlations $g^{(2)}_{\mathrm{S,AS}}((\theta_x{}^{(\mathrm{S})},0),(\theta_x{}^{(\mathrm{AS})},0))$, respectively on anti-diagonals and diagonals, and fitted the Gaussian functions. The approximated number of the retrieved modes dropped from 60 to 10 within the first 2 $\mu$s of storage. The initial number of the modes is considerably higher than in the macroscopic regime discussed in Sec. 7.3. There are two reasons for this favorable increase. Firstly we significantly decreased detection noise thanks to the filtration and the camera systems. That allowed for the detection of angularly broad, yet very weak signals. Secondly we applied twice larger beam diameters. That was supposed to yield a quadruple increase in the number of modes as the Fresnel number $N_{\mathscr{F}}$ was re-scaled from 15 to 60. Indeed, the maximal value displayed in Fig. 7.10(c) equals the Fresnel number. Although these numbers are of estimate character, they fit the theory (Raymer and Mostowski, 1981) surprisingly well. In the inset we can observe that for the larger storage times the number of retrieved modes drops to 1 within about 40 $\mu$s.

### 7.5.5 Spatial correlations mediated by single excitations

Finally we attempted at decreasing the flux of scattered photons to populate individual spin wave modes by single excitations. To perform this, we cooled down the main $^{87}$Rb cell down to 60°C degrees and shortened the pulse durations to $t_{\mathrm{W}} = 1\ \mu\mathrm{s}, 500\ \mathrm{ns}, 250\ \mathrm{ns}$ for the write laser and to $t_{\mathrm{R}} = 500$ ns for the read laser. The Faraday filter at the temperature of 98°C degrees and the magnetic field of about 5 mT let through scattered photons detuned by about 700 MHz.

We shortened the read laser to 780 nm and applied additional interference filters to split spectrally and spatially Stokes and anti-Stokes photons as depicted in Sec. 5.5 in Fig. 5.9. This allowed us to clearly separate the contributions of these two processes on the camera. In particular the angulary broad Stokes was clearly separated from the anti-Stokes region.

Fig. 7.11(a-c) presents correlation maps $g^{(2)}_{\mathrm{S,AS}}((\theta_x{}^{(\mathrm{S})},0),(\theta_x{}^{(\mathrm{AS})},0))$ calculated from $10^6$ frames taken for consecutively decreasing write pulse durations $t_{\mathrm{W}} = 1\ \mu\mathrm{s}, 500\ \mathrm{ns}, 250\ \mathrm{ns}$ for a write power of 20 mW. The photons were counted in regions distributed on a $1 \times 60$ stripe made of adjacent circular regions of 0.05 mrad$^2$ size separated by 0.053 mrad in each Stokes and anti-Stokes scattering region.

Fig. 7.11(d) presents the mean number of photoevents originated by Stokes and anti-Stokes scattering acquired in the small circular regions. These numbers are also rescaled on the right-hand side axis to the effective density of photons per $2w_{\mathrm{speckle}}$ area, which is comparable to the number of excitations per individual spin wave mode. These numbers are corrected for the finite transmission of photons and finite quantum efficiency of the I-sCMOS camera system.

Apparently the values of the $g^{(2)}$ cross-correlations function in Fig. 7.11(a-c) are smaller then 2, which indicates that any expected nonclassical correlations between Stokes and anti-Stokes photons are still corrupted by excessive noise. As can be seen in Fig. 7.11(d), the anti-Stokes scattering rises above a certain background of around 0.02 photoevents per detection region. Since the anti-diagonal widths of the cross-correlation maps Fig. 7.11(a-c) are comparable with the width of the anti-Stokes scattering, above the flat background we can clearly state that the background does not exhibit correlations with the Stokes scattering. Thus, the background should be treated as a source

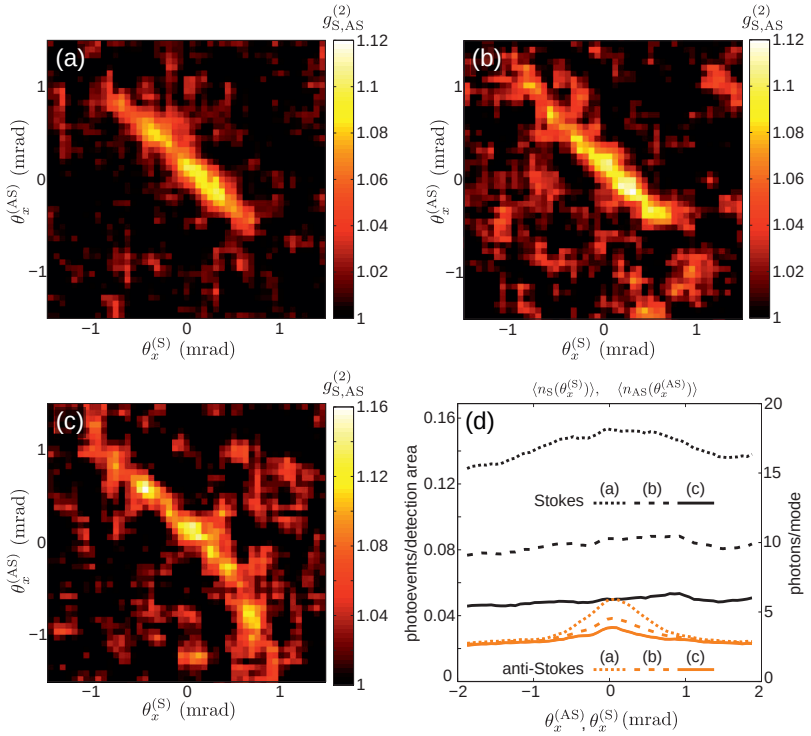


Figure 7.11: Cross-correlation maps $g^{(2)}_{\mathrm{S,AS}}((\theta_x{}^{(\mathrm{S})},0),(\theta_x{}^{(\mathrm{AS})},0))$ for lower energies of write laser pulses containing (a) $8\times10^{10}$, (b) $4\times10^{10}$, (c) $2\times10^{10}$ photons. (d) Angular distribution of the mean number of photoevents per area of 0.05 mrad$^2$ (left axis) or true photon number per mode (right axis). Results unambiguously demonstrate spatial correlations in the regime of single atomic excitations per individual spin wave mode.

of noise that ultimately prevents us from observing the expected nonclassical correlations between Stokes and anti-Stokes photons.

We performed a rough check of the properties of the background. Thanks to the tunability of the Faraday filter transmission lines we verified that the background light had the same frequency as the actual anti-Stokes scattering. We suspect that the background originates from uncorrelated off-resonant Raman scattering driven by the read laser. Probably here we deal with the uncorrelated Stokes scattering on the unpumped fraction of $^{87}$Rb atoms stayed in $F=2$, that would have the same spectral properties as observed. The suggested explanation is in agreement with the facts reported by other groups (van der Wal *et al.*, 2003; Eisaman, 2006) that lower gas temperatures facilitate observation of nonclassical properties in the single-mode memories. Indeed, lower temperatures should enable better pumping efficiencies as the deleterious collisional effects are then relatively less severe.

Remarkably, as presented in Fig. 7.11, we observe that we did reach the level of single excitations per spin wave mode. In this regime broad spatial correlations are still visible. Although the exact state of the atom is hard to determine faithfully, interestingly we deal with a certain collective state in which a large group of atoms occupied by only a few excitations stores the information about the direction of photons seen in the spatial correlation maps.

## 7.6 Conclusions

In this chapter we presented the main results from the setup for generation of spatially multimode Raman scattering. We demonstrated spatial correlations between the Stokes and the time-delayed anti-Stokes scattering. We proved that our system had the capability of storing information about initial spatial distribution of Stokes photons in spin wave atomic excitations for several microseconds. We observed and investigated the parasitic four-wave mixing process seen in the correlations. Ultimately we showed that we were able to create and read out spin wave modes occupied by single excitations on the average. Most of the results presented in this chapter have been addressed in papers (Chrapkiewicz and Wasilewski, 2012; Dąbrowski *et al.*, 2014; Chrapkiewicz *et al.*, 2015a).

### 7.6.1 Classical correlations

In Sec. 7.1 started with a calculation of Hanbury-Brown-Twiss intensity correlations for macroscopic Raman scattering. The measured correlation maps revealed the size of the coherence area for Stokes and anti-Stokes scattering. It was close to a speckle size in single realizations of the process. Moreover, the directional correlations agreed with the phase matching condition. The correlation maps also provided a sound basis for calculating the number of independent spatial modes excited and read out from the atoms in Sec. 7.2.

These have been the first reported results demonstrating spatially multimode capacity of the DLCZ-type (Duan *et al.*, 2001) Raman atomic memory. The number of the created modes was close to the theoretical estimates (Raymer and Mostowski, 1981; Kołodyński *et al.*, 2012). The study showed that the capacity of the memory was mostly affected by diffusional decoherence and it was beneficial to enlarge driving beams sizes. At the macroscopic level the presented results opened the way for further studies on lower light levels.

### 7.6.2 Four-wave mixing

We identified the contribution from another process present at the readout – the Stokes scattering on the plotted correlation maps. In Sec. 7.3 we built a model explaining the interplay of the anti-Stokes and the Stokes scattering at the readout stage. These two processes can be perceived together as four-wave mixing initiated by atomic excitations. In the next experiments we carefully studied how the competing anti-Stokes and Stokes scattering present in readout depended on detuning of a driving laser beam. Based on these results, in Sec. 7.4 we found the absolute values of efficiencies of anti-Stokes readout of collective excitations and we quantified percentage of excitations that were converted into Stokes photons. It turned out that the Stokes process could multiply the initial number of excitations, yet introducing noise.

The four-wave mixing process is currently considered as one of the most significant roadblocks on the way to room-temperature quantum memories in atomic vapors (Reim *et al.*, 2011; Michelberger *et al.*, 2015). In particular it is a source of unconditional noise floor at the readout of Raman-type quantum memories at the single photon level (Reim *et al.*, 2011; Vurgaftman and Bashkansky, 2013; Michelberger *et al.*, 2015). We demonstrated how to suppress four-wave mixing by adjusting the coupling light frequency to the other side of the atomic resonance. Moreover, it may be favorable to use non-collinear configuration where control and quantum fields enter the atomic medium at a small angle. Then the Stokes scattering photons will become directionally distinguishable from the anti-Stokes.

### 7.6.3 Single-photon-level correlations

The final application of the advanced filtration system described in Sec. 5.4 enabled us to reach a relatively high signal-to-noise-ratio in the single-photon-level Raman scattering Sec. 7.5. We evaluated the $g^{(2)}$ cross-correlation functions between the number of photons observed at different directions. We showed that within a few microseconds we were able to retrieve up to several tens of spatial modes. Further decrease in the drive lasers pulse duration led to a regime of single excitations per spin wave mode. Importantly, large atom groups occupied by merely one or few bosonic excitations can collectively store information about Stokes scattered wave vectors. To the best of our knowledge, this has been the first demonstration of storing spatially varying information at the single-photon-level in warm atomic systems.

The next milestone in this research would be the demonstration of nonclassical correlations between Stokes and anti-Stokes photons. From the previous studies on warm atomic vapors mixed with buffer gases we know that this challenging task has only been accomplished in single-mode memory systems (Bashkansky *et al.*, 2012). We identified the next roadblock impeding the observation of quantum effects in our system as imperfect pumping due to collisions in a buffer gas. In consequence, at the readout we produce isotropic and incoherent Stokes scattering of the same frequency as the actual signal. This may be an insurmountable obstacle to achieving high capacity warm atomic quantum memories as we need buffer gases to slow down diffusion.

Nevertheless, the demonstrated effects of spatial correlations at the single photon levels are telltale signs of collective effects in warm atomic clouds. We conjecture that the observed collective phenomena may also be observable without noise in cold atomic systems where certain nonclassical correlations can readily be achieved (Choi *et al.*, 2008; Chaneliere *et al.*, 2005; Bao *et al.*, 2012).

# Part III

# Nonclassical interference of spatially structured photons

In this part we demonstrate the ultimate capabilities of our I-sCMOS camera system which consist in registering nonclassical light, such as single pairs of photons generated in a nonlinear crystal. In Chapter 8 we present the first experimental observation of the spatially resolved Hong-Ou-Mandel interference and study the effects of a limited spatial mode overlap between interfering photons. Finally in Chapter 9 we show the method where two-photon interference is used to retrieve the local phase of the transverse wave function of a single spatially structured photon.

The presented research fits in the contemporary studies utilizing spatial correlations exhibited by nonclassical light. Previous studies using single-photon-sensitive cameras have concentrated predominantly on the ghost imaging scheme (Gatti *et al.*, 2008; Morris *et al.*, 2015), sometimes called quantum imaging (Lugiato *et al.*, 2002; Kolobov, 2007; Gatti *et al.*, 2008), although this scheme can be realized with classical thermal light (Ferri *et al.*, 2005). Other experiments include investigation of spatial correlations from SPDC light (Oemrawsingh *et al.*, 2002; Haderka *et al.*, 2005; Blanchet *et al.*, 2008; Tasca *et al.*, 2013; Machulka *et al.*, 2014) and EPR-paradox measurements (Edgar *et al.*, 2012; Moreau *et al.*, 2012, 2014). Occasionally new types of quantum imaging schemes were proposed, such as sub-shot noise imaging (Brida *et al.*, 2010) or imaging with undetected photons (Lemos *et al.*, 2014). We would like to stress that in almost all of the mentioned aplications cameras always register many ($\gg 100$) photons per frame. The only two exceptions that are known to us, were reported over a decade ago (Abouraddy *et al.*, 2001; Oemrawsingh *et al.*, 2002) and have not lived to be further developed probably because of their unsatisfactorily low single-to-noise ratio in the measured data.

The techniques presented in this chapter may be useful for the super-resolution scheme proposed by Tsang (2009) whose proof-of-principle demonstration was performed using fiber coupled avalanche photodiodes(Rozema *et al.*, 2014; Shin *et al.*, 2011). We expect that our camera will be useful for another super-resolution imaging scheme utilizing photon anti-bunching effect (Gatto Monticone *et al.*, 2014; Schwartz *et al.*, 2013).

**Contribution**

All of the results presented in this part were obtained in close collaboration of R.C. with M.J. Initially M.J. was responsible for the SPDC source setup and R.C. for the camera detection system, software and data analysis but later on the roles were shared. Measurements were typically initiated by R.C and M.J. together and then completed and fine-tuned by M.J., while R.C. provided simultaneous analysis and the necessary software.

K.B. suggested research on the effects of partial spatial distinguishability. R.D.-D. noticed discrepancy between the data and the theory, which was explained by R.C. W.W. proposed the idea of phase reconstruction which was formulated mathematically and performed numerically by R.C., while the measurements were carried out by M.J.

CHAPTER 8

# IMAGING THE HONG-OU-MANDEL INTERFERENCE OF PHOTON PAIRS

In this chapter we describe a spatially resolved observation of the Hong-Ou-Mandel (HOM) interference of highly indistinguishable photon pairs generated in the spontaneous parametric down-conversion process (SDPC) in a system whose relevant parts are sketched in Fig. 8.1. Not only is it the first observation of images of coalesced photon pairs but also an ultimate confirmation of an excellent signal-to-noise ratio and usability of the intensified sCMOS camera system. We utilize precisely determined photons positions, such as in Fig. 8.1(c), to construct mode images and reconstruct joint spatial distributions of two-photon states. Using developed setup and methods we analyze the effects of spatial distinguishability of the interfering photons.

We begin in Sec. 8.1 with a presentation of the general idea of experiments with single pairs of photons registered on the camera. Sec. 8.2 summarizes briefly a standard experimental setup for the generation of photon pairs via the SPDC process and its application in imaging experiments. Then we present the first results of shot-by-shot imaging of coalesced photon pairs in the HOM interference in Sec. 8.3. Thereafter we turn to utilizing the acquired positions of the registered photon pairs. In particular in Sec. 8.4 we show a simple method of coincidence imaging to retrieve single photon mode profiles. Then in Sec. 8.5 we show retrieval of spatial, joint probability distribution of two-photon states. Finally in Sec. 8.6 we analyze the influence of spatial distinguishability on the result of spatially resolved two-photon HOM interference and in Sec. 8.7 we study the role of mode phase structure of a photon.

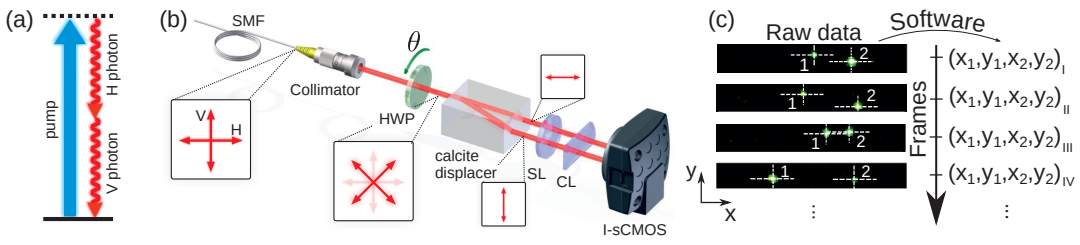


Figure 8.1: (a) Pairs of orthogonally polarized photons are produced in the II-type SPDC process. (b) Simplified scheme of the end part of the setup where photon pairs are imaged on the I-sCMOS camera. (c) Single pairs of photons emerge on low-noise background and they are easily identified and localized.

## 8.1 Experimental overview

In the previous parts we examined general capabilities of I-sCMOS camera system and we studied Raman scattered light of unknown spatial and statistical properties. Although we achieved the single photon level, any expected nonclassical properties of Raman scattering were covered by spurious noise which is a characteristic, yet practically unresolved problem of all warm-atomic systems (Reim *et al.*, 2011; Michelberger *et al.*, 2015).

In this part our central motivation is to study the properties of light truly exhibiting unambiguous nonclassical properties. As we argue in the introductory chapter, the squeezed vacuum produced in the SPDC process remains the easiest available source of nonclassical light. Therefore to focus our studies on nonclassical effects manifested by single photons we combined our camera with a setup source of photons based on the SPDC process.

As yet nonclassical effects studied with cameras have been predominantly performed in the regime where many photons are collected per each frame (Haderka *et al.*, 2005; Blanchet *et al.*, 2008; Machulka *et al.*, 2014). Here our aim is to perform experiments with single photon pairs collected per single camera frame. Similar studies would be hard or impossible with a standard ICCD or EM CCD while the presented experiments are feasible thanks to the high speed and low-noise of the I-sCMOS.

As sketched in Fig. 8.1(a), we use a degenerate SPDC of the second type. In this process photons of orthogonal polarization and equal central frequencies are produced. Orthogonally polarized photons can be readily separated and controlled independently. It is especially convenient for designing setups for study interference where each photon can be controlled and shaped individually.

The degeneracy of the SPDC process is a prerequisite for high indistinguishability between photon spectral modes required for high-visibility Hong-Ou-Mandel interference (Hong *et al.*, 1987) described in Sec. 1.6.3. The spectral modes are determined by the pump spectrum and the phase matching condition dictated by a non-linear crystal.

In Fig. 8.1(b) we depicted an excerpt from the experimental setup essentially presenting the basic manipulation of the photon polarization and its path. We begin with the photons spatially filtered by a single mode fiber which defines the spatial mode of the outgoing orthogonally polarized photons. Using a half-wave plate (HWP) we can rotate the polarization of both photons which then pass through the calcite polarization displacer. If the HWP axes are aligned with photons polarization direction ($\theta = 0^\circ$), the polarization state of the photons is unchanged and the calcite simply displaces two photons redirecting them into two spatially separated beams. Similar results are obtained for $\theta = 45^\circ$ where the roles of photons are effectively swapped and they go into opposite beams.

In between of the aforementioned scenarios, for $\theta = 22.5^\circ$, photons acquire a diagonal polarization depicted in the inset of Fig. 8.1(b). Then the calcite displacer acts exactly as a balanced, 50/50 beam splitter described in Sec. 1.6.1 If the impinging photons are indsitinguishable with respect to all degrees of freedom except for the polarization state, the Hong-Ou-Mandel effect introduced in Sec. 1.6.3 occurs on the displacer. As a result, we expect that the photons will coalesce and they will go in pairs either in the straightforward or in the displaced beam.

Finally, pairs of photons are imaged with a spherical lens (SL) and focused vertically with a cylindrical lens (CL) on the I-sCMOS camera. As depicted in Fig. 8.1(c) we are able to observe clear two-photon events seen as pairs of bright phosphor flashes easily distinguishable from the background. Like before, we determine the positions of photons.

In the following experiments described in the present chapter and in the following one we shall apply the idea of measurement presented above. Although we will introduce structuring of photons,

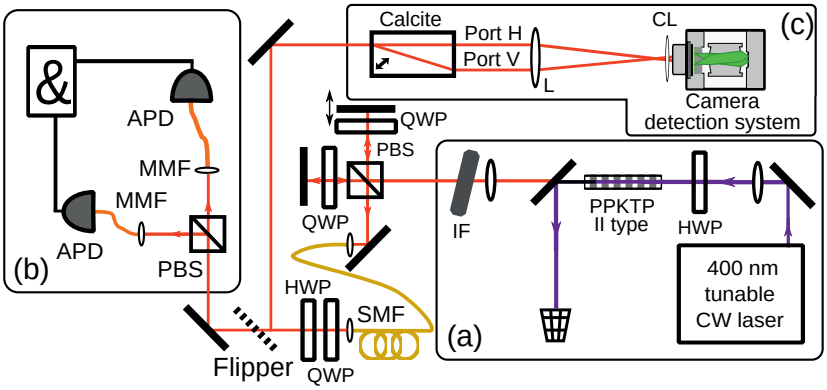


Figure 8.2: Experimental setup for generation and spatially resolved detection of highly indistinguishable photon pairs. (a) Photon pair source based on the SPDC in a type-II PPKTP crystal, followed by the optical delay line. (b) Standard avalanche photodiodes (APD) coincidence setup. (c) Calcite beam displacer imaged onto the front surface of the camera detection system described in Fig.8.1(a). HWP, QWP – half- and quarter-wave plates, PBS – polarizing beam splitter, MMF – multimode fiber, DM – dichroic mirrors.

eventually we always grab frames with photon pairs and process their positions.

## 8.2 Experimental setup

### 8.2.1 SPDC source

**Pump** Our experimental setup depicted in Fig. 8.2 begins with a continuous wave diode pump laser of the ECDL type manufactured by Toptica. We use beams of 8 mW power and 400 nm wavelength. The laser diode head is coupled to a single mode fiber, thus on the output we obtain a high quality beam in the fundamental mode of a width of 200 $\mu$m.

**Crystal** The pump beam enters a periodically poled KTP (PPKTP) non-linear crystal supplied by Raicol Inc. The periodic poling of the crystal domains of a length of 9.2 $\mu$m assures the quasi-phase matching condition (Boyd, 2003) for the pump and photons wavelengths, 400 nm and 800 nm, respectively. We picked a relatively short crystal of a length of 5-mm that assured a photon bandwidth of the order of 1 nm. The temperature of the crystal was stabilized to 24.1°C to ensure maximal and stable overlap between the spectral modes of single photons. The choice of the crystal length was dictated by a compromise between achievable source brightness and the ability to control and filter the spectral modes of the photons. The crystal in a holder is photographed in Fig. 8.3(a).

**Filtering** The pump laser beam after the SPDC is filtered out by a pair of dichroic mirrors. Then we perform several steps to erase any residual distinguishability of the photons with respect to the spectral, temporal and spatial degree of freedom. At first photons are filtered by a narrowband 3-nm full width at half-maximum (FWHM) interference filter (IF) manufactured by Semrock. The filtering is necessary because spectral modes of the photons differ slightly and their wings have to be cut by the filter. Then the photons are overlapped temporarily by means of an optical delay line supplied with a mirror mounted on a motorized stage. Finally the photons enter a single mode fiber that imposes the same fundamental spatial mode on both photons.

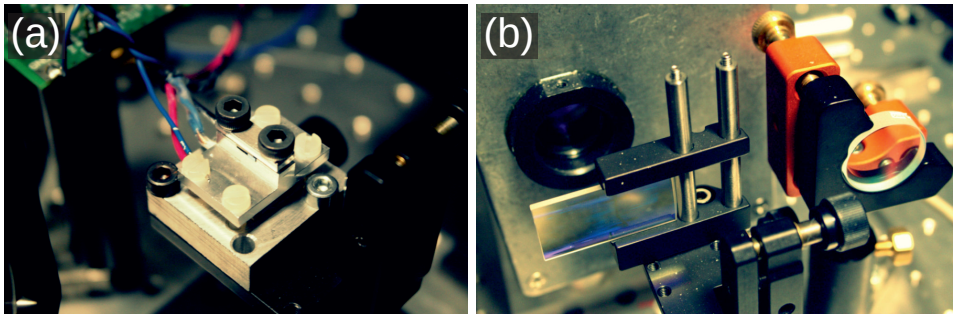


Figure 8.3: (a) The short, 5 mm long PPKTP nonlinear crystal enabling the quasi-phase-matched SPDC process of the II-type. The crystal holder is equipped with a Peltier module used for temperature stabilization. (b) In front of the I-sCMOS camera we place a cylindrical lens focusing photons in the vertical direction.

**Basic properties of the SPDC** To examine the basic properties of the source, we direct photons to multimode fibers (MMF) coupled to avalanche photodiodes (APD) manufactured by Perkin-Elmer. The coincidence setup is shown in Fig. 8.1(b). The signal from the APD goes to a standard NIM coincidence setup and afterwards to FPGA pulse counters. Typically we measure around $7.5 \times 10^5$ single photon events at each APD and up to $1.1 \times 10^5$ coincidences per second. The resulting ratio of coincidence to single counts that equals 15% originates from the losses due to spectral and spatial filtration as well as a finite quantum efficiency of the APD to be around 60%.

### 8.2.2 Imaging and camera setup

As it has been briefly introduced in the previous section, photons leaving the fiber impinge on a birefringent calcite crystal that separates orthogonally polarized paths by 3.2 mm. The rear surface of the calcite displacer is imaged on the photocathode of the I-sCMOS surface with a magnification of 1.1 in the horizontal direction. We placed a cylindrical lens (CL) $f = 30$ mm in front of the camera, as photographed in Fig. 8.3(b), to reduce the vertical size of the acquired region of interest. As a result we could increase the frame rate significantly. For instance we collected data from a 700 px $\times$ 22 px stripe with a frame rate of 7 kHz. This region size corresponds to approximately $9 \times 10^4$ microchannels of the image intensifier.

In the experiment we reduced the stored data by means of real-time preselection of the frames with at least one photo-event. In the further analysis only the frames with exactly two photon-events were taken into account. We checked that the number of frames with a higher number of the detected photons was negligible.

When analyzing the data collected by camera we noticed that there was an excess of closely distanced photo-events. We suspect that one avalanche in the microchannel plate can trigger another spurious avalanche in the proximate channel, thus seldom may we observe two photo-events instead of one. To make our analysis reliable we had to remove all frames where two photo-events appeared closer than 12 sCMOS pixels from each other. This resulted in characteristic diagonal no-events strips shown in Fig. 8.4,8.8.

As compared to the camera settings from Part I and Part II here we had to adjust the image intensifier gate time and simply synchronize it with the sCMOS acquisition. Here the gate triggering pulses were produced by a digital pulse generator manufactured by Stanford, model DG-645.

The gate time adjusts the rate of photon pairs incoming to the camera during a single frame exposure. Although the majority of the detected two-photon events originate from single photon

pairs, some are generated by two photons from two independent pairs. The latter type of event creates accidental coincidences that they decrease the registered visibility of two-photon interference.

The number of accidental coincidences scales quadratically with the gating time and we could trade off their contribution with single pair detection probability which scales up linearly. We adjusted the gate time to 40 ns, which ensured high visibility of the two-photon interference, explained in the next section, as well as provided an acceptable photon flux.

### 8.2.3 Nonclassical properties of photon pairs

With the APD coincidence system we characterized the ability of photon pairs to exhibit Hong-Ou-Mandel interference in standard HOM dip measurement, e.g. (Jachura *et al.*, 2014). Depending on the settings we regularly obtained a HOM visibility ranging from 91% up to 98%, see exemplary measurements in (Jachura and Chrapkiewicz, 2015b). The high visibility of HOM interference is the clear manifestation of nonclassical properties of the light used.

It is also instructive to analyze the simple photon statistics properties measured thereafter on a camera system and compare them with the properties of the Raman light discussed in Sec. 7.5 as well as with the measures of nonclassicality.

The exemplary parameters measured on a camera are as follows. The probability per frame for measuring a coincidence between the two regions: $p_{11} = 1.91 \times 10^{-5}$, the probability for a single photon in first region an none in the latter: $p_{01} = 6.09 \times 10^{-4}$ and in a reversed situation: $p_{10} = 5.08 \times 10^{-4}$. Simple comparison of those numbers yields the eventual efficiency of the whole system which equals 3.5% including the finite transmission of the consecutive elements.

The cross-correlation function between the orthogonal photons equals $g^{(2)}_{HV} = 58$, which significantly exceeds the classical limit of 2. From the above number we can deduce the mean number of photon pairs produced within a coincidence window to be around 0.015. When comparing this number with the simple two-mode squeezed state model in Eqs. (1.33,1.61) in Secs. 1.3.4,1.4.4, we expect the cross-correlation function to be approximately $g^{(2)} \approx 66$, which is close to the measured number.

Finally let us remark that other measures of nonclassicality are significantly more difficult to interpret. For instance the Fano noise reduction factor from Eq. 1.53 equals here $R = 0.991$ which is very close to the border between classical and nonclassical statistics. Concluding, in case of high losses in the setup the cross correlation function $g^{(2)}$ proves to be the most useful measure of nonclassicality.

## 8.3 Shot-by-shot imaging of the HOM interference

We begin the description of particular experiments with the observation of single pairs of photons in the recording of two-photon Hong-Ou-Mandel (HOM) interference (Hong *et al.*, 1987). The HOM interference, introduced in Sec. 1.6.3, is sometimes referred to as “coalescence” as photons appear to be merged together. Which is noteworthy, as yet this effect has been studied exclusively using area-integrating detectors, e.g. (Di Giuseppe *et al.*, 2003), where no spatial resolution is provided.

Here we show that for the first time we have been able to image the photon coalescence effect actually, shot-by-shot and with high spatial resolution. In Fig. 8.4 we show single frames of a camera with two-photon events . We present the following frames omitting those where none or only single photons were registered.

At first in Fig. 8.4(a) we present the situation where photons are temporarily distinguishable thus they do not interfere and the they appear in output modes of the calcite displacer in each possible

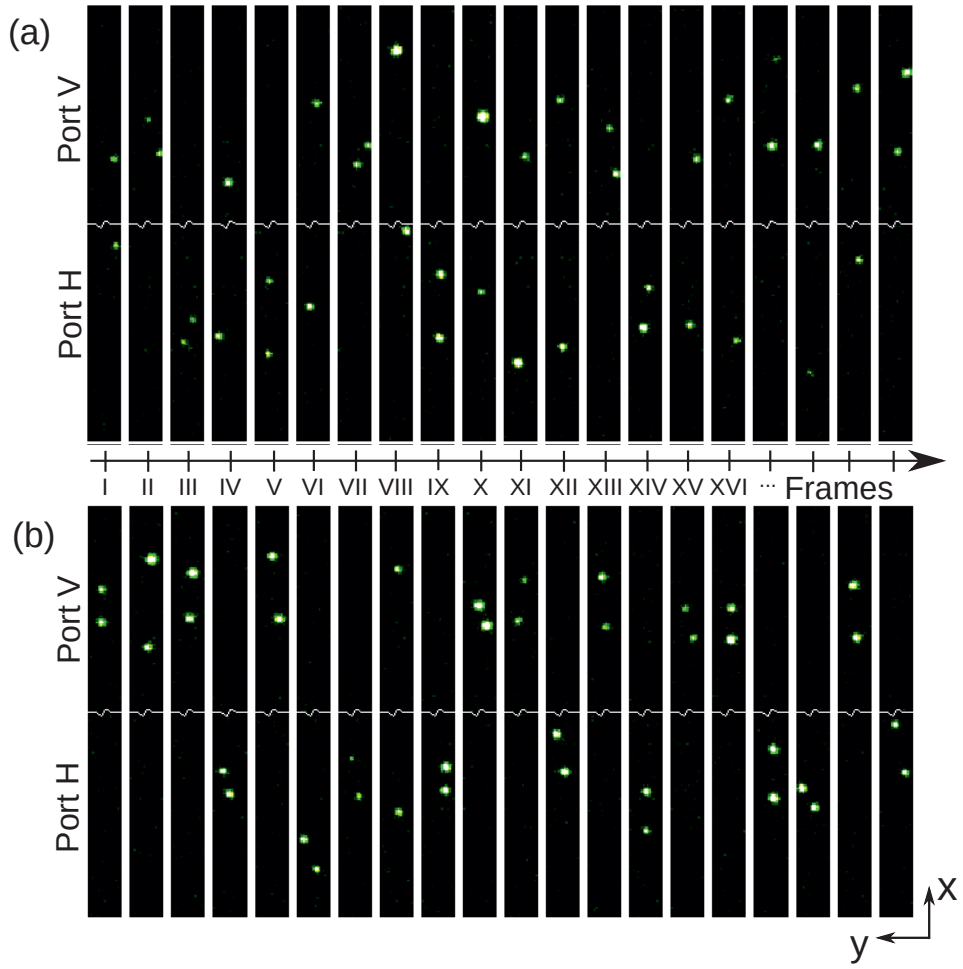


Figure 8.4: 20 camera frames presenting the image of the rear surface of the calcite beam displacer. For better visualization we display only the camera regions where photons appear. (a) Measurements with temporarily distinguishable photons result in their appearance in each configuration of the output ports: HH, VV and HV. (b) Hong-Ou-Mandel interference of virtually indistinguishable photons recorded for the first time. We can see a nearly perfect two-photon coalescence visible as grouping of photons in pairs in HH or VV configurations in all but one of the presented frames.

configuration. Conversely, in Fig. 8.4(b) we see a nearly perfect HOM effect obtained for a full temporal overlap of photon modes. In all but one of the presented frames the photons are detected together, appearing randomly in one of the output ports of the calcite. We can clearly distinguish them spatially within each mode area and they indeed demonstrate excellent two-photon coalescence. We collected the frames and presented them in a video clip (Jachura and Chrapkiewicz, 2015b).

Using the I-sCMOS camera we can naturally quantify the number of two-photon events, similarly to described in Part I. So far such a measurement has only been performed using ultra-low-temperature transition-edge superconducting detectors (Di Giuseppe *et al.*, 2003). In this way we quantified the high visibility of the HOM interference on the camera to be $96.3 \pm 1.1\%$ and more details are presented in (Jachura and Chrapkiewicz, 2015b). The result is comparable to the state of the art for sources based on bulk PPKTP crystals (Kuklewicz *et al.*, 2004). Such high visibility of the

HOM interference confirms both the excellent signal-to-noise ratio of our detection system and the indistinguishability of interfering photons spatial modes.

## 8.4 Coincidence imaging of single-photon-mode profiles

Now we turn to utilizing the coordinates of the detected photons positions. At first in this section we show a simple method of using them to retrieve the spatial structure of single photon modes. The problem of measuring a single photon transverse mode appears in numerous experiments and it is tackled with coincidence imaging schemes which work as follows. In general, as photons in the SPDC are produced in pairs, we can accumulate the positions of the photo-events, provided they are heralded by a photon detection in the conjugate mode. The heralding assures that we detect photons originating almost only from the SPDC process and virtually no dark counts nor background light are accidentally measured.

So far the coincidence imaging scheme has been implemented using ICCD cameras or APD systems. In the former the exposure of raw ICCD images is conditioned on a heralding photon detected by a bucket detector, such as the APD. The acquired images are simply summed to obtain a single photon mode profile (Fickler *et al.*, 2013). By means of APD detectors only one can use one detector as an area-integrating, bucket detector and another one to form the image. One can also apply the knife-edge method to measuring single photon beams parameters (Karpiński *et al.*, 2012). In both approaches to the coincidence imaging presented above the information about a position of the heralding photon is simply lost.

Here we have the capability of recording and spatially resolving both photons inside each pair. We set the HWP presented in Fig. 8.1(b) to the position $\theta = 0°$. Then the orthogonally polarized photons go to different output modes of the calcite displacer and on the camera we observe photon pairs appearing in separate sectors, as exemplified in Fig. 8.5(a). To a certain extent a detection of photon in port H heralds the photon in port V and *vice versa*. Therefore, each of the detected photons can be associated with one of the spatial modes it occupies, yet essentially none of their positions is lost contrary to standard coincidence imaging schemes. We accumulate their both central positions as shown in Fig. 8.5(b) and then we calculate their two-dimensional histogram.

In Fig. 8.5(c) we present a histogram of photon pairs positions constructed out of 5100 detected pairs. We can clearly see the structure of the modes. Here for proof-of-principle demonstration of

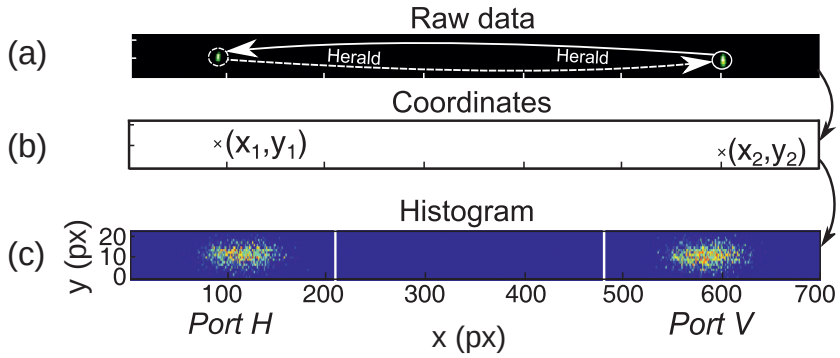


Figure 8.5: Proof-of-principle demonstration of the coincidence imaging of single photons modes. (a) Photons detected in independent modes effectively herald each other (a). Their positions are converted in real time into plain coordinate data (b) which are then accumulated in a histogram of approximately 5000 coincidence events revealing the spatial mode structure of the detected photons (c).

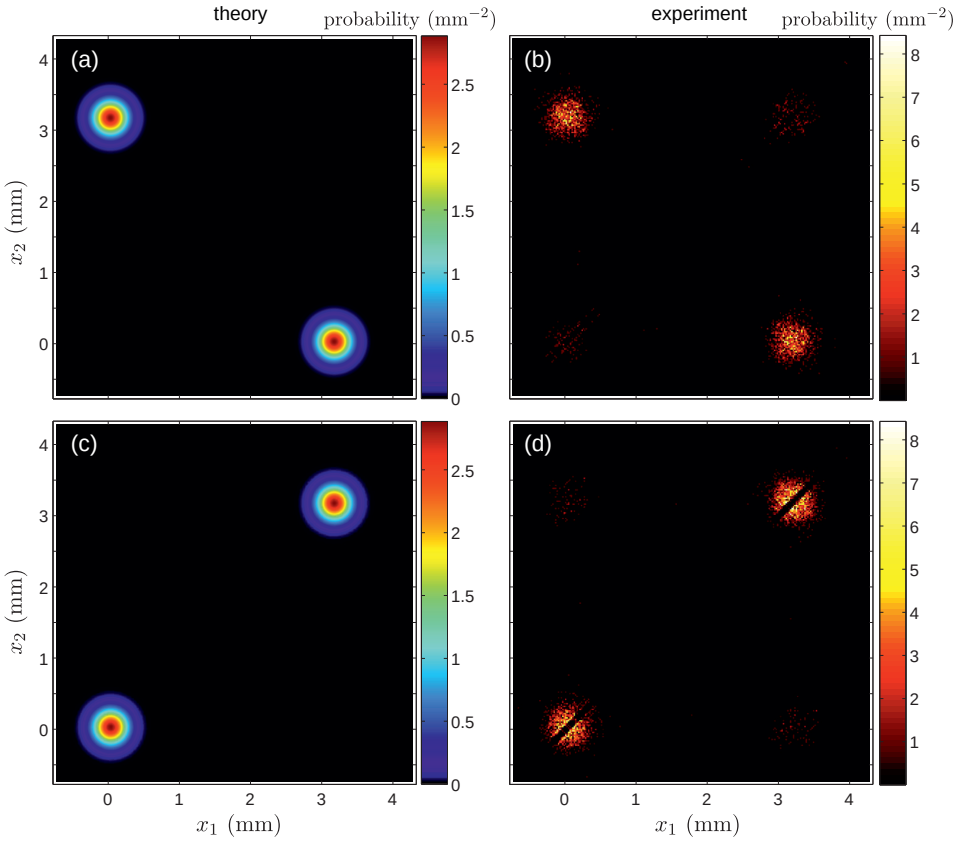


Figure 8.6: Joint probability distribution $p(x_1, x_2)$ of finding one photon at $x_1$ coordinate and the other at $x_2$ on the camera after the calcite displacer. (a) Theoretical prediction for $\theta = 0°$, where two photons go to opposite output ports of the displacer agrees with (b) the measured distribution. (c) Theoretical prediction for coalescing photon pairs after the Hong-Ou-Mandel effect for $\theta = 22.5°$ and (d) the experimental confirmation taken out from shots, such as in Fig. 8.4(b). Diagonal has been removed from analysis due to artificial hardware effects.

the method we used simple Gaussian modes.

The presented scheme has two advantages over traditional coincidence imaging schemes performed on ICCD and described aboves. Firstly, the resolution of the image is well below the image intensifier flash size since we extract the spots positions with subpixel resolution, as described in Part I. Secondly, the noise at each bin of the obtained image is Poissonian. As a result, the shot noise of the number of counts at each histogram bin supersedes the thermal noise of the raw image intensifier response.

## 8.5 Characterization of the joint distribution of two-photon states

Although the presented coincidence imaging scheme has clear advantages over the previous implementations, much more information can be extracted from the measured data. Since we have access to the positions of photons at each shot, we can virtually evaluate all kinds of statistics on the measured data instead of restricting ourselves to presenting simple averages.

Starting from this section we shall now analyze the joint probability distribution $p(x_1, x_2)$ of finding photon pairs at coordinates $x_1$ and $x_2$. Theoretical predictions in some simple scenarios have already been made in the introductory chapter in Sec. 1.6.4, and here we will extend this description to match our experimental results. Vertical coordinates $y_i$ shall be integrated over and omitted later in discussion to simplify the analysis.

Before the analysis of the experimental data from the camera, let us first derive a simple model so as to compare it with the measurements. Let us also evoke the Fig. 8.1(b) to follow the consecutive mode transformation of the photons. We start with the photons leaving single mode fibers and we expect them to be in Gaussian mode described in its waist by a normalized function:

$$f(x) = \frac{1}{\sqrt[4]{\pi w^2/2}} e^{-x^2/w^2}, \tag{8.1}$$

where $w$ is a standard measure of a Gaussian beam waist, here measured independently to be $w = 329\ \mu$m.

Then photons polarizations are rotated by $2\theta$ by the half-wave plate and enter the calcite crystal, separating one path by $D = 3.2$ mm. On the output of the calcite crystal, photons appear in two modes:

$$u_1(x) = \cos(2\theta)h(x) - \sin(2\theta)h(x-D), \tag{8.2}$$

$$u_2(x) = \sin(2\theta)v(x) + \cos(2\theta)v(x-D), \tag{8.3}$$

where $h(x)$ and $v(x)$ denote normalized transverse mode profiles of photons polarized initially in horizontal and vertical directions. For now we assume their mode profiles to be the same: $h(x) = v(x) = f(x)$. The rear surface of the calcite crystal is imaged on the camera and we expect to measure there the modes of the shape defined by the above formulas.

As we argue in Sec. 1.6.4, the expected joint probability distribution has the following form:

$$p(x_1, x_2) = \frac{1}{2}|u_1(x_1)u_2(x_2) + u_1(x_2)u_2(x_1)|^2. \tag{8.4}$$

In Fig. 8.6 we plot the theoretical joint probability distribution together with the measured data. Fig. 8.6(a-b) compare probability distributions for the HWP setting $\theta = 0°$, where empirical map has been constructed based on 1400 events. We clearly see that photons always appear in opposite camera regions.

Then we rotate the HWP to $\theta = 22.5°$ so as to obtain the Hong-Ou-Mandel effect, as observed in single shots in Fig. 8.4(b). The theoretical prediction presented in Fig. 8.6(c) clearly indicates that now we expect photons to appear in pairs close to each other, always within the same region of the camera. Indeed, the empirical joint probability distribution from 1600 two-photon events depicted in Fig. 8.6(d) agrees well with our expectations. The majority of two-photon events can be found near the diagonal of the map in two spots. As described in Sec. 8.2.2 we removed two-photon events appearing closer than 12 pixels due to artificial hardware effects. That resulted in no events on the diagonal seen as a black stripe.

As compared to the ideal scenario in Fig. 8.6(c), here we observe the residual events seen in the upper-left and bottom-right corners of the map. They correspond to a small fraction of pairs of the photons that did not undergo the HOM interference due to the finite distinguishability of their spectral modes. As a result ca. 4% of photon events went to the opposite output calcite modes. The result of a finite visibility of HOM interference due to all the other degrees of freedom, such as the

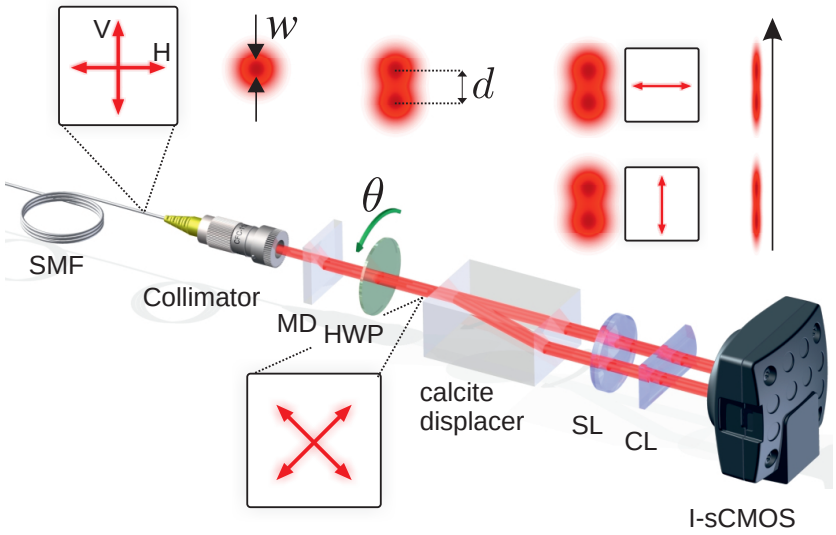


Figure 8.7: Setup for studying the effects of finite spatial distinguishability of photons in the two-photon interference. The setup is extended as compared that in Fig. 8.1(a) by a calcite mode displacer (MD), which displaces the vertically polarized photon by $d$. The half-wave plate (HWP) is set to $\theta = 22.5°$ like for the HOM interference. The calcite rear surface is imaged on the camera by a spherical lens (SL), wheras a cylindrical lens (CL) reduces the vertical size of the acquisition region to speed up the camera frame rate. The mode structure along the consecutive parts of the setup is presented above.

spectral one, can be described by the following formula originating from a complex expansion of Eq. 8.4:

$$p(x_1,x_2) = \frac{1}{2}\Big(|u_1(x_1)|^2|u_2(x_2)|^2 + |u_1(x_2)|^2|u_2(x_1)|^2\Big) + \mathcal{V}\,\mathrm{Re}\{u_1(x_1)u_2(x_2)u_1^*(x_2)u_2^*(x_1)\}, \tag{8.5}$$

where the last interference term is scaled by the visibility parameter $\mathcal{V}$. It can be readily checked that finite visibility leads to the appearance of Gaussian spots in the upper-left and bottom-right corners. In the extreme case of no visibility, the first two terms of Eq. 8.5 result in four equal-amplitude Gaussian spots seen in joint probability distribution maps.

## 8.6 Influence of the spatial distinguishability of photons on the two-photon interference

Till now we have studied spatially resolved HOM interference of photons that were spatially indistinguishable. Now we turn to examining the effect of finite, controllable spatial distinguishability between the photons. We shall study a simple case where two photons initially shaped by a single mode fiber are now slightly displaced in the transverse direction, as shown in Fig. 8.7. The further part of the setup remains unchanged and we perform measurements for the HWP setting $\theta = 22.5°$ to focus on the two-photon interference effects.

The displacement between the photons is accomplished by inserting a short calcite crystal into the previous setup shown in Fig. 8.1(b), displacing the vertically polarized photon by $d = 220$ $\mu$m. The radius of the photon modes equals $w = 329$ $\mu m$ as before. Now the single photons mode profiles

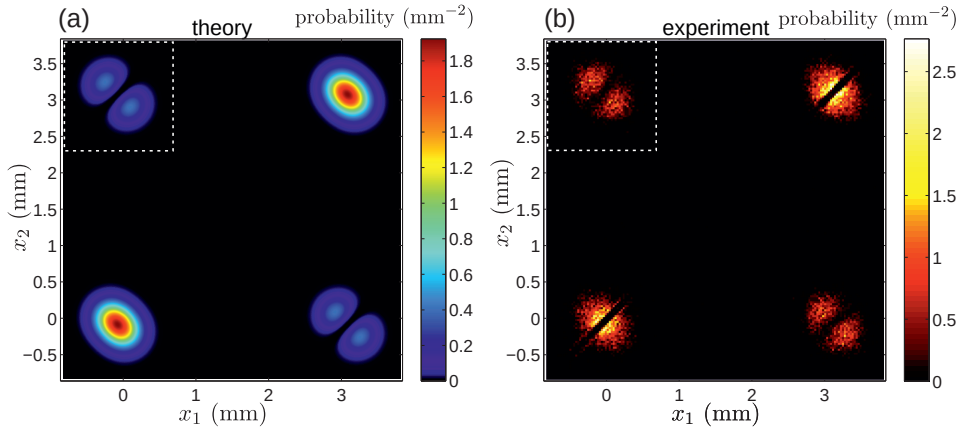


Figure 8.8: (a) Theoretical and (b) experimental joint probability distributions $p(x_1, x_2)$ upon displacing a vertically polarized photon mode by $d$. The upper-left corner marked by white-dashed square corresponds to the events caused by the residual distinguishability between the photons. In case of spatial distinguishability from the applied mode displacing, we observe a double-spot structure that will be carefully analyzed in further considerations.

are described as follows: $h(x) = f(x)$, $v(x) = f(x-d)$, where $f(x)$ denotes the Gaussian function from Eq. 8.1.

The expected joint probability distribution for spatially resolved coincidences to be measured on the camera is described by Eqs. (8.2-8.4) and its evaluation is plotted in Fig. 8.8(a). Next, in Fig. 8.8(b) we present the experimental demonstration for 8300 two-photon events. At first glance both maps are similar, yet a more careful analysis will reveal that this is only a qualitative resemblance.

As we argued before, any events seen in the upper-left (bottom-right) sector of the map denoting the coincidences in opposite output ports are deviations from the perfect HOM interference, illustrated in Fig. 8.6(c). While keeping the photons modes highly overlapping in all degrees of freedom but $x$, we can focus on almost pure effects of finite spatial distinguishability on the measured probability patterns.

The upper-left corners of the joint probability distributions are studied separately in Fig. 8.9. We can give a theoretical formula for this part of the probability distribution for $\mathcal{V} = 1$:

$$\tilde{p}(x_1, x_2) = \frac{1}{4}|(h(x_1)v(x_2 - D) - h(x_2 - D)v(x_1)|^2. \tag{8.6}$$

At first, let us note that if photons modes overlap entirely in the full range, i.e. $\forall_x h(x) = v(x)$, the probability of coincidence events is zero in the whole sector. This corresponds to the perfect HOM interference, such as presented in Fig. 8.4(c).

In our specific case of the displaced modes, the two terms of Eq. 8.6 cancel out if and only if:

$$\tilde{p}(x_1, x_2) = 0 \Leftrightarrow \forall_{i=1,2} h(x_i) = v(x_i) \Leftrightarrow x_2 = x_1 + D. \tag{8.7}$$

The condition in the above equation yields no events seen on the diagonal of the corner sector of the joint probability distribution, as presented in Fig. 8.9(a). Such situation can be explained as follows. The product of the mode amplitudes in one camera region at a certain point has the opposite sign and cancels out with the mode amplitude product in the other camera region for a point separated

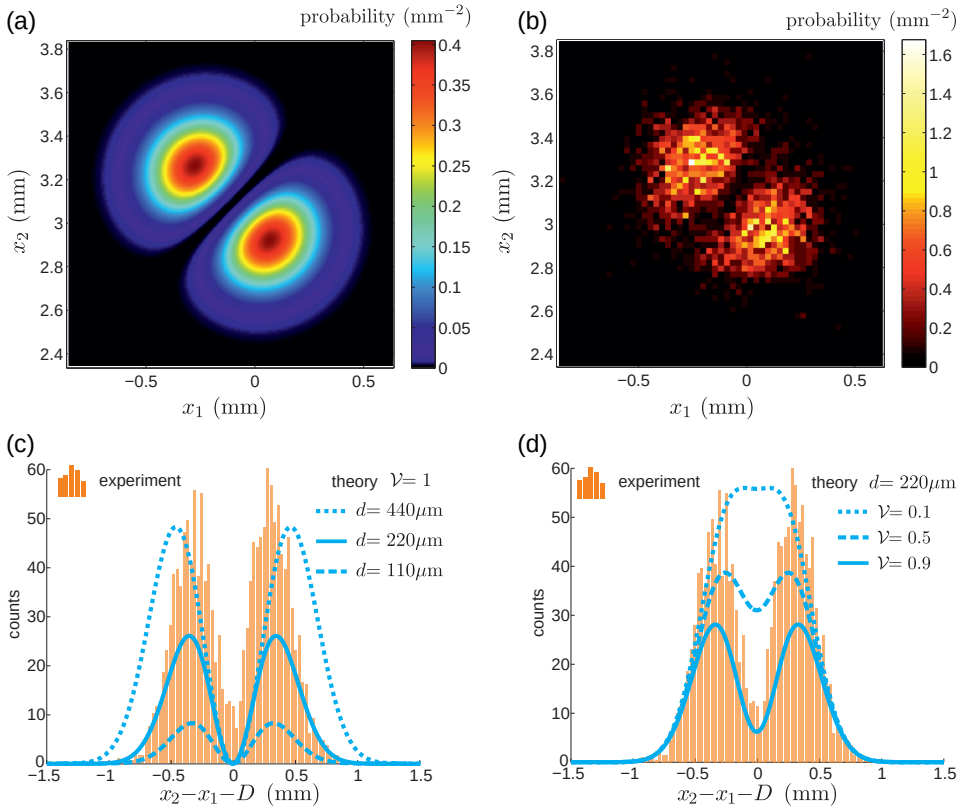


Figure 8.9: Upper-left corner of the maps of joint probability distribution $p(x_1, x_2)$ from Fig. 8.8 is related to deviations from perfect HOM interferece. (a) The theoretically predicted structure drops to zero on the diagonal. (b) Although the measured distribution resembles the theoretical one, the number of the measured events is twice as high as compared to the theoretical predictions. (c-d) Projections of counts distribution, measured in $4 \times 4$ px$^2$ bins, onto the antidiagonal. Their comparison with the model reveals high and unexpected discrepancies. (c) The model evaluated for three different mode displacements ($d = 220$ $\mu m$ was expected from auxiliary measurements) and (d) for three finite visibilities $\mathcal{V}$ due to different degrees of freedom.

exactly by $D$. Therefore, the likelihood of coincidence events separated horizontally by $D$ drops to zero due to perfect destructive interference.

The empirical distribution of coincidence events presented in Fig. 8.9(b) virtually vanishes on the antidiagonal and has a similar shape and size to that in the theoretical prediction. The total number of the measured coincidence events was about 3000 which constituted 36% of the total number of two-photon events. In contrast the expected contribution of opposite region coincidences should be 19%. Such a high discrepancy certainly deserves further explanations[1].

To facilitate the comparison of the experiment with the theoretical model we integrated the probability distributions over the diagonal direction and multiplied them by the total number of the registered events. As a result, we present in Fig. 8.9(c,d) the distributions of the coincidence counts

[1]Although our early studies were devoted to highlighting the effects of finite spatial distinguishaiblity in the two-photon interference, which was novel as such, the presented experimental scheme quickly found a further, even more appealing application in quantum metrology (Jachura *et al.*, 2015). Therefore the full agreement of the experimental results with the theoretical model was a prerequisite for further analysis in the context of precise measurements facilitated by the presented setup.

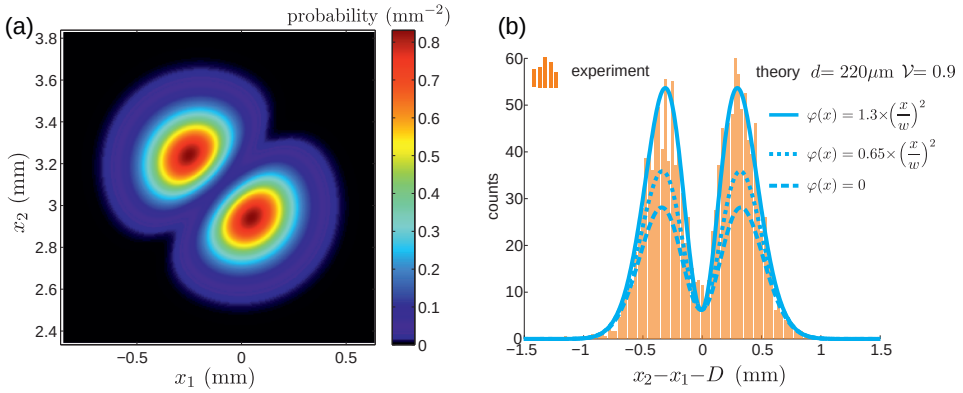


Figure 8.10: Extension of the theoretical model onto single photon wavefront distortions $\varphi(x)$ introduced by the imaging system fully explains the measured data. (a) The joint probability distribution $\tilde{p}(x_1, x_2)$ after the inclusion of the quadratic phase $\varphi(x)$ imprinted on both modes of the photons. The structure of distribution delusively resembles the previous one but yields twice as much events, which can be seen in (b) the projection of the number of counts on the antidiagonal. Theoretical plots drawn for visibility $\mathcal{V} = 0.9$ whose finite value is responsible for a subtle increase in the number of events seen on the diagonal $x_2 = x_1 + D$. Good agreement of the model with the measured data is obtained for the following phase structure $\varphi(x) = 1.3x^2/w^2$.

subjected to $4 \times 4$ pixels binning summed over the diagonal direction and indexed by coordinates $x_2 - x_1 - D$ in the antidiagonal direction.

At first, in Fig. 8.9(c) we compare the experiment with the theoretical models described by Eq. 8.6 for a different mode displacement $d$, which is the most significant parameter of the presented model. We see that within a high range of $d$ parameters its variations cannot explain the high number of the collected coincidence events, as they change the shape of the distribution simultaneously. As depicted in Fig. 8.9(d), we also verified the influence of the finite visibility $\mathcal{V}$ on the HOM interference due to other degrees of freedom described by Eq. 8.5. Although here we can easily raise the distribution amplitude, we excessively elevate the dip on the diagonal which is inconsistent with the outcome of the measurement .

All combinations of the values of the parameters in the presented model have failed to explain the obtained experimental data. It led us to the suspicion that the presented model had to be incomplete.

## 8.7 Influence of the single photon phase structure

In the presented experiment we exerted very precise and measurable control over the mode widths $w$ as well as the mode separation $d$. Additionally we independently measured the mode overlap in the vertical direction. Last but not least, we controlled the spectral-temporal mode overlap yielding the visibility $\mathcal{V}$ of the HOM interference measured by means of an auxiliary setup with avalanche photodiodes. Seemingly all the parameters have been included[2].

Although we have carefully imaged the surface of the calcite displacer on the I-sCMOS photocathode, the imaging system may have introduced some phase structuring of the photons. Indeed in the general case, imaging systems introduce a spatially varying phase imprinted on the images.

[2]Any systematic errors, non-ideal properties of all setup parameters were carefully measured and found to be insignificant.

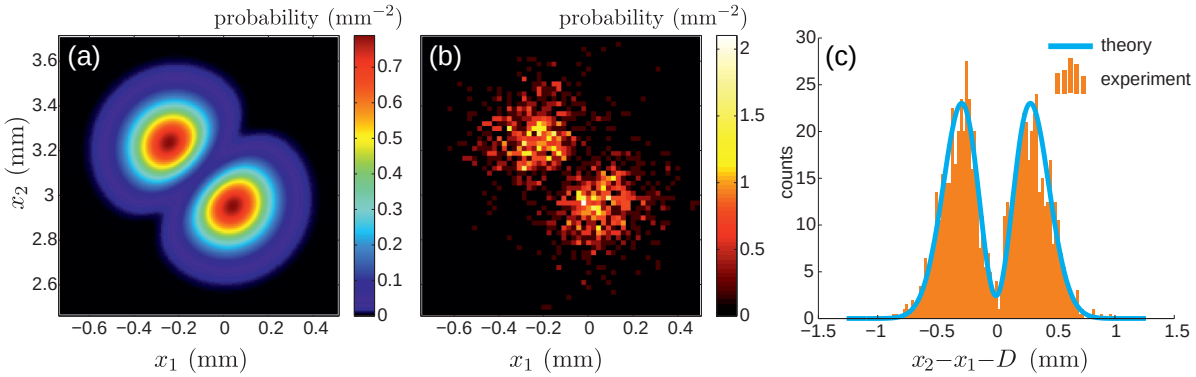


Figure 8.11: Redesign of the imaging setup assured an entirely flat phase $\varphi(x) = 0$ of the photons on the camera frontal surface. As a result, just in the first trial, we obtained perfect agreement of (a) theoretical predictions with (b) empirical probability distribution, clearly seen in (c) the projections of the number of counts on the antidiagonal.

Despite the fact both photons acquire virtually the same phase structure $\varphi(x)$ with respect to their mode center, their displacement leads to additional, previously overlooked distinguishability factor.

Now we extend the model so as to include the possible quadratic phase introduced by the imaging sytem. Now the individual single photon modes on the camera are defined as

$$h(x) = f(x)\exp(i\varphi(x)),\ v(x) = f(x-d)\exp(i\varphi(x-d)), \tag{8.8}$$

where we assume the quadratic phase structure

$$\varphi(x) = \alpha_2 \times \left(\frac{x}{w}\right)^2, \tag{8.9}$$

where $\alpha_2$ denotes a quadratic phase acquired by a mode at the $w$ radius distance.

Fig. 8.10 presents the model described by Eq. 8.5 with the quadratic phase profile included. Although the theoretical map of probability of coincidences $\tilde{p}(x_1, x_2)$ evaluated in Fig. 8.10(a) looks like before, we can see in Fig. 8.10(b) in the projections on the antidiagonal that we successfully matched the theoretical model with the theory. Indeed, as presented in Fig. 8.10(b), the proper choice of the amplitude of the phase quadratic term $\alpha_2 = 1.3$ in Eq. 8.9 can match not only the number of coincidence events but also the shape of the measured counts distribution.

To ultimately confirm the fact that we can faithfully and reliably predict experimental results in our setup we modified it so as to achieve the flat phase profile of both photons at the camera front surface. It was achieved by setting the waist of the Gaussian modes that leave the SMF fiber near the calcite displacer and then by constructing a phase preserving $4f$ imaging system[3].

The modified system yielded narrower photon modes to be measured by $w = 260\ \mu$m parameter. In Fig. 8.11 we present the empirical map of the coincidence events distribution $\tilde{p}(x_1, x_2)$ from the accumulated 1480 events of the 5650 two-photon events measured in total. The visibility from all auxiliary degrees of freedom was found to be $\mathcal{V} = 0.93$. The fraction of coincidence events was then 26.2% but since the mode width has changed, the theoretical expectation increased to 26.45%. Remarkably these numbers were virtually equal after ensuring the flatness of phase profiles.

In Fig. 8.11(b) we present the count distributions projected on the antidiagonal direction, labeled $x_2 - x_1 - D$. As compared to our previous considerations, here we immediately obtained perfect, quantitative agreement of the theory with the experiment. The results prove our full control

[3]This system is reused in the experiments presented in the next Chapter 9, where it is described in detail.

over and understanding of the process, setup, measurements and the analysis. Moreover here we see that the single photon phase structure significantly contributes to the distinguishability between the other photons although it might not be seen at first glance. Since the measured distributions of the joint probability seem to be highly sensitive to the aforementioned structure, this motivated us to apply our setup to measuring the single photon phase structure which has been hard to determine using any methods known so far.

## 8.8 Conclusions

### 8.8.1 HOM effect

To sum up, we presented the spatially resolved observation of the HOM interference of photon pairs. Photon pairs were produced via the SPDC process realized in a nonlinear PPKTP crystal. They interfered on the calcite displacer and were imaged on the I-sCMOS camera operated in the photon-counting regime. We directly observed clearly resolved pairs of photoevents randomly appearing in one of the two regions corresponding to the displacer output ports. We achieved a high visibility > 96% of the measured two-photon interference confirming the high signal-to-noise ratio of the camera system.

Remarkably this is the first such direct observation of the well known HOM effect. Beforehand it has only been measured on single pixel detectors as the so-called "HOM dip" seen in coincidence events (Hong *et al.*, 1987; Jachura *et al.*, 2014). The results were published in (Jachura and Chrapkiewicz, 2015b) and their summary appeared in (Jachura and Chrapkiewicz, 2015a).

### 8.8.2 Coincidence imaging

Then we utilized the photons positions to acquire spatial information about photons states. At first we postselected only the events where exactly one photon was found in each mode region. Then we accumulated two-dimensional histograms of photons positions revealing their initial mode structure. Such a procedure is equivalent to the coincidence imaging of the single-photon spatial mode structure (Karpiński *et al.*, 2012); here, however, we simultaneously gain information about the mode of each photon.

Positions of both photons were used to construct maps of joint probability distribution. Such maps provided the full information that can be gained from the shot-to-shot localization of photon pairs. Indeed, the presented maps allowed a clear distinction between two-photon states, such as the product or the N00N ($N = 2$) state. Assuming the purity of the two-photon state, the presented maps can be treated as the modulus square of the two-photon transverse wave functions.

### 8.8.3 Effects of spatial distinguishability of photons

Finally we found the off-diagonal part of the joint probability distribution maps to be sensitive to any distinguishability between photons. By providing high overlap between photon temporal-spectral modes we were able to focus on the effects of partial spatial distinguishability between photons. We analyzed theoretically several simple examples of how spatial distinguishability influences the expected joint probability distributions.

Then we implemented a proof-of-principle experimental demonstration for photons in two spatially displaced modes. The comparison of the experimental results with the theoretical predictions initially revealed high inconsistency that could not be explained by measurements errors. Careful

studies indicated that the internal phase structure of photons imprinted by imaging system led to additional subtle spatial distinguishability between photons. Indeed, the application of the phase-preserving $4f$ imaging system and precise control of the photon phase yielded joint probability distributions in perfect agreement with our simple model. These observations became the foundations for the general method of single photon phase retrieval presented in the next chapter.

The measurements presented in Sec. 8.6 have already found their applications in a novel meteorological protocol described in our recent paper (Jachura *et al.*, 2015). Those results indicate that the careful design of the spatial mode, such as the displacement studied here, connected with spatially resolved detection of photons can raise the precision of certain quantum interferometry schemes above the shot noise level.

### 8.8.4 Further perspectives

The results presented in this chapter are the first high signal-to-noise ratio measurements of photon pairs with the use of cameras. Only a few earlier papers have reported observations of the low-visibility two-photon interference (Abouraddy *et al.*, 2001) as well as of the low-contrast spatial correlation from the SPDC (Oemrawsingh *et al.*, 2002).

The presented techniques are valuable steps towards the exploration of the spatial correlation exhibited by nonclassical light generated in photonic systems (Moreau *et al.*, 2014). Moreover, they provide an appealing framework for building quantum-enhanced super-resolution imaging systems (Rozema *et al.*, 2014; Krishnaswami *et al.*, 2014).

Further evolution of cameras should enable even faster acquisition of two-dimensional images resolving spatially and temporally single photons. We anticipate that the most promising technologies include cryogenic nanowires (Dauler *et al.*, 2014), time-stamp functionality (John *et al.*, 2012) as well as direct electronic readout of the charge from a microchannel plate.

CHAPTER 9

# HOLOGRAPHIC MEASUREMENT OF A SINGLE-PHOTON TRANSVERSE WAVE FUNCTION

Based on our previous results, in this chapter we derive and demonstrate the ultimate method for characterizing the spatial structure of a single photon. Regardless of the fact that a single photon does not have a global phase, here we demonstrate that its local phase structure can be retrieved in a measurement scheme adopted from classical holography. The procedure returns a complete, complex wave function of a single photon in a transverse degree of freedom.

At first in Sec. 9.1 we introduce the general idea of measuring the single photon transverse phase structure, as summarized in Fig. 9.1. Then in Sec. 9.2 we present exemplary theoretical predictions for various local phase structures of a photon.

In 9.3 we extend our experimental setup introduced in Chapter 8. Then in Sec. 9.4 we present and discuss raw measurements results of photons mode amplitude and coincidence distribution. The spatial phase structure of a single photon is retrieved in Sec. 9.5 using the presented numerical algorithm. Finally, in Sec. 9.6, we present two possible generalizations of the method.

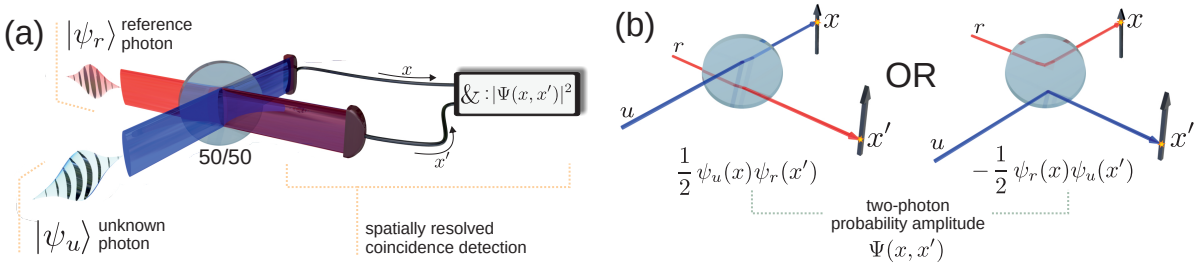


Figure 9.1: (a) Quantum interference of two spatially structured photons on a 50/50 beam splitter. We repeatedly overlap an *unknown* photon $|\psi_u\rangle$ to be characterized with a *reference* (known) photon $|\psi_r\rangle$ with a flat local phase. The coincidence events localized at $x$ and $x'$ are used to determine the joint probability distribution $|\Psi(x,x')|^2$ which is sensitive to any structural differences between the transverse wave functions of the photons $\psi_u(x)$ and $\psi_r(x)$ including the local variations of their phases. (b) The observed coincidence event originates from non-destructive interference of probability amplitudes of two classically exclusive but quantum-mechanically coexisting scenarios presented in the left and right panes.

## 9.1 Overview of the method of a hologram of a single photon (HSP)

In the previous chapter, in Sec. 8.6, we have demonstrated an experimental method for studying the influence of spatial distinguishability on the joint probability distributions of two-photon events. While carrying out the experiment, we unexpectedly observed that the measured coincidence patterns were very sensitive to single photons local phase structures. This motivated us to investigate this phenomenon in deep. As a result we developed a novel method for measuring the structure of a single photon phase, resorting to techniques known from holography.

### 9.1.1 Coarse-grained transverse wave function

In Sec. 1.2.3 we presented a concise description of a wave function[1] of a paraxial photon in the spatial domain, which match the scope of this chapter. In particular we discussed a coarse grain wave function that in the transverse $x$ degree of freedom reads as $\psi(x)$. It should simply be treated as a probability amplitude of finding a photon on a transversely located detector within a space of a size exceeding the wavelength scale.

Although the measurement of $|\psi(x)|^2$, which stands for probability distribution, is a relatively simple and straightforward task to do with our I-sCMOS camera, the determination of the photon phase structure $\varphi(x) = \arg(\psi(x))$ is an incomparably harder challange. Thus far it has been measured using indirect tomographic techniques (Smith *et al.*, 2005) or weak measurement approach (Lundeen *et al.*, 2011).

### 9.1.2 Classical holography

As a matter of fact, the most developed and accurate methods of measuring the spatial phase structure of classical light are offered by interferometry. Among them, holography, invented by Gabor (1948), is the quintessence of encoding the complete phase-amplitude information about the detected light.

Holography allows recording of three-dimensional information about the shape of an object by imprinting the distorted wavefront $\phi(x,y)$ of the scattered light in a flat interference fringe pattern shaped as $\cos^2(\phi(x,y)/2)$, called a hologram. Later it can be used to imprint the phase structure to mimic the original light as if it propagated from the object.

Nowadays holograms are recorded using high resolution digital cameras. Displaying them digitally also became a standard experimental routine achieved by the development of liquid crystal spatial light modulators (SLM). SLM are also commonly applied to tailor single photon spatial structure (Fickler *et al.*, 2012). In spite of all those technical advances, till now there have been no complimentary methods for direct holographic recording of a photon shape.

### 9.1.3 Indeterminate global phase of a single photon

To be created, a hologram requires a very stable phase relations with a regular wave-front reference light. This condition also implies that holography practically does not apply to a situation where an object and the reference light come from two unsynchronized light sources or the stable phase relation cannot be ensured for fundamental reasons.

[1] Here, in this chapter we shall purposefully switch to the term “wave function” instead of “mode function”. Both terms are equivalent for a single photon description, but “wave function” is more commonly known to be related with probability distributions.

Holography has never investigated a single photon phase structure because, contrary to coherent light, single photons have an entirely indeterminate phase. This feature has been stressed by the Dirac's statement that "interference between two different photons never occurs" (Dirac, 1981). The indeterminate phase stems from perfect rotational symmetry of photon Wigner function in the phase space (Lvovsky *et al.*, 2001) or alternatively from the particle number–phase Heisenberg uncertainty principle $\Delta n \Delta\varphi \geq 1/2$, which applied to the well-defined number of particles (e.g. $n = 1$) results in an infinite phase-uncertainty.

The above reasoning explains why the spatial shape of a photon described by its wave function has never benefited from interferometric precision and a simplicity provided by the holography methods.

### 9.1.4 Application of nonclassical interference

Here we propose and experimentally demonstrate the method of creating a hologram of a single photon (HSP) encoding full information about its spatial structure given by the complex wave function $\psi(x) = \langle x|\psi\rangle$ (Lundeen *et al.*, 2011). HSP can be obtained if the standard first-order interference of optical fields is replaced by the nonclassical interference of spatially varying two-photon probability amplitudes and if we extend the detection to two detectors.

The idea of HSP, sketched in Fig. 9.1(a), relies on overlapping of the unknown photon $|\psi_u\rangle$ to be characterized with a known[2] reference photon $|\psi_r\rangle$ having a flat local phase. The overlapping takes place on the 50/50 beam splitter. Both photons are assumed to ideally occupy the same spectral and temporal modes. As we already know, if photons are additionally spatially indistinguishable they will undergo the Hong-Ou-Mandel effect (Hong *et al.*, 1987) discussed previously.

Here, similarly to Sec. 8.6, we shall focus on spatial features distinguishing the photons. Local differences between the photons wave functions $\psi_u(x)$ and $\psi_r(x)$ prevent them from ideal two-photon coalescence, thus the observation of spatially localized coincidences $(x, x')$ serves as a sensitive probe of the spatial structure of the unknown photon.

As we depict in Fig. 9.1(b), such a coincidence event can originate from two classically exclusive events: either from the transmission or the reflection of both photons at the beam splitter. These two events are fundamentally indistinguishable and they account simultaneously for the two-photon probability amplitude $\Psi(x, x')$ describing one photon localized at position $x$ and the other at $x'$. The two-photon probability amplitude can be intuitively expressed with the Feynman's path integral formalism as:

$$\Psi(x, x') = \frac{1}{2}(\langle x|\psi_u\rangle\langle x'|\psi_r\rangle - \langle x|\psi_r\rangle\langle x'|\psi_u\rangle). \tag{9.1}$$

As we will argue in the next sections, the measurement of the joint probability distribution described by the modulus square of the above Eq. 9.1 $|\Psi(x, x')|^2$ contains the full information about the photon phase structure and similarly to classical holograms they preserve full information about the object light wave front. In analogy, this fact provoked us to call the measured pattern $|\Psi(x, x')|^2$ a hologram of a single photon (HSP).

[2] As we show in Sec. 9.6 the method can be readily generalized to characterize two unknown photons.

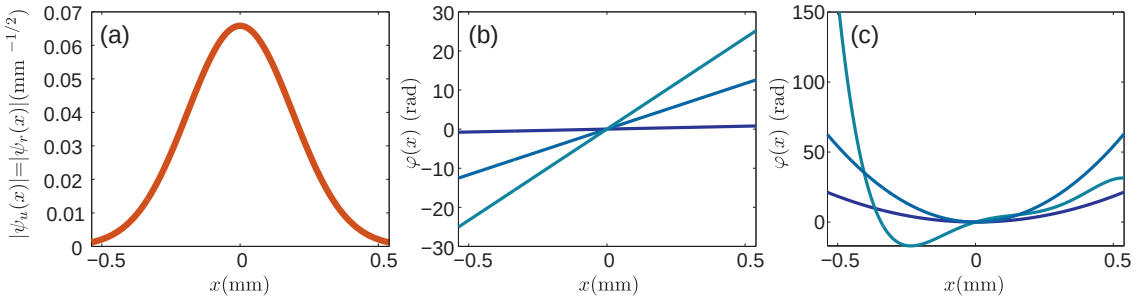


Figure 9.2: (a) Model Gaussian amplitude, $w = 269$ $\mu$m of the unknown and reference photons $|\psi_u(x)| = |\psi_r(x)|$ used in all theoretical examples and corresponding to the experimental demonstration. (b) Three linear, (c) quadratic and polynomial phase structures of the unknown photon $\varphi(x) = \arg(\psi_u(x))$ used in further HSP examples. Constant offset of phase is arbitrary and it has no physical meaning. For the experimental demonstration we used one of the presented quadratic phase profile defined as $\varphi(x) = 1.69 \times (x/w)^2$.

## 9.2 Encoding of the local phase structure in HSP

### 9.2.1 General form of the HSP and its interpretation

Let us first analyze the feature of the patterns of joint probability distribution $|\Psi(x,x')|^2$ that can encode the *local* phase structure of the photon regardless of its entirely indeterminate *global* phase. We assume the flat phase of the reference photon $\arg(\psi_r(x)) = \text{const}$ and the structured local phase of the unknown photon $\varphi(x) = \arg(\psi_u(x))$. Both phases are defined up to the additive constant. Then the pattern of HSP has the following complex expansion, where similarly to Eq. (8.5) we include a finite visibility $\mathcal{V}$ due to other degrees of freedom:

$$|\Psi(x,x')|^2 = \frac{1}{4}(|\psi_u(x)|^2|\psi_r(x')|^2 + |\psi_r(x)|^2|\psi_u(x')|^2) - \frac{\mathcal{V}}{2}|\psi_u(x)||\psi_u(x')||\psi_r(x)||\psi_r(x')|\cos(\varphi(x)-\varphi(x')). \tag{9.2}$$

The mathematical structure of Eq. (9.2) resembles a mathematical structure of a simple classical interference pattern to some extent. The first two terms have the meaning of the intensity terms whereas the last one is the phase-dependent interference term. Here however, we deal with a two-dimensional structure originating from the nonclassical interference of two one-dimensional wave functions. The last interference term is entirely insensitive to any constant offset of the phase pattern $\varphi(x)+\text{const}$, as opposed to classical interference fringes known to be extremely sensitive to any phase drifts or fluctuations.

The formula describing HSP given in Eq. (9.2) has a particularly simple form when both amplitudes of photons are equal $|\psi_u(x)| = |\psi_r(x)|$. Then it is expressed as follows:

$$|\Psi(x,x')|^2 = \frac{1}{2}|\psi(x)|^2|\psi(x')|^2(1-\mathcal{V}\cos(\varphi(x)-\varphi(x'))). \tag{9.3}$$

Noticeably, here the cross-sections of HSP have a very intuitive interpretation. For a fixed $x' = x'_0$ we obtain:

$$|\Psi(x,x'=x'_0)|^2 = \frac{1}{2}|\psi(x)|^2 c_0(1-\mathcal{V}\cos(\varphi(x)-\varphi_0)), \tag{9.4}$$

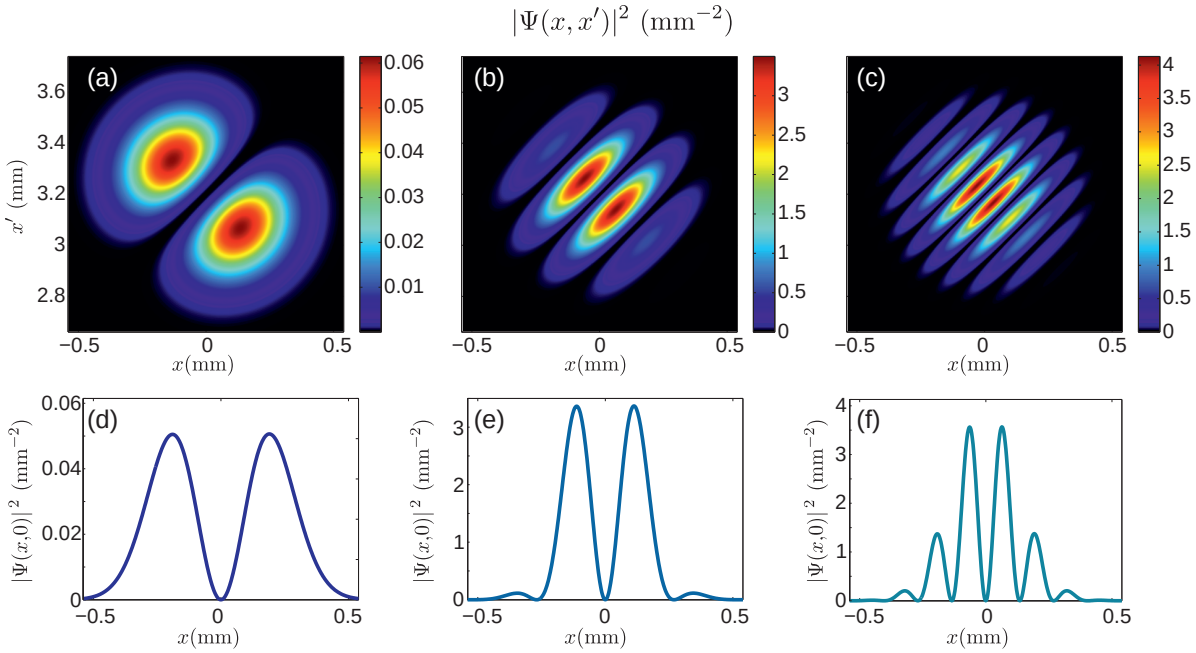


Figure 9.3: Encoding of the local phase in the HSP, represented by a spatial probability distribution of the coincidence events $|\Psi(x,x')|^2$, is particularly simple and intuitive for the linear phase $\varphi(x) = \alpha_1 x/w$ of the unknown photon. We plotted the HSP for the photons in two Gaussian modes with identical amplitudes $|\psi_u(x)| = |\psi_r(x)|$, as in Fig. 9.2(a), and for the phases in Fig. 9.2(b) for the following parameters: (a) $\alpha_1 = \pi/8$, (b) $\alpha_1 = 2\pi$, (c) $\alpha_1 = 4\pi$. (d-f) The cross-sections are equivalent to standard classical interference patterns, yet they are produced by nonclassical interference, such as that in Fig. 9.1(b).

where the constants read as $c_0 = |\psi(x_0')|^2$, $\varphi_0 = \varphi(x_0')$. Remarkably the mathematical form of Eq. (9.4) is now exactly the same as for classical interference of two electric fields of the same amplitude where one field has a phase profile $\varphi(x) - \varphi_0$.

As we know, in the classical interference patterns the phase offset $\varphi_0$ shifts fringes. As we explained by Eq. 9.4 each cross-section of HSP contains a classical-like interference pattern. Changing the cut line position $x'$ we observe the moved fringes. The effect is equivalent to a change in the relative phase between two classical interfering fields.

Concluding the interpretation, let us remark that the interference patterns in HSP originate from an entirely different, nonclassical phenomenon of interference of two-photon probability amplitudes. Below we give several examples of HSP structures, further elucidating the phase encoding. Then, in the measurements, not only will we confirm the mathematically derived HSP structure experimentally, but we also will retrieve the single photon local phase $\varphi(x)$ to determine its full, complex wave function $\psi(x) = |\psi(x)|e^{i\varphi(x)}$.

### 9.2.2 Linear phase coding

What we begin with is perhaps the simplest example of the HSP where an unknown photon is assumed to have the linear phase profile. We assume that both the reference and the unknown photon have now equal Gaussian amplitudes $|\psi_u(x)| = |\psi_r(x)|$ defined in Eq. (8.1) by the $w$ parameter and depicted in Fig. 9.2(a). The linear phase of the unknown photon is assumed to be $\varphi(x) = \alpha_1 x/w$, as plotted in Fig. 9.2(b) for three different values: $\alpha_1 = \pi/8, 2\pi, 4\pi$. The corresponding HSP structures

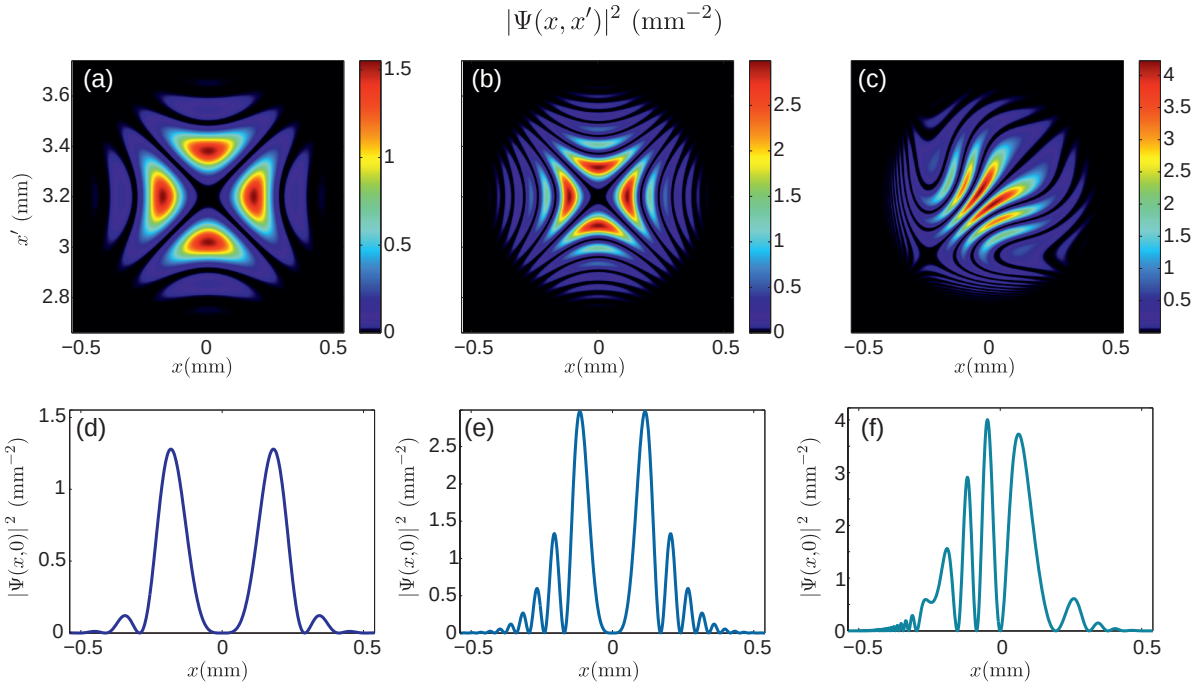


Figure 9.4: HSP ($|\Psi(x,x')|^2$) encoding of (a-b) quadratic $\varphi(x) = \alpha_2 \times (x/w)^2$ and (c) fifth-order polynomial phase structures presented in Fig. 9.2(c). (a) The structure for $\alpha_2 = 1.69 \times \pi$ was chosen for experimental demonstration. (d-f) The cross-section reveals classical-like interference fringes for the phase shift defined by the cross-section cut line.

with their central horizontal cross-sections are depicted in Fig. 9.3.

In Fig. 9.3(a), for $\alpha_1 = \pi/8$ the resulting HSP shape is similar to the previously described structures appearing in Sec. 8.6-8.7, yet it originates from pure phase distinguishability between the photons. In the next plots Fig. 9.3(b-c) we observe a higher number of visible fringe nodes which can be counted approximately by the $2\alpha_1/\pi$ parameter. Beneath in Figs. (d-f) we present the corresponding HSP cross-sections. As we argued before, they are identical with ordinary classical interference patterns. Which is noteworthy, as seen in Fig. 9.3(f), the envelope of the HSP has a smaller width than wave function amplitude, as in Fig. 9.2(a) This is because the HSP is proportional to the amplitude square, as given by Eq. (9.4)

### 9.2.3 Polynomial phase coding

Next, we turn to analyzing the HSP structures for more complex phase profiles presented in Fig. 9.2(c). In Fig. 9.4 we show the HSP for quadratic and fifth order polynomial phases. In particular the plots in the second row, Fig. 9.4(d-f), present the HSP cross-section that again are equivalent to standard interference fringes obtained in an analogous classical situation, as described by Eq. (9.4). Here, however, the phase offset $\varphi_0$ varies non-linearly across the consecutive cross-sections resulting in patterns seen above in Fig. 9.4(a-c).

In Fig. 9.4(a,b) we presented the HSP for the quadratic phase profile $\varphi(x) = \alpha_2 \times (x/w)^2$. The structure in Fig. 9.4(a) for $\alpha_2 = 1.69 \times \pi$ was chosen for experimental demonstration. Fig. 9.4(b) presents the HSP for a steeper phase profile $\alpha_2 = 5 \times \pi$ resulting in a higher number of visible nodes. For comparison Fig. 9.4(c) presents the HSP for a generic fifth-order polynomial local phase struc-

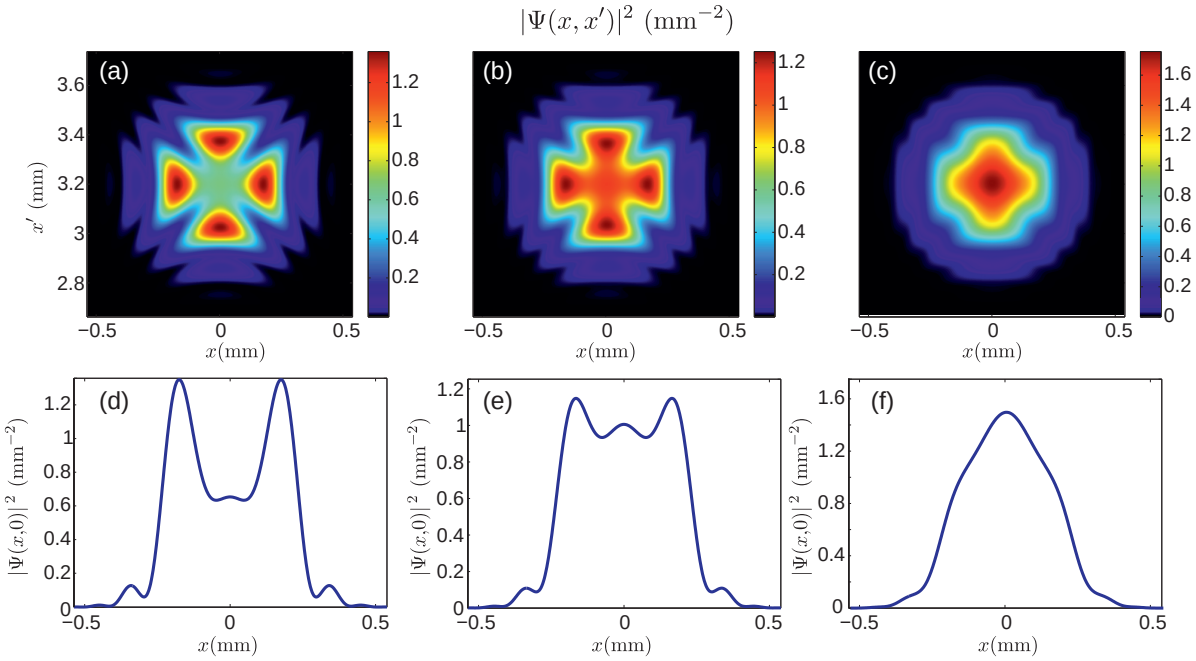


Figure 9.5: Influence of a finite visibility $\mathcal{V} < 1$ on the HSP seen in joint probability distribution pattern $|\Psi(x,x')|^2$ for the quadratic phase profile selected for the experimental demonstration. Coincidence patterns $|\Psi(x,x')|^2$ are presented for (a) $\mathcal{V} = 0.9$, (b) $\mathcal{V} = 0.5$, (c) $\mathcal{V} = 0.1$ and (d-f) beneath we plot their central cross-sections $|\Psi(x,0)|^2$.

ture.

From the presented examples we can see that for perfect visibility $\mathcal{V} = 1$ the diagonal of the HSP is always zero. The patters are also symmetrical with respect to the diagonal. Moreover, if the phase structure is symmetric then the HSP has four axes of symmetry.

Since the concept of HSP is new and, despite of the given examples and explanations, HSP structures might still be considered unobvious we present more examples in Appendix E, also for discontinuous functions.

### 9.2.4 Influence of the finite visibility $\mathcal{V} < 1$

As we are about to demonstrate experimentally the HSP structure similar to that illustrated in Fig. 9.4(a), let us discuss briefly the consequences of finite spectral distinguishability of the interfering photons. Fig. 9.5 extends the scenario from Fig. 9.4(a) to three finite visibility parameters $\mathcal{V} = 0.9, 0.5, 0.1$. As can be seen from the presented plots, the characteristic cross-like shape remains relatively clear for visibilities of 0.5 and higher, as seen in Fig. 9.5(a-b). In contrast, for the smallest visibility parameter 0.1, in Fig. 9.5(c), the initial HSP structure is barely visible and the joint probability distribution is dominated by a Gaussian profile obscuring the fringe structure.

## 9.3 Setup for measuring the hologram of a single photon

In order to demonstrate experimentally the HSP method, we can utilize most parts of the setup exploited in the previous Chapter 8. Essentially, the setup consists of a source of highly indistinguishable photon pairs and involves spatially resolved detection provided by the I-sCMOS camera.

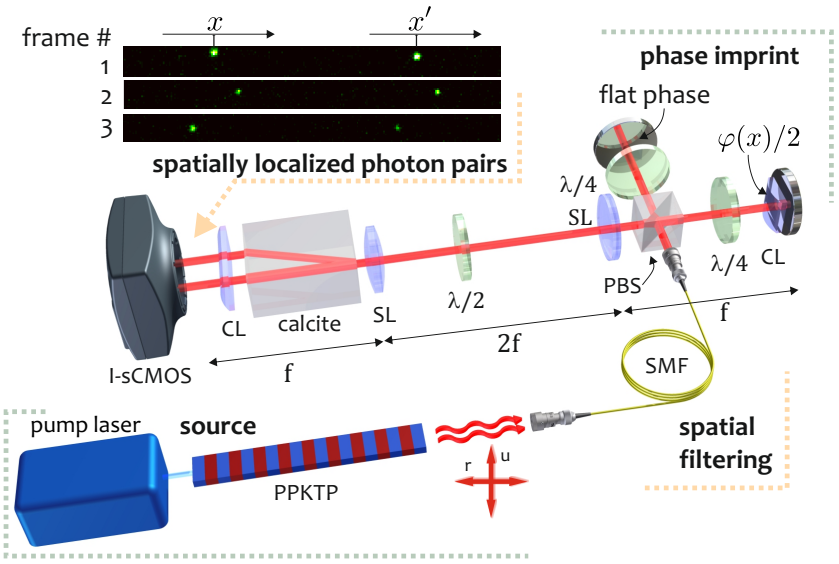


Figure 9.6: Experimental setup for measuring the HSP. Pairs of orthogonally polarized photons generated in the degenerated SPDC are prepared in the same spectral mode. The photons are transmitted through a single mode fiber, separated by the polarization beam splitter (PBS) and matched temporally. Moreover, at a flat wavefront surface on the mirror, a phase profile $\varphi(x)$ is imprinted on an unknown photon during its double-pass propagation through a cylindrical lens imprinting a quadratic phase depicted in Fig. 9.2(a). We localize photons leaving two distinct ports of the beam-splitter implemented collinearly as a half-wave-plate (HWP, $\lambda/2$) and going through a calcite crystal by means of the I-sCMOS camera. Both the flat wavefront surface of the reference photon and the phase-impriting cylindrical lens surface are mapped onto the camera with a phase-preserving $4f$ system.

As compared to the previous implementation, it requires a new imaging system and the phase imprinting system. The idea of the experimental setup is presented in Fig. 9.6 and its full photography is shown in Fig. 9.7. Now let us briefly review the consecutive parts of the setup and discuss its modifications as compared to its version from Chapter 8.

### 9.3.1 Photon source

As can be seen in Fig. 9.7, the source and the imaging and detection parts of the system have been placed on separate breadboards. The source part was devoid of the delay line, placed in the imaging system. The generated photons of orthogonal polarizations were subjected to spectral filtering and then entered the single mode fiber (SMF).

### 9.3.2 Phase imprint

The HSP structure shown in Fig. 9.4(a), selected for experimental demonstration, originated from the quadratic phase imprinted on one photon to be characterized, called the unknown photon, and the flat phase of the other, called the reference photon. Thus, the photons leaving the fiber were split and then directed to the variable-arm-length delay line in a Michelson-Morley interferometer configuration that has previously been used before the SMF coupling.

We inserted a cylindrical lens of the focal length $f_c = 75$ mm in the proximity of one of the mirrors, as photographed in the close-up in Fig. 9.8. The cylindrical lens imprinted a quadratic phase profile in the horizontal direction on the unknown photon during its propagation back and forth.

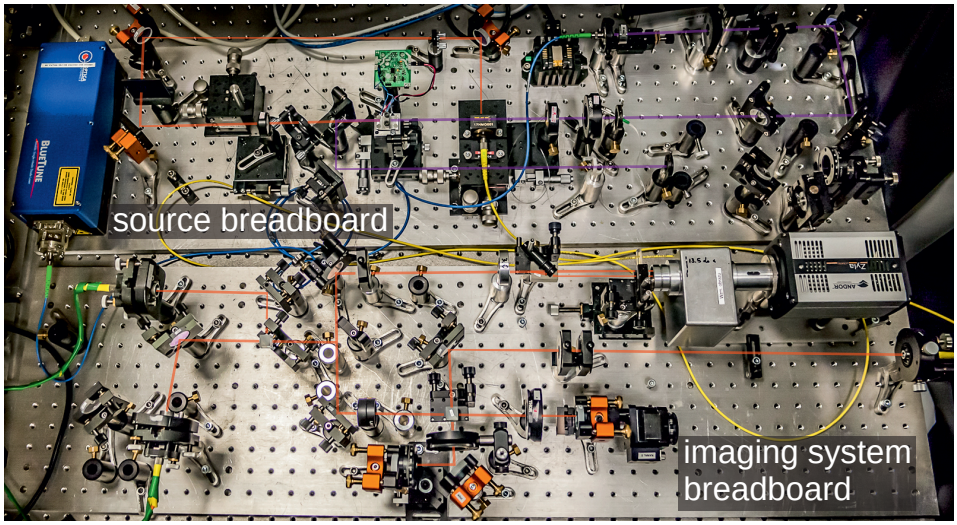


Figure 9.7: The photograph of the setup shows the compact system built on two breadboards, interlinked via single mode fiber (SMF) connection. In the source part we produce orthogonally polarized photons subsequently coupled to the SMF fiber. On the breadboard of the imaging system we split the photons into two paths, apply spatial structuring of the phase and we match temporal modes of the photons. Finally pairs of photons are imaged by a $4f$ system on the I-sCMOS camera, seen in the upper-right corner of the breadboard. For auxiliary measurements of HOM visibility, photons can be directed to multimode fibers and the to avalanche photodiodes, as seen in the bottom-left corner.

The imprinted phase profile can be expressed by experimental parameters: $\varphi(x) = kx^2/2R$, where $R = f_c/2$ stands for the radius of the imprinted phase curvature, and $k$ for the photon wave number.

The lengths of the delay line arms were adjusted to overlap photons temporally. We performed reference measurements of the HOM effect on the avalanche photodiodes setup after the cylindical lens was removed. We achieved high indistinguishability the photon pairs resulting in a visibility HOM interference of 91%.

### 9.3.3 Imaging system

The crucial extension of the majority of the content presented in Chapter 8 was the achievement of precise control of the photon phase structure along the consecutive parts of the setup. In particular we set the flat-phase waists of the mode coming out from a fiber collimator precisely on the surfaces of the mirrors in the delay line system. It has been achieved by varying the longitudinal position of the lens in the output collimator of the SMF fiber.

Then, similarly as in Sec. 8.7 we applied the $4f$ imaging system using two lenses of a focal length $f = 200$ mm, relaying the inverted amplitude and the flat phase structure of the reference photon on the camera. Likewise, the quadratic phase profile of the unknown photon was transferred without distortions. Either the flat or the expected quadratic phase of the photons were confirmed by auxiliary measurements involving classical laser beams transmitted through the SMF fiber. The measurements of phase structure of the classical beams were performed with a spatial shearing interferometry scheme realized using an additional calcite displacer inserted after the last spherical lens.

The radius of both Gaussians of the beams was measured to be $w = 269$ $\mu$m and it corresponded to the function presented in Fig. 9.2(a), as well as all the HSP transverse dimensions.

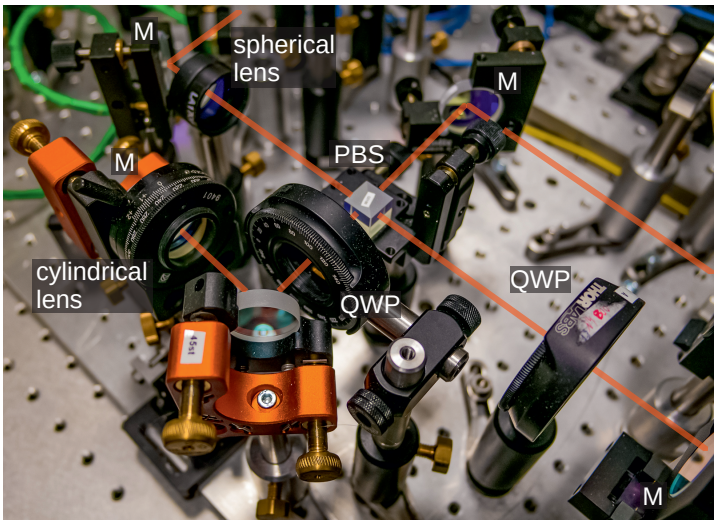


Figure 9.8: Photograph of the phase imprinting and the delay line system. Photons entering the setup from the right are split on the polarization beam splitter (PBS). The spatial phase structuring is applied on horizontally polarized photon during its double pass through a cylindrical lens. The lens is placed in the rotational stage in the near proximity of the dielectric mirror (M). The vertically polarized photon goes directly to the other mirror (M), placed on the motorized translation stage, whose position is adjusted to match temporal modes of both photons. Double pass through quarter wave plates (QWP) directs both photons to the same port of PBS and then to a spherical lens, separated from the delay line mirror surfaces by $f = 200$ mm.

### 9.3.4 Camera setting

We acquired a $1000 \times 20$ pixel region of interest selected on the sCMOS camera corresponding to approximately $11.5 \times 10^4$ microchannels with a frame rate of 7 kHz. We set the time gate of the image intensifier to 30 ns. This value was optimized for a pump laser power of 8 mW ensuring that virtually no accidental coincidences or more than two photons per frame were detected. Moreover, the chosen time gate corresponded to a dark count rate of $4 \times 10^{-7}$ per frame per single photon area which could be neglected in further analysis.

## 9.4 Experimental measurement of the HSP

### 9.4.1 Amplitude measurement

At first we measured the amplitude of the wave functions $|\psi_{u,r}(x)|$. This was a relatively straightforward procedure performed in the setup presented in Fig. 9.6 by setting the half wave plate ($\lambda/2$) to $\theta = 0°$. In consequence we measured the squared amplitudes of both photons directly following our coincidence imaging scheme presented in Sec. 8.4 and integrating over the vertical direction. In Fig. 9.9 we juxtapose the directly measured squared amplitudes of the unknown and reference photons.

### 9.4.2 Raw HSP measurement

Next we proceed to the HSP measurement by setting the HWP to $\theta = 22.5°$ similarly as in most experiments described in Chapter 8. We grabbed $1.8 \times 10^8$ camera frames collecting 5700 two-photon

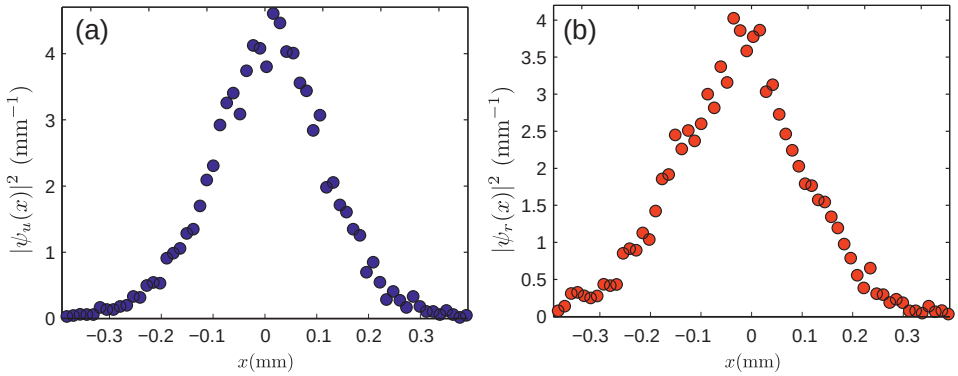


Figure 9.9: Directly measured modulus square of the photon transverse wave functions (a) for the unknown photon $|\psi_u(x)|^2$ and (b) for the reference photon $|\psi_r(x)|^2$.

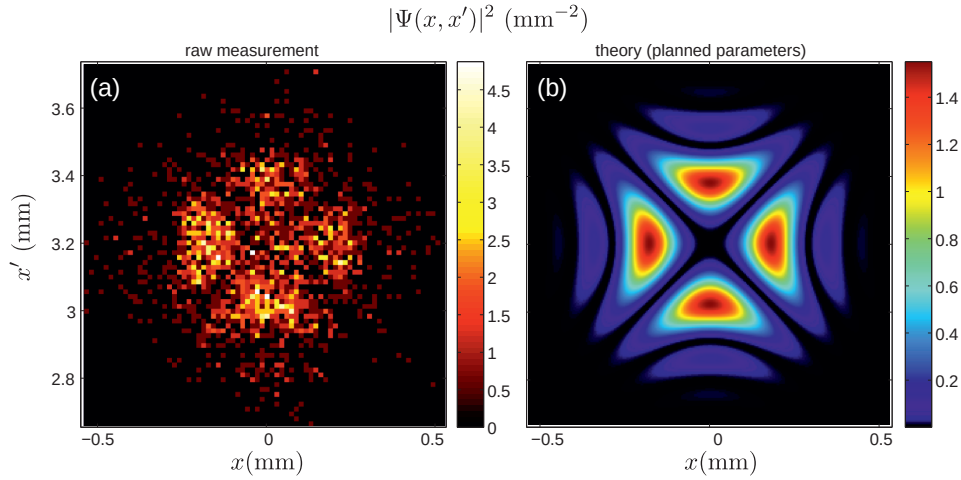


Figure 9.10: (a) Direct measurement of the HSP structure constructed from the empirical joint probability distribution of two-photon events $|\Psi(x,x')|^2$. (b) Same-scale comparison with the theoretical model created for the purpose of the experiment design.

events. Such a severe reduction of the photon flux was indispensable to achieve high two-photon interference uncorrupted by accidental coincidence events.

In Fig. 9.10(a) we present the measured HSP constructed from 2230 two-photon events. The measured structure resembles the theoretically predicted cross-like shape presented for comparison in Fig. 9.10(b).

The presented result is the first proof-of-principle demonstration of the HSP method and, as we see from Fig. 9.10(a-b), it yields structures supporting our theoretical predictions. Below we shall present in-depth analysis of this empirical pattern.

## 9.5 Retrieval of a complex, single-photon transverse wave function

Now we will demonstrate the practical decoding of phase $\varphi(x)$ from the measured HSP showing quantitative agreement with the assumed model parameters.

Recovery of the phase from a given interferogram is a canonical problem in classical holography and interferometry which can be solved using one of the numerous well-established methods,

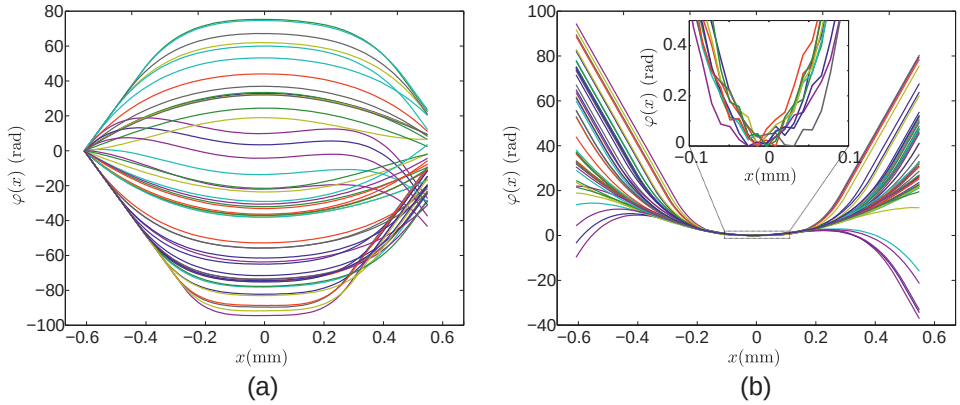


Figure 9.11: (a) The direct outcome of the phase retrieval algorithm, where the first point of phase was fixed to zero. (b) Since hologram structures are neither sensitive to the phase offset nor to convexity, we set all of their central local minima to zero and unified convexity of the functions. Inset: the zoom into the retrieved phase structure shows the fluctuation originated from the local search algorithm.

such as that presented by Servin *et al.* (1997). They are easily adapted to the HSP method, as the coincidence pattern defined by Eq. (9.2) has a mathematical structure closely resembling classical interferograms.

### 9.5.1 Cross sections

As we argued before in Sec. 9.2, the unknown photon local phase structure is encoded in each horizontal (or vertical) cross-section of the HSP. In an idealized scenario where both interfering photons have the same amplitude $|\psi_u(x)| = |\psi_r(x)|$ and are indistinguishable in all other degrees of freedom, i.e. where $\mathcal{V} = 1$, we can simply revert Eq. (9.4) to obtain:

$$\varphi(x) = 2\arcsin\frac{|\Psi(x,x_0')|}{|\psi_u(x)||\psi_u(x_0')|} + \varphi(x_0'). \tag{9.5}$$

Noticeably a fixed $x_0'$ coordinate selects a single cross section of the HSP and a single absolute value of the wave function evaluated in this particular point. They can both be measured by replacing a spatially resolving detector by a single-pixel counter at one beam splitter port. In our case due to the scarcity of data contained in the empirical cross-sections we are going to jointly utilize all collected coincidence events.

### 9.5.2 Phase-retrival algorithm

To reduce the uncertainty of a determined $\varphi(x)$, it is beneficial to incorporate all of the measured data points to retrieve the phase. We found it efficient to apply a numerical search of $\varphi(x)$ that matches the measured HSP best, by solving the optimization problem according to the general idea suggested by Servin *et al.* (1997). In fact the applied scheme is similar to the reconstruction schemes presented in Chapters 2 and 3, however, here we shall deal with a truly non-linear rather then convex optimization problem. We shall find the minimum of the following functional:

$$\min_{\varphi(x)} ||\,|\Psi(x,x')|^2 - |\Psi_{\mathrm{rec}}^{(\varphi)}(x,x')|^2\,||, \tag{9.6}$$

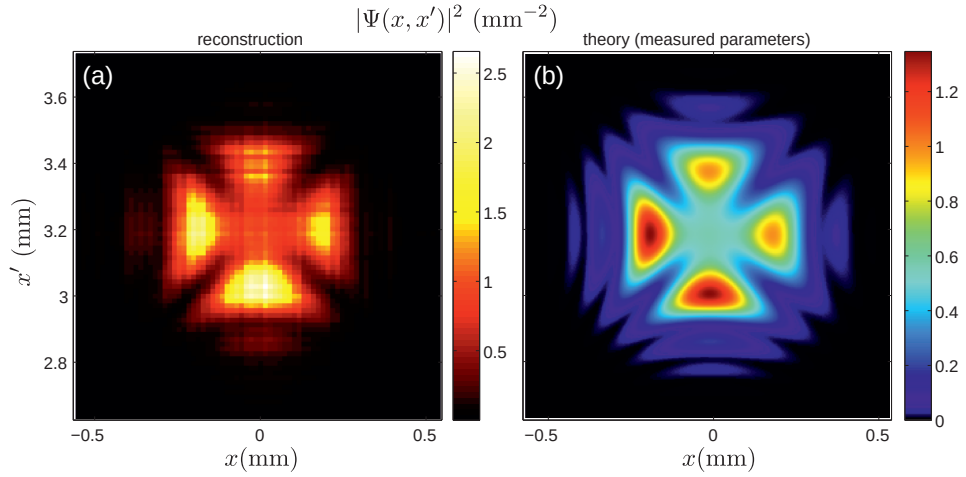


Figure 9.12: (a) The reconstructed HSP structure, presenting the modelled HSP for the measured amplitude profiles (Fig. 9.9) and the average of the phase profiles seen in Fig. 9.11. In some sense the reconstructed structure is a smoothed profile of the empirical distribution depicted in Fig. 9.10(a). (b) The outcome of theoretical model fed with phase from a polynomial fit to the reconstructed phase values.

where $|\Psi(x,x')|^2$ stands for the measured empirical distribution and $|\Psi^{(\varphi)}_{\mathrm{rec}}(x,x')|^2$ is a functional defined by Eq. (9.2) constructed from the measured amplitudes $|\psi_{u,r}(x)|$ depending on the vectorized phase profile $\varphi(x)$ to be found, and $||\cdot||$ is the Frobenius norm of the matrix. We can additionally set the visibility $\mathcal{V}$ as a free parameter to be found.

Since the general global search is a computationally hard problem, we divided our optimization into two simpler subsequent steps. At first we assumed that $\varphi(x)$ in Eq. (9.6) is a general fourth-order polynomial and we ran a global search finding its coefficient and the visibility parameter. Afterwards the local optimization problem with free, unconstrained values of the discretized $\varphi(x)$, starting from the solution found in the global search.

As the phase is defined up to an additive constant, it is convenient to work with the first derivative of the phase vector and after applying the optimization procedure integrate them by setting the first value of the retrieved, discretized $\varphi(x)$ to zero.

The technical details of the implementation of the above procedure are summarized in Appendix D.

### 9.5.3 Uncertainty of results

To account for the uncertainty of the empirical HSP in the phase retrieval in Fig. (9.10)(a) and to find the accuracy of our method, we applied the Monte-Carlo approach. We repeated the phase retrieval procedure 5000 times, each time randomizing $|\Psi(x,x')|^2$, $|\psi_u(x)|$ and $|\psi_r(x)|$ by drawing the initial counts values at each pixel from the corresponding Poissonian distributions. In each realization we obtained $|\Psi^{(\varphi)}_{\mathrm{rec}}(x,x')|^2$ and the corresponding vector of phase.

The results of the subsequent runs of the Monte-Carlo approach resulted in the phase profiles presented in Fig. 9.11(a). Due to insensitivity to the offset, the first value of all of them is fixed to the same constant equals zero. Moreover, since the cosine function HSP definition in Eq. 9.2 does not distinguish the sign of its argument, the retrieved phases can be either concave or convex in in the vicinity of their central positions, as seen in Fig. 9.11(a).

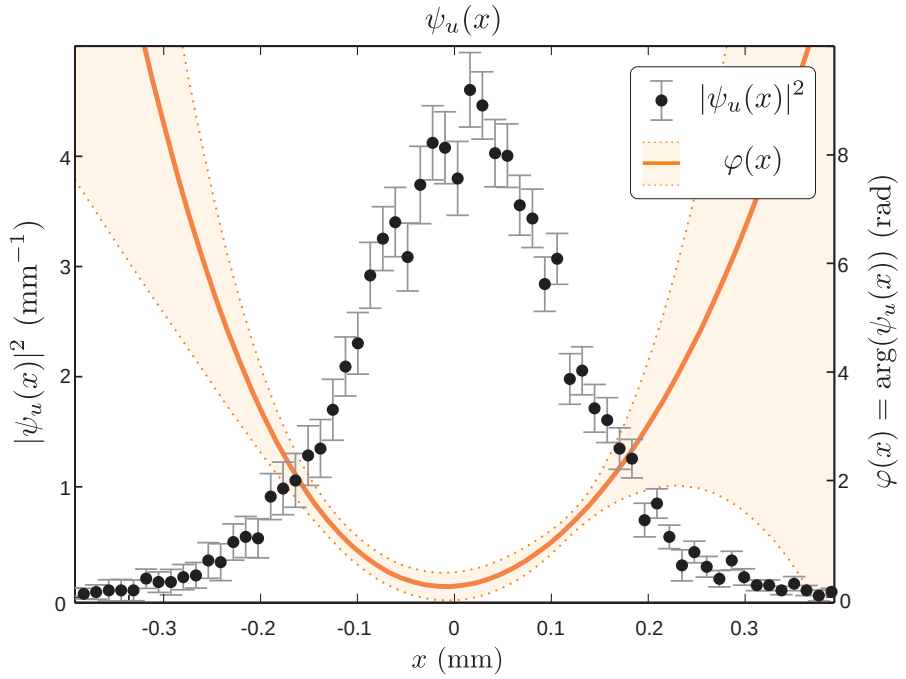


Figure 9.13: Full complex wave function of the photon $\psi_u(x)$ found in the experiment. We plot the modulus square $|\psi_u(x)|^2$ and the local phase $\varphi(x) = \arg(\psi_u(x))$ of the wave function together with the marked uncertainties found in the Monte-Carlo procedure. The retrieved phase profile is in good agreement with the experimental design.

To make the phase profiles comparable, we unified their convexities and set their minima to the same zero value. Both operation were entitled since they did not influence the corresponding $|\Psi^{(\varphi)}_{\mathrm{rec}}(x,x')|^2|$ shapes. The results of these two steps are displayed in Fig. 9.11(b). As can be seen, the central curvatures of the phase profile are very similar. In the close-up on the central region, shown in the inset, we see small fluctuations originated from the local search with all values freed.

Ultimately, as the final results we took the means of the multiple realizations of the Monte-Carlo procedure while we took the standard deviation calculated from the set of obtained phase values as the uncertainty of phase retrieval.

During the procedure we also found the visibility to be 71%. The decrease in the initially measured value can be explained by additional photons distinguishability in the vertical direction as well as the deterioration of spectral or temporal mode overlap during the long measurement run.

The reconstructed HSP for the determined mode amplitudes and the retrieved phase structure is presented in Fig. 9.12(a). In Fig. 9.12(b) we compare the reconstruction with our theoretical model fed with the retrieved phase profile found in the reconstruction. Comparison of Fig. 9.12(a-b) reveals high similarity between both structures.

### 9.5.4 Complete wave function

In Fig. 9.13 we show the complete complex wave function $\psi_u(x)$ of an unknown photon, i.e. its measured amplitude and the phase extracted from its HSP along with the uncertainty ranges. A slight displacement of the minimum of the phase profile with respect to the center of wave function amplitude explains the visible asymmetry of the reconstructed HSP, presented in Fig. 9.12.

The curvature radius of the reconstructed local phase wavefront of the photon was determined to be $R = 34 \pm 1.5$ mm. This value stands in good agreement with the phase imprint expected from a double pass through the cylindrical lens of the focal length $f_c = 75$ mm. Furthermore, the uncertainty of the reconstructed phase is below $2\pi/25$ in the central region and it diverges only on the edges of the wave function due to the scarcity of the registered counts. This number referring to classical beam characterization denotes the precision of a wave front measurement to be about 30 nm.

## 9.6 Generalizations of the HSP method

Below we present two possible generalizations that facilitate the application of the HSP in state-of-the-art experiments with spatially structured photons.

### 9.6.1 Generalization to the reference photon of an unknown local phase structure

The HSP method can be readily extended to the case where both $\psi_u(x)$ and $\psi_r(x)$ are unknown by applying spatial shearing, i.e. displacing one of the photons by a known transverse distance. As $|\psi_u(x)|$ and $|\psi_r(x)|$ are directly measurable, one only has to find their phase structures $\varphi_u(x) = \arg(\psi_u(x))$, $\varphi_r(x) = \arg(\psi_r(x))$, both defined up to the additive constant. Then the coincidence pattern takes the same mathematical form as in Eq. (9.2) with the phase $\varphi(x)$ interpreted as the difference of the photon phases:

$$\varphi(x) = \varphi_u(x) - \varphi_r(x). \tag{9.7}$$

Following the previously described procedure of the phase retrieval we can find $\varphi(x) - \varphi(x')$, which is equivalent to finding the phase up to an additive constant.

Then we can apply the small transverse displacement $\delta x$ of the reference photon, e.g. similarly to Sec. (8.6):

$$\psi_r(x) \to \psi_r(x + \delta x), \tag{9.8}$$

and repeat the phase retrieval procedure to find $\varphi'(x) - \varphi'(x')$, where:

$$\varphi'(x) = \varphi_u(x) - \varphi_r(x + \delta x). \tag{9.9}$$

By subtracting the results of these two measurements we obtain:

$$\begin{aligned} &\varphi(x) - \varphi(x') - \Big(\varphi'(x) - \varphi'(x')\Big) = \\ &= \varphi_r(x + \delta x) - \varphi_r(x) - \Big(\varphi_r(x' + \delta x) - \varphi_r(x')\Big) \simeq \Big(\frac{\mathrm{d}\varphi_r(x)}{\mathrm{d}x} - \frac{\mathrm{d}\varphi_r(x')}{\mathrm{d}x'}\Big)\delta x. \end{aligned} \tag{9.10}$$

Integration of the above formula determines $\varphi_r(x)$ up to an additive constant and, in consequence, the phase of the unknown photon $\varphi_u(x)$ according to Eq. (9.7).

### 9.6.2 Generalization onto the measurements of the two-dimensional spatial phase structures

Here we provide formulas and demonstrations for one-dimensional wave functions, which, nevertheless, all hold true if we replace one-dimensional photon positions by two-dimensional vectors:

$$(x, x') \to (\mathbf{r}, \mathbf{r}'). \tag{9.11}$$

In this generalized scheme one could measure the four-dimensional distribution of coincidences $|\Psi(\mathbf{r},\mathbf{r}')|^2$ and repeat the optimization procedures for phase retrieval to obtain two dimensional phase structure $\varphi(\mathbf{r})$. The measurement of four-dimensional set of data $|\Psi(\mathbf{r},\mathbf{r}')|^2$ requires high data collection speed and is currently a challenging task requiring cutting-edge technologies, such as sensors equipped with time-stamping functionality (John *et al.*, 2012) or matrices of superconducting nanowires detectors (Allman *et al.*, 2015).

If the spatially resolved detector is too slow to obtain a high-resolution four dimensional distribution of coincidences $|\Psi(\mathbf{r},\mathbf{r}')|^2$, one can apply a simplified procedure by measuring a single cross-section of HSP, such as $|\Psi(\mathbf{r},0)|^2$. As we argued in Sec. (9.2) such a cross-section, here a two-dimensional function, is entirely equivalent to the classical interference pattern.

The HSP cross-section can be measured with the state-of-the-art ghost imaging technology (Gatti *et al.*, 2008; Morris *et al.*, 2015) and standard coincidence imaging schemes described in Sec. (8.4). Acquisition could be performed in the similar scheme as in Fig. (9.1)(a) where one detector has two-dimensional resolution and the second is localized in small area centered in $\mathbf{r}' = 0$ and collects photons there . The second detector plays a similar role to bucket detectors from standard coincidence imaging, yet here it triggers photoevents that are well localized. Finally multiple triggering of an intensified camera gate within the open shutter of a collecting sensors, such as CCD or sCMOS, would enable fast acquisition of the average photon distribution.

## 9.7 Conclusions

In conclusion, here we present a novel method for characterizing a single photon transverse structure. We measured a transverse wave function of a single photon — its amplitude and its phase. Although the amplitude of the wave function can be directly read from the empirical probability distribution which can be easily measured by single-photon-sensitive spatially resolved detection systems, determination of the single-photon local phase remains a challenging problem. The most important result of this chapter was reported in the paper (Chrapkiewicz *et al.*, 2015b).

### 9.7.1 Analogy to classical holograms

The presented method was called the hologram of a single photon as it shares many similarities with classical holography capable of recording the full phase-amplitude information about the examined light. In particular it relies on the interference of a photon with a flat phase, called the reference photon, with the photon of an unknown phase structure – the counterpart of the light scattered from an object. Here, however, we had to circumvent the problem associated with the entirely indeterminate phase of single photons. Therefore, instead of measuring the first-order interference of the electric fields, highly sensitive to the relative phase between the reference and investigated light, we utilized an essentially different concept.

Our method relied on quantum interference between two-photon probability amplitudes. We performed the measurements of the joint probability distribution of detecting spatially localized coincidences observed on two separate regions of the camera sensor. It turned out that the probability distributions contained the full information about the photon phase structure similarly to classical holograms. Thus, we were able to apply similar phase retrieval algorithms eventually yielding the phase profile of one of the photon which agreed with our predictions.

### 9.7.2 Applicability

The presented method is insensitive to phase fluctuations between the unknown and the reference photon. Instead it requires high overlap of their spectral and temporal modes. This overlap characterized by the visibility parameter $\mathcal{V}$ can be high and stable for photons generated by different sources. In particular the Hong-Ou-Mandel interference has been shown for the photons generated by two independent spontaneous parametric down-conversion (SPDC) sources (Kaltenbaek *et al.*, 2006), quantum dots (Patel *et al.*, 2010) or two entirely dissimilar sources (Bennett *et al.*, 2009).

The presented method can be useful for a full characterization of single photon shapes in a situation where they could not be predicted or determined in equivalent classical measurements. For instance it would suit the characterization of true single photons generated in Raman scattering, as described in Part II. Moreover, our holographic method can be practical in the characterization of single photon shapes after propagation through turbulent air (Krenn *et al.*, 2015). Nowadays such free space communication is tested for its applicability in quantum cryptography. Encoding of qubits in spatial modes of single photons draws serious attention of the researchers (Vallone *et al.*, 2014; Walborn *et al.*, 2006).

Let us note that our method can be readily implemented in the mathematically equivalent spectral domain, where however, the single photon characterization is already quite advanced and numerous characterization methods have been demonstrated (Wasilewski *et al.*, 2007; Specht *et al.*, 2009; Beduini *et al.*, 2014).

Last but not least we would like to remark that the presented technique can also be applied to measuring wave functions of other bosons since it relies solely on multiparticle bosonic interference. Recently the HOM interference of integer spin atoms has been demonstrated (Lopes *et al.*, 2015). Interestingly those measurements utilize similar detection technique, i.e. a microchannel plate. It seems that an analogous measurement of the hologram of a single atom and further retrieval of its wave function should be feasible.

The presented dissertation entitled "Generation and characterization of spatially structured few-photon states of light" has demonstrated new approaches of generation of few-photon states of light and the characterization of their spatial structure and statistical properties. Across this thesis we predominantly use a new imaging tool – the intensified sCMOS camera that has been precisely characterized in terms of applications in quantum optics. We built and characterized a new source of photons based on spatially multimode warm atomic memory. Finally we demonstrated the first studies on the spatially resolved Hong-Ou-Mandel effect and based on them we proposed and demonstrated a novel holographic method of characterizing a single photon transverse wave function.

Most of the presented results have been published in journals and underwent peer-review verification. Some of the newer results are either pending peer reviews or are planned to be elaborated on and published soon.

In the present dissertation we expand the content of the papers relating to the scope of this thesis. On the one hand, we describe many technical details so as to facilitate possible future repetitions of selected parts of the research. On the other hand, we attempt to keep the whole dissertation consistent, instructive, self-explanatory and approachable for beginner graduate students in the similar field. To accomplish this, we add a comprehensive introductory Chapter 1 which introduces important literature and theoretical background on a level accessible for a broader group of physicists.

Below we briefly review the most important findings of the consecutive parts of the thesis. Next we discuss the perspectives and possible applications of our results.

## Most important findings

### Part I

The intensified sCMOS camera, constructed by us and characterized in Chapter 2, is a new tool for quantum optics and, to the best of our knowledge, we have been the first to use it in this field. The technique enhances technologically the previously used intensified CCD cameras as it has a significantly higher frame rate and much lower sensor noise levels. Esspecially the high frame rate turn out to be crucial for operating in the photon counting mode applied for studying nonclassical light properties, as described in Part III. We are familiar only with two previous applications of ICCD cameras which operate using both photon counting and photon localization for the study of spatial correlations from the SPDC (Oemrawsingh *et al.*, 2002) and for the double-slit experiment (Oemrawsingh *et al.*, 2002), which were not continued afterwards.

In Chapter 3 we present a general model of photon counting that relates to multipixel detectors (Afek *et al.*, 2009; Kalashnikov *et al.*, 2012) and cameras or other photon number resolving detectors, such as loop detectors (Banaszek and Walmsley, 2003; Rehacek *et al.*, 2003; Webb and Hunt-

ington, 2009). The results highlight the deleterious saturation effects on counts statistics leading to artificially nonclassical features. This is an important property of many detection setups. Thus, nowadays much effort is devoted to a proper description and characterization of the states of light measured with such detectors (Sperling *et al.*, 2012b,a; Kiesel and Vogel, 2012; Sperling *et al.*, 2013). Our findings from Chapter 3 have proved to be useful in several papers by other groups (Sperling *et al.*, 2015; Piacentini *et al.*, 2015; Smith *et al.*, 2015; Vidrighin *et al.*, 2015; Heilmann *et al.*, 2015).

Then we discuss the recently proposed and demonstrated concept of quantum detector tomography (Lundeen *et al.*, 2008; Feito *et al.*, 2009) to characterize photon counting properties of our I-sCMOS camera. In Chapter 4 we present the first tomographic characterization of photon counting properties of the imaging device. These results are also relevant to ICCD cameras. As far as we know, we have been the first to present a reconstruction of photon statistics based on the outcome of the tomography process. In this way we remove artificially nonclassical properties from the detected count statistics. The results of our tomographic approach can qualify the investigated state to the classical or nonclassical group and it provides high-fidelity initial photon statistics. Similar reconstruction processes relied previously on a theoretical model of devices (Haderka *et al.*, 2005; Blanchet *et al.*, 2008) which are generally hard to construct and verify.

The results of this part have been published so far in papers: (Chrapkiewicz *et al.*, 2014a; Chrapkiewicz, 2014).

### Part II

The Part II focuses on spatial and statistical properties of light generated in atomic memory. The generation, storage and retrieval of spatially multimode light is a unique approach since the majority of the reported setups were limited to the single spatial mode of light only (van der Wal *et al.*, 2003; Reim *et al.*, 2011; Bashkansky *et al.*, 2012). The storage and retrieval of spatially multimode light delivered from an external source have been demonstrated in a warm atomic setup for coherent beams only (Longdell *et al.*, 2008; Higginbottom *et al.*, 2012) and never approached the single photon regime.

In Chapter 5 we describe a setup for the atomic memory. We present an original filtering system that allows us to pass undistorted spatial structure of generated photons while stopping the driving laser beams detuned by only ca. 0.014 nm. The filtering scheme is extended as compared to the previously reported single-stage systems (Zielińska *et al.*, 2012; Stack *et al.*, 2015). Moreover, the concept and the demonstration of a magnetically broadened absorption filter has not been reported before.

Chapter 6 presents the first observation of generation, storage and retrieval of spatially multimode Raman scattering. It operates in the general scheme proposed by Duan *et al.* (2001). Furthermore, we achieve relatively long storage times for a fundamental mode up to 80 $\mu$s as compared with similar single-mode warm atomic setups with storage times up to 7 $\mu$s .

Along with the characterization of the memory setup we also propose and demonstrate a new method of measuring diffusion coefficients of alkali atoms in buffer gases. This has been the first method since 1960s-1970s and it allows more accurate measurements of the diffusion coefficients of rubidium in selected noble buffer gases; importantly, this method has enabled the first measurement in xenon ever performed. These results can be important for the design of warm atomic memory setups, such as (Firstenberg *et al.*, 2009, 2013) or for experiments with hyperpolarized xenon (Fink *et al.*, 2005). The reported values of diffusion coefficients have already turned out to be useful for microwave imaging (Horsley *et al.*, 2015).

In Chapter 7 we broadly consider spatial correlations between photons produced in time-delayed Stokes and anti-Stokes scattering processes. Such time-delayed spatial correlations between photons are reported for the first time in warm atomic systems. Moreover they have been not observed for cold atomic systems. So far spatial correlations between photons have only been observed in instantaneous nonlinear processes, such as instantaneous four-wave mixing in atomic vapors (Boyer *et al.*, 2008b,a) or SPDC in nonlinear crystals (Oemrawsingh *et al.*, 2002; Haderka *et al.*, 2005). In the measurements of spatial correlations we are able to resolve the contribution of the Stokes process at the readout and characterize its properties with respect to the driving laser beams detunings. Our findings turned out relevant to the other type of Raman memories where the Stokes scattering process at the readout stage is the main source of noise (Saunders *et al.*, 2015; Nunn *et al.*, 2015). Moreover, the demonstration of single-photon-level spatial correlations between the-time delayed Raman scattered photons is indicative of a nontrivial spatially varying collective state of atoms and has not been reported for warm atomic systems so far.

The results of this part have been published in papers: (Chrapkiewicz and Wasilewski, 2012; Chrapkiewicz *et al.*, 2014b; Dąbrowski *et al.*, 2015). Single-photon-level correlations have been mentioned in the conference paper (Chrapkiewicz *et al.*, 2015a) and they are pending publication in journals. Two demonstrated technical concepts of magnetically broadened tunable filter and precise focal length calibration are patent pending (Chrapkiewicz and Wasilewski, 2014, 2015).

### Part III

Part III characterizes the spatial structure of light exhibiting unambiguous nonclassical properties. In Chapter 8 we report the observation of the Hong-Ou-Mandel interference with spatial resolution. We are able to imagethe grouping of photons into pairs resolving localized photons individually. This has been the first qualitatively new and the most direct observation of this well-known phenomenon in nearly 30 years of observing it as the Hong-Ou-Mandel dip seen in the drop in the coincidence counts (Hong *et al.*, 1987; Jachura *et al.*, 2014).

Then we present studies utilizing joint probabilities of two-photon events. The only comparable research have studied spatial interference of two- and multiphoton states using either scanning fiber tips (Peeters *et al.*, 2009) or fiber bundles (Rozema *et al.*, 2014). We applied our ability to spatially resolve photons during HOM interference to study the influence of their controllablly introduced spatial distinguishability. This issue has not been considered previously. Importantly we achieve high control over all of the experimental parameters to obtain an excellent conformity of the theoretical models with the experimental data.

Finally in Chapter 9 we propose and demonstrate a novel method of comprehensive characterization of the spatial structure of a single photon. So far only tomographic (Smith *et al.*, 2005) or weak-values measurement methods (Lundeen *et al.*, 2011) have been used. To some extent, the presented method is similar to the recording of holograms but it utilizes second-order nonclassical interference. It is entirely insensitive to the global phase of photons — known to be indeterminate. The method offers significant simplicity of the setup: it merely relies on the beam-splitter transformation and spatially resolved detection. What is more, high interferometric precision can be reached.

Direct spatially resolved observation of the HOM effect has been reported in the paper[1] (Jachura and Chrapkiewicz, 2015b). Further results were described in manuscripts (Jachura *et al.*, 2015;

[1] Our paper (Jachura and Chrapkiewicz, 2015b) has been distinguished by the Optical Society editors in the "Spotlight on optics" series, and it has been selected as one of the most exciting peer-review research reports in optics that appeared in 2015 year (Jachura and Chrapkiewicz, 2015a).

Chrapkiewicz *et al.*, 2015b) and they are pending peer review in journals.

## Outlook

Below we indicate the supposed directions of further studies as well as possible applications of our findings, the developed methods and experimental tools. Firstly we discuss possible implications of the results from each of the parts of the thesis. Then we present possible synergistic combinations of results from different parts.

### Part I: single-photon-sensitive cameras and reconstruction techniques

The presented I-sCMOS camera has already proved to be useful for quantum optics experiments and we expect its further popularization as first commercial equipment have only just become available (Andor, 2015). The camera might find straightforward applications in super-resolving imaging utilizing measurements of the photon anti-bunching effect (Gatto Monticone *et al.*, 2014; Schwartz *et al.*, 2013). The recently presented demonstration using EM CCD camera (Schwartz *et al.*, 2013) could benefit from I-sCMOS capabilities in terms of visibility of the observed photon anti-bunching effect.

The tomographic characterization directly applies to the research devoted to the study of nonclassical correlations of photons produced in the high-gain SPDC process (Haderka *et al.*, 2005). Additionally we imply that the presented techniques can characterize spatial and statistical properties of nonclassical light produced in the instantenous four-wave mixing process in warm rubidium vapors (Boyer *et al.*, 2008b).

Finally we anticipate that the next generation of cameras will provide us with even more powerful tools. The most promising emerging technologies are matrices of superconducting nanowires of a superior quantum efficiency (Dauler *et al.*, 2014) and intensified CMOS cameras supplied with time-stamping functionality offering both spatial and temporal resolution (John *et al.*, 2012). In both cases the presented tomographic characterization will be indispensable for operating in high-photon-number regime.

### Part II: $N$-photon generator

The most promising application of the presented spatially multimode memory is an enhanced source of photons. In Fig. FR&O.1 we present exemplary schemes for an enhanced single- and multiple photon generator. Let us explain the schemes below, briefly discuss their application and provide literature references.

Contemporary sources of heralded photons produced in the SPDC process (Hadfield, 2009) have to be operated in a very low-gain regime to suppress the contribution of a higher number of photons. This requirement suppresses the rate of single photons as well. Furthermore, single photons are generated at uncontrollable and random moments. A possible avenue to surpass these limits of SPDC sources is to synchronize multiple sources using single photon routers (Ma *et al.*, 2011). This approach requires very fast, low-jitter routers which are available. Yet, the setting up of multiple, independent SPDC sources is difficult and hardly scalable in practice.

A spatially multimode memory, such as ours, could circumvent the limits of SPDC sources and serve as an efficient source of single photons. As we discuss in Part II, the detection of a Stokes photon in a certain direction can determine the direction of an anti-Stokes photon emission. In consequence an anti-Stokes photon is emitted in a certain direction which can be known a few

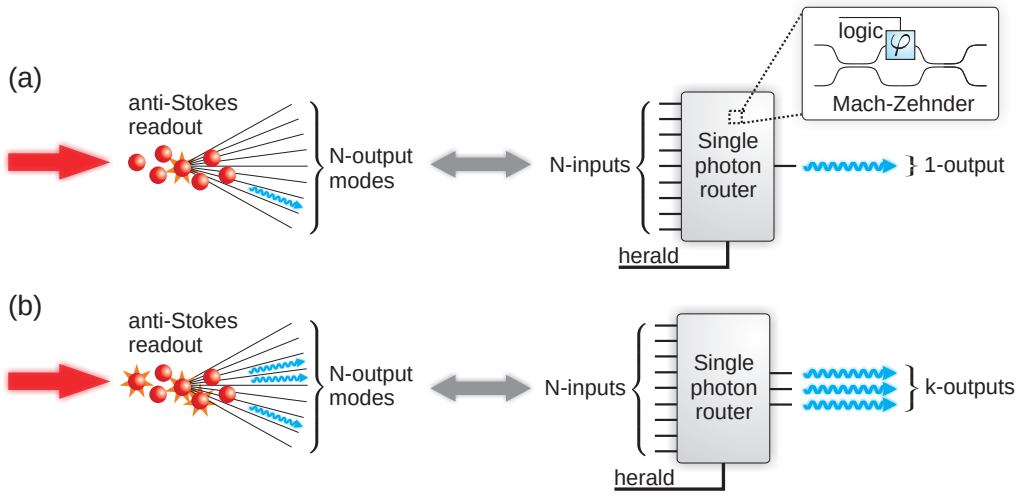


Figure FR&O.1: (a) Enhancement of the single photon generation rate. An anti-Stokes photon generated in spatially multimode memory is emitted in the direction determined by prior Stokes-photon generation and detection. The information about the expected direction of photon emission can be given a few microseconds in advance, prior to the anti-Stokes process, which is long enough to prepare and to reconfigure the single photon router architecture. A single photon router (Ma *et al.*, 2011) consists of multiple Mach-Zender interferometers with adjustable phases on the interferometer arms. The router always redirects photons from one of the numerous inputs to the single output port. (b) With a large number of spatial modes of the memory at our disposal, the chance of $N$-photon events in different modes grows significantly. A similar single photon router scheme can be used to predictably seed several output ports, each with a single photon.

microseconds in advance. Effectively, as presented in Fig. FR&O.1(a), the anti-Stokes photon is produced in one of finite-solid-angle sectors marked with dashed lines. The number of the depicted finite-solid-angle sectors is similar to the number of the spatial modes available in the memory.

For the majority of possible applications in quantum optics a single photon has to be emitted always in the same spatial mode. To achieve this, a photon generated in an arbitrary but previously known direction can practically be redirected to, for instance, one single mode fiber by means of the aforementioned single photon router (Ma *et al.*, 2011). Regardless of the direction of the photon emission, the single photon router architecture can be prepared in advance so as to redirect a photon always to the same output port. Hundreds of nanoseconds up to several microseconds of the available memory time is well above the state-of-the-art router capabilities offering response time on the level of single nanoseconds (Ma *et al.*, 2011).

The presented solution has a certain advantage over the SPDC sources – one can scale up the number of the memory modes by increasing the Fresnel number of the driving beams, and at the same time keeping the probability of generating a photon per mode low . As a result we can effectively produce a single photon in one mode with negligible contribution of pairs, threes etc. The chances of having a single photon in any mode during one experimental sequence increase with the number of modes. In this way, by using a large number of spatial modes of the memory, one could construct a nearly deterministic source of single photons.

If the number of the available modes is very high, the chances for populating higher number of independent modes, each with a single photon,rises significantly. As presented in Fig. FR&O.1(b), we can register several acts of single photon emission, each in different mode. As before, we can have prior knowledge about where those photons are produced based on the previous Stokes photons detection. The single router scheme can now have multiple outputs and we can populate them

by multiple photon states of the product form $|1\rangle \otimes \ldots \otimes |1\rangle$. Such states are essential for linear optics quantum computing systems (Knill *et al.*, 2001), as well as for quantum simulations using photonic chips (Peruzzo *et al.*, 2010b; Spring *et al.*, 2013). The presented approach involves only one high-capacity memory and one single photon router (Ma *et al.*, 2011) in contrast to the previous scheme of enhanced multiple photon generation with multiple quantum memories and multiple SPDC sources (Nunn *et al.*, 2013).

### Part III: metrology and characterization of the shape of a photon from an unknown source

In Part III we discuss the most direct consequences of combining photons spatial distinguishability with their spatially resolved detection. We have already applied this approach as well as the results presented in this thesis to the quantum metrology (Jachura *et al.*, 2015). Now let us briefly mention that from the metrological point of view a single photon spatial mode can be treated as a useful resource, whereas spatially resolved detection can represent more general quantum measurements. Careful design of both spatial mode and complimentary measurement can lead the increase in precision of some interferometric measurements. Remarkably, the obtained measurement precision exhibits quantum enhancement in the situations where for the same number of used photons no known interferometric method yields precision better than the shot-noise limit. We anticipate that this approach, as entirely new, will be further exploited.

Let us also comment on the possible evolution and applications of the method of a hologram of a single photon, such as presented in Fig. FR&O.2. In Chapter 9 we already suggest straightforward generalizations of the method on two unknown photons and for measurements of two dimensional photon structures. Those generalizations are necessary for characterizing photons with orbital angular momentum (OAM). Photons in OAM modes have already found applications in fundamental research (Fickler *et al.*, 2012). They are considered to be promising candidates for qubit coding in quantum communication in free space (Krenn *et al.*, 2015) because contrary to the polarization state, the spatial structure of a photon may remain relatively undisturbed during the propagation through turbulent air. Future development of such free space quantum communication channels will require appropriate methods for characterization of single photon shapes. In particular their local phase structure will have to be known in order to couple photons to single mode fibers.

Independently of the possible motivations for measuring a single photon transverse wave function, our method should be realistically applied for different sources of reference and unknown photons (Kaltenbaek *et al.*, 2006; Bennett *et al.*, 2009; Patel *et al.*, 2010), quantum dots (Patel *et al.*, 2010) or two entirely dissimilar sources (Bennett *et al.*, 2009).

Finally let us stress that the presented method can also be applied to other bosons, such as atoms, where very similar setup components necessary for the hologram scheme, are already implemented (Lopes *et al.*, 2015). Therefore, the possible applications of the presented method can go beyond pure optics.

### Possible combinations of the results from different parts of the thesis

The combination of some of the results from Part I and Part III have already been performed and presented. Possible tomography of a camera might be performed using single photons instead of coherent states. Analogous approaches have been demonstrated where nonclassical light is used to calibrate a detector (Perina *et al.*, 2012).

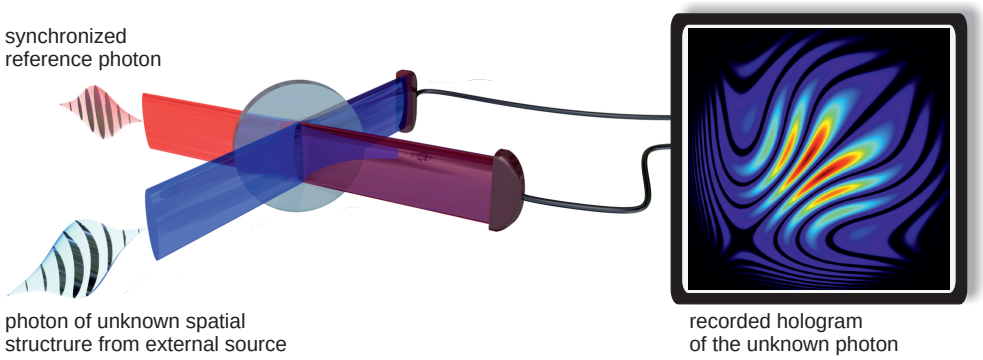


Figure FR&O.2: Photons of an unknown spatial structure, such as generated in atomic memory, can be precisely characterized using the proposed and demonstrated method of the hologram of a single photon. To perform this tasks, reference photons have to be prepared in close spectral and temporal modes, which is possible if they are generated by another, phase unrelated source (Kaltenbaek *et al.*, 2006; Bennett *et al.*, 2009; Patel *et al.*, 2010).

The combination of tomography and the reconstruction methods from Part I can be useful for studying Raman scattering from Part II. As we have discussed, on the single-photon-level Raman scattering the noise from the fluorescence prevents us from observing nonclassical properties. The signal to noise ratio increases significantly for larger numbers of photons. Tomography is indispensable to properly characterize any nonclassical features of photon statistics of high-photon-number Raman scattering the statistics reconstruction preceded by the camera.

Finally the methods derived in Chapter 9, Part III, might be useful to characterize the shape of a single photon generated in the atomic memory from Part II. Accurate coupling of single photons to the single mode inputs of the photon routers will require proper compensation of the single photon wave front. Such a wave front cannot be determined by means of any independent, classical measurement. Recording the hologram of a single photon should be feasible and thus serve as an efficient way to accomplish this task.

# Appendices

APPENDIX A

# DERIVATIONS OF COUNTS STATISTICS ON MULTIPLEXED ON-OFF DETECTORS

Below we discuss the most important steps in deriving the moments of counts statistics for multiplexed on-off detectors illuminated by coherent and multimode thermal states. We derive formulas in Eqs. (3.8,3.9,3.13,3.14,3.15) and show the methods to derive more general formulas for higher moments of counts statistics.

## A.1 Stirling number of the second kind

In Chapter 3 we discuss a model for multiplexed on-off detectors and provide a formula Eq. (3.4) derived by Paul *et al.* (1996) for conditional probabilities of measuring $k$ counts with $n$ impinging photons $p_N(k|n)$. The formula is expressed by the Stirling number of the second kind defined as follows:

$$S(n,k) = \frac{1}{k!}\sum_{i=0}^{k}(-1)^i\binom{k}{i}(k-i)^n. \tag{A.1}$$

To evaluate the moments of counts statistics we shall use two mathematical properties of the Stirling number of the second kind (Weisstein, 2015):

$$\sum_{n=k}^{\infty} S(n,k)\frac{x^n}{n!} = \frac{1}{k!}(e^x-1)^k, \tag{A.2}$$

$$\sum_{n=k}^{\infty} S(n,k)x^n = \frac{(-1)^k}{(1-\frac{1}{x})_k}, \tag{A.3}$$

where $(\cdot)_n$ denotes the Pochhammer symbol defined as $(y)_n \equiv \Gamma(y+n)/\Gamma(y)$, where $\Gamma$ is the well-known gamma function.

## A.2 Moments of counts statistics for coherent states

To derive the moments of probability distributions for the counts we shall evaluate the average values of polynomial functions $\chi(k)$ of counts by following Eq. (3.4):

$$\langle \chi(k) \rangle = \sum_{k=0}^{N} \chi(k) \binom{N}{k} k! \sum_{n=k}^{\infty} \frac{1}{N^n} S(n,k) f_n, \tag{A.4}$$

where $f_n$ denotes the photon statistics.

To evaluate Eq. (A.4) for coherent state statistics, $f_n = \bar{n}^n e^{-\bar{n}}/n!$ we first directly use Eq. (A.2):

$$e^{-\bar{n}} \sum_{n=k}^{\infty} \frac{1}{n!} \left(\frac{\bar{n}}{N}\right)^n S(n,k) = \frac{1}{k!} e^{-\bar{n}} (e^{-\bar{n}/N} - 1)^k. \tag{A.5}$$

Then we have to apply the standard property of the binomial symbol:

$$\sum_{k=0}^{N} \binom{N}{k} a^k = (1+a)^N, \tag{A.6}$$

for $a = (e^{-\bar{n}/N} - 1)^k$.

To calculate $\langle k \rangle$ and $\langle k^2 \rangle$ for coherent states, the first and the second derivative of Eq. (A.6) over the parameter $a$ has to be taken. Eventually we obtain Eq. (3.8) and Eq. (3.9) presented in Chapter 3.

## A.3 Moments of counts statistics for multi-mode thermal states

To evaluate Eq. (A.4) for single- and multimode thermal states let us consider the photons statistics presented in a general form:

$$f_n^{(a,b)} = ab^n. \tag{A.7}$$

Such statistics can be readily associated with the single mode thermal state of the mean $\langle n \rangle$ for:

$$a = (1 + \langle n \rangle)^{-1}, \quad b = \langle n \rangle / (1 + \langle n \rangle). \tag{A.8}$$

Then, using the property Eq. (A.3), we find the average of any function of counts for given statistics $f_n^{(a,b)}$:

$$\langle \chi(k) \rangle_{f_n^{(a,b)}} = a \sum_{k=0}^{N} \chi(k) \binom{N}{k} k! \frac{(-1)^k}{(1 - N/b)_k}. \tag{A.9}$$

The sum Eq. (A.9) can be computed to obtain the first and the second moment of the counts statistics:

$$\langle k \rangle_{f_n^{(a,b)}} = \frac{abN}{(b-1)(b(N-1) - N)}, \tag{A.10}$$

$$\langle k^2 \rangle_{f_n^{(a,b)}} = \frac{ab(b+1)N^2}{(b-1)(b(N-2) - N)(b + N - bN)}. \tag{A.11}$$

These are the exact formulas for single mode thermal statistics after substitution Eq. (A.8).

We are also able to find moments of counts distribution for multimode thermal statistics. Let us consider the following probability distribution:

$$g_n = a \frac{(n+m)!}{n!} b^{n+m}. \tag{A.12}$$

It can be re-expressed using Eq. (A.7):

$$g_n = a\left(\frac{\partial}{\partial b}\right)^m b^{n+m} = \left(\frac{\partial}{\partial b}\right)^m b^m f_n. \tag{A.13}$$

Note that $g_n$ can be readily associated with the $\mathscr{M}$-mode thermal state described in Eq. (1.45) with the average number of photons $\langle n\rangle$ for

$$a = \frac{1}{\Gamma(\mathscr{M})}\left(\frac{\mathscr{M}}{\langle n\rangle + \mathscr{M}}\right)^{\mathscr{M}},\ b = \frac{\langle n\rangle}{(\mathscr{M} + \langle n\rangle)},\ m = \mathscr{M} - 1. \tag{A.14}$$

To calculate the moments of counts statistics for the multi-mode thermal input statistics $g_n$, we combine Eq. (A.4) and Eq. (A.13):

$$\langle \chi(k)\rangle_{g_n} = \left(\frac{\partial}{\partial b}\right)^m b^m \langle \chi(k)\rangle_{f_n^{(a,b)}} \tag{A.15}$$

After the evaluation of the above formula for the moments previously found on statistics $f_n^{(a,b)}$ in Eqs. (A.10-A.11) we analytically compute moments for each $\mathscr{M}$ and $N$, as we exemplify in Chapter 3 in Eqs. (3.13,3.14,3.15). Another example can be:

$$\langle k^2\rangle_{\mathrm{Th},\mathscr{M}=2} = \frac{\langle n\rangle N^2\left(\langle n\rangle^3 + 6\langle n\rangle^2 N + 3\langle n\rangle N(2N+1) + 4N^2\right)}{(\langle n\rangle + N)^2(\langle n\rangle + 2N)^2}. \tag{A.16}$$

We calculated formulas for higher $\mathscr{M}$ and $N$ to obtain Fig. 3.7 and Fig. 3.8 where we studied the influence of saturation effects on the nonclassical measures evaluated for counts statistics.

APPENDIX B

# CONVEX OPTIMIZATION PROBLEMS IN THE CVX SOFTWARE

## B.1 Exemplary problem in the CVX

CVX is a powerful package in Matlab capable of solving optimization problems in disciplined convex programming (Grant *et al.*, 2015). To be specific, it can find global minima of virtually any convex function subject to additional conditions in the form of a set of linear inequalities.

The simplest example to grasp the essence and the basic syntax of the CVX package is the linear fitting via the least squares method. Let consider following equation:

$$\mathbf{Ax} = \mathbf{b}, \tag{B.1}$$

where $\mathbf{x}$ is the unknown $n$-elements vector to find and $\mathbf{A}$ and $\mathbf{b}$ are known matrix and vector respectively. The problem can be reformulated as a minimization of the matrix Frobenius norm discussed in Chapter 3, Sec. 3.9:

$$\min_{\mathbf{x}} ||\mathbf{Ax} - \mathbf{b}||. \tag{B.2}$$

We can also add some linear constraints on vector $\mathbf{x}$, such as its minimum and maximum values:

$$\mathbf{x}_{\min} \leq \mathbf{x} \leq \mathbf{x}_{\max}. \tag{B.3}$$

The code solving a minimization problem defined in Eq. (B.2) under constraints from Eq. (B.3) is particularly simple and can be run as a Matlab script:

```
cvx_begin
    variable x(n)                   % search for a vector "x" of a length "n"
    minimize(norm(A*x-b,'fro'))     % solve the problem
    subject to                      % applying following constraints on "x"
        xmin <= x <= xmax
cvx_end
```

The command `variable` defines a vector or matrix to be found, `minimize` sets the problem and `subject to` defines the constraints. Moreover, `norm(·,'fro')` represents the Frobenius norm $||\cdot||$.

Within the block `cvx_begin` – `cvx_end` the vector `x` exist as an abstract set of $n$ variables to be found. After the evaluation `x` is passed to the Matlab workspace and can be immediately used as a standard Matlab vector.

## B.2 Reconstruction of conditional probabilities Π

Problem defined in Eq. (3.26) under the conditions of Eq. (3.22) can be directly solved in a very similar manner as a least squared optimization with some constraints. We search for a matrix Π of $(k_{max}+1)\times(M+1)$ dimensions which is lower triangular and represents distributions of the conditional probabilities meeting the constraints defined in Eq. (3.22) Below we present an excerpt from the Matlab code running the CVX optimization:

```
1  cvx_begin
2      variable PI((kmax+1),(M+1)) lower_triangular; % searching for matrix with p(k|n)
3
4      % definition of regularization function
5      reg_fun=0;
6      for n=1:(M+1)
7          for k=1:kmax
8              reg_fun=reg_fun+(PI(k,n)-PI(k+1,n))^2;
9          end
10     end
11
12     % problem of camera calibration
13     minimize(norm(C-F*PI,'fro')+gamma*reg_fun);
14
15     subject to
16         0 <= PI <= 1;
17         sum(PI,2)==ones((L+1),1);
18
19 cvx_end
```

The names used in the above code are literally rewritten from Eq. (3.26), such as Π →`PI`, $\gamma$ →`gamma` etc. Note that `reg_fun` defined in lines 5-10 is in fact a function taking the unknown variable set `PI` as arguments, yet such a definition is easily processed by the CVX.

The code requires counts and photon statistics `C` and `F` as input variables in a Matlab workspace.

## B.3 One-dimensional statistics reconstruction

The problem of the reconstruction of one-dimensional photon statistics $f_n$ defined in Eq. (3.27) belongs to the same class as discussed above. It is solved by the analogous code excerpt:

```
1  cvx_begin
2      variable f(1,M+1); % searching for one-dimensional statistics
3
4      % definition of regularization function
5      reg_fun=0;
6      for n=1:M
7          reg_fun=reg_fun+(f(n)-f(n+1))^2;
8      end
9
10     % problem of one-dimensional reconstruction
```

```
    minimize(norm(c-f*PI,'fro')+gamma*reg_fun)

    subject to
        0<=f<=1;
        sum(f)==1;

cvx_end
```

In particular the CVX routine requires the vector of counts statistics `c` and set of conditional probabilities `PI`.

## B.4 Joint statistics reconstruction

The reconstruction of joint statistics $f_{n_1,n_2}$, gathered in the matrix $\mathbf{F}'$ of size $(M+1)\times(M+1)$, is performed by solving the problem defined in Eq. (3.29) with the constraints in Eq. (3.30).

```
cvx_begin
    variable F(M+1,M+1); % searching for joint statistics

    % definition of regularization function
    reg_fun=0;
    for n1=1:M
        for n2=1:M
            reg_fun=reg_fun+(F(n1,n2)-F(n1,n2+1))^2; % horizontal regularization
            reg_fun=reg_fun+(F(n1,n2)-F(n1+1,n2))^2; % vertical regularization
            reg_fun=reg_fun+(F(n1,n2)-F(n1+1,n2+1))^2; % diagonal regularization
        end
    end

    % problem of joint statitics reconstruction
    minimize(norm(C-PI1'*F*PI2,'fro')+gamma*reg_fun);

    subject to
        0 <= F <= 1;
        sum(sum(F))==1;

cvx_end
```

Here the CVX script has to be seeded by two sets of conditional probabilities `PI1` and `PI2`, as well as the joint counts statistics in matrix `C`.

APPENDIX C

# TUNABLE ABSORPTION FILTER ON $^{85}$RB

## C.1 Filter construction

The absorption filter is used in Part II to stop strong laser beams and transmit the Raman-scattered single photons of frequencies lying outside of the filter bandwidth. In Fig. C.1 we present a technical drawing of the filter, front and side view. The main parts of the filter is a 30-cm long rubidium $^{85}$Rb cell placed in transverse static magnetic field produced by ferrite magnets. The whole filter is inserted inside a two-layer soft-steel magnetic shielding that confines the magnetic field inside the filter to suppress stray external fields down to $10^{-4}$ T. We heat the vapors in the Rubidium cell using a high-power resistor mounted under the cell which dissipates around 80 W of power.

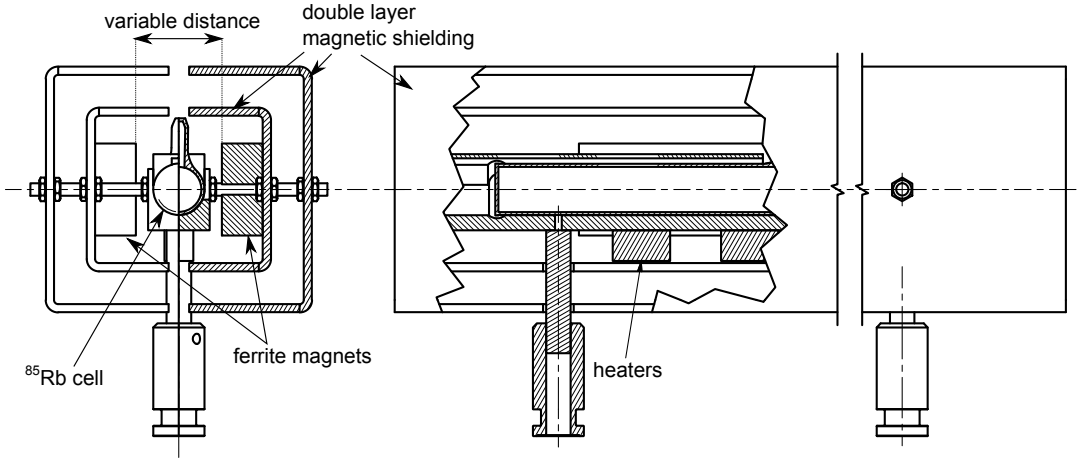


Figure C.1: Technical drawing of a magnetically tuned absorption filter based on $^{85}$Rb isotope. Broadening of the filter lines is achieved by changing the variable distance between the ferrite magnets. The filter is embedded in a two-layer magnetic shielding protecting the main quantum memory cell from corrupting stray magnetic field.

## C.2 Filter tuning using a transverse magnetic field

Transverse magnetic field inside the filter is emitted by ferrite magnets located on both sides of the rubidium cell. By changing the distance between the magnets we effectively alter the magnetic field inside the cell and thence the line broadening, as shown in Fig. C.2. The width of the absorption spectrum controlled by the magnetic field ranges from 5.5 GHz up to 8.4 GHz. As we mentioned in Chapter 5, we used a magnetic field of $10^{-2}$ T corresponding to a 9-cm distance between magnets.

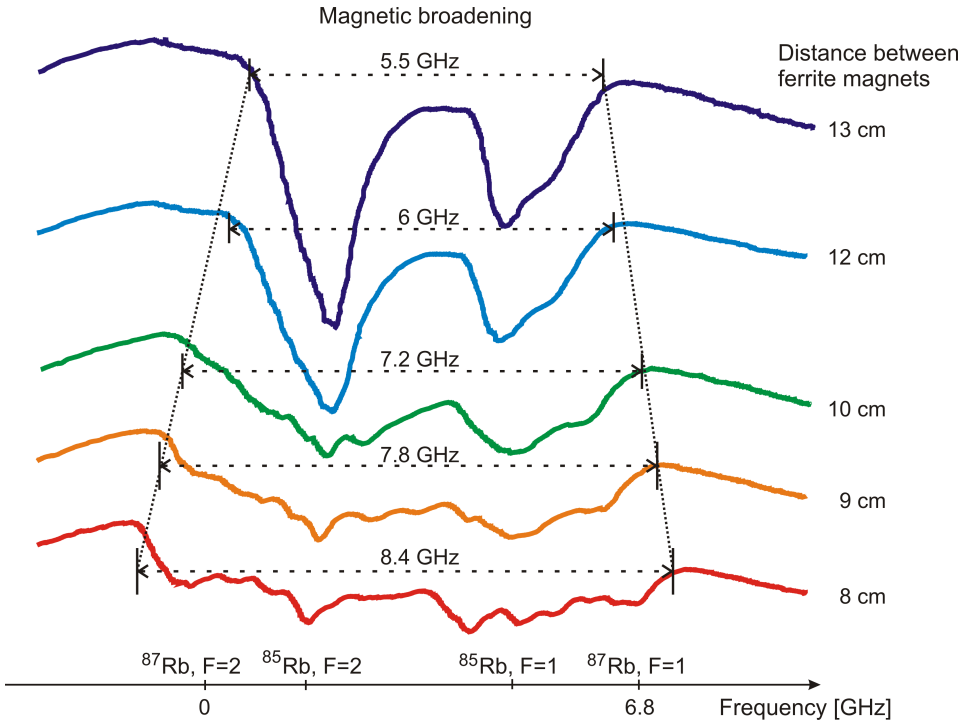


Figure C.2: Large broadening of the lines of the absorption filter due to transverse magnetic field, tuned by changing the distance between the ferrite magnets. For visualization the presented transmission spectra were measured below the operation temperature, at $T = 60°$ C. For our operation we selected a distance of 9 cm corresponding to $10^{-2}$ T inside the cell with $^{85}$Rb. The spectra are juxtaposed vertically, with proportions preserved.

APPENDIX D

# NUMERICAL RECONSTRUCTION OF THE WAVE-FUNCTION PHASE

The single photon phase reconstruction problem has been solved by using the algorithm presented in Chapter 9 in Sec. 9.5. Here we present fragments of software codes written in Matlab that perform the subsequent steps of the phase retrieval process.

## D.1 Exemplary nonlinear optimization problem in Matlab

Before we discuss the solution of the actual phase reconstruction problem, let us show a simple example of the global optimization problem that can be tackled using Matlab. Let us consider the problem of finding the minimum of a function:

$$f(x_1, x_2) = x_1^2 + (x_2 - 2)^2 + 1. \tag{D.1}$$

Obviously, the minimum is for $x_1 = 0$ and $x_2 = 2$. Let us test if we can get the same result using Matlab. The global minimum of $f(x_1, x_2)$ can be easily found numerically using the following routine:

```
opts = optimset('Algorithm','interior-point');
problem = createOptimProblem('fmincon','objective',...
 @(x) x(1).^2 + (x(2)-2).^2+1,'x0',[1,1],'lb',[-5,-5],'ub',[5,5],'options',opts);
gs = GlobalSearch;
[x,f] = run(gs,problem)
```

The function $f(x_1, x_2)$ has been passed as the Matlab's anonymous function `@(x) x(1).^2 + (x(2)-2).^2+1`. We have also set the starting point `'x0'` and the lower `'lb'` and upper bounds `'ub'`. The output of `GlobalSearch` is the following and yields easily predicted and expected result:

```
GlobalSearch stopped because it analyzed all the trial points.
All 17 local solver runs converged with a positive local solver exit flag.
x =
0.0000 2.0000
f =
1.0000
```

## D.2 Global search of polynomial phase coefficients

The general optimization problem Eq. (9.6) of phase retrieval can be tackled similarly to the previous example. At first we define the anonymous Matlab's function `psirec_highorder` to be minimized. We also define two auxiliary functions: `phasefun_highord` — for generating a polynomial phase profile and `cosphase_highord` for evaluating a cosine function.

```
phasefun_highord=
    @(poly_params)polyval([poly_params,0],(1:length(ind1))-round(length(ind1)/2));
cosphase_highord=
    @(poly_params)cos(phasefun_highord(poly_params)'*ones(1,length(ind1))-ones(length(ind1),1)
     *(phasefun_highord(poly_params)+pi));
psirec_highorder=
    @(V,poly_params) intensity_term_amp+V*interf_term_amp.*cosphase_highord(poly_params);
```

`intensity_term_amp` and `interf_term_amp` are the local variables that exist outside the scope of the functions. They denote the intensity and the interference terms of Eq. (9.6) and are taken from auxiliary measurements.

Then the general global search problem is formulated using the following sets of commands:

```
fcost_param_highorder= @(params) norm(psiemp-psirec_highorder(params(1),params(2:end)),'fro');

opts = optimset('Algorithm','interior-point');
sval=0.12;
boundval=0.5;
problem = createOptimProblem('fmincon','objective',...
    fcost_param_highorder,'x0',[0.7,0,0,sval^2,0],'lb',...
    [0.5,-boundval^4,-boundval^3,-boundval^2,-boundval],'ub',...
    [1,boundval^4,boundval^3,boundval^2,boundval],'options',opts);
gs = GlobalSearch;
[Vphase_gs_rec,fcost_rec] = run(gs,problem)
```

The returned vector `Vphase_gs_rec` consist of visibility and polynomial parameters defining the phase profile.

## D.3 Local search with all phase values freed

To perform a local search we apply the previously found solutions as a starting point. As before, we have to define the anonymous functions to seed the optimization engine:

```
phase_free=@(phase_diff) [0,cumsum(phase_diff)]; % phase integral
cosphase_free=...
    @(phase_diff) cos(phase_free(phase_diff)'*ones(1,length(ind1))...
            -ones(length(ind1),1)*(phase_free(phase_diff)+pi));
psirec_free=@(V,phase_diff) intensity_term_amp+V*interf_term_amp.*cosphase_free(phase_diff);
fcost_free= @(params) norm(psiemp-psirec_free(params(1),params(2:end)),'fro');
```

The local search can be implemented using the Matlab function `fmincon`:

```
Vphase_ls_rec = fmincon(fcost_free,[Vphase_gs_rec(1),...
    diff(phasefun_highord(Vphase_gs_rec(2:end))+0.1*rand(1,length(ind1)))],...
```

```
    [],[],[],[],[0.5,-3*ones(1,length(ind1)-1)],[1,3*ones(1,length(ind1)-1)]);
```

The results of the reconstruction are the visibility, the phase profile and the reconstructed HSP map:

```
V_rec=Vphase_ls_rec(1);
modarg1=phase_free(Vphase_ls_rec(2:end));
psi_rec=psirec_free(Vphase_ls_rec(1),Vphase_ls_rec(2:end));
```

## D.4 Monte-Carlo approach to determining the reconstruction precision

The whole optimization procedure has to be repeated many times starting from randomized values of the measured data. We simply draw new count values using the function `poissrnd`, with the code fragment below:

```
Navg=5000; % number of Monte-Carlo runs
V_avgvec=zeros(Navg,1);      % visibility vector

for
    ii=1:Navg        [modabs1,modarg1,modabs2,psi_rec,V_rec]=...
        moderetr(poissrnd(psi0_measured),poissrnd(psi45_measured),poissrnd(psi90_measured),
    ind1,ind2);
    modabs1_avgvec(ii,:)=modabs1; %stores mode1 amplitude
    modabs2_avgvec(ii,:)=modabs2; %stores mode2 amplitude
    modarg1_avgvec(ii,:)=modarg1; %stores mode1 phase profile
    psi_rec_avgvec(ii,:)=psi_rec(:); %reconstructed HSP map
    V_avgvec(ii)=V_rec; % visibility found from reconstruction
end
```

`psi0_measured, psi45_measured, psi90_measured` are the maps of coincidence events and they are used to seed function `moderetr` performing the whole optimization procedure.

## D.5 Comparing phase profiles

Finally we unify the convexity and the minima of phase profiles to average them out in the following way:

```
modarg1_avgvec_comp=modarg1_avgvec;
for ii=1:Navg
    df=diff(modarg1_avgvec(ii,40:50)); % central region
    if (df(end)-df(1))<0 % convexity test
        modarg1_avgvec_comp(ii,:)=-modarg1_avgvec(ii,:);
    else
        modarg1_avgvec_comp(ii,:)=modarg1_avgvec(ii,:);
    end
    % unifying the common minima
    modarg1_avgvec_comp(ii,:)=modarg1_avgvec_comp(ii,:)-min(modarg1_avgvec_comp(ii,40:60));
end
```

APPENDIX E

# GALLERY OF THEORETICAL SINGLE-PHOTON HOLOGRAMS FOR VARIOUS SPATIAL PHASE STRUCTURES

Since the concept of the hologram of a single photon (HSP) described in Chapter 9 is a new one (Chrapkiewicz *et al.*, 2015b), it will be instructive to give further examples of HSP phase coding. In the following sections we exemplify the HSP structures for certain continuous and noncontinuous phase structures $\varphi(x)$ of an unknown photon which yield corresponding structures of joint probability of coincidence events $|\Psi(x,x')|^2$, described by Eq. (9.2).

## E.1 Higher order polynomial phase

In Sec. 9.2 we mostly considered linear and quadratic phase structure. It should be instructive to see the next-order polynomial functions. For clear visualization we omit the axes and keep them consistent with the maps plotted in Chapter 9. As we see below for the even functions describing the phase, the HSP has four axes of symmetry, whereas for the odd functions the HSP has two axes of symmetry.

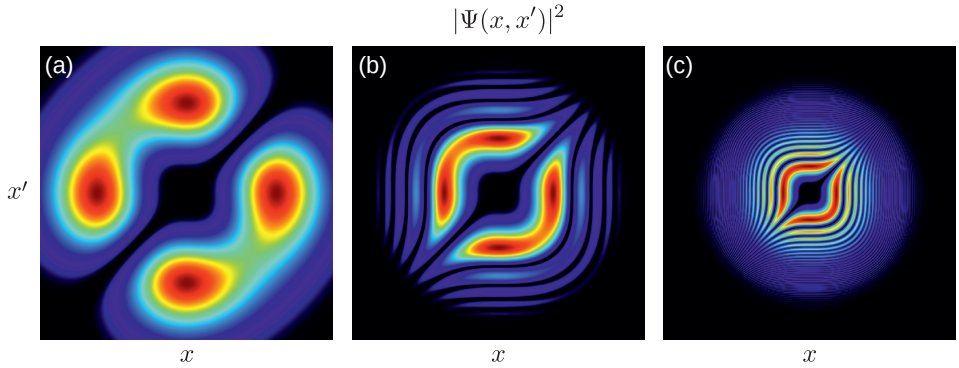


Figure E.1: HSP structures $|\Psi(x,x')|^2$ plotted for the third-order polynomial phase $\varphi(x) = \alpha_3 \times (x/w)^3$ for the following parameters: (a) $\alpha_3 = \pi/10$, (b) $\alpha_3 = 5\pi$, (c) $\alpha_3 = 20\pi$. In this following examples the omitted axes are consistent with those in Chapter (9).

Moreover, we clearly see that the HSP vanishes in the middle for higher-order polynomial terms. This is because the corresponding phase structure is relatively flat in the central region yielding high photon indistinguishability.

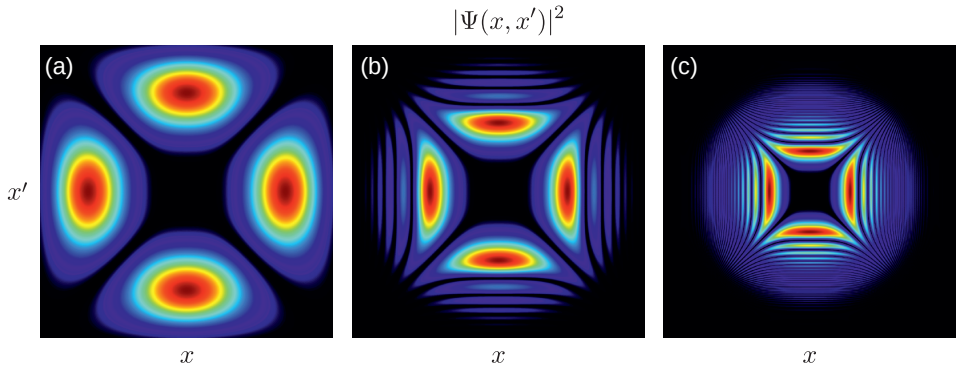


Figure E.2: HSP structures $|\Psi(x,x')|^2$ plotted for fourth-order polynomial phase $\varphi(x) = \alpha_4 \times (x/w)^4$ for the following parameters: (a) $\alpha_4 = \pi/10$, (b) $\alpha_4 = 2\pi$, (a) $\alpha_4 = 10\pi$.

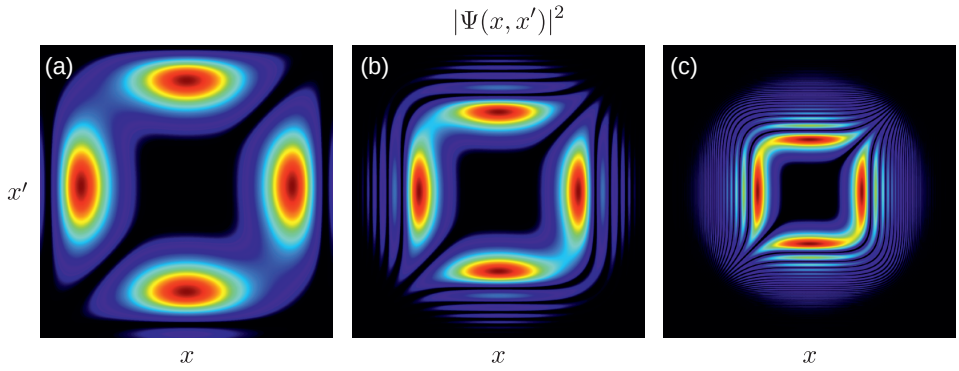


Figure E.3: HSP structures $|\Psi(x,x')|^2$ plotted for the fifth-order polynomial phase $\varphi(x) = \alpha_5 \times (x/w)^5$ for the following parameters: (a) $\alpha_5 = \pi/10$, (b) $\alpha_5 = \pi$, (a) $\alpha_5 = 5\pi$.

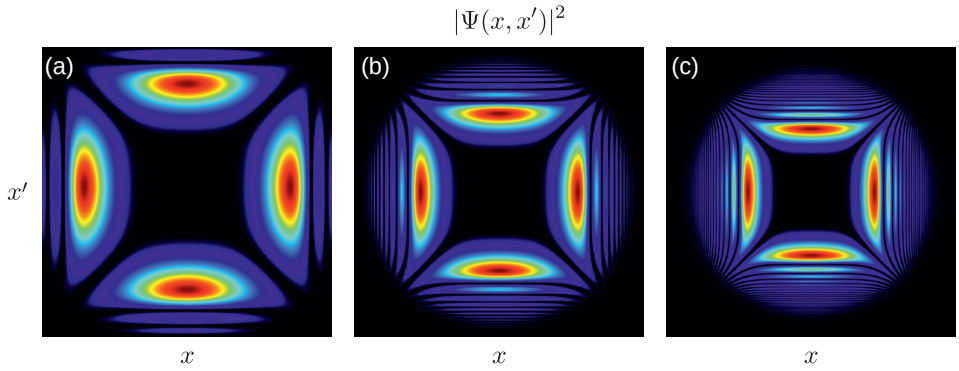


Figure E.4: HSP structures $|\Psi(x,x')|^2$ plotted for the sixth-order polynomial phase $\varphi(x) = \alpha_6 \times (x/w)^6$ for the following parameters: (a) $\alpha_6 = \pi/10$, (a=b) $\alpha_6 = \pi/2$, (a) $\alpha_6 = 2\pi$.

## E.2 Step function phase

Below we also present the HSP structures for the discontinuous functions describing phase profiles.

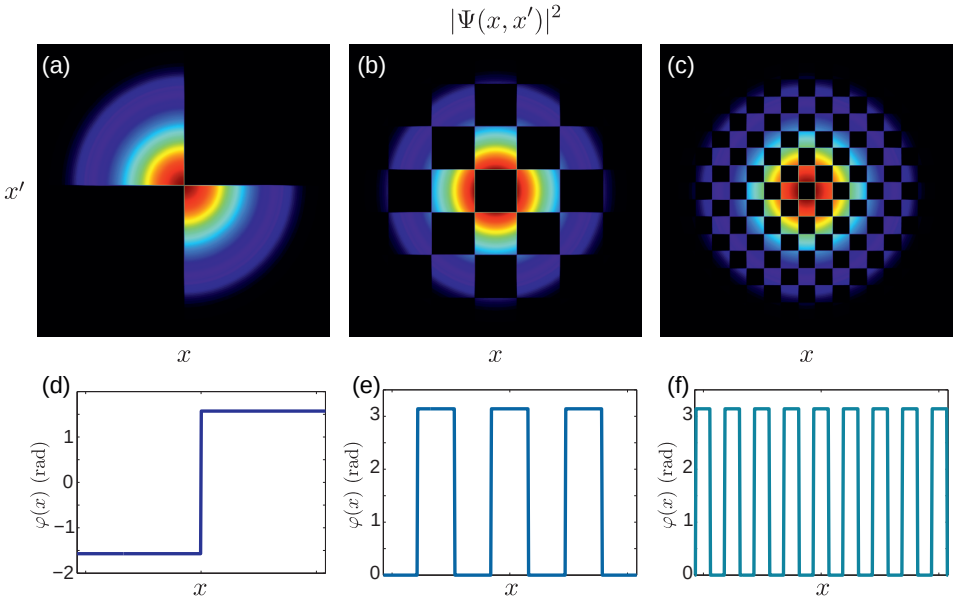


Figure E.5: (a-c) HSP structures $|\Psi(x,x')|^2$ plotted for the (d-f) corresponding phase profiles $\varphi(x)$ described by the plotted periodic step functions.

## E.3 Miscellaneous phase structures

Finally let us draw the generic HSP structures for more generic phase functions.

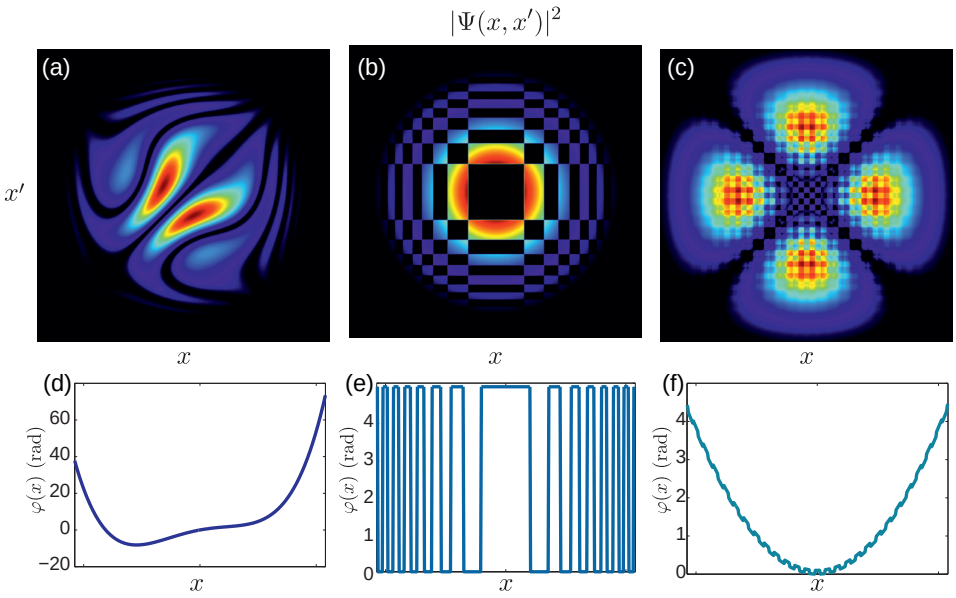


Figure E.6: (a-c) HSP structures $|\Psi(x,x')|^2$ plotted for the (d) generic polynomial phase (e) non-periodic step function and (f) a quadratic phase with an imprint of step function.

# BIBLIOGRAPHY


Abouraddy, A. F., G. Di Giuseppe, T. M. Yarnall, M. C. Teich, and B. E. A. Saleh (2012), "*Implementing one-photon three-qubit quantum gates using spatial light modulators*," Physical Review A **86** (5), 050303.

Abouraddy, A. F., M. B. Nasr, B. E. A. Saleh, A. V. Sergienko, and M. C. Teich (2001), "*Demonstration of the complementarity of one- and two-photon interference*," Physical Review A **63** (6), 063803.

Achilles, D., C. Silberhorn, C. Sliwa, K. Banaszek, I. A. Walmsley, M. J. Fitch, B. C. Jacobs, T. B. Pittman, and J. D. Franson (2004), "*Photon-number-resolving detection using time-multiplexing*," Journal of Modern Optics **51** (9-10), 1499.

Afek, I., O. Ambar, and Y. Silberberg (2010), "*High-NOON states by mixing quantum and classical light.*" Science **328** (5980), 879.

Afek, I., A. Natan, O. Ambar, and Y. Silberberg (2009), "*Quantum state measurements using multipixel photon detectors*," Physical Review A **79** (4), 043830.

Allman, M. S., V. B. Verma, M. Stevens, T. Gerrits, R. D. Horansky, a. E. Lita, F. Marsili, a. Beyer, M. D. Shaw, D. Kumor, R. Mirin, and S. W. Nam (2015), "*A near-infrared 64-pixel superconducting nanowire single photon detector array with integrated multiplexed readout*," Applied Physics Letters **106** (19), 192601.

Andor, (2012), *Zyla 5.5 sCMOS*, Tech. Rep.

Andor, (2015), *Andor's iZyla sCMOS*, Tech. Rep.

Arditi, M., and T. R. Carver (1964), "*Hyperfine Relaxation of Optically Pumped Rb87 Atoms in Buffer Gases*," Physical Review **136** (3A), A643.

Aspuru-Guzik, A., and P. Walther (2012), "*Photonic quantum simulators*," Nature Physics **8** (4), 285.

Banaszek, K., and I. A. Walmsley (2003), "*Photon counting with a loop detector*," Optics Letters **28** (1), 52.

Bao, X.-H., A. Reingruber, P. Dietrich, J. Rui, A. Duck, T. Strassel, L. Li, N.-L. Liu, B. Zhao, and J.-W. Pan (2012), "*Efficient and long-lived quantum memory with cold atoms inside a ring cavity*," Nature Physics **8** (7), 517.

Basden, A. G., C. A. Haniff, and C. D. Mackay (2003), "*Photon counting strategies with low-light-level CCDs*," Monthly Notices of the Royal Astronomical Society **345** (3), 985.

Bashkansky, M., F. K. Fatemi, and I. Vurgaftman (2012), "*Quantum memory in warm rubidium vapor with buffer gas*," Optics Letters **37** (2), 142.

Beduini, F. A., J. A. Zielińska, V. G. Lucivero, Y. A. de Icaza Astiz, and M. W. Mitchell (2014), "*Interferometric Measurement of the Biphoton Wave Function*," Physical Review Letters **113** (18), 183602.

Bell, J. S. (1964), "*On the Einstein Podolsky Rosen paradox*," Physics **1** (3), 195.

Bennett, A. J., R. B. Patel, C. A. Nicoll, D. A. Ritchie, and A. J. Shields (2009), "*Interference of dissimilar photon sources*," Nature Physics **5** (10), 715.

Bennett, C. H., and G. Brassard (1984), "*Quantum Cryptography: Public key distribution and coin tossing*," in *Proceedings of the IEEE International Conference on Computers, Systems, and Signal Processing, Bangalore*, p. 175.

Bhaskar, N., W. Happer, and T. McClelland (1982), "*Efficiency of Spin Exchange between Rubidium Spins and Xe129 Nuclei in a Gas*," Physical Review Letters **49** (1), 25.

Białynicki-Birula, I. (1996), "*Photon Wave Function*," Progress in Optics **36**, 245.

Białynicki-Birula, I. (1998), "*Exponential Localization of Photons*," Physical Review Letters **80** (24), 5247.

Białynicki-Birula, I., and Z. Białynicka-Birula (2004), "*QED Quantum theory of the electromagnetic field*," in *Encyclopedia of Modern Optic*, edited by B. D. Guenther (Elsevier, Amsterdam) p. 211.

Białynicki-Birula, I., and Z. Białynicka-Birula (2012), "*Uncertainty Relation for Photons*," Physical Review Letters **108** (14), 140401.

Białynicki-Birula, I., and Z. Białynicka-Birula (2013), "*The role of the Riemann-Silberstein vector in classical and quantum theories of electromagnetism*," Journal of Physics A: Mathematical and Theoretical **46** (5), 053001.

Blais, A., R.-S. Huang, A. Wallraff, S. Girvin, and R. Schoelkopf (2004), "*Cavity quantum electrodynamics for superconducting electrical circuits: An architecture for quantum computation*," Physical Review A **69** (6), 062320.

Blanchet, J.-L., F. Devaux, L. Furfaro, and E. Lantz (2008), "*Measurement of Sub-Shot-Noise Correlations of Spatial Fluctuations in the Photon-Counting Regime*," Physical Review Letters **101** (23), 233604.

Bouchiat, M. A. (1972), "*Evidence for Rb-Rare-Gas Molecules from the Relaxation of Polarized Rb Atoms in a Rare Gas. Experimental Results*," The Journal of Chemical Physics **56** (7), 3703.

Boyd, R. W. (2003), *Nonlinear Optics*, 2nd ed. (Academic Press, San Diego).

Boyd, S. P., and L. Vandenberghe (2004), *Convex Optimization*, 1st ed. (Cambridge University Press, Cambridge).

Boyer, V., A. Marino, and P. Lett (2008a), "*Generation of Spatially Broadband Twin Beams for Quantum Imaging*," Physical Review Letters **100** (14), 143601.

Boyer, V., A. M. Marino, R. C. Pooser, and P. D. Lett (2008b), "*Entangled images from four-wave mixing*." Science **321** (5888), 544.

Brida, G., L. Ciavarella, I. P. Degiovanni, M. Genovese, L. Lolli, M. G. Mingolla, F. Piacentini, M. Rajteri, E. Taralli, and M. G. A. Paris (2012), "*Quantum characterization of superconducting photon counters*," New Journal of Physics **14** (8), 085001.

Brida, G., M. Genovese, and I. Ruo Berchera (2010), "*Experimental realization of sub-shot-noise quantum imaging*," Nature Photonics **4** (4), 227.

Brion, E., L. H. Pedersen, and K. Mølmer (2007), "*Adiabatic elimination in a lambda system*," Journal of Physics A: Mathematical and Theoretical **40** (5), 1033.

Bussieres, F., N. Sangouard, M. Afzelius, H. de Riedmatten, C. Simon, and W. Tittel (2013), "*Prospective applications of optical quantum memories*," Journal of Modern Optics **60** (18), 1519.

Bustard, P. J., J. Erskine, D. G. England, J. Nunn, P. Hockett, R. Lausten, M. Spanner, and B. J. Sussman (2015), "*Nonclassical correlations between terahertz-bandwidth photons mediated by rotational quanta in hydrogen molecules.*" Optics Letters **40** (6), 922.

Bustard, P. J., R. Lausten, D. G. England, and B. J. Sussman (2013), "*Toward Quantum Processing in Molecules: A THz-Bandwidth Coherent Memory for Light*," Physical Review Letters **111** (8), 083901.

Chaneliere, T., D. N. Matsukevich, S. D. Jenkins, S.-Y. Lan, T. A. B. Kennedy, and A. Kuzmich (2005), "*Storage and retrieval of single photons transmitted between remote quantum memories.*" Nature **438** (7069), 833.

Chang, D. E., A. S. Sørensen, E. A. Demler, and M. D. Lukin (2007), "*A single-photon transistor using nanoscale surface plasmons*," Nature Physics **3** (11), 807.

Chapman, S., and T. G. Cowling (1991), *The Mathematical Theory of Non-uniform Gases*, 3rd ed. (Cambridge University Press, Cambridge).

Childress, L., J. M. Taylor, A. S. Sørensen, and M. D. Lukin (2005), "*Fault-tolerant quantum repeaters with minimal physical resources and implementations based on single-photon emitters*," Physical Review A **72** (5), 052330.

Choi, K. S., H. Deng, J. Laurat, and H. J. Kimble (2008), "*Mapping photonic entanglement into and out of a quantum memory.*" Nature **452** (7183), 67.

Chrapkiewicz, R. (2014), "*Photon counts statistics of squeezed and multimode thermal states of light on multiplexed on-off detectors*," Journal of the Optical Society of America B **31** (10), B8.

Chrapkiewicz, R., M. Dąbrowski, and W. Wasilewski (2015a), "*High-Capacity, Single-Photon-Level Warm Atomic Memory Storing up to 120 Spatial Modes*," in *CLEO: 2015 Postdeadline Paper Digest* (OSA, Washington, D.C.) p. JTh5B.8.

Chrapkiewicz, R., M. Jachura, W. Wasilewski, and K. Banaszek (2015b), "*Hologram of a single photon*," arXiv:1509.02890.

Chrapkiewicz, R., and W. Wasilewski (2012), "*Generation and delayed retrieval of spatially multimode Raman scattering in warm rubidium vapours*," Optics Express **20** (28), 29540.

Chrapkiewicz, R., and W. Wasilewski (2014), "*Przestrajalny, waskopasmowy filtr optyczny do filtrowania wiazek laserowych i sposob filtrowania wiazek laserowych*," Polish Patent Office, P.408059.

Chrapkiewicz, R., and W. Wasilewski (2015), "*Uklad pomiarowy do wyznaczania polozenia plaszczyzny ogniskowej i dlugosci ogniskowej ukladu optycznego oraz sposob wyznaczania polozenia plaszczyzny ogniskowej i dlugosci ogniskowej ukladu optycznego*," Polish Patent Office, P.412267.

Chrapkiewicz, R., W. Wasilewski, and K. Banaszek (2014a), "*High-fidelity spatially resolved multiphoton counting for quantum imaging applications.*" Optics Letters **39** (17), 5090.

Chrapkiewicz, R., W. Wasilewski, and C. Radzewicz (2014b), "*How to measure diffusional decoherence in multimode rubidium vapor memories?*" Optics Communications **317**, 1.

Clausen, C., I. Usmani, F. Bussières, N. Sangouard, M. Afzelius, H. de Riedmatten, and N. Gisin (2011), "*Quantum storage of photonic entanglement in a crystal.*" Nature **469** (7331), 508.

Crespi, A., M. Lobino, J. C. F. Matthews, A. Politi, C. R. Neal, R. Ramponi, R. Osellame, and J. L. O'Brien (2012), "*Measuring protein concentration with entangled photons*," Applied Physics Letters **100** (23), 233704.

Crespi, A., R. Osellame, R. Ramponi, D. J. Brod, E. F. Galvao, N. Spagnolo, C. Vitelli, E. Maiorino, P. Mataloni, and F. Sciarrino (2013), "*Integrated multimode interferometers with arbitrary designs for photonic boson sampling*," Nature Photonics **7** (7), 545.

Cui, J.-M., F.-W. Sun, X.-D. Chen, Z.-J. Gong, and G.-C. Guo (2013), "*Quantum Statistical Imaging of Particles without Restriction of the Diffraction Limit*," Physical Review Letters **110** (15), 153901.

Dada, A. C., J. Leach, G. S. Buller, M. J. Padgett, and E. Andersson (2011), "*Experimental high-dimensional two-photon entanglement and violations of generalized Bell inequalities*," Nature Physics **7** (9), 677.

Dauler, E. a., M. E. Grein, A. J. Kerman, F. Marsili, S. Miki, S. W. Nam, M. D. Shaw, H. Terai, V. B. Verma, and T. Yamashita (2014), "*Review of superconducting nanowire single-photon detector system design options and demonstrated performance*," Optical Engineering **53** (8), 081907.

Davis, K. M., K. Miura, N. Sugimoto, and K. Hirao (1996), "*Writing waveguides in glass with a femtosecond laser*," Optics Letters **21** (21), 1729.

Demkowicz-Dobrzański, R., M. Jarzyna, and J. Kołodyński (2014), "*Quantum limits in optical interferometry*," Progress in Optics **60**, 345.

Demkowicz-Dobrzański, R., J. Kołodyński, and M. Guta (2012), "*The elusive Heisenberg limit in quantum-enhanced metrology*," Nature Communications **3**, 1063.

Di Giuseppe, G., M. Atatüre, M. Shaw, A. Sergienko, B. Saleh, M. Teich, A. Miller, S. Nam, and J. Martinis (2003), "*Direct observation of photon pairs at a single output port of a beam-splitter interferometer*," Physical Review A **68** (6), 063817.

Dirac, P. A. M. (1981), *The Principles of Quantum Mechanics*, 4th ed. (Oxford Uniersity Press, Oxford).

Dąbrowski, M., R. Chrapkiewicz, and W. Wasilewski (2014), "*Hamiltonian design in readout from room-temperature Raman atomic memory*," Optics Express **22** (21), 26076.

Dąbrowski, M., R. Chrapkiewicz, and W. Wasilewski (2015), "*Magnetically tuned, robust and efficient filtering system for spatially multimode quantum memory in warm atomic vapors*," Journal of Modern Optics (Quantum Memories).

Drummond, P. D., and Z. Ficek, Eds. (2004), *Quantum Squeezing* (Springer-Verlag, Berlin Heidelberg).

Duan, L.-M. M., M. D. Lukin, J. I. Cirac, and P. Zoller (2001), "*Long-distance quantum communication with atomic ensembles and linear optics.*" Nature **414** (6862), 5788.

Edgar, M., D. Tasca, F. Izdebski, R. Warburton, J. Leach, M. Agnew, G. Buller, R. Boyd, and M. Padgett (2012), "*Imaging high-dimensional spatial entanglement with a camera*," Nature Communications **3**, 984.

Einstein, A. (1905), "*Uber einem die Erzeugung und Verwandlung des Lichtes betreffenden heuristischen Gesichtspunkt*," Annalen der Physik **4**, 132.

Einstein, A., B. Podolsky, and N. Rosen (1935), "*Can Quantum-Mechanical Description of Physical Reality Be Considered Complete?*" Physical Review **47** (10), 777.

Eisaman, M. D. (2006), *Generation, Storage, and Retrieval of Nonclassical States of Light using Atomic Ensembles*, Ph.D. thesis.

Eisaman, M. D., A. André, F. Massou, M. Fleischhauer, a. S. Zibrov, and M. D. Lukin (2005), "*Electromagnetically induced transparency with tunable single-photon pulses.*" Nature **438** (7069), 837.

Eisaman, M. D., L. Childress, A. André, F. Massou, A. Zibrov, and M. D. Lukin (2004), "*Shaping Quantum Pulses of Light Via Coherent Atomic Memory*," Physical Review Letters **93** (23), 1.

Ekert, A. K. (1991), "*Quantum cryptography based on Bell's theorem*," Physical Review Letters **67** (6), 661.

Feito, A., J. S. Lundeen, H. Coldenstrodt-Ronge, J. Eisert, M. B. Plenio, and I. a. Walmsley (2009), "*Measuring measurement: theory and practice*," New Journal of Physics **11** (9), 093038.

Ferri, F., D. Magatti, A. Gatti, M. Bache, E. Brambilla, and L. A. Lugiato (2005), "*High-Resolution Ghost Image and Ghost Diffraction Experiments with Thermal Light*," Physical Review Letters **94** (18), 183602.

Fickler, R., M. Krenn, R. Lapkiewicz, S. Ramelow, and A. Zeilinger (2013), "*Real-Time Imaging of Quantum Entanglement*," Scientific Reports **3**, 1914.

Fickler, R., R. Lapkiewicz, W. N. Plick, M. Krenn, C. Schaeff, S. Ramelow, and A. Zeilinger (2012), "*Quantum entanglement of high angular momenta.*" Science **338** (6107), 640.

Fink, A., D. Baumer, and E. Brunner (2005), "*Production of hyperpolarized xenon in a static pump cell: Numerical simulations and experiments*," Physical Review A **72** (5), 053411.

Firstenberg, O., P. London, M. Shuker, A. Ron, and N. Davidson (2009), "*Elimination, reversal and directional bias of optical diffraction*," Nature Physics **5** (9), 665.

Firstenberg, O., M. Shuker, A. Ron, and N. Davidson (2013), "*Colloquium: Coherent diffusion of polaritons in atomic media*," Reviews of Modern Physics **85** (3), 941.

Fleischhauer, M., A. Imamoglu, and J. Marangos (2005), "*Electromagnetically induced transparency: Optics in coherent media*," Reviews of Modern Physics **77** (2), 633.

Franz, F. (1965), "*Rubidium Spin Relaxation in the Rare Gases Under Ultraclean Conditions*," Physical Review **139** (3A), A603.

Franzen, W. (1959), "*Spin Relaxation of Optically Aligned Rubidium Vapor*," Physical Review **115** (4), 850.

Fukuda, D., G. Fujii, T. Numata, K. Amemiya, A. Yoshizawa, H. Tsuchida, H. Fujino, H. Ishii, T. Itatani, S. Inoue, and T. Zama (2011), "*Titanium-based transition-edge photon number resolving detector with 98% detection efficiency with index-matched small-gap fiber coupling.*" Optics Express **19** (2), 870.

Gabor, D. (1948), "*A New Microscopic Principle*," Nature **161** (4098), 777.

Garrison, J., and R. Chiao (2008), *Quantum Optics* (Oxford University Press, Oxford).

Gatti, A., E. Brambilla, and L. Lugiato (2008), "*Quantum imaging*," Progress in Optics **51**, 251.

Gatto Monticone, D., K. Katamadze, P. Traina, E. Moreva, J. Forneris, I. Ruo-Berchera, P. Olivero, I. Degiovanni, G. Brida, and M. Genovese (2014), "*Beating the Abbe Diffraction Limit in Confocal Microscopy via Nonclassical Photon Statistics*," Physical Review Letters **113** (14), 143602.

Gerry, C., and P. Knight (2005), *Introductory Quantum Optics* (Cambridge University Press).

Giovannetti, V., S. Lloyd, and L. Maccone (2006), "*Quantum Metrology*," Physical Review Letters **96** (1), 010401.

Giovannini, D., J. Romero, V. Poto ek, G. Ferenczi, F. Speirits, S. M. Barnett, D. Faccio, and M. J. Padgett (2015), "*Spatially structured photons that travel in free space slower than the speed of light*," Science **347** (6224), 857.

Gisin, N., G. Ribordy, W. Tittel, and H. Zbinden (2002), "*Quantum cryptography*," Reviews of Modern Physics **74** (1), 145.

Giustina, M., A. Mech, S. Ramelow, B. Wittmann, J. Kofler, J. Beyer, A. Lita, B. Calkins, T. Gerrits, S. W. Nam, R. Ursin, and A. Zeilinger (2013), "*Bell violation using entangled photons without the fair-sampling assumption.*" Nature **497** (7448), 227.

Giustina, M., M. A. M. Versteegh, S. Wengerowsky, J. Handsteiner, A. Hochrainer, K. Phelan, F. Steinlechner, J. Kofler, J.-A. Larsson, C. Abellan, W. Amaya, V. Pruneri, M. W. Mitchell, J. Beyer, T. Gerrits, A. E. Lita, L. K. Shalm, S. W. Nam, T. Scheidl, R. Ursin, B. Wittmann, and A. Zeilinger (2015), "*A significant-loophole-free test of Bell's theorem with entangled photons*," arXiv:1511.03190 .

Glorieux, Q., J. B. Clark, A. M. Marino, Z. Zhou, and P. D. Lett (2012), "*Temporally multiplexed storage of images in a gradient echo memory*," Optics Express **20** (11), 12350.

Goodman, J. W. (2015), *Statistical Optics*, 2nd ed. (Wiley, New Jersey).

Gorshkov, A. V., A. André, M. D. Lukin, and A. S. Sørensen (2007), "*Photon storage in* $\Lambda$ *-type optically dense atomic media. II. Free-space model*," Physical Review A **76** (3), 033805.

Grant, M. C., S. P. Boyd, and C. R. Inc (2015), *The CVX's User Guide*, Tech. Rep.

Haas, F., J. Volz, R. Gehr, J. Reichel, and J. Esteve (2014), "*Entangled states of more than 40 atoms in an optical fiber cavity.*" Science **344** (6180), 180.

Haderka, O., J. Perina, and M. Hamar (2005), "*Direct measurement and reconstruction of nonclassical features of twin beams generated in spontaneous parametric down-conversion,*" Physical Review A **71** (3), 4.

Hadfield, R. (2009), "*Single-photon detectors for optical quantum information applications,*" Nature Photonics **3** (12), 696.

Haffner, H., C. Roos, and R. Blatt (2008), "*Quantum computing with trapped ions,*" Physics Reports **469** (4), 155.

Hamamatsu, (2009), *Image intensifiers*, Tech. Rep.

Hanbury Brown, R., and R. Q. Twiss (1956), "*A Test of a New Type of Stellar Interferometer on Sirius,*" Nature **178** (4541), 1046.

Happer, W. (1972), "*Optical Pumping,*" Reviews of Modern Physics **44** (2), 169.

Harpsoe, K. B. W., M. I. Andersen, and P. Kjægaard (2012), "*Bayesian photon counting with electron-multiplying charge coupled devices (EMCCDs),*" Astronomy & Astrophysics **537**, A50.

Hedges, R. E. M., D. L. Drummond, and A. Gallagher (1972), "*Extreme-Wing Line Broadening and Cs-Inert-Gas Potentials,*" Physical Review A **6** (4), 1519.

Heifetz, A., A. Agarwal, G. C. Cardoso, V. Gopal, P. Kumar, and M. Shahriar (2004), "*Super efficient absorption filter for quantum memory using atomic ensembles in a vapor,*" Optics Communications **232** (1-6), 289.

Heilmann, R., J. Sperling, A. Perez-Leija, M. Graefe, M. Heinrich, S. Nolte, W. Vogel, and A. Szameit (2015), "*Divide-and-Conquer: An integrated photon-counting scheme,*" arXiv:1502.04932 .

Hell, S. W., and J. Wichmann (1994), "*Breaking the diffraction resolution limit by stimulated emission: stimulated-emission-depletion fluorescence microscopy,*" Optics Letters **19** (11), 780.

Hensen, B., H. Bernien, A. E. Dréau, A. Reiserer, N. Kalb, M. S. Blok, J. Ruitenberg, R. F. L. Vermeulen, R. N. Schouten, C. Abellán, W. Amaya, V. Pruneri, M. W. Mitchell, M. Markham, D. J. Twitchen, D. Elkouss, S. Wehner, T. H. Taminiau, and R. Hanson (2015), "*Experimental loophole-free violation of a Bell inequality using entangled electron spins separated by 1.3 km,*" arXiv:1508.05949 .

Heshami, K., D. G. England, P. C. Humphreys, P. J. Bustard, V. M. Acosta, J. Nunn, and B. J. Sussman (2015), "*Quantum memories: emerging applications and recent advances,*" arXiv:1511.04018 .

Higginbottom, D. B., B. M. Sparkes, M. Rancic, O. Pinel, M. Hosseini, P. K. Lam, and B. C. Buchler (2012), "*Spatial-mode storage in a gradient-echo memory,*" Physical Review A **86** (2), 023801.

Hogervorst, W. (1971), "*Diffusion coefficients of noble-gas mixtures between 300 K and 1400 K,*" Physica **51** (1), 59.

Holstein, T., and H. Primakoff (1940), "*Field Dependence of the Intrinsic Domain Magnetization of a Ferromagnet*," Physical Review **58** (12), 1098.

Hong, C. K., Z. Y. Ou, and L. Mandel (1987), "*Measurement of subpicosecond time intervals between two photons by interference*," Physical Review Letters **59** (18), 2044.

Hong, P., J. Liu, and G. Zhang (2012), "*Two-photon superbunching of thermal light via multiple two-photon path interference*," Physical Review A **86** (1), 013807.

Horsley, A., G.-X. Du, and P. Treutlein (2015), "*Widefield microwave imaging in alkali vapor cells with sub-100 micrometer resolution*," New Journal of Physics **17** (11), 112002.

Hosseini, M., G. Campbell, B. M. Sparkes, P. K. Lam, and B. C. Buchler (2011), "*Unconditional room-temperature quantum memory*," Nature Physics **7** (10), 794.

Hosseini, M., B. M. Sparkes, G. Hétet, J. J. Longdell, P. K. Lam, and B. C. Buchler (2009), "*Coherent optical pulse sequencer for quantum applications.*" Nature **461** (7261), 241.

Howell, J. C., R. S. Bennink, S. J. Bentley, and R. W. Boyd (2004), "*Realization of the Einstein-Podolsky-Rosen Paradox Using Momentum- and Position-Entangled Photons from Spontaneous Parametric Down Conversion*," Physical Review Letters **92** (21), 210403.

Huang, B., M. Bates, and X. Zhuang (2009), "*Super-Resolution Fluorescence Microscopy*," Annual Review of Biochemistry **78** (1), 993.

Humphreys, P. C., W. S. Kolthammer, J. Nunn, M. Barbieri, A. Datta, and I. A. Walmsley (2014), "*Continuous-Variable Quantum Computing in Optical Time-Frequency Modes Using Quantum Memories*," Physical Review Letters **113** (13), 130502.

Jachura, M., and R. Chrapkiewicz (2015a), "*Optics & Photonics News*," Optics & Photonics News (Optics in 2015), 42.

Jachura, M., and R. Chrapkiewicz (2015b), "*Shot-by-shot imaging of Hong-Ou-Mandel interference with an intensified sCMOS camera.*" Optics Letters **40** (7), 1540.

Jachura, M., R. Chrapkiewicz, R. Demkowicz-Dobrzański, W. Wasilewski, and K. Banaszek (2015), "*Mode engineering for realistic quantum-enhanced interferometry*," arXiv:1504.05435 .

Jachura, M., M. Karpiński, C. Radzewicz, and K. Banaszek (2014), "*High-visibility nonclassical interference of photon pairs generated in a multimode nonlinear waveguide*," Optics Express **22** (7), 8624.

John, J. J., M. Brouard, a. Clark, J. Crooks, E. Halford, L. Hill, J. W. L. Lee, a. Nomerotski, R. Pisarczyk, I. Sedgwick, C. S. Slater, R. Turchetta, C. Vallance, E. Wilman, B. Winter, and W. H. Yuen (2012), "*PImMS, a fast event-triggered monolithic pixel detector with storage of multiple timestamps*," Journal of Instrumentation **7** (08), C08001.

Johnson, M. W., M. H. S. Amin, S. Gildert, T. Lanting, F. Hamze, N. Dickson, R. Harris, A. J. Berkley, J. Johansson, P. Bunyk, E. M. Chapple, C. Enderud, J. P. Hilton, K. Karimi, E. Ladizinsky, N. Ladizinsky, T. Oh, I. Perminov, C. Rich, M. C. Thom, E. Tolkacheva, C. J. S. Truncik, S. Uchaikin, J. Wang, B. Wilson, and G. Rose (2011), "*Quantum annealing with manufactured spins.*" Nature **473** (7346), 194.

Kalashnikov, D. A., S.-H. Tan, T. S. Iskhakov, M. V. Chekhova, and L. A. Krivitsky (2012), "*Measurement of two-mode squeezing with photon number resolving multipixel detectors.*" Optics Letters **37** (14), 2829.

Kaltenbaek, R., B. Blauensteiner, M. Żukowski, M. Aspelmeyer, and A. Zeilinger (2006), "*Experimental Interference of Independent Photons,*" Physical Review Letters **96** (24), 240502.

Karpiński, M., C. Radzewicz, and K. Banaszek (2012), "*Dispersion-based control of modal characteristics for parametric down-conversion in a multimode waveguide,*" Optics Letters **37** (5), 878.

Keller, O. (2005), "*On the theory of spatial localization of photons,*" Physics Reports **411** (1-3), 1.

Kelly, J., R. Barends, A. G. Fowler, A. Megrant, E. Jeffrey, T. C. White, D. Sank, J. Y. Mutus, B. Campbell, Y. Chen, Z. Chen, B. Chiaro, A. Dunsworth, I.-C. Hoi, C. Neill, P. J. J. O'Malley, C. Quintana, P. Roushan, A. Vainsencher, J. Wenner, A. N. Cleland, and J. M. Martinis (2015), "*State preservation by repetitive error detection in a superconducting quantum circuit,*" Nature **519** (7541), 66.

Kiefer, W., R. Löw, J. Wrachtrup, and I. Gerhardt (2014), "*Na-Faraday rotation filtering: The optimal point,*" Scientific Reports **4**, 6552.

Kiesel, T., and W. Vogel (2012), "*Complete nonclassicality test with a photon-number-resolving detector,*" Physical Review A **86** (3), 032119.

Kim, H.-C., and Y. H. Lee (1999), "*Hermite-Gaussian and Laguerre-Gaussian beams beyond the paraxial approximation,*" Optics Communications **169** (1-6), 9.

Kimble, H. J. (2008), "*The quantum internet.*" Nature **453** (7198), 1023.

Kimble, H. J., M. Dagenais, and L. Mandel (1977), "*Photon antibunching in resonance fluorescence,*" Physical Review Letters **39** (11), 691.

Knill, E., R. Laflamme, and G. J. Milburn (2001), "*A scheme for efficient quantum computation with linear optics.*" Nature **409** (6816), 46.

Kolobov, M. I., Ed. (2007), *Quantum Imaging* (Springer, New York).

Kołodyński, J., J. Chwedenczuk, and W. Wasilewski (2012), "*Eigenmode description of Raman scattering in atomic vapors in the presence of decoherence,*" Physical Review A **86** (1), 013818.

Krenn, M., J. Handsteiner, M. Fink, R. Fickler, and A. Zeilinger (2015), "*Twisted photon entanglement through turbulent air across Vienna,*" arXiv:1507.06551 .

Krishnaswami, V., C. J. F. Van Noorden, E. M. M. Manders, and R. A. Hoebe (2014), "*Towards digital photon counting cameras for single-molecule optical nanoscopy,*" Optical Nanoscopy **3** (1), 1.

Kuklewicz, C., M. Fiorentino, G. Messin, F. Wong, and J. Shapiro (2004), "*High-flux source of polarization-entangled photons from a periodically poled KTiOPO4 parametric down-converter,*" Physical Review A **69** (1), 013807.

Kuzmich, a., W. P. Bowen, A. D. Boozer, A. Boca, C. W. Chou, L.-M. Duan, and H. J. Kimble (2003), "*Generation of nonclassical photon pairs for scalable quantum communication with atomic ensembles.*" Nature **423** (6941), 731.

Lee, K. C., M. R. Sprague, B. J. Sussman, J. Nunn, N. K. Langford, X.-M. Jin, T. Champion, P. Michelberger, K. F. Reim, D. England, D. Jaksch, and I. A. Walmsley (2011), "*Entangling macroscopic diamonds at room temperature.*" Science **334** (6060), 1253.

Lemos, G. B., V. Borish, G. D. Cole, S. Ramelow, R. Lapkiewicz, and A. Zeilinger (2014), "*Quantum imaging with undetected photons*," Nature **512** (7515), 409.

LIGO Collaboration, (2013), "*Enhanced sensitivity of the LIGO gravitational wave detector by using squeezed states of light*," Nature Photonics **7** (8), 613.

Longdell, J. J., M. J. Sellars, P. K. Lam, B. C. Buchler, G. Hétet, J. J. Longdell, M. J. Sellars, P. K. Lam, and B. C. Buchler (2008), "*Multimodal Properties and Dynamics of Gradient Echo Quantum Memory*," Physical Review Letters **101** (20), 203601.

Lopes, R., A. Imanaliev, A. Aspect, M. Cheneau, D. Boiron, and C. I. Westbrook (2015), "*Atomic Hong-Ou-Mandel experiment*," Nature **520** (7545), 66.

Lowe, I., and S. Gade (1967), "*Density-Matrix Derivation of the Spin-Diffusion Equation*," Physical Review **156** (3), 817.

Lugiato, L. A., A. Gatti, and E. Brambilla (2002), "*Quantum imaging*," Journal of Optics B: Quantum and Semiclassical Optics **4** (3), S176.

Lundeen, J. S., A. Feito, H. Coldenstrodt-Ronge, K. L. Pregnell, C. Silberhorn, T. C. Ralph, J. Eisert, M. B. Plenio, and I. A. Walmsley (2008), "*Tomography of quantum detectors*," Nature Physics **5** (1), 27.

Lundeen, J. S., B. Sutherland, A. Patel, C. Stewart, and C. Bamber (2011), "*Direct measurement of the quantum wavefunction.*" Nature **474** (7350), 188.

Lvovsky, A. I. (2015), "*Squeezed light*," in *Photonics, Volume 1, Fundamentals of Photonics and Physics*, edited by D. L. Andrews, Chap. 5 (Wiley, West Sussex).

Lvovsky, A. I., H. Hansen, T. Aichele, O. Benson, J. Mlynek, and S. Schiller (2001), "*Quantum State Reconstruction of the Single-Photon Fock State*," Physical Review Letters **87** (5), 2.

Lvovsky, A. I., B. C. Sanders, and W. Tittel (2009), "*Optical quantum memory*," Nature Photonics **3** (12), 706.

Ma, X.-s., S. Zotter, J. Kofler, T. Jennewein, and A. Zeilinger (2011), "*Experimental generation of single photons via active multiplexing*," Physical Review A **83** (4), 043814.

Machulka, R., O. Haderka, J. Perina, M. Lamperti, A. Allevi, and M. Bondani (2014), "*Spatial properties of twin-beam correlations at low- to high-intensity transition.*" Optics Express **22** (11), 13374.

Maiman, T. H. (1960), "*Stimulated Optical Radiation in Ruby*," Nature **187** (4736), 493.

Mandel, L., and E. Wolf (1995), *Optical Coherence and Quantum Optics* (Cambridge Univeristy Press, Cambridge).

Manz, S., T. Fernholz, J. Schmiedmayer, and J.-W. Pan (2007), "*Collisional decoherence during writing and reading quantum states*," Physical Review A **75** (4), 040101.

Matsko, A. B., O. Kocharovskaya, Y. Rostovtsev, G. R. Welch, A. S. Zibrov, and M. O. Scully (2001), "*Slow, ultraslow, stored, and frozen light*," Advances In Atomic, Molecular, and Optical Physics **46**, 191.

Maurer, P. C., G. Kucsko, C. Latta, L. Jiang, N. Y. Yao, S. D. Bennett, F. Pastawski, D. Hunger, N. Chisholm, M. Markham, D. J. Twitchen, J. I. Cirac, and M. D. Lukin (2012), "*Room-temperature quantum bit memory exceeding one second*." Science **336** (6086), 1283.

McCarron, D. J., I. G. Hughes, P. Tierney, and S. L. Cornish (2007), "*A heated vapor cell unit for dichroic atomic vapor laser lock in atomic rubidium*," Review of Scientific Instruments **78** (9), 093106.

Merali, Z. (2011), "*First sale for quantum computing*," Nature **474** (18).

Michelberger, P. S., T. F. M. Champion, M. R. Sprague, K. T. Kaczmarek, M. Barbieri, X. M. Jin, D. G. England, W. S. Kolthammer, D. J. Saunders, J. Nunn, and I. a. Walmsley (2015), "*Interfacing GHz-bandwidth heralded single photons with a warm vapour Raman memory*," New Journal of Physics **17** (4), 043006.

Moore, S. (2007), "*Commercializing Quantum Keys*," IEEE Spectrum **44** (3), 15.

Moreau, P.-A., F. Devaux, and E. Lantz (2014), "*Einstein-Podolsky-Rosen Paradox in Twin Images*," Physical Review Letters **113** (16), 160401.

Moreau, P.-A., J. Mougin-Sisini, F. Devaux, and E. Lantz (2012), "*Realization of the purely spatial Einstein-Podolsky-Rosen paradox in full-field images of spontaneous parametric down-conversion*," Physical Review A **86** (1), 010101.

Morris, P. A., R. S. Aspden, J. E. C. Bell, R. W. Boyd, and M. J. Padgett (2015), "*Imaging with a small number of photons*," Nature Communications **6**, 5913.

Mostowski, J., and B. Sobolewska (1984), "*Transverse effects in stimulated Raman scattering*," Physical Review A **30** (1), 610.

Nunn, J., T. F. Champion, J. Munns, C. Qiu, D. Saunders, and I. A. Walmsley (2015), "*Bad Cavities for Good Memories: Storing Broadband Photons with Low Noise*," in *CLEO: 2015* (OSA, Washington, D.C.) p. FTh4B.1.

Nunn, J., N. Langford, W. Kolthammer, T. Champion, M. Sprague, P. Michelberger, X.-M. Jin, D. England, and I. Walmsley (2013), "*Enhancing Multiphoton Rates with Quantum Memories*," Physical Review Letters **110** (13), 133601.

O'Brien, J. L. (2007), "*Optical quantum computing*." Science **318** (5856), 1567.

Oemrawsingh, S. S. R., W. J. van Drunen, E. R. Eliel, and J. P. Woerdman (2002), "*Two-dimensional wave-vector correlations in spontaneous parametric downconversion explored with an intensified CCD camera*," Journal of the Optical Society of America B **19** (10), 2391.

Ono, T., R. Okamoto, and S. Takeuchi (2013), "*An entanglement-enhanced microscope*," Nature Communications **4**, 2426.

Pampaloni, F., and J. Enderlein (2004), "*Gaussian, Hermite-Gaussian, and Laguerre-Gaussian beams: A primer*," arXiv:0410021 [physics] .

Parniak, M., and W. Wasilewski (2013), "*Direct observation of atomic diffusion in warm rubidium ensembles*," Applied Physics B **116** (2), 415.

Patel, R. B., A. J. Bennett, I. Farrer, C. A. Nicoll, D. A. Ritchie, and A. J. Shields (2010), "*Two-photon interference of the emission from electrically tunable remote quantum dots*," Nature Photonics **4** (9), 632.

Paul, H. (1982), "*Photon antibunching*," Reviews of Modern Physics **54** (4), 1061.

Paul, H., P. Törmä, T. Kiss, and I. Jex (1996), "*Photon Chopping: New Way to Measure the Quantum State of Light*," Physical Review Letters **76** (14), 2464.

Peeters, W., J. Renema, and M. van Exter (2009), "*Engineering of two-photon spatial quantum correlations behind a double slit*," Physical Review A **79** (4), 043817.

Perina, J., O. Haderka, V. Michalek, and M. Hamar (2012), "*Absolute detector calibration using twin beams*," Optics Letters **37** (13), 2475.

Peruzzo, A., M. Lobino, J. C. F. Matthews, N. Matsuda, A. Politi, K. Poulios, X.-Q. Zhou, Y. Lahini, N. Ismail, K. Worhoff, Y. Bromberg, Y. Silberberg, M. G. Thompson, and J. L. OBrien (2010a), "*Quantum Walks of Correlated Photons*," Science **329** (5998), 1500.

Peruzzo, A., M. Lobino, J. C. F. Matthews, N. Matsuda, A. Politi, K. Poulios, X.-Q. Zhou, Y. Lahini, N. Ismail, K. Worhoff, Y. Bromberg, Y. Silberberg, M. G. Thompson, and J. L. OBrien (2010b), "*Quantum Walks of Correlated Photons*," Science **329** (5998), 1500.

Peyronel, T., O. Firstenberg, Q.-Y. Liang, S. Hofferberth, A. V. Gorshkov, T. Pohl, M. D. Lukin, and V. Vuletić (2012), "*Quantum nonlinear optics with single photons enabled by strongly interacting atoms.*" Nature **488** (7409), 57.

Piacentini, F., M. P. Levi, A. Avella, M. López, S. Kück, S. V. Polyakov, I. P. Degiovanni, G. Brida, and M. Genovese (2015), "*Positive operator-valued measure reconstruction of a beam-splitter tree-based photon-number-resolving detector*," Optics Letters **40** (7), 1548.

Pittman, T. B., Y. H. Shih, D. V. Strekalov, and A. V. Sergienko (1995), "*Optical imaging by means of two-photon quantum entanglement*," Physical Review A **52** (5), R3429.

Planck, M. (1901), "*Ueber irreversible Strahlungsvorgange*," Annalen der Physik **311** (12), 818.

Radnaev, A. G., Y. O. Dudin, R. Zhao, H. H. Jen, S. D. Jenkins, A. Kuzmich, and T. A. B. Kennedy (2010), "*A quantum memory with telecom-wavelength conversion*," Nature Physics **6** (11), 894.

Rarity, J., P. Tapster, E. Jakeman, T. Larchuk, R. Campos, M. Teich, and B. Saleh (1990), "*Two-photon interference in a Mach-Zehnder interferometer*," Physical Review Letters **65** (11), 1348.

Raymer, M. G. (2004), "*Quantum state entanglement and readout of collective atomic-ensemble modes and optical wave packets by stimulated Raman scattering*," Journal of Modern Optics **51** (12), 1739.

Raymer, M. G., and J. L. Carlsten (1977), "*Simultaneous Observations of Stimulated Raman Scattering and Stimulated Collision-Induced Fluorescence*," Physical Review Letters **39** (21), 1326.

Raymer, M. G., and J. Mostowski (1981), "*Stimulated Raman scattering: Unified treatment of spontaneous initiation and spatial propagation*," Physical Review A **24** (4), 1980.

Rehacek, J., Z. Hradil, O. Haderka, J. Perina, and M. Hamar (2003), "*Multiple-photon resolving fiber-loop detector*," Physical Review A **67** (6), 061801.

Reid, M. D., and D. F. Walls (1986), "*Violations of classical inequalities in quantum optics*," Physical Review A **34** (2), 1260.

Reim, K. F., P. Michelberger, K. C. Lee, J. Nunn, N. K. Langford, and I. A. Walmsley (2011), "*Single-Photon-Level Quantum Memory at Room Temperature*," Physical Review Letters **107** (5), 053603.

Reim, K. F., J. Nunn, V. O. Lorenz, B. J. Sussman, K. C. Lee, N. K. Langford, D. Jaksch, and I. A. Walmsley (2010), "*Towards high-speed optical quantum memories*," Nature Photonics **4** (4), 218.

Rivest, R. L., A. Shamir, and L. Adleman (1978), "*A method for obtaining digital signatures and public-key cryptosystems*," Communications of the ACM **21** (2), 120.

Rousseau, D. L., G. D. Patterson, and P. F. Williams (1975), "*Resonance Raman Scattering and Collision-Induced Redistribution Scattering in I 2*," Physical Review Letters **34** (21), 1306.

Rozema, L. a., J. D. Bateman, D. H. Mahler, R. Okamoto, A. Feizpour, A. Hayat, and A. M. Steinberg (2014), "*Scalable Spatial Superresolution Using Entangled Photons*," Physical Review Letters **112** (22), 223602.

Saari, P. (2012), *Quantum Optics and Laser Experiments*, edited by S. Lyagushyn (InTech) Chap. 3.

Salart, D., A. Baas, J. A. W. van Houwelingen, N. Gisin, and H. Zbinden (2008), "*Spacelike Separation in a Bell Test Assuming Gravitationally Induced Collapses*," Physical Review Letters **100** (22), 220404.

Saunders, D. J., J. H. D. Munns, T. F. M. Champion, C. Qiu, K. T. Kaczmarek, E. Poem, P. M. Ledingham, I. A. Walmsley, and J. Nunn (2015), "*A Cavity-Enhanced Room-Temperature Broadband Raman Memory*," arXiv:1510.00462 .

Schumaker, B. L., and C. M. Caves (1985), "*New formalism for two-photon quantum optics. II. Mathematical foundation and compact notation*," Physical Review A **31** (5), 3093.

Schwartz, O., J. M. Levitt, R. Tenne, S. Itzhakov, Z. Deutsch, and D. Oron (2013), "*Superresolution Microscopy with Quantum Emitters*," Nano Letters **13** (12), 5832.

Schwartz, O., and D. Oron (2012), "*Improved resolution in fluorescence microscopy using quantum correlations*," Physical Review A **85** (3), 033812.

Scully, M. O., and M. S. Zubairy (1997), *Quantum Optics*, 1st ed. (Cambridge University Press).

Servin, M., J. L. Marroquin, and F. J. Cuevas (1997), "*Demodulation of a single interferogram by use of a two-dimensional regularized phase-tracking technique*," Applied Optics **36** (19), 4540.

Shalm, L. K., E. Meyer-Scott, B. G. Christensen, P. Bierhorst, M. A. Wayne, M. J. Stevens, T. Gerrits, S. Glancy, D. R. Hamel, M. S. Allman, K. J. Coakley, S. D. Dyer, C. Hodge, A. E. Lita, V. B. Verma, C. Lambrocco, E. Tortorici, A. L. Migdall, Y. Zhang, D. R. Kumor, W. H. Farr, F. Marsili, M. D. Shaw, J. A. Stern, C. Abellán, W. Amaya, V. Pruneri, T. Jennewein, M. W. Mitchell, P. G. Kwiat, J. C. Bienfang, R. P. Mirin, E. Knill, and S. W. Nam (2015), "*A strong loophole-free test of local realism*," arXiv:1511.03189 .

Shen, Y. R. (1974), "*Distinction between resonance Raman scattering and hot luminescence*," Physical Review B **9** (2), 622.

Shin, H., K. W. C. Chan, H. J. Chang, and R. W. Boyd (2011), "*Quantum Spatial Superresolution by Optical Centroid Measurements*," Physical Review Letters **107** (8), 083603.

Shor, P. W. (1997), "*Polynomial-Time Algorithms for Prime Factorization and Discrete Logarithms on a Quantum Computer*," SIAM Journal on Computing **26** (5), 1484.

Shuker, M., O. Firstenberg, R. Pugatch, A. Ron, and N. Davidson (2008), "*Storing Images in Warm Atomic Vapor*," Physical Review Letters **100** (22), 223601.

Siegman, A. E. (1986), *Lasers* (University Science Books, Sausalito, California).

Simon, C., M. Afzelius, J. Appel, a. Boyer de la Giroday, S. J. Dewhurst, N. Gisin, C. Y. Hu, F. Jelezko, S. Kröll, J. H. Müller, J. Nunn, E. S. Polzik, J. G. Rarity, H. De Riedmatten, W. Rosenfeld, a. J. Shields, N. Sköld, R. M. Stevenson, R. Thew, I. a. Walmsley, M. C. Weber, H. Weinfurter, J. Wrachtrup, and R. J. Young (2010), "*Quantum memories*," The European Physical Journal D **58** (1), 1.

Simonite, T. (2014), "*Google Launches Effort to Build Its Own Quantum Computer*," MIT Technology Review .

Smith, B. J., B. Killett, M. G. Raymer, I. a. Walmsley, and K. Banaszek (2005), "*Measurement of the transverse spatial quantum state of light at the single-photon level*," Optics Letters **30** (24), 3365.

Smith, R. A., D. V. Reddy, D. L. Vitullo, and M. G. Raymer (2015), "*Verification of a Heralded, Two-Photon Fock State with a Gang of Detectors*," in *Frontiers in Optics 2015* (OSA, Washington, D.C.) p. FTu3G.2.

Spagnolo, N., C. Vitelli, M. Bentivegna, D. J. Brod, A. Crespi, F. Flamini, S. Giacomini, G. Milani, R. Ramponi, P. Mataloni, R. Osellame, E. F. Galvão, and F. Sciarrino (2014), "*Experimental validation of photonic boson sampling*," Nature Photonics **8** (8), 615.

Specht, H. P., J. Bochmann, M. Mücke, B. Weber, E. Figueroa, D. L. Moehring, and G. Rempe (2009), "*Phase shaping of single-photon wave packets*," Nature Photonics **3** (8), 469.

Sperling, J., W. Vogel, and G. S. Agarwal (2012a), "*Sub-Binomial Light*," Physical Review Letters **109** (9), 093601.

Sperling, J., W. Vogel, and G. S. Agarwal (2012b), "*True photocounting statistics of multiple on-off detectors*," Physical Review A **85** (2), 023820.

Sperling, J., W. Vogel, and G. S. Agarwal (2013), "*Correlation measurements with on-off detectors*," Physical Review A **88** (4), 043821.

Sperling, J., W. Vogel, and G. S. Agarwal (2015), "*Balanced homodyne detection with on-off detector systems: Observable nonclassicality criteria*," EPL (Europhysics Letters) **109** (3), 34001.

Spring, J. B., B. J. Metcalf, P. C. Humphreys, W. S. Kolthammer, X.-M. Jin, M. Barbieri, A. Datta, N. Thomas-Peter, N. K. Langford, D. Kundys, J. C. Gates, B. J. Smith, P. G. R. Smith, and I. A. Walmsley (2013), "*Boson sampling on a photonic chip*," Science **339** (6121), 798.

Stack, D. T., P. J. Lee, and Q. Quraishi (2015), "*Simple and efficient absorption filter for single photons from a cold atom quantum memory.*" Optics Express **23** (5), 6822.

Stantchev, R. I., B. Sun, S. M. Hornett, P. A. Hobson, G. M. Gibson, M. J. Padgett, and E. Hendry (2015), "*Non-invasive, near-field terahertz imaging of hidden objects using a single pixel detector*," arXiv:1509.03138 .

Steane, A. (1998), "*Quantum computing*," Reports on Progress in Physics **61** (2), 117.

Tasca, D. S., M. P. Edgar, F. Izdebski, G. S. Buller, and M. J. Padgett (2013), "*Optimizing the use of detector arrays for measuring intensity correlations of photon pairs*," Physical Review A **88** (1), 013816.

Taylor, M. A., J. Janousek, V. Daria, J. Knittel, B. Hage, H.-A. Bachor, and W. P. Bowen (2013), "*Biological measurement beyond the quantum limit*," Nature Photonics **7** (3), 229.

Tittel, W., J. Brendel, H. Zbinden, and N. Gisin (1998), "*Violation of Bell Inequalities by Photons More Than 10 km Apart*," Physical Review Letters **81** (17), 3563.

Tsang, M. (2009), "*Quantum Imaging beyond the Diffraction Limit by Optical Centroid Measurements*," Physical Review Letters **102** (25), 253601.

Vallone, G., V. D'Ambrosio, A. Sponselli, S. Slussarenko, L. Marrucci, F. Sciarrino, and P. Villoresi (2014), "*Free-space quantum key distribution by rotation-invariant twisted photons*," Physical Review Letters **113** (6), 1.

Vanier, J., J.-F. Simard, and J.-S. Boulanger (1974), "*Relaxation and frequency shifts in the ground state of Rb85*," Physical Review A **9** (3), 1031.

Veissier, L., A. Nicolas, L. Giner, D. Maxein, A. S. Sheremet, E. Giacobino, and J. Laurat (2013), "*Reversible optical memory for twisted photons.*" Optics Letters **38** (5), 712.

Vidrighin, M. D., O. Dahlsten, M. Barbieri, M. S. Kim, V. Vedral, and I. A. Walmsley (2015), "*Photonic Maxwell's demon*," arXiv:1510.02164 .

Vurgaftman, I., and M. Bashkansky (2013), "*Suppressing four-wave mixing in warm-atomic-vapor quantum memory*," Physical Review A **87** (6), 63836.

van der Wal, C. H., M. Eisaman, A. Andre, R. L. Walsworth, D. Philips, A. S. Zibrov, and M. D. Lukin (2003), "*Atomic Memory for Correlated Photon States*," Science **301** (5630), 196.

Walborn, S. P., D. S. Lemelle, M. P. Almeida, and P. H. S. Ribeiro (2006), "*Quantum Key Distribution with Higher-Order Alphabets Using Spatially Encoded Qudits*," Physical Review Letters **96** (9), 090501.

Wasilewski, W. (2007), *Źródła fotonów w łączności kwantowej*, Ph.D. thesis.

Wasilewski, W., P. Kolenderski, and R. Frankowski (2007), "*Spectral Density Matrix of a Single Photon Measured*," Physical Review Letters **99** (12), 123601.

Wasilewski, W., A. I. Lvovsky, K. Banaszek, and C. Radzewicz (2006), "*Pulsed squeezed light: Simultaneous squeezing of multiple modes*," Physical Review A **73** (6), 063819.

Webb, J. G., and E. H. Huntington (2009), "*Photostatistics reconstruction via loop detector signatures*," Optics Express **17** (14), 11799.

Weisstein, E. W. (2015), "*Stirling Number of the Second Kind*," From MathWorld–A Wolfram Web Resource .

Wolfgramm, F., C. Vitelli, F. A. Beduini, N. Godbout, and M. W. Mitchell (2012), "*Entanglement-enhanced probing of a delicate material system*," Nature Photonics **7** (1), 28.

Wootters, W. K., and W. H. Żurek (1982), "*A single quantum cannot be cloned*," Nature **299** (5886), 802.

Zielińska, J. A., F. A. Beduini, N. Godbout, and M. W. Mitchell (2012), "*Ultranarrow Faraday rotation filter at the Rb D1 line.*" Optics Letters **37** (4), 524.